Final Report

FDOT Contract NO.: BDV24-977-17

DEVELOPMENT OF A SINKHOLE RISK EVALUATION PROGRAM

Prepared by:

Boo Hyun Nam, Ph.D. (Principal Investigator)
Ryan Shamet, M.S., E.I.
Moataz Soliman, M.S.
Dingbao Wang, Ph.D.
Hae-Bum Yun, Ph.D.

Department of Civil, Environmental, and Construction Engineering
University of Central Florida
12800 Pegasus Drive, 442B, Engineering II
Orlando, FL 32816

Developed for the

Project Manager: David Horhota, P.E., Ph.D.

June 2018

DISCLAIMER

The opinions, findings, and conclusions expressed in this publication are those of the authors and not necessarily those of the Florida Department of Transportation or the U.S. Department of Transportation.

SI (MODERN METRIC) CONVERSION FACTORS (from FHWA)

Approximate Conversions to SI Units

Symbol	When You Know	Multiply By	To Find	Symbol
		Length		
in	inches	25.4	millimeters	mm
ft	feet	0.305	meters	m
yd	yards	0.914	meters	m
mi	miles	1.61	kilometers	km
		Area		
in^2	square inches	645.2	square millimeters	mm^2
ft^2	square feet	0.093	square meters	m^2
yd^2	square yard	0.836	square meters	m^2
ac	acres	0.405	hectares	ha
mi^2	square miles	2.59	square kilometers	km^2
		Volume		
fl oz	fluid ounces	29.57	milliliters	mL
gal	gallons	3.785	liters	L
ft^3	cubic feet	0.028	cubic meters	m^3
yd^3	cubic yards	0.765	cubic meters	m^3
		NOTE: volumes greater than 1000 L shall be shown in m^3		
		Mass		
oz	ounces	28.35	grams	g
lb	pounds	0.454	kilograms	kg
T	short tons (2000 lb)	0.907	megagrams (or "metric ton")	Mg (or "t")
		Temperature (exact degrees)		
°F	Fahrenheit	5 (F-32)/9 or (F-32)/1.8	Celsius	°C
		Illumination		
fc	foot-candles	10.76	lux	lx
fl	foot-Lamberts	3.426	$candela/m^2$	cd/m^2
		Force and Pressure or Stress		
lbf	poundforce	4.45	newtons	N
lbf/in^2	poundforce per square inch	6.89	kilopascals	kPa

Approximate Conversions from SI Units				
Symbol	**When You Know**	**Multiply By**	**To Find**	**Symbol**
Length				
mm	millimeters	0.039	inches	in
m	meters	3.28	feet	ft
m	meters	1.09	yards	yd
km	kilometers	0.621	miles	mi
Area				
mm^2	square millimeters	0.0016	square inches	in^2
m^2	square meters	10.764	square feet	ft^2
m^2	square meters	1.195	square yards	yd^2
ha	hectares	2.47	acres	ac
km^2	square kilometers	0.386	square miles	mi^2
Volume				
mL	milliliters	0.034	fluid ounces	fl oz
L	liters	0.264	gallons	gal
m^3	cubic meters	35.314	cubic feet	ft^3
m^3	cubic meters	1.307	cubic yards	yd^3
Mass				
g	grams	0.035	ounces	oz
kg	kilograms	2.202	pounds	lb
Mg (or "t")	megagrams (or "metric ton")	1.103	short tons (2000 lb)	T
Temperature (exact degrees)				
°C	Celsius	1.8C+32	Fahrenheit	°F
Illumination				
lx	lux	0.0929	foot-candles	fc
cd/m^2	candela/m^2	0.2919	foot-Lamberts	fl
Force and Pressure or Stress				
N	newtons	02.225	poundforce	lbf
kPa	kilopascals	0.145	poundforce per square inch	lbf/in^2

* SI is the symbol for the International System of Units. Appropriate rounding should be made to comply with Section 4 of ASTM E380. (Revised March 2003)

TECHNICAL REPORT DOCUMENTATION PAGE

1. Report No.	2. Government Accession No.	3. Recipient's Catalog No.
4. Title and Subtitle Development of a Sinkhole Risk Evaluation Program		5. Report Date June 2018
		6. Performing Organization Code
7. Author(s) Boo Hyun Nam, Ryan Shamet, Moataz Soliman, Dingbao Wang, Hae-Bum Yun		8. Performing Organization Report No.
9. Performing Organization Name and Address University of Central Florida 4000 Central Florida Blvd. Orlando, FL 32816-2450		10. Work Unit No. (TRAIS)
		11. Contract or Grant No. BDV24-977-17
12. Sponsoring Agency Name and Address		13. Type of Report and Period Covered
		14. Sponsoring Agency Code

15. Supplementary Notes
Dr. David Horhota of the State Materials Office at the Florida Department of Transportation served as the project manager for this project.

16. Abstract
Sinkholes are a complex, natural problem that requires the understanding of multiple disciplines such as geology, geochemistry, groundwater, and geotechnical engineering. The goal of this proposed research is to develop an integrated program that can evaluate the level of sinkhole risk (or vulnerability) so that geotechnical engineers are properly guided for design and remediation projects. This report presents (1) development of a high-resolution groundwater-recharge model and map, (2) a systematic procedure to identify and evaluate the level of sinkhole raveling and subsequent vulnerability based on *in situ* CPT methods, (3) a pilot project that develops an *in situ* sensing/monitoring program, and (4) a numerical analysis stability technique to estimate the safety against soil collapse for the detected conditions. The project has developed several characterization tools which can be implemented for sinkhole vulnerability assessment of a project from a geotechnical and hydrogeology perspective. The tools include a high-resolution groundwater map, contour of groundwater flow based on *in situ* piezometers, raveling chart and sinkhole resistance ratio (SRR), and finite element (FE) based stability analysis. These tools may either be implemented separately, or together, to better understand the vulnerability of a sinkhole.

17. Key Word	18. Distribution Statement
Sinkhole, Risk, Groundwater, Piezometer, CPT, Finite element (FE) analysis	

19. Security Classif. (of this report)	20. Security Classif. (of this page)	21. No. of Pages	22. Price
		166	

Form DOT F 1700.7 (8-72) Reproduction of completed page authorized

ACKNOWLEDGEMENTS

This research was funded by the Research Center of the Florida Department of Transportation (FDOT). Dr. David Horhota of the FDOT State Materials Office served as the project manager and provided the overall direction for the project. Thank you to FDOT District 5 Geotechnical Department, especially Kathy Gray and Mike Byerly for their assistance with project inception and data sharing. The authors are also thankful for the supports of Mr. Ton Tu and Drs. Han Xiao and Manoj Chopra in the Department of Civil, Environmental, and Construction Engineering at the University of Central Florida, as well as the State Materials Office drill/exploration team for their valuable field work and expertise.

EXECUTIVE SUMMARY

Florida is considered as one of the most sinkhole-active areas in the United States. With sinkhole incidents making the news on a weekly basis, the "sinkhole problem" seems to only be increasing as Florida's population and infrastructure expand into virgin, fragile karst terrain. Due to the unpredictability and sudden formation of cover-collapse-style sinkholes, the development of a sinkhole detection and monitoring technique is imperative to minimize the sinkhole-induced hazards. Several methods have been used in the past to evaluate future sinkhole vulnerability at a site, either prior to or after sinkhole formation was detected. These methods include intrusive geotechnical tests, such as Standard Penetration Tests (SPT) and Cone Penetration Tests (CPT), non-destructive geophysical methods, and sensor-based groundwater monitoring methods. However, few studies are available that offer a comprehensive understanding of the sinkhole mechanism and risk evaluation techniques, through combining geotechnical, hydrogeological, and in-depth numerical modeling aspects.

The objective of this study is to develop an integrated program that can evaluate the level of sinkhole risk (or vulnerability) so that geotechnical engineers are properly guided for design and remediation projects. The specific work tasks of this study are (1) to develop a high-resolution recharge map, (2) to develop a systematic procedure to evaluate the level of sinkhole vulnerability based on *in situ* CPT methods, (3) to explore a pilot project that includes an in situ sensing/monitoring program, and (4) to develop a numerical analysis stability technique to estimate the factor of safety against soil collapse for the detected conditions. The project delivers four analysis techniques discussed in this report, including long-term critical hydraulic gradient identification, predictive groundwater recharge model (MODFLOW), raveling chart and sinkhole resistance ratio from CPTs, and numerical stability modeling of detected raveled cavity (Plaxis 2D). Each one of the techniques can be used independently or in combination, for assessment and evaluation of premature sinkhole formation within a project site. Examples of implementation of each evaluation technique, at project sites in Florida where sinkhole activity has been identified, are also presented in this report in each respective chapter. Guidelines are also established for each technique, in an effort to standardize the analysis methodology to maximize accuracy of results.

The first technique discussed (Chapter 3) is the use of a piezometer array within a project site to monitor and detect irregular behavior in the groundwater elevations, which may identify concentrated groundwater recharge or internal soil erosion. When piezometers are strategically and properly spaced within a site, interpolation and contouring mapping between piezometer locations can be used to estimate the hydraulic gradients (i.e., $\Delta H/L$) within the surficial soils. In areas where these gradients are very large (e.g., either smaller length "L" or large difference in head "ΔH"), the vulnerability of internal erosion is very high because the seepage force within soil is directly proportional to the hydraulic gradient. The piezometric elevations within a site, obtained from the piezometers, is also required for calibration of the groundwater recharge predictive model.

The second technique (discussed in Chapter 4) is the development and use of a high-resolution groundwater recharge map, using MODFLOW. Because Florida's cover-collapse sinkholes are a

result of a covered and submerged karst limestone, it is widely accepted that a major driving mechanism of sinkhole formation and subsequent collapse is the natural (or man-induced) recharge of water from a surficial aquifer to the Floridan Aquifer system. Therefore, where there is higher recharge rate, the soil is more vulnerable to sinkhole formation. This has been verified in previous studies which identified a correlation between reported sinkholes and previous understanding of regional groundwater recharge rates (Gray, 1994) (Xiao et al., 2016). The importance of this study, however, is the procedure to develop a high-resolution model and map which can be utilized for site characterization, rather than the previously developed regional recharge maps. Using the numerical model program of MODFLOW, along with input of site piezometric and hydrogeological parameters, a map of predictable recharge rate values was developed for two study sites, with a spatial resolution of 9.8 x 9.8 ft (or 3 x 3 m). Then, by correlating ranges of recharge rate with density of the historically reported sinkhole occurrence, a relative risk of sinkhole formation was assigned for each category. The resulting map can be used to not only predict the amount of groundwater recharge at various locations within a project, but also to identify the potential risk of sinkhole formation with high-resolution spatially.

The third technique developed a refined analysis method using the Cone Penetration Test (discussed in Chapter 5). Although many studies have correlated CPTs resistance values with soil behavior types, as well as other geotechnical design parameters, there is a lack of research regarding CPT resistance value criteria in karst soils; especially those which have experienced internal erosion or loosening due to sediment transport. CPT data was collected from several known sinkhole-active sites where the loose soil detected above the limestone was verified to be raveled based on known sinkholes within a few feet of the CPT sounding. The CPT data was normalized and filtered to obtain ranges of values for both tip resistance (Q_{tn}) and sleeve friction (f_s) measurements, which represent the verified raveled material. These value thresholds were plotted on a scatter plot, allowing for easy identification of raveled material during initial subsurface exploration. Also formulated was an update to the CPT comparison sinkhole index (i.e., Raveling Index) first proposed by FDOT engineers Foshee and Bixler (1994). The raveling index was updated to include the CPT tip resistance and estimated *in situ* overburden stress. Coined as the *Sinkhole Resistance Ratio*, this index shows a stronger correlation between sinkhole-collapsed sites and non-collapsed raveling sites. The proposed Sinkhole Resistance Ratio (SRR) can quickly be calculated for each CPT location and can be used to identify the expanse and severity of the current state sinkhole formation.

The fourth analysis technique developed and presented in this report is the stability charts using Finite Element Modeling (FEM) through PLAXIS 2D (Chapter 6). These stability charts allow for quick estimation of the factor of safety (FS) against collapse. The required inputs for the chart are simply the encountered raveling zone thicknesses and the non-raveled density and cohesion values – easily estimated through CPT correlations. The resulting point within the stability chart will lie within a zone of *Factor of Safety* against shear failure. Therefore, any soil conditions yielding a FS close to, or less than, 1.0 are believed to be an extremely unstable condition. These charts can also be helpful when estimating how an additional surface loading (e.g., shallow foundation structure or embankment) may affect the stability of the current karst soil conditions.

TABLE OF CONTENTS

LIST OF FIGURES

LIST OF TABLES

LIST OF ABBREVIATIONS

CPT	-	Cone Penetration Test
FDOT	-	Florida Department of Transportation
FHWA	-	Federal Highway Administration
FSRI	-	Florida Sinkhole Research Institute
SBT	-	Soil Behavior Type
SPT	-	Standard Penetration Test
TSF	-	Tons per square foot (2000 lbs/ft^2)
USGS	-	United State Geological Survey

1. INTRODUCTION

1.1. Problem Statement

Sinkholes are a major geohazard in Florida, which are life-threatening and cause significant damage to civil infrastructure. Numerous studies on sinkholes have been conducted from geological and hydrogeological viewpoints, and general sinkhole mechanisms have been identified. Cover-collapse and cover-subsidence sinkholes are common in Florida. Sinkhole vulnerability assessment is no simple task, and many times these events occur with only minutes of warning before the ground gives way. Central Florida sinkholes are a culmination of soil instability, geological formation and degradation, and hydrological extreme events and are more frequent in times following severe drought (Tihansky, 1999). Due to this combination of factors, exact sinkhole collapse processes are difficult to predict.

The soil structure above the limestone where cavities (e.g., crack, fissure, etc.) exist becomes structurally weak over time due to the growth of those cavities in limestone and the development of piping and erosion in the clay layer on top of the limestone (soils classified as the *Hawthorn Group*). Based on the geological and geotechnical formations, groundwater plays a critical role to trigger sinkholes in Florida. Groundwater recharge, which is due to a higher head in the surficial aquifer (undifferentiated soils) than that of the confined aquifer (karst sedimentary rock), significantly affects the occurrence of sinkholes. These findings help explain how Florida sinkholes form, and this information is beneficial in managing surface water and groundwater.

Civil (and geotechnical) engineers dealing with design, remediation, and construction projects of civil infrastructure near/on sinkhole-active zones still need more practical and quantifiable information with respect to sinkhole risk rating. Often, geotechnical engineers are tasked to estimate the level of sinkhole risk during initial subsurface investigation for structural design or if/when suspicious settlement cracks are detected in an existing structure. However, there is still no systematic and scientific means that can evaluate the level of sinkhole risk (or vulnerability), especially from a geotechnical engineering perspective.

1.2. Project Description

In this report, the researchers investigated a method of evaluation for common sinkholes in Florida (especially central Florida). The tools presented in this study were developed to aid the geotechnical engineer to expand on analyses used in Florida for site-specific risk assessment of sinkhole formation. The project was primarily focused on two known (or suspected) sinkhole-active sites where comprehensive subsurface exploration and site characterization were previously performed. *In situ* pore-water pressure measurement was used to validate the groundwater recharge prediction model. In addition, the groundwater measurement and other available characterizing data (e.g., CPT, boring, soil properties, etc.) were used as inputs to the stability analysis model.

The research team studied the detailed mechanism of Florida's sinkholes and quantified the influence of major parameters (e.g., recharge, overburden soil thickness, soil properties, etc.) on sinkhole development through physical groundwater model tests. To address this issue, the research team

needed a diverse (but essential) research background in geomaterials, soil erosion and piping, water resource engineering (e.g., interaction of surface water and groundwater), *in situ* sensing and monitoring along with advanced data processing.

1.2.1. Research Objectives

Sinkholes are a complex natural problem that requires understanding of multi-disciplines such as geology, geochemistry, groundwater, and geotechnical engineering. The goal of this proposed research is to develop an integrated program that can evaluate the level of sinkhole risk (or vulnerability) so that geotechnical engineers are properly guided for design and remediation projects. The objectives of this proposed research are: (1) to develop a high-resolution recharge map, (2) to develop a systematic procedure to evaluate the level of sinkhole vulnerability based on *in situ* CPT methods, (3) to explore a pilot project that develops an *in situ* sensing/monitoring program (the pilot project will be aimed at measuring and monitoring groundwater condition over time so as to help the sinkhole vulnerability assessment), and (4) to develop a numerical analysis stability technique to estimate the factor of safety against soil collapse for the detected conditions.

1.2.2. Research Scope

The scope of this research can be divided into three main sections regarding the three disciplinaries used to assess site sinkhole vulnerability and risk. The three categories are: 1) site characterization tools, 2) groundwater monitoring application, and 3) numerical modeling. Each category is first introduced and discussed as an independent sinkhole risk evaluation tool, then presented as a comprehensive evaluation program. A case study is also shown for a project site through implementing all three categories and how to assess vulnerability to sinkhole formation and potential future risk to infrastructure.

2. BACKGROUND

2.1. Karst Terrain

Geologically speaking, the Florida Peninsula is a relatively juvenile land mass. However, its formation process has consisted of many environmental changes contributing to its unique geology and consequent geotechnical engineering concerns. With each varying ice age, the landmass which we now call Florida has emerged and been submerged below the sea level. During times of submergence, shallow warm-water coral reefs form and die, depositing varying levels of calcium and magnesium carbonate on the sea floor. Meanwhile, ancient rivers rooted in the Appalachian Mountains, flow south and deposit alluvial sediment over the submerged Florida peninsula, creating deltas and salt marshes.

As the sea level slowly recedes and the exposed Florida peninsula expands, varying sand deposits created from wave erosion start to accumulate over the carbonate deposits and alluvial sediment. Over time, the marine and river deposited matter, now with increased stresses from the sandy overburden, lithify to form carbonate-based sedimentary rock such as limestone, dolostone, and coquina. Repetition of this process, as the sea levels rise and fall, expose and conceal these layers of growing carbonate rock. In some areas, water traveling along the ground surface erodes the protective sandy overburden and river deposits (now consolidated into impermeable clay). The exposed carbonate rock experiences weathering both physically and chemically by the slightly acidic surface water. Cavities form within the soluble carbonate rock, and as the geological cycle repeats itself, water becomes trapped within the buried rock like a sponge. This process leads to the formation of what is known as karst topography or terrain.

Although karst terrains can be found in many areas of the world (i.e., the *Kraški rob¸* a large limestone plateau located Slovenia in which the word “karst” is derived from), Florida’s karst environment is unique because it creates the Floridan aquifer system (FAS). The fine-grained soil deposited by rivers and marine sediment, over time, compressed into a layer of silt and clay laying directly over the porous bedrock. This formation is known to geologists as the Hawthorn Group. Compared to the cavity ridden bedrock below it, the Hawthorn Group is widely considered ‘impermeable’ and it acts as an impedance for infiltrating groundwater. The result is a dual aquifer system: an unconfined, or surficial, aquifer of perched groundwater over the aquitard layer, and a confined aquifer located within the pores and cavities of the bedrock formations. The vertical travel of surface water through the surficial aquifer and impermeable layer filters the water allowing many Floridians to utilize the FAS as a reliable source of clean drinking water. Also, in areas where sections of the FAS is exposed near or at the ground surface, the crystal clear freshwater flows out of limestone fissures, forming springs. These springs not only create vast ecosystems which encourage sustainability of Florida’s endangered species, but they also draw tourists in from all over the state/country, boosting the local economies.

2.2. Karst Features in Central Florida

Although there are great benefits resulting from karst geology, there are also many hazards. Arguably the most well-known geohazard resulting from karst geology are sinkholes. These concentrated instances of severe subsidence can wreak havoc on infrastructure supported on shallow foundations. As Florida's urban areas sprawl out to virgin karst terrain, sinkholes have been occurring more frequently and causing more damages than ever before (Florida Office of Insurance Regulation, 2010). Although mechanisms for sinkhole formation have been thoroughly studied by geologists and hydrologists (Tihansky, 1999) (Wilson & Beck, 1992), there is still a strong need for research in the field of sinkhole detection and risk assessment from a geotechnical engineering perspective.

2.2.1. Sinkhole Formation

Dissolution of Bedrock

Most sinkhole occurrences in central Florida originate from the dissolution of the soluble carbonate bedrock. The composition and height of overburden soils then governs the specific type of sinkhole which is most probable to form. Florida's bedrock formations consist of varying ages of limestone and dolomite; both rocks composed primarily of calcium carbonate ($CaCO_3$). The solution process begins as rainwater absorbs a slight amount of carbon dioxide. As water percolates, downward through the soil, the groundwater picks up even more carbon dioxide, generated by decaying organic matter. This results in a weak carbonic acid, which attacks the limestone as it seeps into fissures and recharges the Floridan aquifer. The following dissolution process is summarized in the below chemical equations.

$$H_2O + CO_2 \rightarrow H_2CO_3 \qquad \text{.....Eq. 2.1}$$

(Rainwater absorbs carbon dioxide gas to form carbonic acid)

$$H_2CO_3 + CaCO_3 \rightarrow 2HCO_{3\,(aq)}^{-} + Ca_{(aq)}^{2+} \qquad \text{.....Eq. 2.2}$$

(carbonic acid reacts with limestone and yields dissolved bicarbonate ions and calcium ions)

The movement of water vertically through the rock medium follows the most favorable pathway, usually following a fissure or fracture. Over time, these pathways dissolve more rapidly than the surrounding areas because it carries more water. Because it is now larger, the favored fissures can transmit water in even greater quantities, therefore self-accelerating the erosion process. Because of this process, it is more common to find fewer, yet larger, connected networks of cavities within the limestone with competent rock in between (i.e., the "swiss cheese block look"), rather than a vast plain of dissolved rock. These connected cavities allow sediment transport and erosion of the fine-grained soil above the limestone which is the starting mechanism for sinkhole formation.

Erosion of Overburden Soil

Due to the varying thickness of cover soils over the soluble bedrocks in central Florida, sinkhole formation type and collapse size is dependent on the type and formation of the finer-grained stratigraphy of the overburden soils. Although some areas in North Florida, where the limestone is exposed on the surface, experience rock ceiling collapse sinkholes, central Florida sinkholes are almost always caused by downward migration of soil particles into the cavities within the bedrock. The thickness, types, and densities of the overburden soils greatly affect the type of sinkhole probable to form as shown in Figure 2-1. The vertical migration of soil sediment downwards into the limestone cavities can be caused by gravity or, expedited by seepage forces from groundwater recharging the deeper aquifers. These areas of higher recharge rates have also shown direct correlation to higher sinkhole occurrences (Gray, 1994). Degrading infrastructure, such as utility lines (e.g., sewer and stormwater lines) or even leaking pools, can also play a major role in sinkhole formation; speeding up the natural erosive processes.

The average thickness of overburden soils varies greatly in the central Florida region. Generally, the thicker the overburden soil layer, the less likely a sinkhole is to occur. However, if a sinkhole does form, it is more likely to be much larger in diameter and depth compared to other sinkholes in the state. This is evident by the numerous relic sinkholes in this region (Area IV (pink), Figure 2-1). An example of such can be found underneath Deep Lake, just south of the town of Arcadia, Florida. This near perfect circular lake has been mapped by divers and discovered to be over 300 feet deep. The presence of a debris pile and distinct hour-glass shaped walls also suggests this mysterious lake was formed by a deep cover-collapse sinkhole. The type of overburden soils in a certain region plays an imperative role in their susceptibility to erosion into the limestone voids, thus affecting the type of sinkhole formed. The next section discusses the generalized classifications of sinkholes in central Florida.

2.2.2. Sinkhole Classification

Sinkholes can be classified into general categories based on their formation type and typical landscape. These classifications are commonly referenced in engineering and geology literature. In central Florida, where the bedrock is primarily limestone and the overburden soils are majority clayey or silty sands to clean sands, there are three general categories of sinkholes: solution, cover-subsidence, and cover-collapse. A report published by the US Geological Survey (USGS) in cooperation with the Florida Sinkhole Research Institute (FSRI), classified sinkholes the following way (Beck & Sinclair, 1986):

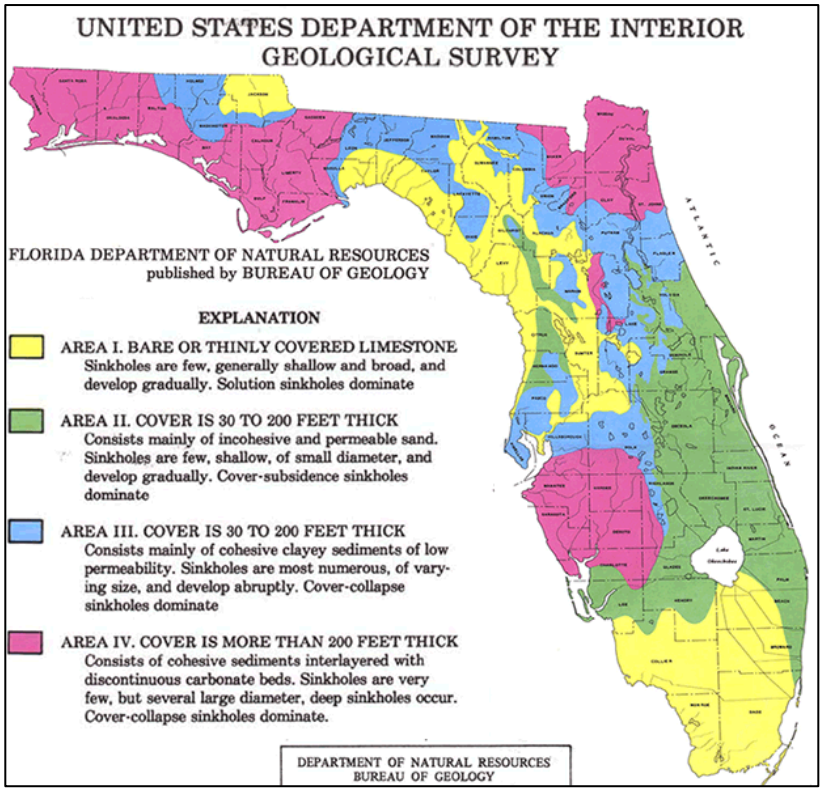

Figure 2-1. Florida sinkhole type map

Figure 2-2. (left) Solution sinkhole, (right) cover subsidence sinkhole underneath roadway (Source: FDOT)

Solution Sinkholes

In areas where limestone is exposed or thinly covered by permeable sands, solution sinkholes are most common. These sinkholes generally tend to be smaller in size but more frequent and easily triggered by rain events. In Central Florida, solution sinkholes are common just north-east of Tampa in a geomorphological structure known as the Ocala platform. In this area (Area I in Figure 2-1) the depth to water table is much greater than the surrounding area, therefore solution sinkholes often result in dry karst caves. Figure 2-2 (left) shows a picture of an irregularly shaped solution sinkhole in Newberry, Florida. This sinkhole formed after a large rain event eroded the thinly covered clayey sand into the pores of the underlain limestone. The depth of sinkhole measured about 6 feet, but the expanse was only a few feet wide. Large voids susceptible to devastating collapse commonly do not form because subsidence of the thin cover material, if any, occurs as the limestone surface dissolves. During site development, grading and filling can usually trigger these sinkholes, allowing contractors to identify and fill before any structure is placed on the sensitive limestone area. Because these sinkholes often open into large interconnected cavities within the limestone, an isolated solution sinkhole on a site is a seldom occurrence, therefore a thorough investigation of the surrounding geology should be performed before developing in this area.

Cover-Subsidence Sinkholes

In areas where the limestone is covered by thicker soil deposits that are relatively non-cohesive and permeable, sinkholes develop by subsidence. Individual particles of sand move downwards into the voids of the weathered limestone with cavities; like sand passing through an hour-glass. Since the overburden soils are non-cohesive, a structural arch is not able to develop, thus a subterranean void cannot fully form. Formation time for cover-subsidence sinkholes can vary from hundreds of years, to a couple days depending on the overburden thickness and water movement within the stratigraphy. These types of sinkholes are most common in the eastern part of central Florida (Area II, Figure 2-1). Figure 2-2 (right) shows an example of a cover-subsidence sinkhole forming underneath US-27 in Polk County. Much slower than a cover-collapse sinkhole, a cover-subsidence sinkhole can still result in extensive differential settlement over large areas. Leaking utility lines or poorly designed roadway drainage systems can also form cover-subsidence sinkholes by washing and eroding away the soil underneath.

Cover-Collapse Sinkholes

In west-central Florida, the sandy cover becomes gradually more cohesive with depth. A dense layer of slightly over-consolidated clayey sand or sandy clay overlaying the limestone surface (Hawthorn Group) can act as a bridge over a developing cavity. The cohesion within this dense layer can develop and support arching effects with no noticeable signs of settlement on the surface. Once the stability of the soil arch is compromised either by extensive internal erosion, additional surcharge surface loading, or extreme seepage forces, a cover-collapse sinkhole will form.

Cover-collapse sinkholes are generally the most devastating and can collapse with only minutes of warning. Figure 2-3 shows two photos of cover-collapse sinkholes occurring in west-central Florida. SPT borings performed near both collapses showed a thick clay layer overlaying the

cavity-ridden limestone. As the limestone cavity grew underneath, the cohesion within the clayey sand could hold up the soils above it; like a bridge. Eventually, collapse of the clay layer into the cavities occurred, resulting in the "throat" of the sinkhole (apparent in the left photo, highlighted by the dashed circle). The sandy sediment above then fails and collapses into the void, creating the larger diameter of collapse seen. Secondary collapses can continue as slope failure of the sandy soils continues, expanding the overall sinkhole size.

Although cover-collapse sinkholes provide little time for warning on the surface, the forming subterranean void can be detected using various subsurface exploration tests. However, a single test encountering an abnormally loose layer of cohesive soils directly above the weathered limestone does not necessarily mean a cover-collapse sinkhole is imminent. The information and findings presented in this report are focused on identifying and evaluating sinkhole formation.

Figure 2-3. Photos of devastating cover-collapse sinkholes in central Florida
(Source: FGS & FDOT)

2.3. Sinkhole Detection in Practice

Premature sinkhole detection is required to successfully mitigate a forming sinkhole before any structural damages occur to infrastructure; limiting the additional costs for repair. Figure 2-4 presents a theoretical project cost timeline for sinkhole mitigation/repair. In this timeline, we can see there is a crucial moment where mitigation becomes repair, causing the cost to increase substantially. This moment in time is the excessive ground surface settlements over a large area, a cover-collapse, or severe slope failure in a cover-subsidence sinkhole. Perhaps the largest uncertainty in the sinkhole cost timeline is, unfortunately, time itself. Sinkhole subterranean void growth and collapse is a very difficult aspect to quantify. Complete collapse and opening of the sinkhole usually takes only a couple minutes or hours, however, the forming void underneath may be a result of hundreds or even million years of internal erosion at the rock-soil interface. Current techniques are being further developed to provide an early warning system of sinkhole collapse (Rizzo & Dettman, 2017), however the sinkhole risk assessment cannot be fully understood over time unless the rate of erosion is characterized.

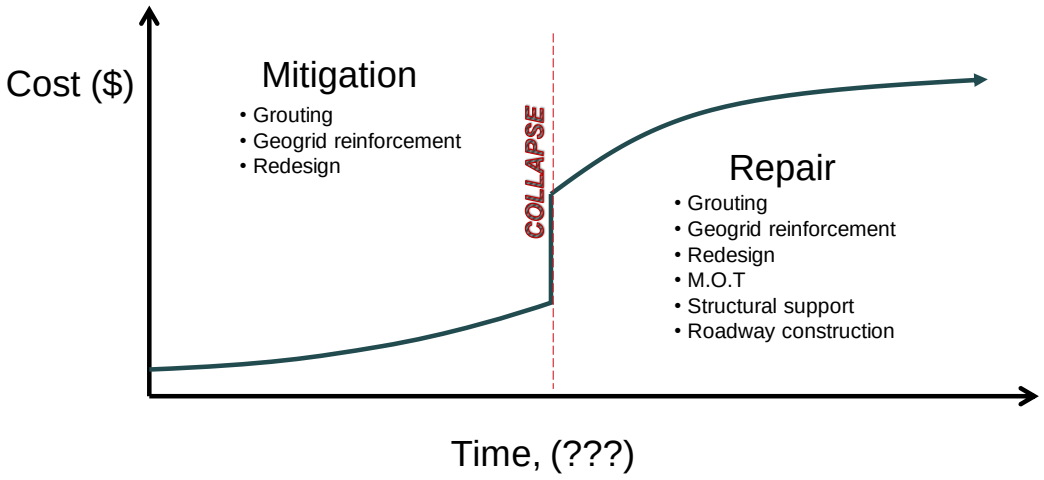

Figure 2-4. Conceptual cost timeline for sinkhole mitigation and repair

2.3.1. Subsurface Exploration Testing

A forming sinkhole may be detected using a single test showing very low strength soils at a certain depth at which does not agree with the surrounding soils comparable to the expected density from its original formation. Initial subsurface exploration tests, such as SPT and CPT, can identify these anomalous soil layers which may suggest a forming sinkhole.

Standard Penetration Testing (SPT)

SPTs are valuable in sinkhole detection because they can retrieve soil samples. Laboratory testing and soil classification can then be performed to identify the stratigraphy of the subsoil conditions, allowing engineers to better estimate whether soils may be suggestive of sinkhole formation. SPTs also provide penetration resistance data in the form of the number of blow counts (N) it takes to advance the sampling tip in 6-inch increments into the soil by a 140 lb hammer dropped 30 inches. In extremely loose sands or in soft clays, the drilling rods and sampling tip will advance into the soil under the self-weight of the rods or the hammer, without any additional forces being applied. These instances are labeled as “weight of hammer” or “weight of rod” conditions (WH or WR). When isolated cases of these conditions occur within a site, especially at reasonable depth directly above a refusal layer, sinkhole formation may be the cause. Further investigation is then commonly performed whether by additional SPTs or by geophysical testing. Figure 2-5 presents example soil boring logs from SPTs performed on the same project site in central Florida (Professional Services Industries, Inc. , 2014). The left boring shows a relatively normal soil stratigraphy consistent with the expected geology. The boring log on the right, however, encountered a significant region of very weak sandy soils at a depth of 60 feet, as shown by WR and the note that the rod fell from 63.5’ to 78.5’. Another SPT sign of problematic loose soils includes the complete loss of drilling fluid (usually bentonite slurry) that is circulated during the drilling to keep the bore-hole from collapsing. If loss of circulation occurs (denoted by the ‘←100%’ symbol), this means the drill tip progressed into a soil layer with similar characteristics to a void; that is, the soil is so loose that

the viscous bentonite mud is able to breach and travel through that layer away from the bore-hole. The boring log on the right side of Figure 2-5 presents an anomaly which warrants further investigation.

Cone Penetration Testing (CPT)

CPTs can also be used to detect potential forming sinkholes under the same principle discussed above regarding SPTs. However, instead of the blow count (N), CPTs record penetration resistance in the form of tip resistance (q_c) and sleeve friction (f_s) by pushing a probe hydraulically at a steady rate. This method is much more accurate at locating discrete horizons or discrepancies in the soil strata since the data collection rate is much higher than that of the SPT. However, the inability to obtain soil samples for lab testing or visual classification is a major limitation of the CPT, especially when using a single test to estimate site stratigraphy or geohazard potential. Therefore, "ground-truthing" is a common technique used when implementing CPTs for subsurface investigation. By conducting a CPT next to a conventional boring (such as an SPT), the CPT soil strength measurements (q_c and f_s) can be validated with actual soil type and index properties to provide a more accurate stratigraphy estimation. This technique is especially important when characterizing subsoil at a site with known karst geology. Figure 2-6 presents such an example of ground-truthing where a CPT tip resistance curve (q_c) with abnormally low values at a depth above the refusal layer, correlates strongly with the SPT suggesting sinkhole formation (see WH or WR conditions). SPT N-value trends strongly correlate with CPT tip resistance values (q_c) trends with depth. Once ground-truthing has been performed, CPTs can be performed throughout the site at a much quicker rate than that of SPTs, allowing for an efficient subsurface exploration and characterization (Rogers, 2006).

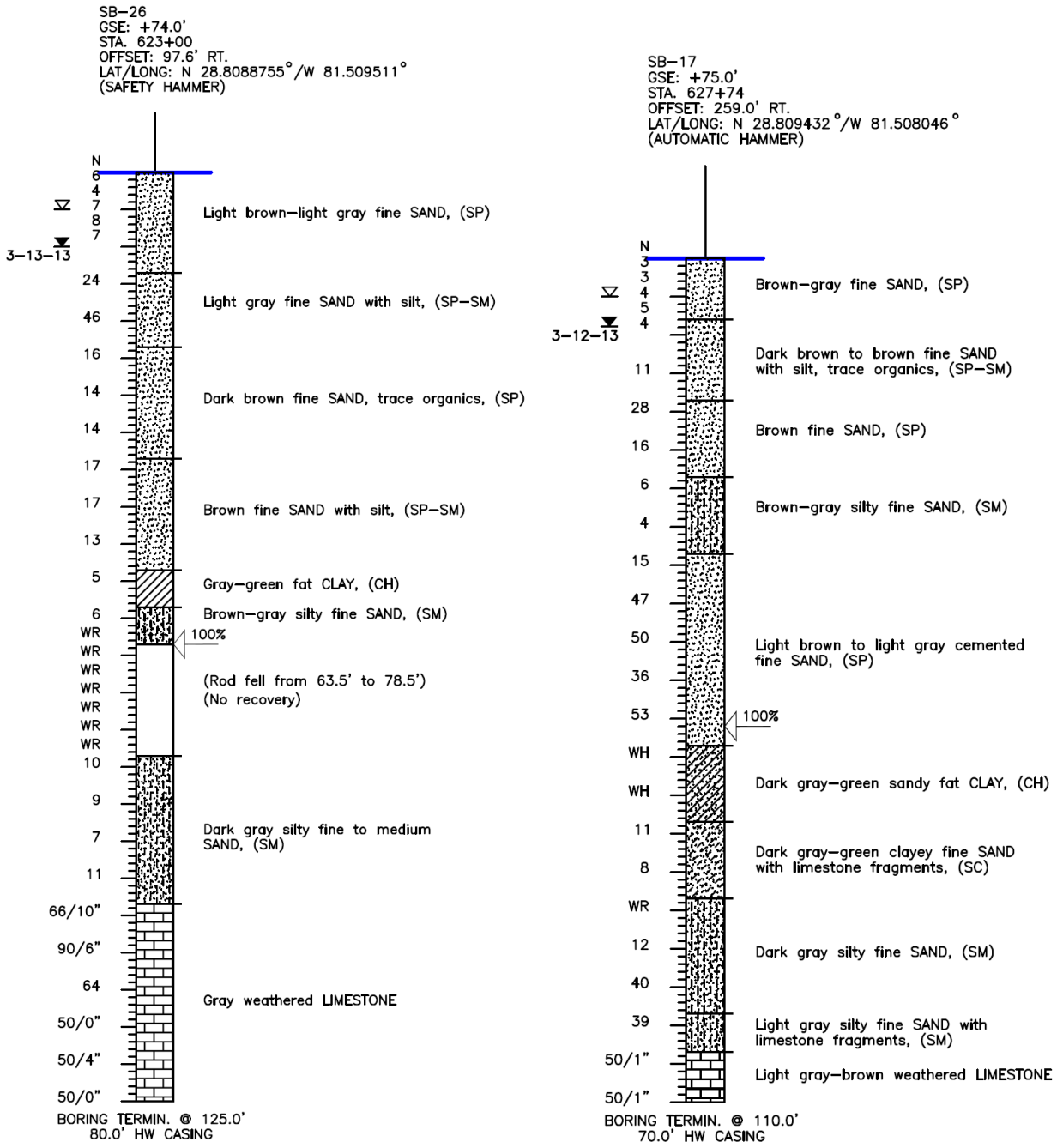

Figure 2-5. Example SPT boring logs in central Florida

(Source: Professional Services Industries, 2014)

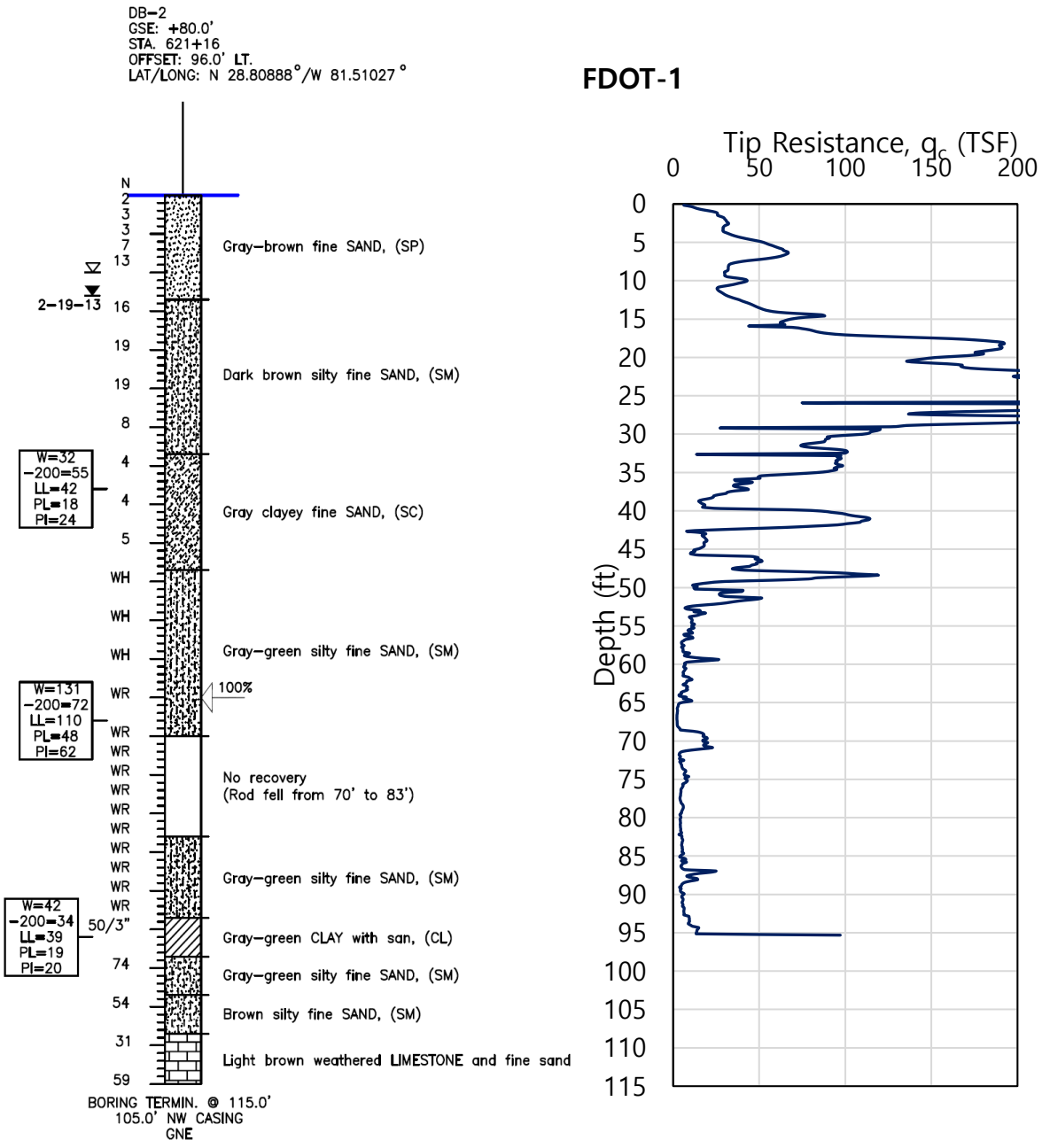

Figure 2-6. Example of "ground-truthing" between CPT q_c curve and SPT N-value

(Source: Professional Services Industries, 2014)

2.3.2. Geophysical Testing

Ground Penetrating Radar (GPR)

Ground Penetrating Radar (GPR) is widely used as a non-intrusive technique to locate subterranean anomalies such as buried pipes or abrupt changes in soil density. GPRs emit and receive electromagnetic waves (10 to 3,000 MHz) and use the respective time-lag information between transmissions to survey and "map" a cross-sectional area. Although most effective at shallower depths, GPRs are being more commonly employed for sinkhole detection as lower-frequency antennas are being developed to obtain improved resolution at greater depths. Specialized contractors and geophysicists have shown GPR is a functional method to detect a sinkhole anomaly (Professional Services Industries, Inc. 2014; Bullock & Dillman, 2003), but after detection, there is little information that can be obtained from the GPR data. Also, GPR data can be very difficult to interpret, especially when attempting to draw conclusions about potential sinkhole size or severity from the results. From the GPR refraction plot, engineers and geophysicists can easily identify areas with differing densities, but there is still a lack of a standardized methodology for characterizing the subsoil and correlating GPR results to soil strength parameters, severely limiting the GPR as an effective subsoil investigation technique.

Electrical Resistivity Indexing (ERI)

Electrical resistivity surveying is a geophysical method in which an electrical current is applied to the earth and the subsequent response is measured at the ground surface to determine the resistance of the underlying soil. Implanted electrodes read the electrical potential as volts and then, using Ohm's Law, are converted to resistivity values. Resistivity of earth materials is controlled by several properties, including composition, water content, and effective permeability (Professional Services Industries, Inc. , 2014). Through inversion modeling of the ER data, a resistance map of the subsoil along the investigated tract can be developed. Like GPR, ER has proven to be able to detect subterranean air-filled voids such as abandoned mine shafts (Sheets, 2002), however, the two techniques also share similar limitations. Interpretation of ER data is a very specialized task and requires extensive experience and knowledge of statistical modeling, soil electrical conductivity parameters, local geology, and expected soil composition. Geophysical testing methods, such as GPR and ER, are more commonly implemented to identify potential sinkhole zones or anomalies within the karst subsoil and are used in conjunction with SPT and CPT for site characterization, never as a lone technique.

3. SITE GROUNDWATER MONITORING

3.1. Introduction

The initial task performed in this study was the development of a continuous groundwater monitoring system and to implement such design at two known sinkhole-active sites. The monitoring system was operated with a signal processing algorithm to detect any abnormal signatures in the time histories of the sensor data, which could be related to prior or posterior causes of sinkhole events.

Two active sinkhole sites were selected. The first site is on the recently constructed toll-road, Wekiva Parkway (SR-429), about two thousand feet from the State Road 46 connector. The interchange is located in Section 27, Township 19 South and Range 27 East of Lake County, Florida. The location of Wekiva Parkway site is shown in Figure 3-1. There are three bridges at this site in which two of them are overpass bridges for future traffic, and the other one, which was originally planned as a roadway embankment, was constructed due to subsurface karst conditions encountered during previous studies. The second site is FDOT's retention pond located on the south side of the junction of State Road 26 and County Road 235 in Newberry, Florida. This site was selected because this is a well-known site where many *in situ* subsurface tests were conducted and sinkhole activity is currently occurring. The site location is shown in Figure 3-2.

Figure 3-1. Location of Wekiva Parkway sensor project area

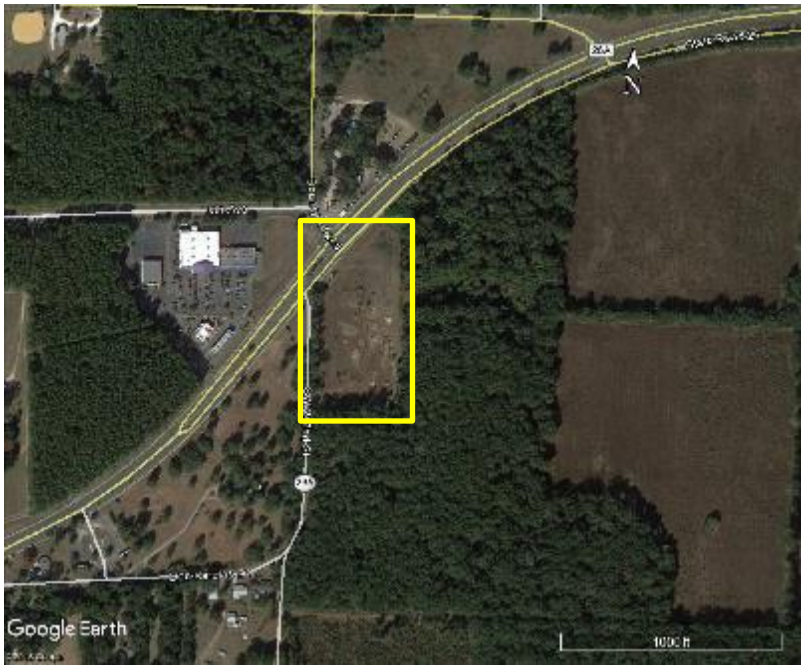

Figure 3-2. Location of Newberry detention pond sensor project area

3.2. Methodology

3.2.1. Equipment

In this study, piezometer *model 4500S-350kPa* from Geokon was used to measure water level. Model 4500S vibrating wire piezometer is used for long–term measurements of fluid pressures such as groundwater elevations and pore pressures when buried directly in embankments, fills, etc. It also can be installed inside boreholes, observation wells and standard (>19 mm diameter) piezometer riser pipe (Geokon, 2016). The selected sensors have very high-resolution and accuracy - 0.025 percent and ± 0.1 percent of Full Scale (F.S.) reading, respectively. Assuming the specific weight of water is 9.81 kN/m^3 and the sensor is placed 10 m underwater, the theoretical reading pressure is 98.1 kPa. The resolution of the sensor in this case is $0.025\% \times 98.1\, kPa = 0.0245\, kPa$ or 2.5 mm; meaning the sensor is able to detect any changes in water level larger than or equal to 2.5 mm. The accuracy of the sensor is ± 0.1 percent of Full Scale reading that means the actual pressure reading of the sensor may range from 98.00 kPa to 98.2 kPa. Details of sensors' specifications are listed in Table 3-1.

Table 3-1. Specification of Model 4500S – 350 kPa Piezometer

Model	Rated pressure	Over range	Resolution	Accuracy	Temperature range	Length x Diameter
4500S	350kPa	2×350kPa	0.025%F.S.	± 0.1%F. S.	$-20℃\ to\ 80℃$	133x19.1 mm

The input pulse train to the sensors and the output signal from the sensors were transmitted and received by dataloggers. There were five dataloggers at the first site (the intersection of State Road 46 and State Road 429 located in Sorrento, Florida) in which four of them were 4-channel dataloggers and the last one was a 16-channel datalogger as shown in Figure 3-3. The second site in Newberry, Florida only used one 16-channel datalogger. There are two types of signals received by dataloggers. The first and most important type of signal is called "Digits". The "Digits" for the vibrating wire transducer output when using linear conversion, calculated based on the following equation: $Digits = Frequency^2 \times 10^{-3}$. The frequency in this equation is the resonant frequency of the transducer measured in Hertz. For example, a piezometer sensor reading 9000 digits corresponds to a frequency 3,000 Hz. The second type of signal is temperature from thermistors embedded in piezometer sensors. Temperature at the depth where the sensor is located is used for pressure calibration since specific gravity of water varies over temperature. Measured data will be stored in 320K bytes of EEPROM memory, which translates into a memory storage capacity of 10,666 arrays for a 4-channel datalogger and 3,555 arrays for the 16-channel. Each array consists of the datalogger ID, day, time, battery voltage, datalogger temperature, vibrating wire sensor reading, and the sensor temperature. If data is sampled with a rate of 30 minutes per sample, it takes 222 days for the 4-channel and 74 days for the 16-channel to fill up the memory.

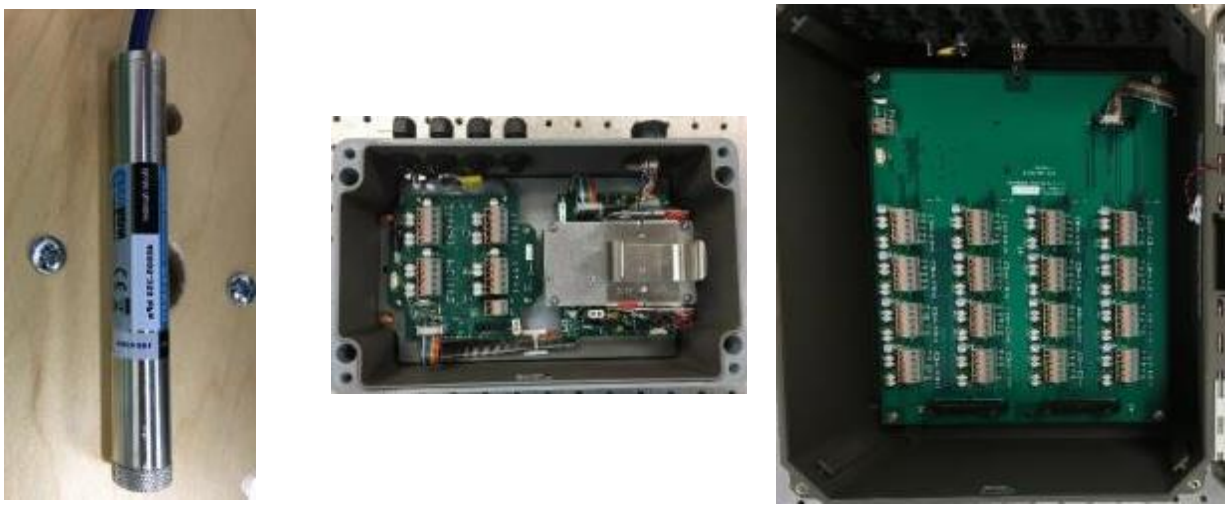

Figure 3-3. Sensor and dataloggers used in this study, (left) Geokon piezometer 4500S-350kPa, (middle) Geokon Datalogger model *8002-4*, and (right) Geokon Datalogger Model *8002-16*

To properly collect and record the piezometric readings on a consistent time interval, the collection software called "LogView" was used. All of the test parameters such as sampling rate, duration of measurement, data types, date, and time can be be imputted into the dataloggers for operation. This software is also capable of calculating hydrostatic water pressure at the location of the sensor using the following equation:

$Pressure = Calibration\ factor \times (Current$ "digits" $reading - Initial$ "digits" $reading)$
or $P = G \times (G_1 - G_0)$. Calibration factor (G) is unique for each sensor, which can be found in the

calibration report from the manufacture. Since the piezometers are installed in the field, which is an uncontrolled environment, the temperature may vary; hence, temperature correction is necessary. The pressure equation accounted for the temperature change is:

$$P = G(G_1 - G_0) + K(T_1 - T_0) \quad \text{.....Eq. 3.1}$$

Where, G is vibrating wire gate factor
K is thermistor factor
G_1 and G_0 are current and initial "Digits" readings
T_1 and T_0 are current and initial temperature readings

After water pressures are determined, the height of the water column above the sensors can be calculated easily by dividing the measured pressure by the specific gravity of water.

3.2.2. Installation of Piezometers

The ideal scenario is to place the piezometer sensors within a stratum consisting of primarily sandy soils since it has high hydraulic conductivity, so any changes in water level can be measured quickly and more accurately. Adversely, clayey soils are avoided because of high fines content (% passing the No. 200 sieve), which may clog the piezometer's filter leading to erroneous results.

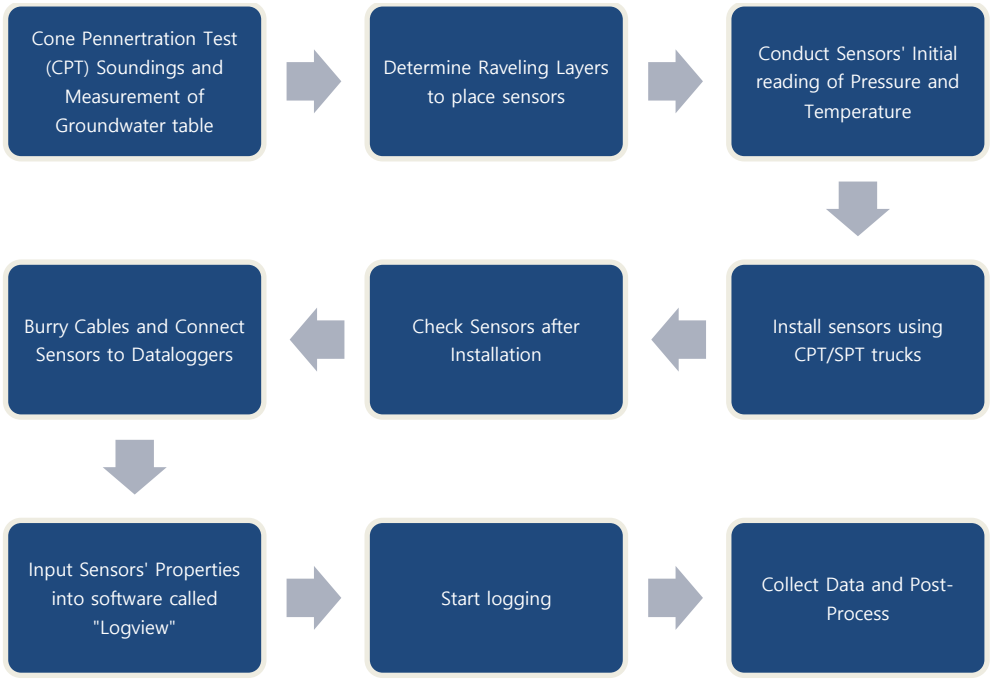

Figure 3-4. Flow chart of sensor installation

Figure 3-4 presents the general procedure of identifying the sensor depth and procedure for collecting data. Determination of the exact raveling depths, as well as the location and spacing of the sensors, will be discussed in Chapters 5 and 7 of this report, respectively.

The most sensitive step of the groundwater monitoring procedure is the fourth step which is to install sensors at the predetermined depth using CPT or SPT trucks. During the installation process, sensors were protected by an adapter. One end of the adapter was connected to the rod from the CPT/SPT truck and the other end was sealed by a sacrificial cone-tip, which was connected to the sensor via a small cable (fishing leader line was used in this case). Details of the adapter's dimensions and image are shown in Figure 3-5. When the desired depth was achieved, adapter and sensor were held in place for about 15 minutes before the drill rods were hydraulically raised. During this process, the sacrificial cone-tip from the adapter remained at the desired depth, thus holding the sensor at the same depth by means of the fishing leader line. To make sure all sensors worked after installation, they were checked using a handheld reader device; then, the values were compared to the theoretical pressure for each sensor. The next steps were to bury the cables and connect the sensors to the dataloggers, input sensors' properties into the LogView software, start logging, collect data, and perform post-processing.

Installation of the piezometers at the Newberry retention pond site followed a more traditional method. The first step of the installation process was to measure the initial values of pressure and temperature of each piezometer in the field (above ground). This step needed to be handled with a high degree of attention since all of the following readings used these initial values as references. To read the initial value, first the piezometer filter was removed in order to let the piezometer adapt with the *in situ* pressure and temperature and after about five minutes the initial values were read by the handheld reader device, as shown in Figure 3-7. The next step was to drill, wash, and case the piezometer wells, to a depth of 30 feet below grade. Once the piezometer was lowered into the cased boring, approximately 2 lb of clean concrete sand was poured down the casing to hold the piezometer in place. Then, the casing was removed while insuring minimal disturbance to the piezometer and piezometer cable. Once the casing was removed, additional concrete sand was poured down the open hole as well as bentonite "plug" chips and pea-gravel. The piezometers were then checked with a handheld reader device, similarly to the Wekiva site procedure.

The final steps were to bury the cables in the ground and to connect them to the datalogger. Due to the hard soil and limestone near the surface, a rock trencher was used to create a 6" deep line to bury the cables. In areas where the cables crossed over outcrops of limestone, concrete sand and limestone aggregate was used to fill the drilled trench. Once this was accomplished, the sensors' properties were input into the LogView software and logging commenced. The pictures shown in Figure 3-6 are from the installation process at the Newberry site.

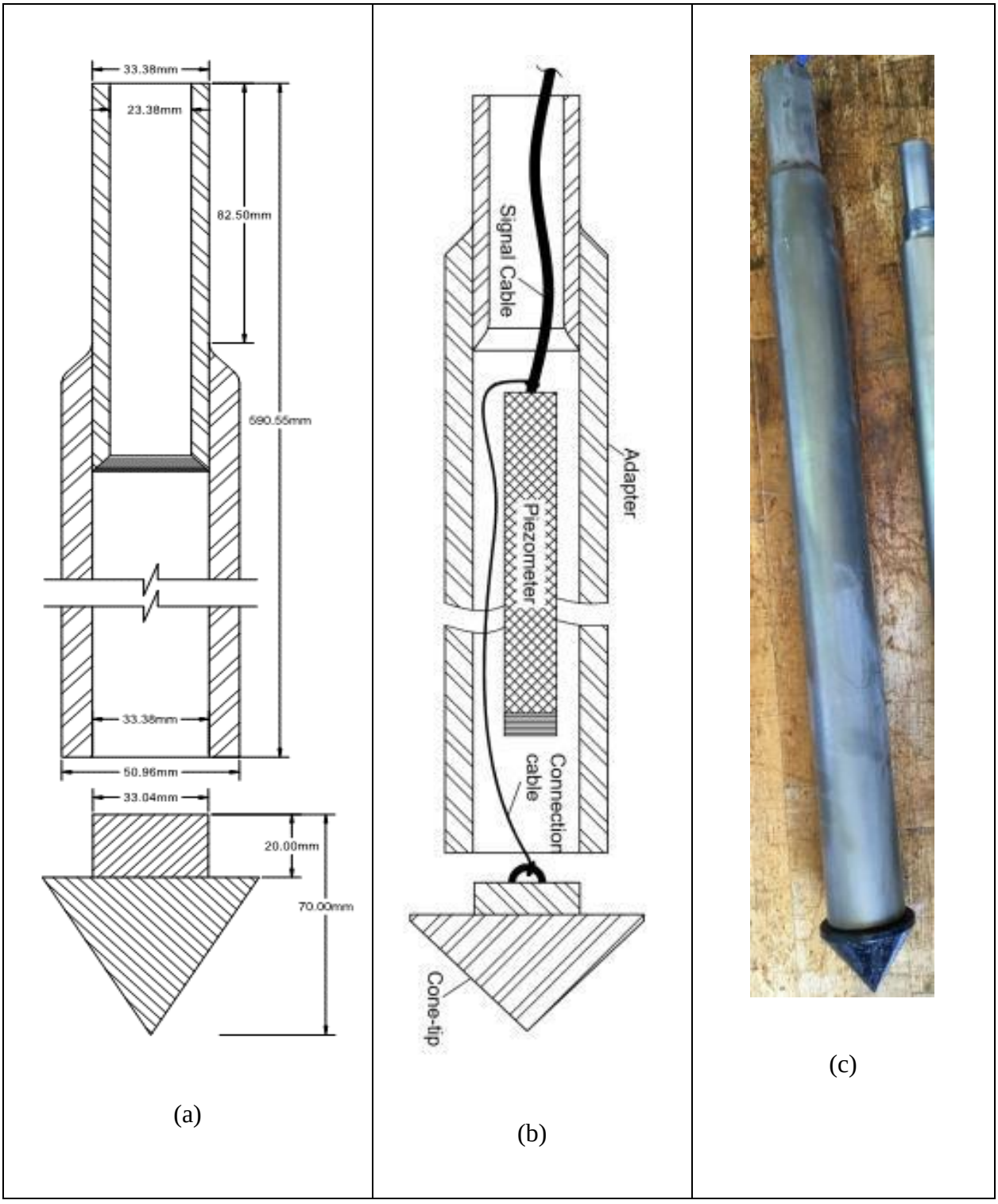

Figure 3-5. (a) Schematic drawing of the adapter, (b) detail connections of sensor and sacrificial cone-tip, and (c) actual image of the adapter

(a)

(b)

(c)

(d)

Figure 3-6. (a) 4" diameter casing used during drilling, (b) drilling of hole and washing of soil cuttings, (c) filling of casing once piezometer lower in and (d) finished borehole with installed piezometer

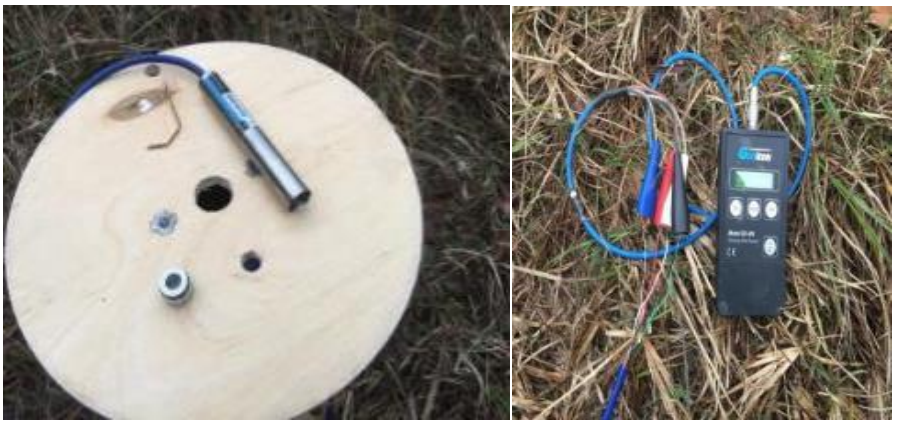

Figure 3-7. (left) Piezometer and rolled cable and (right) Geokon piezo handheld reader

3.2.3. Surveying

Depth of groundwater table (GWT) was measured twice for each sensor location. The first time right after each CPT sounding, and the second time right after the installation of each sensor. The depths of GWT presented in Table 3-1 were the average values between the two measurements. Ground surface elevation was measured using the total station method. In this survey, a theodolite (model DT-100 manufactured by Topcon) and its accessories were used. A point with known elevation (75 ft), located in the south retaining wall of the bridge on Ramp O as shown in Figure 3-8 (left), was used as a benchmark. Five total stations were set up during the survey process. The first station was set at the position of sensor 1-5. From this station, the elevations and directions of all sensors in Zone 1 and sensor 2-4 in Zone 2 were measured. The second station was set at the position of sensor 2-4 because elevation of this location was determined from the first station. Elevations and directions (compared to the north direction) of the remaining three sensors of Zone 2 were determined. The next station was set in Zone 3 as shown in Figure 3-8 (right). Elevations and directions of five out of seven sensors in Zone 3, except sensors 3-6 and 3-7, were determined. Because sensors 3-6 and 3-7 were located beyond the fences, another station was created to measure these sensors. The last station was set up in Zone 4 because both sensors in this zone were out of sight from the other zones. After surface elevations of the desired locations were determined, elevations of groundwater table and sensors were calculated and presented in Table 3-2.

Figure 3-8. (left) Location of benchmark used for Wekiva and (right) image of station in Zone 3

Table 3-2. Summary elevations of GWT and sensors for Wekiva

Zones	Sensor No.	S/N	Sensor depth (ft)	Depth of GWT (ft)	Surface Elevation (ft)	Elevation of GWT (ft)	Elevation of Sensors (ft)
1	1-1	1337248	51.70	10.30	74.47	64.17	22.77
	1-2	1608973	58.30	10.60	75.47	64.87	17.17
	1-3	1617085	73.00	10.57	75.63	65.06	2.63
	1-4	1609795	28.80	10.70	75.375	64.68	46.58
	1-5	1609797	44.00	10.70	74.45	63.75	30.45
	1-6	1617091	46.00	10.60	76.25	65.65	30.25
	1-7	1617088	42.00	10.10	71.68	61.58	29.68
2	2-1	1604360	55.11	3.24	70.065	66.83	14.96
	2-2	1609794	60.14	7.69	74.745	67.06	14.61
	2-3	1617095	68.44	4.00	70.605	66.61	2.17
	2-4	1617098	49.70	8.15	73.225	65.08	23.52
3	3-1	1617087	41.03	4.63	71.405	66.78	30.38
	3-2	1617094	41.22	4.51	71.785	67.28	30.56
	3-3	1617092	76.00	5.85	72.485	66.64	-3.52
	3-4	1617097	45.97	7.83	73.375	65.55	27.40
	3-5	1617084	45.18	8.80	74.315	65.52	29.13
	3-6	1617093	61.04	5.34	71.935	66.60	10.89
	3-7	1617096	24.25	9.75	75.155	65.41	50.91
4	4-1	1617086	45.72	13.00	76.655	63.66	30.93
	4-2	1617089	60.63	12.55	75.825	63.28	15.20

3.2.4. Signal Processing

A moving average technique was used to show the change in piezometric levels of water over time. This method helps smooth out the input signals by filtering out noise from random signal fluctuations. Output data is presented by frames. Each frame shows the mean values of one day of piezometric data. The next frame is four hours apart from the preceded frame. Thus, one day's data will be shared by six frames. If any abnormal signals occur, it will be repeated six times; this will minimize missing a valuable signal.

ArcGIS software from Environmental Systems Research Institute (ESRI) was used to analyze piezometric data from 20 sensors. In the first step, sensors information such as latitude, longitude, depth of sensors, identification of sensors, as well as the fluctuations of piezometric pressure over time are imported into the program. Based on the sensor identification, ArcGIS can sort and match sensor coordinates and piezometric data at a desired time frame, then the mean values can be calculated using the statistics toolbox. In the next step, twenty mean values of piezometric data from twenty sensors serve as known points. Information from all points other than these 20 known points were interpolated using the Inverse Distance Weighting (IDW) method. IDW is a multivariate interpolation technique used to predict a value for any unmeasured location. IDW searches known values surrounding the prediction location. The measured values closer to the prediction location have more influence on the predicted values than those further away. This technique assumes each measured point has a local influence and diminishes with distance. The weight for each unknown point is proportional to the inverse distance raised to the power value *p*. If p = 0, there is no decrease with distance. The predicted value will be the mean values in the searched neighborhood. The weights for the distant points decrease substantially when p increases. The illustrations of search neighborhood and decrease of weight with distance are shown in Figure 3-19 (left) and Figure 3-19 (right), respectively (Environmental Systems Research Institute (ESRI), 2016). The mathematical expression for this method is shown in the following equation.

$$z_j = \frac{\sum_{i=0}^{n}\left(\frac{z_i}{d_{ij}^{p}}\right)}{\sum_{i=0}^{n}\left(\frac{1}{d_{ij}^{p}}\right)} \qquad \text{.....Eq. 3.2}$$

Where, z_j = prediction value
p = power of the interpolation function
z_i = measured value at point i
d_{ij} = distance from point i to point j

From the results of the IDW interpolation method, equivalent piezometric contour lines can be generated easily for the intervals of interest. An equipotential line is a line along which the potential head at all points is equal. If piezometers are placed at different points along the equipotential line, the water level will rise to the same level in all of them. A contour interval of 2 feet is used for this analysis. The end result for each frame includes a transparent color map of the IDW results, piezometric contour lines, and base map of the site. When all created frames are put together and played in the sequence of time, fluctuation of piezometric pressures over time can be represented as a 2D video image.

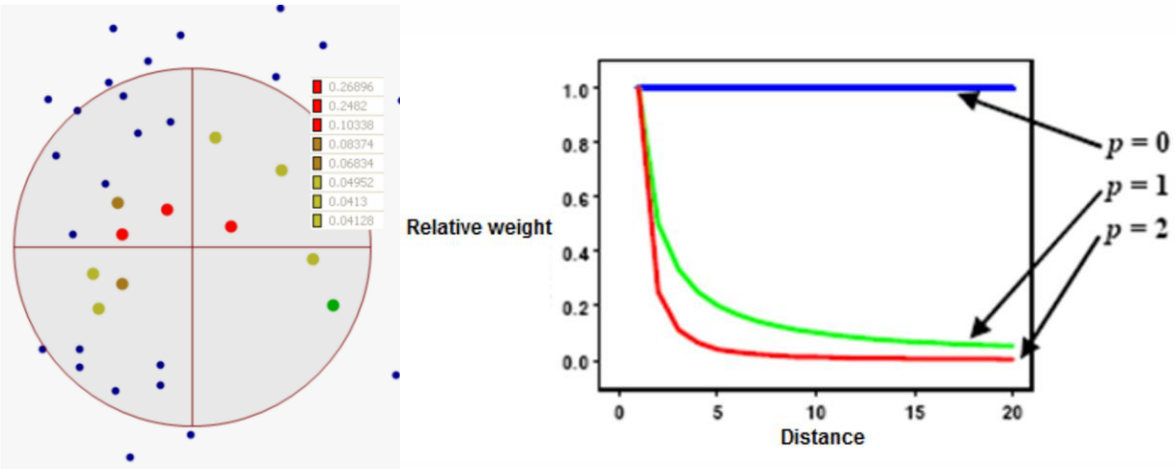

Figure 3-9. (left) IDW search neighborhood illustration and (right) decrease of weight with distance illustration (ESRI 2016)

3.3. Key Findings

The piezometer sensors at the Wekiva site have been functioning since August 21, 2016. The 20 piezometers record the piezometric head above the vibrating wire sensor every 30 minutes. The complete plot of piezometric data through the last recording, is shown in Figure 3-10 below. Unfortunately, there were several ranges of time when data was not measured due to external factors such as construction crews accidently cutting the buried cables, battery failure, and flooding of the data logger during extreme rain events (Hurricane Irma). However, even with the missing data at some locations, the recorded dataset is sufficient to calibrate the groundwater recharge model (discussed in the next chapter). A HOBO rain gauge was installed near Zone 3 at Wekiva, which has been collecting rainfall information since its installation on January 7, 2017. This data is valuable for comparing sensor lag time which may indicate the infiltration rate of storm-water runoff to be detected by the piezometers. This information is also required as an input for the recharge model. Figure 3-11 shows the plot of each rain event at Wekiva with its intensity measured in millimeters of rainfall (mm) which converts to $0.001m^3$, or 1 liter of water, to fall on one square meter of earth. It can be seen that the rainfall plots have similar trends when compared with the piezometric elevations shown in Figure 3-10.

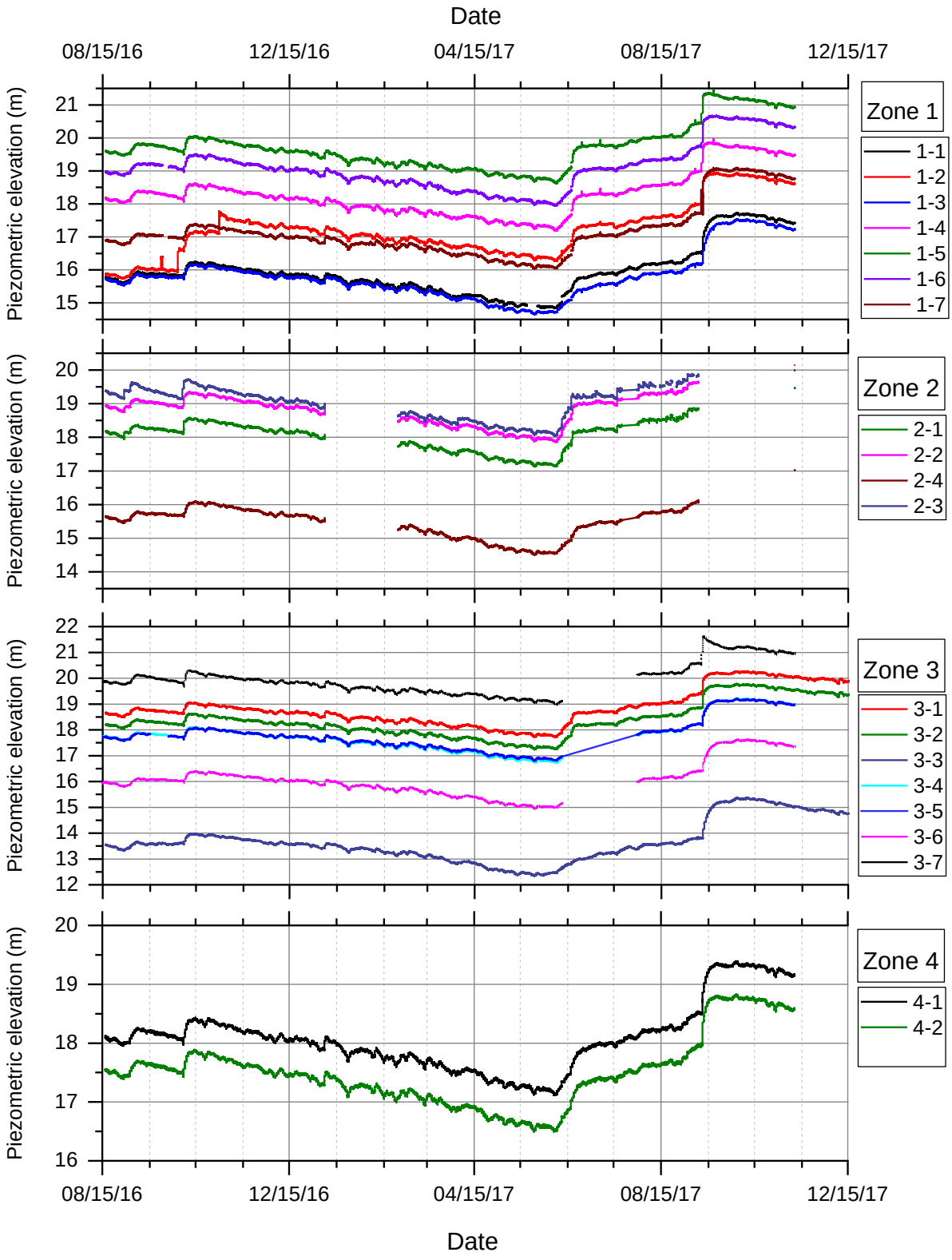

Figure 3-10. Piezometric elevation changes over time of Wekiva Parkway zones

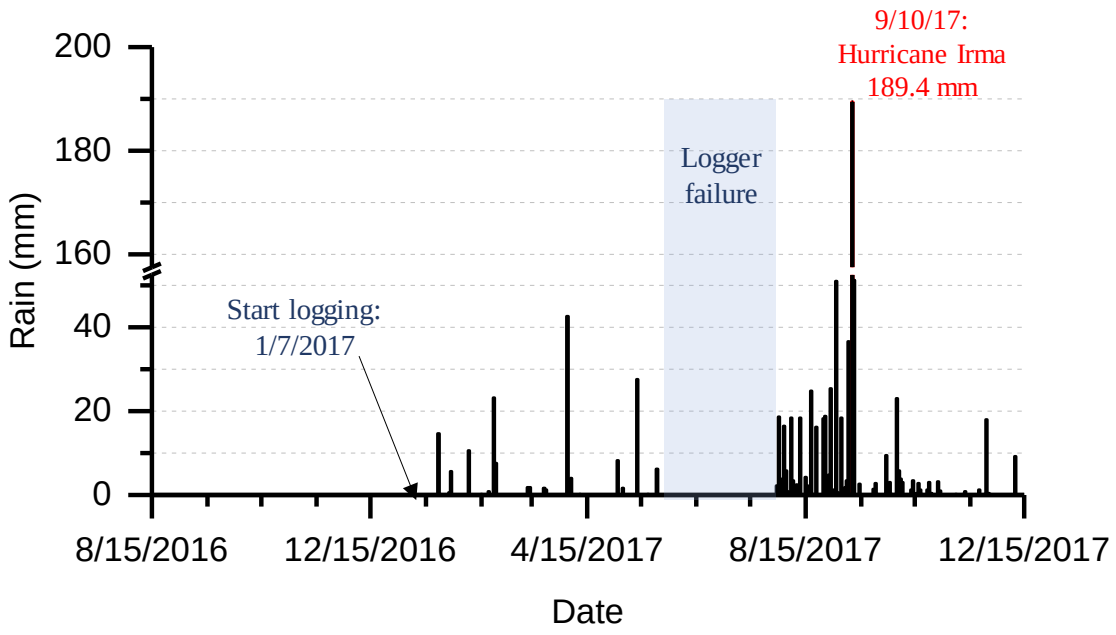

Figure 3-11. Rainfall information over study period at the Wekiva Parkway site

The piezometric and rainfall data is not only required for calibration of the developed recharge groundwater model but can be utilized for further analysis regarding identification of potential sinkholes forming as a result of internal raveling. As previously discussed, concentrated points of groundwater recharge through the Hawthorn Group of clayey and silty soils, will result in larger seepage forces and are believed to be the initiation point of soil raveling. These points can be roughly identified through mapping the piezometric elevations at each sensor location, with respect to each other, as a contour. Although the exact point of recharge requires a full array of sensors around the exact point, two sensors can still be used to identify potential recharge areas within the vicinity of the sensors. Shown in Figure 3-12 is the contour of the averaged piezometric elevations from the 20 sensors in the month of June 2017. Although the spatial variation requires interpolation between sensor locations, we can still clearly identify anomalies where large hydraulic gradients are being detected between sensors (i.e., large difference in head over relatively short distances). These locations (highlighted in Figure 3-12 by the dashed circles) should be a focal point of further subsurface investigation such as a grid of CPT soundings or additional piezometer installation (to increase resolution). Several studies have shown that the seepage force and critical shear stress to initiate internal erosion is a function of hydraulic gradient (Reddi & Bonala, 1997); therefore, these zones of large gradients should be considered as highly susceptible to soil raveling.

Deviations in gradient intensity over time, especially when compared to the influence of extreme rain events, may also be a way to further identify potential sinkhole formation. Assuming the distance between any two piezometers does not change, and that each sensor location is experiencing identical amounts of infiltrating water from precipitation, any permanent deviations in the difference between piezometric head may be a result of a change of permeability of the soil which could be the result of internal erosion. Figure 3-13 shows an example of two sensors

experiencing a difference in head over time. These sensors can be seen in Figure 3-12 at point A. Although these two sensors show a large hydraulic gradient between them (suggesting the presence of significant seepage) we see in Figure 3-13 that over time, the gradient generally does not change. There is a slight deviation in head difference responding to the rain events such as the first rain after a drought and hurricane Irma. However, even with those extreme rain events, the head difference only deviates by a couple of centimeters and seems to rebound back to the baseline value of 5.1 m shortly after hurricane Irma.

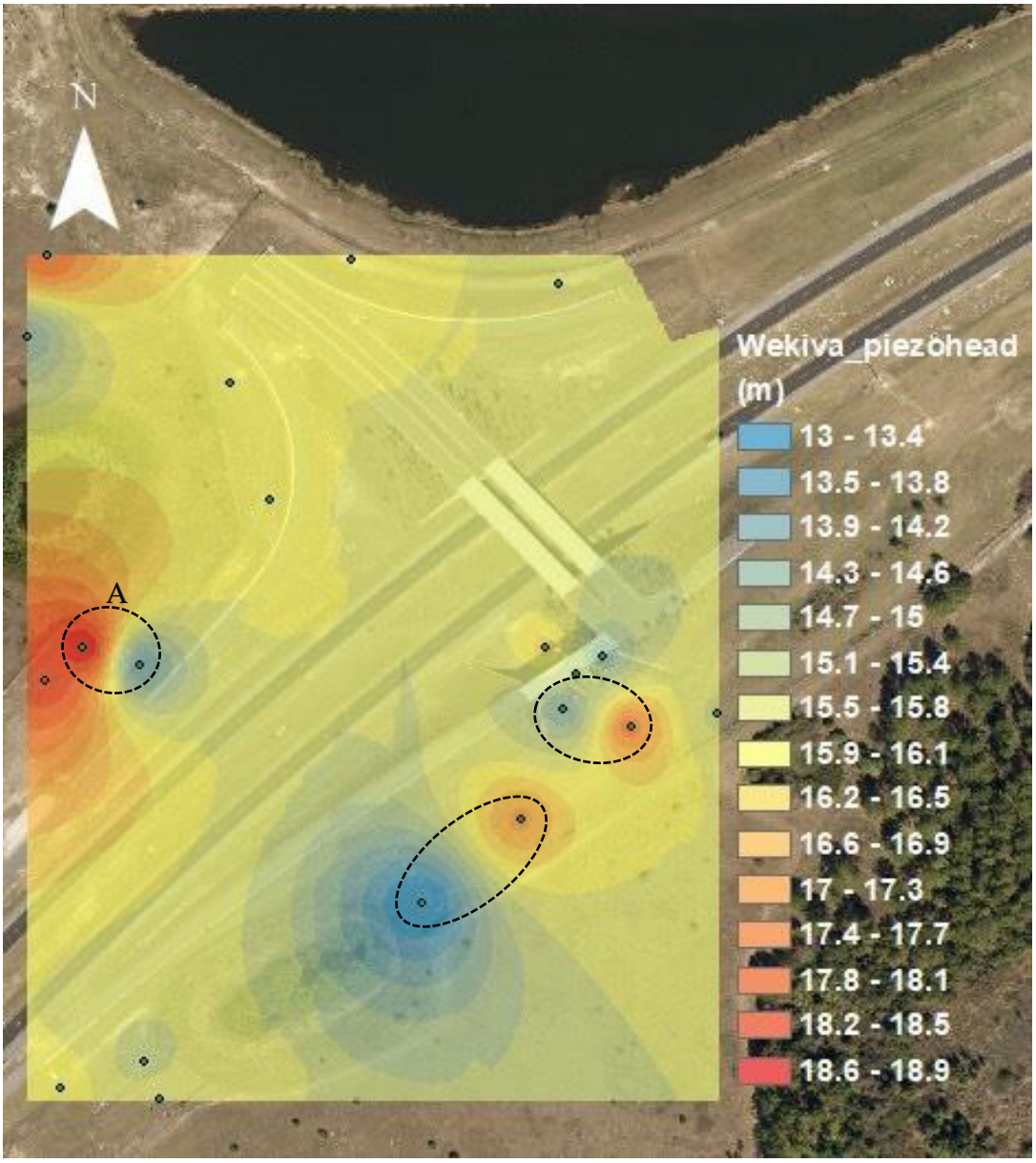

Figure 3-12. Example contouring of piezometric head at Wekiva with highlighted potential extreme gradients (dashed) – month of August 2017

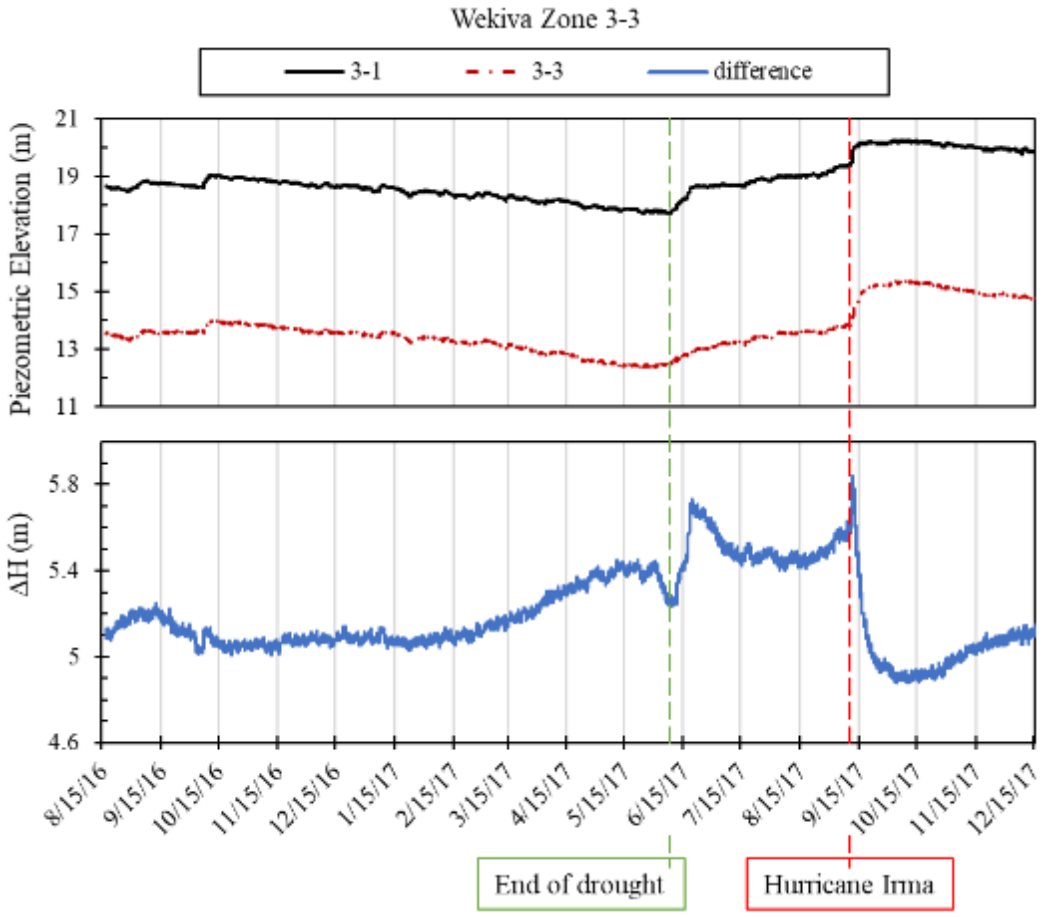

Figure 3-13. Head difference over time between sensors 3-1 and 3-3

Further monitoring and data collection over time will allow a clearer representation of groundwater recharge patterns at the site. Since the hydraulic gradient did not seem to show any permanent change during the monitoring period, it can be concluded that no significant internal erosion occurred within the location of point A, as a result of hurricane Irma. However, due to the expected presence of concentrated recharge within location A, the risk for soil raveling at that location should still be considered quite high. Even if no change in gradient was detected over the relatively short monitoring period, the large seepage forces occurring within the soil column due to the measured hydraulic gradients are believed to be the primary driving mechanism for cover-collapse sinkholes; especially when coupled with cavernous, karst limestone.

3.4. Summary

In this chapter, the equipment required, procedures utilized, and analysis methodologies to implement *in situ* piezometer sensors at a site in central Florida for sinkhole risk assessment was presented. The groundwater monitoring system explained in this chapter is also a required step to retrieve valuable data to effectively calibrate the groundwater recharge numerical model, presenting in the following chapters. The use of piezometric elevation contouring within a site can

also help identify locations that may be at risk of soil raveling due to high localized head differences (or hydraulic gradients). These locations should be studied further with exploration tests to understand the current soil density state as well as the progression of raveling if loose soils are detected. Methods to identify and quantify soil raveling using such exploration techniques (such as Cone Penetration Testing) is discussed in Chapter 5 of this report.

4. REGIONAL GROUNDWATER MODELING

4.1. Introduction

Several studies have shown that there is a strong correlation between the estimated recharge rate of the Floridan aquifer with the frequency of sinkhole occurrence (Gray, 1994; Tihansky, 1999; Beck & Sinclair, 1986). As one could expect, in areas where there is less impedance of vertical groundwater flow into the Floridan aquifer, there is a greater probability of internal raveling of soils into limestone cavities, which could subsequently form a sinkhole. Therefore, when assessing the comprehensive vulnerability to sinkhole formation at a location, the potential groundwater recharge should be considered. This chapter presents the methodology and findings from the creation of a high-resolution groundwater recharge map. More specifically, this chapter is divided into three main sections: (1) development of the high-resolution groundwater flow models (using MODFLOW software) for two study sites; (2) model calibration based on recorded piezometer data; and (3) high-resolution recharge maps that indicate risk of sinkhole occurrence.

Figure 4-1 shows the locations of the site of the Wekiva Parkway Bridge (Site 1) at Mt. Plymouth, Florida, and the site of the detention pond (Site 2) at Newberry, Florida. The piezometers were installed and monitored as discussed in Chapter 3. The average groundwater data during the one-year monitoring period were used to calibrate the steady-state groundwater models developed for Site 1 and Site 2. The models are capable of estimating recharge at a spatial resolution of 3 m by 3 m.

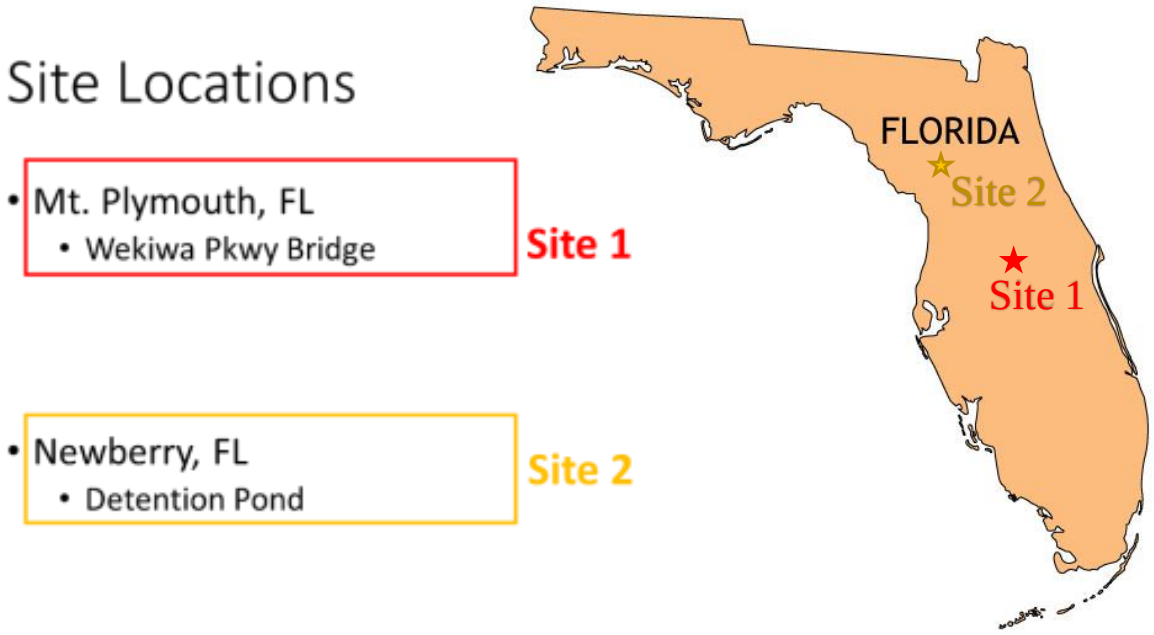

Figure 4-1. Location of the two study sites where piezometer data was monitored

4.1.1. Simulation Code

The implemented regional-scale and local-scale models were simulated using the MODFLOW-2005 computer code currently released by U.S. Geological Survey (Harbaugh, 2005). MODFLOW-2005 is a three-dimensional (3D) finite-difference groundwater model that can simulate steady and non-steady flow in an irregularly shaped flow system in which aquifer layers can be confined, unconfined, or a combination of confined and unconfined. Groundwater flow from/to external stresses, such as flow to wells, areal recharge, evapotranspiration, flow to drains, and flow through river beds, can be simulated. It has been widely applied to many case studies and is the most frequently used groundwater modeling tool (Anderson & Woessner, 2001).

4.2. Numerical Modeling of the Wekiva Parkway Site

4.2.1. Model Development

To evaluate sinkhole potential, it is important and necessary to develop a groundwater flow model which is able to simulate the recharge rate from the overlying unconfined surficial aquifer to the underlying confined Floridan aquifer. The main challenge in developing this groundwater model is a lack of sufficient historical hydrologic data for defining the boundary conditions. To define the model boundaries, it is necessary to understand the spatial and temporal variation in the water table and the general patterns of groundwater flow within the study area and its vicinity. Thus, a regional scale groundwater flow model was developed in this study before the development of the groundwater flow model of the focused area shown in Figure 4-1. The model domain of the regional scale groundwater model was much larger than the focused area. The outputs of the regional-scale groundwater model, especially the water table elevation and contours, were used as model inputs for developing the target groundwater flow model for the focused sites. The target groundwater flow model developed for the study area was named as local-scale model with higher spatial resolution. Therefore, in this study, two groundwater models were developed, including a regional-scale model and a high-resolution local-scale model.

The regional-scale model included three layers (surficial aquifer, upper confining unit, and upper Floridan aquifer) to simulate the spatial variation of water levels in the surficial soil layer and the confined limestone layer. The regional scale model acted as a ‘reference’ model, and the outputs of the regional-scale model (especially the simulated water levels of each layer) provided the input data for developing the high-resolution local-scale model. The local-scale high-resolution model was then calibrated with the recorded piezometer data in the field. After calibration, the model output was exported for further analysis on risk assessment of sinkhole occurrence.

Another challenge in developing the above-mentioned regional-scale and local-scale models was a lack of sufficient subsurface field-measured data including hydraulic conductivity, locations, and dimensions of underground karstic cavities and voids. Therefore, typical values from literature were used and reasonable assumptions were made to simplify the model development procedures.

4.2.2. Regional-Scale Model

Model Domain

The study area is at the intersection of SR-46 and the newly opened Wekiva Parkway SR-429 connector (2014), as shown in Figure 4-2 .The boundaries of the regional-scale model domain marked in a black solid-line curve in the figure, were determined to extend off-site in order to: (1) minimize the boundary effect, (2) reduce simulation error caused by local-scale groundwater flow simulation, (3) include more field-measured geologic and geophysical data, and (4) include more hydrologic and hydrogeologic data. The boundaries of the model domain were characterized by the hydrologic boundaries normal to the flow direction (or parallel to the flow direction). The hydrologic boundaries were obtained from simulated water levels from the north-central Florida Groundwater Flow model – a developed and calibrated groundwater flow model from the St. Johns River Water Management district (Motz et al., 1995). Note that the blue arrows in Figure 4-2 indicate the flow directions of regional groundwater simulated by the north-central Florida groundwater flow model.

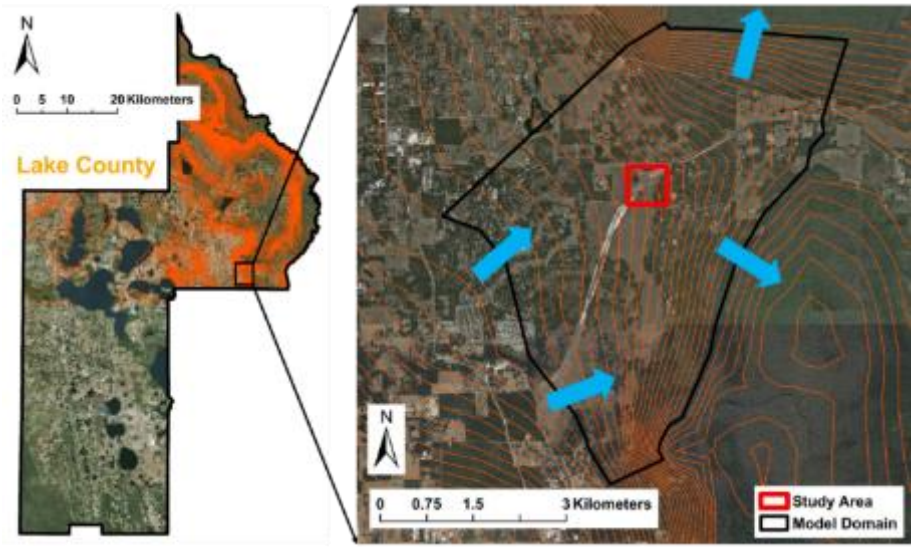

Figure 4-2. Spatial domain of developed groundwater flow model for Site 1 (Wekiva)

Discretization

Model discretization is an important controlling factor of model implementation. A fine discretization can reduce simulation error and provide more accurate model outputs, while a coarse discretization can increase simulation errors and provide less accurate model outputs. However, a fine discretization model takes longer to run than a coarse discretization model. Therefore, careful selection of a proper discretization size is crucial in numerical modeling to achieve both sufficient accuracy of simulation and reasonable computation time.

For the regional-scale model, the model domain was horizontally discretized into 248 rows and 218 columns with a uniform grid spacing of 30 m by 30 m (see Figure 4-3). The model domain was vertically divided into three layers (see Figure 4-3b). Layer 1 represented the surficial aquifer primarily composed of fine to medium sand. Layer 2 represented the upper confining unit primarily composed of clay and sandy clay. Layer 3 represented the upper Floridan aquifer consisting of several sequences of limestone and dolostone. The spatial discretization of the model domain is shown in Figure 4-3. The top elevation of each layer was shown in Figure 4-4a, 4b, and 4c, respectively. Noted that the top elevation of Layer 1 representing the land surface elevation was obtained from USGS National Elevation Dataset (U.S. Geological Survey, 2009), and the top elevations of Layers 2 and 3 were obtained from the maps showing the locations and elevations of various hydro-stratigraphic units within the study area (Williams & Kunainsky, 2016).

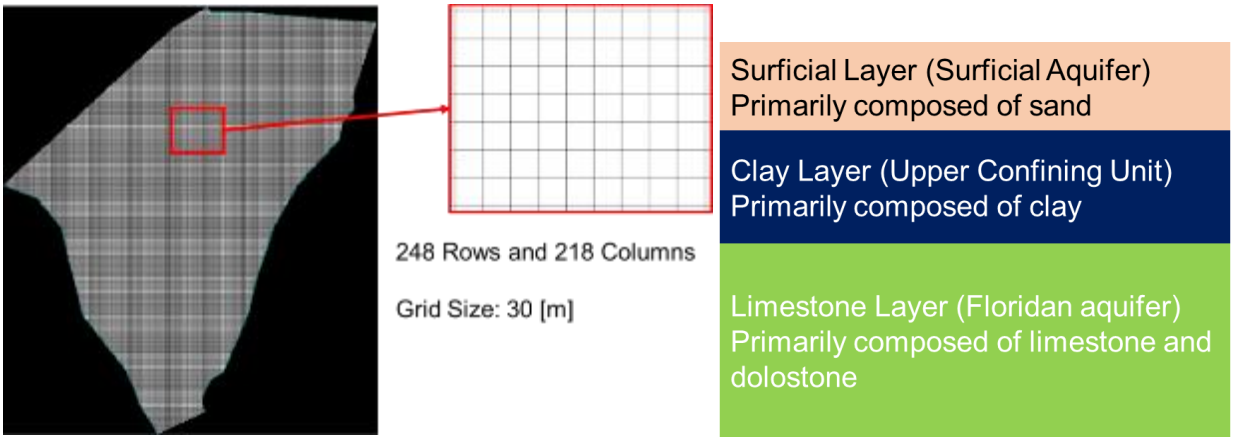

Figure 4-3. Spatial discretization of regional-scale model (horizontally and vertically) for Site 1

Parameters

Because of the limitations of available field-measured hydrogeologic data, the authors used the calibrated hydrogeologic parameters from the developed and calibrated north-central Florida Groundwater Flow model (Motz et al. 1995) as shown in Table 4-1. For Layer 1, the horizontal and vertical hydraulic conductivities are 30 m/d and 3 m/d, respectively, and the porosity is 0.2. For Layer 2, the horizontal and vertical hydraulic conductivity are 1 m/d and 0.1 m/d, respectively, and the porosity is 0.3. For Layer 3, the horizontal and vertical hydraulic conductivities are 600 m/d and 60 m/d, respectively, and the porosity is 0.4.

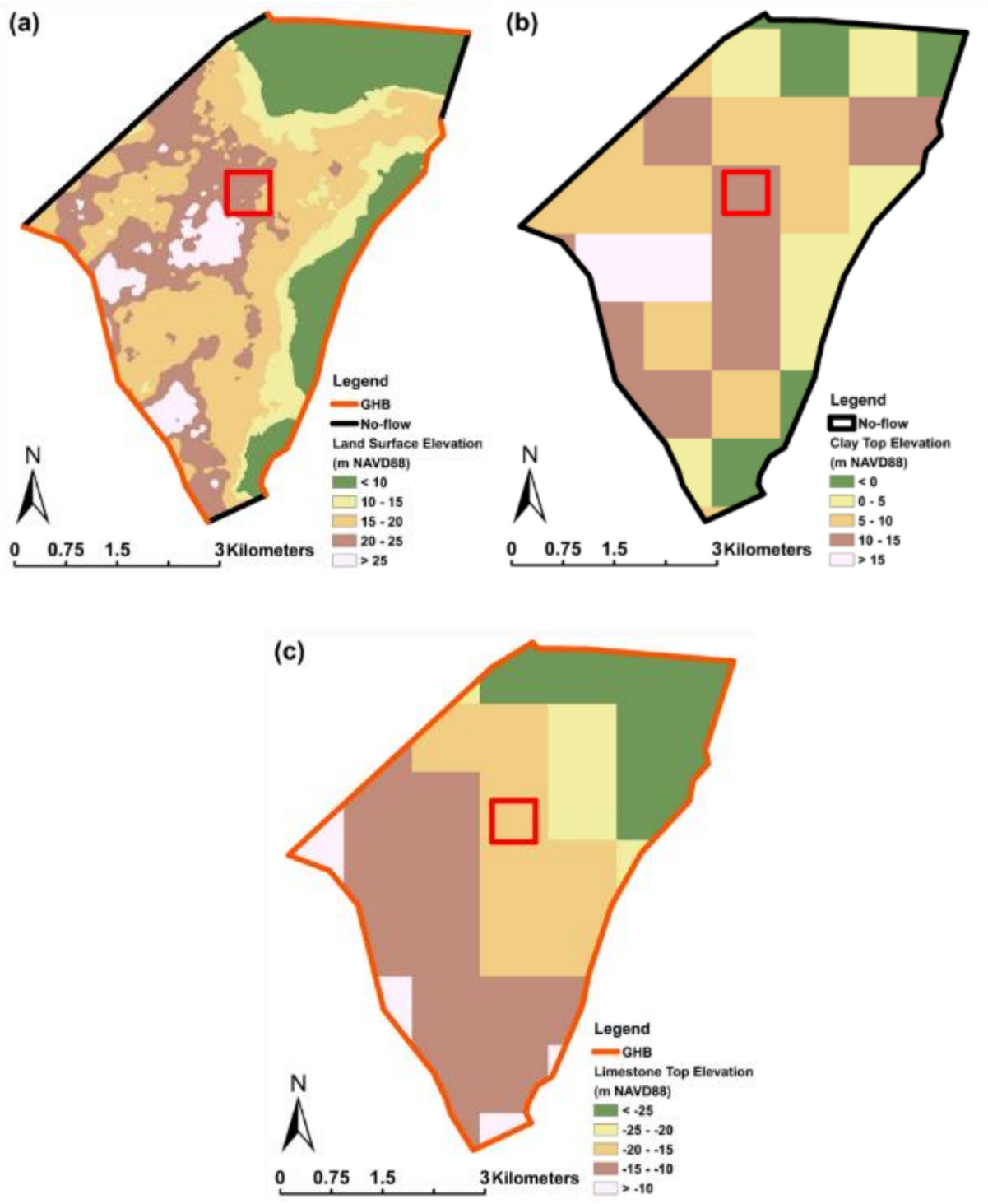

Figure 4-4. Boundary conditions and spatial variation of top elevation of:
(a) Layer 1; (b) Layer 2; (c) Layer 3

Table 4-1. Hydrogeologic parameters for Site 1

Layer	Parameter	Value
1	Horizontal Hydraulic Conductivity	30 [m/d]
	Anisotropy	0.1
	Porosity	0.2
2	Horizontal Hydraulic Conductivity	1 [m/d]
	Anisotropy	0.1
	Porosity	0.3
3	Horizontal Hydraulic Conductivity	600 [m/d]
	Anisotropy	0.1
	Porosity	0.4

Boundary Conditions

For Layer 1, no-flow boundary and general-head boundary were used to represent the hydrologic boundaries as shown in Figure 4-4a. The no-flow boundary was assigned to the inactive areas that were located outside the model domain since the groundwater flows in the inactive areas were not simulated. The general-head boundary was assigned to the model boundary where a groundwater exchange between inside and outside of the model domain occurred. The reference water levels and values of conductance were obtained from the developed and calibrated north-central Florida Groundwater Flow model. Recharge boundary and evapotranspiration boundary were used to represent the exchange between surface water and groundwater on top of Layer 1. To set up the values for recharge boundary, the infiltration rate was calculated from the measured daily rainfall from the rain gauge “SR46A” operated by St. Johns River Water Management District. Values for the evapotranspiration boundary and the potential evapotranspiration were obtained from the USGS Florida Evapotranspiration Network data collection sites, and the extinction depth was determined from the updated land use and land cover map from St. Johns River Water Management District.

For Layer 2, the no-flow boundary was used to represent the hydrologic boundaries as shown in Figure 4b because Layer 2 represented the confining unit which has very low hydraulic conductivity, hence the groundwater flow in and out of the model domain was considered negligible.

For Layer 3, no-flow boundary, general-head boundary and pumping well boundary were used to represent the hydrologic boundaries as shown in Figure 4-4c. Similarly, the no-flow boundary was assigned to the inactive areas, and the general-head boundary was assigned to the model boundary where groundwater exchange between inside and outside of the study area occurred. The reference water levels and values of conductance were obtained from the developed and calibrated north-central Florida Groundwater Flow model. The pumping well boundary was assigned to represent the groundwater production wells constructed in the limestone layer. The pumping rate and well depth were obtained from the St. Johns River Water Management District consumptive use permit.

Initial Conditions

The initial conditions of water levels of each layer were obtained from the output of the developed and calibrated north-central Florida Groundwater Flow model, previously discussed.

Simulation Results

The simulated water level of Layer 1, which represented the water table elevation, is shown in Figure 4-5. Based on the simulation results, contours of water level were generated. Based on the generated contours, the general pattern of groundwater flow exhibits the flow from southwest to northeast. Based on the generated contours, the boundary of the local-scale high-resolution model could be determined. The model domain of the local-scale high-resolution model is shown in Figure 4-5. The objective of developing the regional-scale model was to understand the general pattern of groundwater flow in the study area and its vicinity to identify and delineate the model domain of the local-scale high-resolution model. The regional-scale groundwater model acts as a 'pre-run' model, and the output of the regional-scale groundwater model provides the input data for developing the local-scale high-resolution model. The local-scale high-resolution model is calibrated by recorded piezometer data, and the outputs of the calibrated local-scale high-resolution model are used for further analysis on the development of high-resolution recharge map, regression model for estimating recharge rate, and diagram showing the risk level of sinkhole formation for each recharge level.

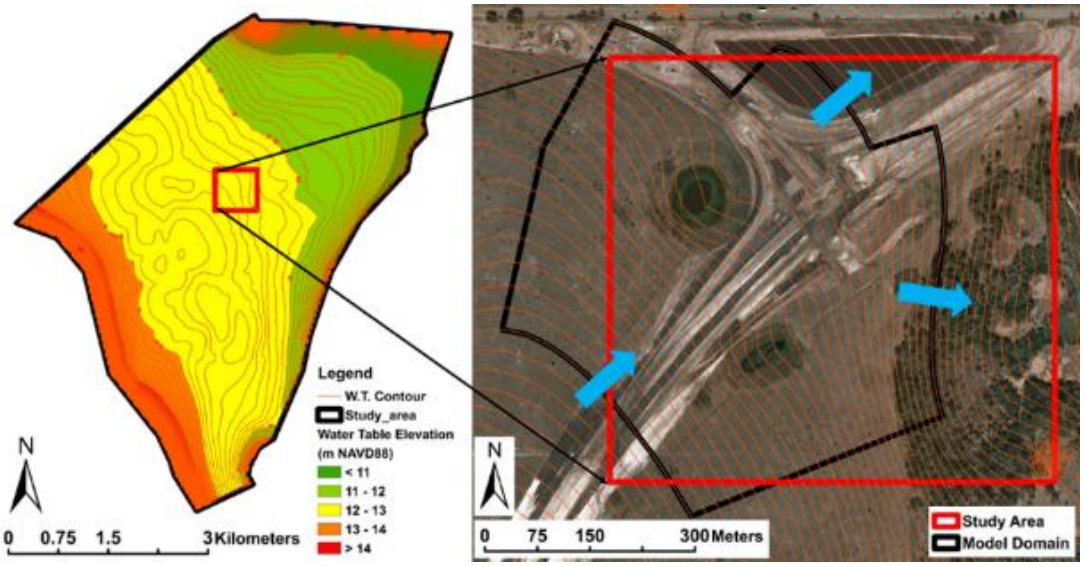

Figure 4-5. Water table elevation simulated by the region-scale model and the model domain of the local-scale model

4.2.3. Local-Scale Model

Model Domain

The study area is the Wekiva Parkway site located at the center of the regional-scale MODFLOW model domain as shown in Figure 4-5. The boundary of the model domain is marked in a black solid-line polygon in Figure 4-5. Figure 4-6 shows an example of a SPT boring log collected in the study area. The soil classification data collected from the SPT boring logs were used to estimate soil characteristics such as hydraulic conductivity and more details are described later in this section. The boundary of the model domain was characterized by the hydrologic boundaries either normal to the flow direction or parallel to the flow direction as indicated by the simulated water level from the above-mentioned regional-scale model. The criterion of defining the boundary of local-scale high-resolution model was identical to the criterion used to define the boundary of the regional-scale model described earlier.

Discretization

The purpose of implementing the high-resolution local-scale model was to improve the spatial resolution by finer spatial discretization horizontally and vertically, therefore generating a high-resolution recharge map which may be used to assess the risk level of sinkhole occurrence from a hydrological perspective.

Horizontally, the model domain was discretized into 235 rows and 211 columns with a uniform grid spacing of 3 m by 3 m; vertically, the model domain was divided into five layers (see Figure 4-7). This was different from the discretization criterion of the regional-scale model with a uniform grid spacing of 30 m horizontally and 3 layers vertically. For the local-scale high-resolution model, the model domain was discretized into 5 layers based on the soil property data collected from the SPT tests. An example of a SPT boring log (SPT Boring Log SB-2) collected in the study area is shown in Figure 4-6 and the site stratigraphy estimated from the boring log is also presented in the figure. Through assessment of the SPT boring logs, the overburden soil above the limestone layer was divided into four layers. Layer 1 was loose gray-brown fine sand. Layer 2 was medium dense dark brown silty fine sand. Layer 3 was medium dense brown silty sand. Layer 4 was soft gray sandy lean clay. Therefore, for the high-resolution local-scale groundwater model, from top to bottom, Layers 1, 2, 3, and 4 represented different soil layers and Layer 5 represented the limestone layer. The spatial discretization of the model domain is shown in Figure 4-7.

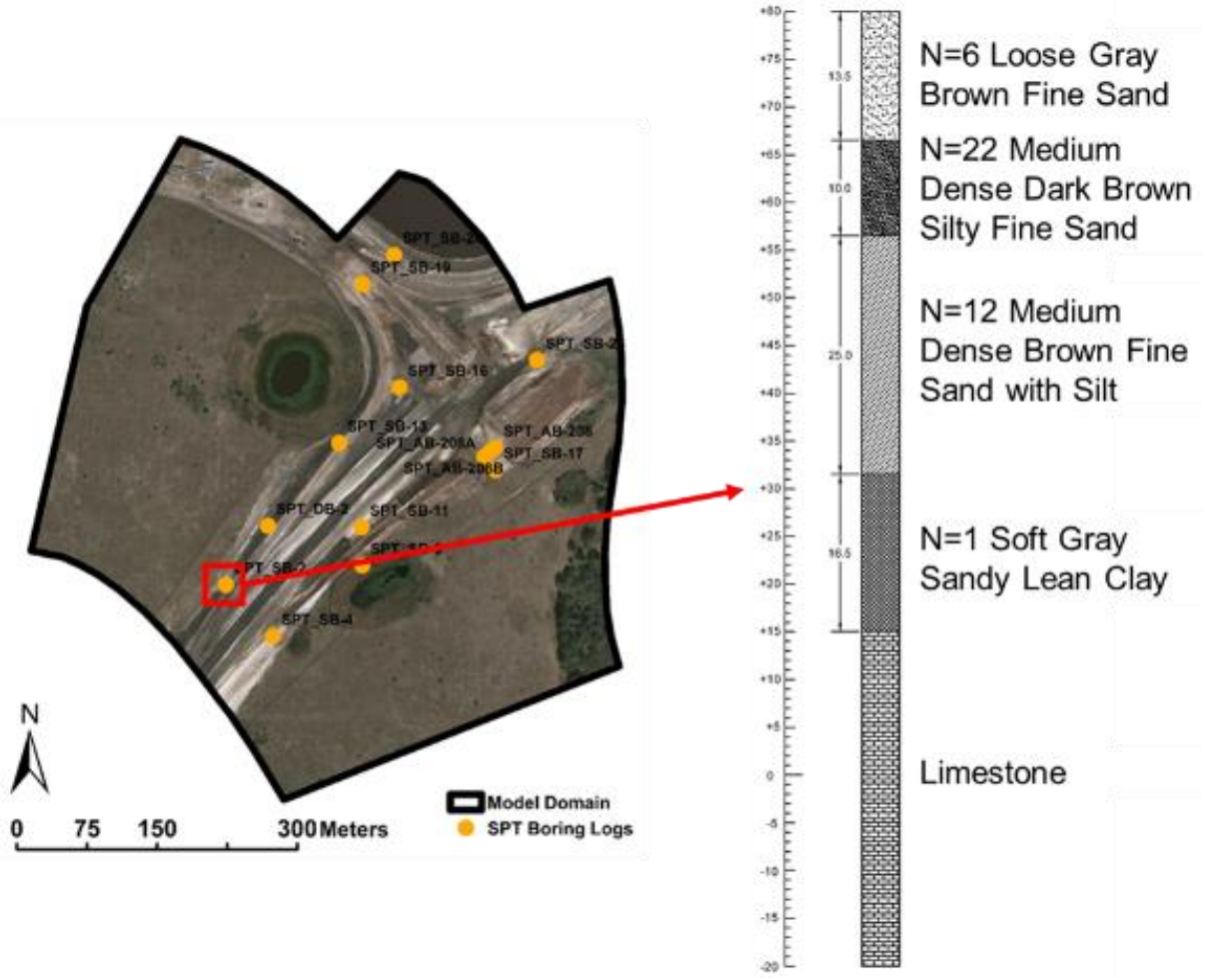

Figure 4-6. Example of SPT boring stratigraphy, performed in study area

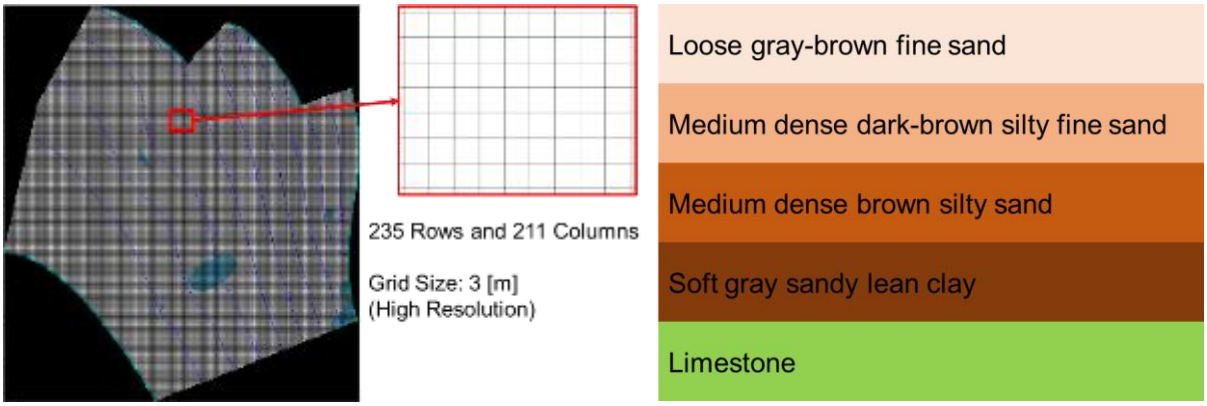

Figure 4-7. Spatial discretization of local-scale model (horizontally and vertically) for Site 1

Parameters

The hydrologic parameters such as porosity, specific storage, and specific yield used in the local-scale groundwater model were the same as the regional-scale model as shown in Table 4-1 except for the hydraulic conductivity. The local-scale model was discretized into five layers. Layers 1, 2, 3, and 4 represent the overburden surficial soils, and Layer 5 represents the underlying limestone layer. Soil properties, particularly hydraulic conductivity in this study, varies spatially. The spatial variation of hydraulic conductivity of each layer is different because the soil characteristics are different in each layer. In the regional-scale model developed previously, the spatial variation of hydraulic conductivity was not considered due to lack of *in situ* field measured soil data. However, in the local-scale groundwater model, the spatial variation of hydraulic conductivity was taken into consideration as the soil characteristics could be estimated from the 12 SPT boring logs. The soil classification data collected from the 12 SPT tests enabled estimating the spatial variation of hydraulic conductivity. The criterion of determining the spatial variation of hydraulic conductivity is described below.

In total, there were 12 SPT boring within the model domain of the local-scale groundwater model. Take the boring log named 'SB-2' for example (Figure 4-6). From Figure 4-6, it was concluded there are four layers above the limestone layer, including loose gray-brown fine sand, medium dense dark brown silty fine sand, medium dense brown silty sand, and soft gray sandy lean clay. Each type of soil has its own characteristics. For fine sand, the typical range of hydraulic conductivity varies from 0.02 – 20 m/d (Domenico & Schwartz, 1990). Thus, the hydraulic conductivity value selected to represent Layer 1 was the averaged max and min value of the range (chosen as 10 m/d). For silty fine sand, the typical range of hydraulic conductivity varies from 0.001 – 0.5 m/d (Domenico and Schwartz 1990). Thus, the hydraulic conductivity value selected to represent Layer 2 was chosen as 0.25 m/d. For silty sand, the typical range of hydraulic conductivity varies from 0.0005 – 0.1 m/d (Domenico & Schwartz 1990). Thus, the hydraulic conductivity value selected to represent Layer 3 was chosen as 0.05 m/d. For sandy clay, the typical range of hydraulic conductivity varies from 0.001 – 0.01 m/d (Domenico & Schwartz 1990). Thus, the hydraulic conductivity value selected to represent Layer 4 was chosen as 0.005 m/d (the average value of 0.001 m/d and 0.01 m/d). For limestone, the typical range of hydraulic conductivity varies from 0.1 – 2000 m/d (Domenico & Schwartz 1990). The hydraulic conductivity of limestone has a correlation with rock-quality designation (RQD). Qureshi et al. (2014) conducted a study on the relationship between limestone permeability and RQD, and developed an empirical equation to calculate the value of limestone hydraulic conductivity based on RQD. Based on the RQD and the empirical equation, the hydraulic conductivity value selected to represent Layer 4 was calculated to be 3.0 m/d.

Note that there were 12 SPT boring logs that were used for soil classifications. The soil characteristics collected from the other 11 SPT boring logs were analyzed in the same manner and the hydraulic conductivity values were obtained in the same way. Once the hydraulic conductivity values at the 12 SPT boring log sites were obtained, a kriging interpolation method was used to generate the spatial variation of hydraulic conductivity from Layers 1 to 4 as shown in Figure 4-8a, 8b, 8c, and 8d, respectively.

The spatial variation of hydraulic conductivity in Layers 1, 2, 3, and 4 were imported into the high-resolution model. It should be noted that these values were based on soil type and the exact values of hydraulic conductivity were still unknown. Ideally, an aquifer pumping test would provide more accurate localized hydraulic conductivity values. However, these values act as an effective initial estimate and can be adjusted if necessary later in the calibration process.

Boundary Conditions

The no-flow boundary, general-head boundary, recharge boundary, and evapotranspiration boundary were used to generate the high-resolution local-scale model. For Layer 1, no-flow boundary and general-head boundary were used to represent the hydrologic boundaries that have zero flux exchange and non-zero flux exchange. The no-flow boundary was assigned to the inactive areas that were located outside the model domain since the groundwater flows in the inactive areas were not simulated. The general-head boundary was assigned to the model boundary where a groundwater exchange between the inside and outside of the model domain occurred. The reference water levels and conductance values were obtained from the output of the regional-scale groundwater model. Recharge boundary and evapotranspiration boundary were used to represent the exchange between surface water and groundwater on top of Layer 1. In order to set up the values for recharge boundary, the infiltration rate was calculated from the daily recorded measured rainfall from rain gauge SR46A operated by St. Johns River Water Management District. Infiltration refers to the rainwater that seeps downward towards the groundwater, and the infiltration rate refers to the amount of rainwater penetrating the ground over a period of time. The infiltration rate is high in the area that has a low water table, and the infiltration rate is low in the area that has a high water-table. At the marshes located in the study area, the water table approaches and emerges from the land surface, while the infiltration rate is very low and was assumed to be zero for simplification. Values for the evapotranspiration boundary and the potential evapotranspiration were obtained from the USGS Florida Evapotranspiration Network data collection sites, and the extinction depth was determined from the updated land use and land cover map from St. Johns River Water Management District. The boundary conditions applied to Layer 1 were shown in Figure 4-9a. For Layers 2, 3, and 4, the boundary conditions were implemented in the same manner under the same criterion that no-flow boundary was assigned to the inactive areas that were located outside the model domain because the groundwater flows in the inactive areas were not simulated and general-head boundary was assigned to the model boundary where a groundwater exchange between inside and outside of the model domain occurred. The boundary conditions applied to Layers 2 through 4 are shown in Figure 4-9b. For Layer 5, general-head boundary was assigned to the entire model boundary because limestone is highly permeable and groundwater exchange between model boundaries would always exist.

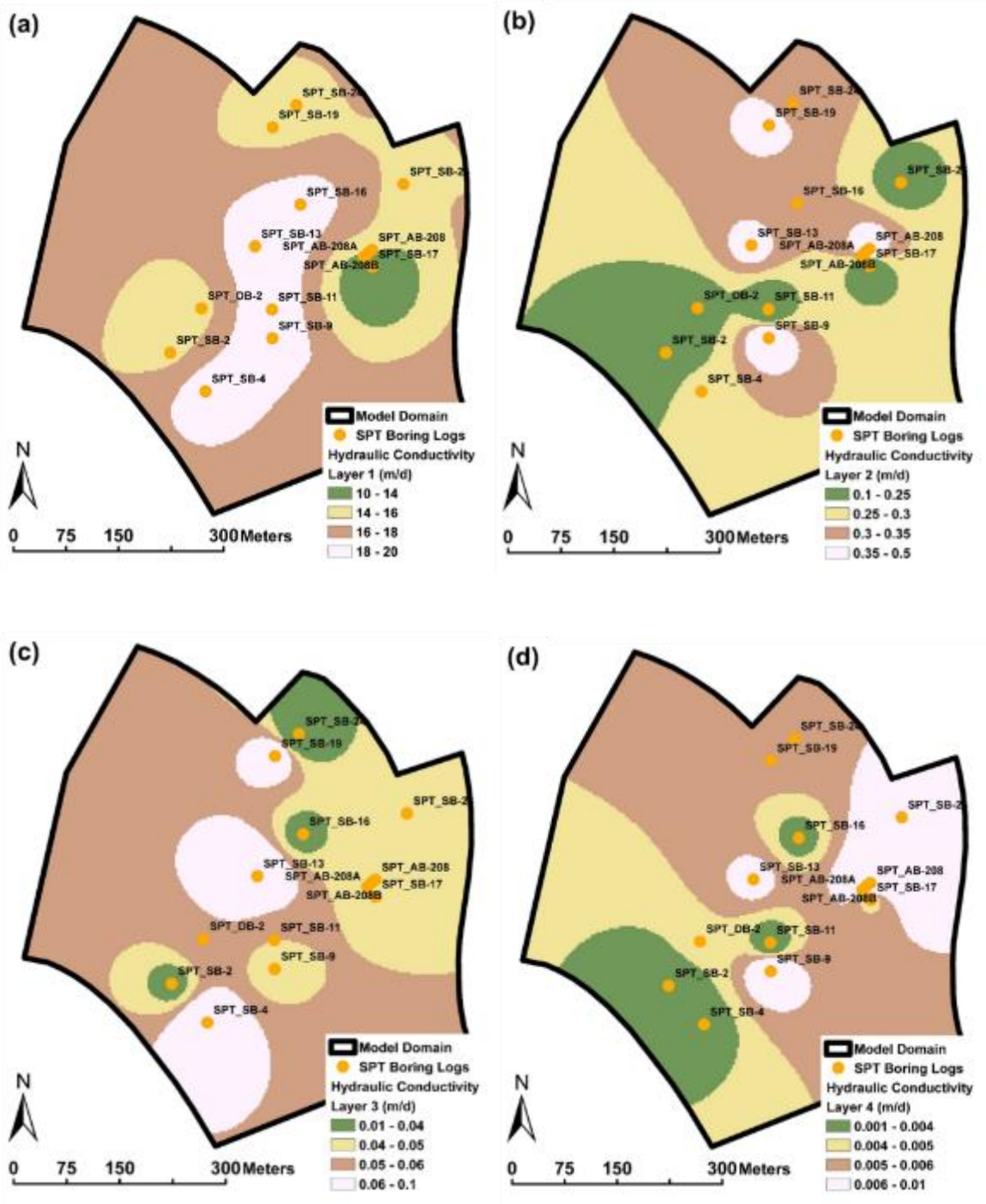

Figure 4-8. Estimate hydraulic conductivities,
(a) Layer 1, (b) Layer 2, (c) Layer 3, and (d) Layer 4

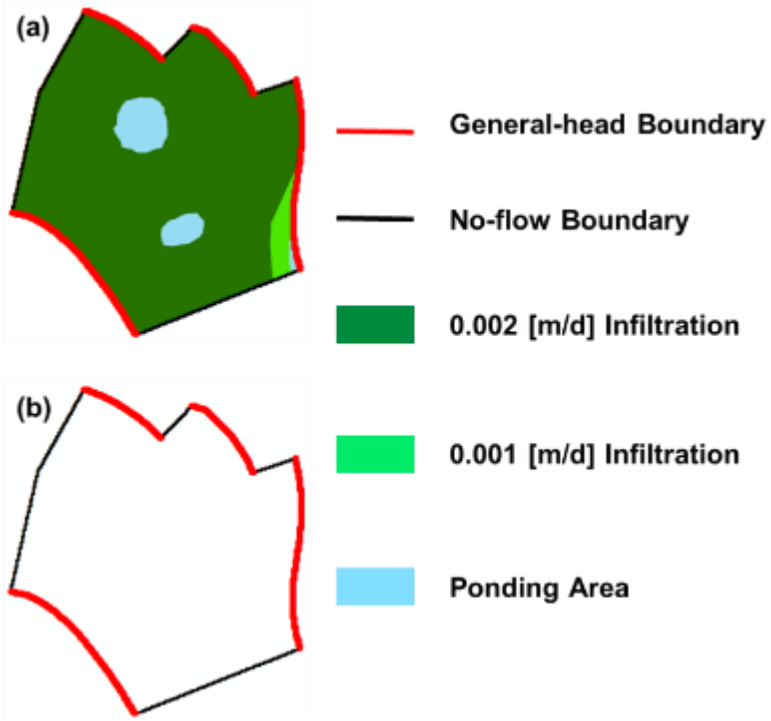

Figure 4-9. Boundary conditions applied to (a) Layer 1 and (b) Layer 2

Initial Conditions

The initial conditions refer to the initial water table elevation and potentiometric elevation before simulation. The initial water table elevation and potentiometric elevations were obtained from the output of the regional-scale model previously described.

4.2.4. Calibration

The water table elevation simulated by the local-scale model was calibrated with the observed water table elevation measured by the *in situ* piezometers. The model calibration was achieved through a trial-and-error method by adjusting the values of hydraulic conductivity of each layer until the simulated water levels match the observed water levels to a satisfactory degree. It is important to note that the values of hydraulic conductivity of Layers 1, 2, 3, 4, and 5 were adjusted within a reasonable range (not allowed to exceed the maximum typical value while not allowed to be lower than the minimum typical value). In total, there were 20 piezometers installed to measure and monitor water table status from August 17, 2016 to July 30, 2017, as shown in Figure 4-10. The water table elevation varies seasonally dependent on the seasonal rainfall. The seasonal variation of water level measured by Piezometer 1-2 is presented in Figure 4-10, and the annual-averaged water table elevation measured from the 20 piezometers are tabulated in Table 4-2. The simulated water level from Layer 1 was used for calibration, because it represents the water table of the simulated site.

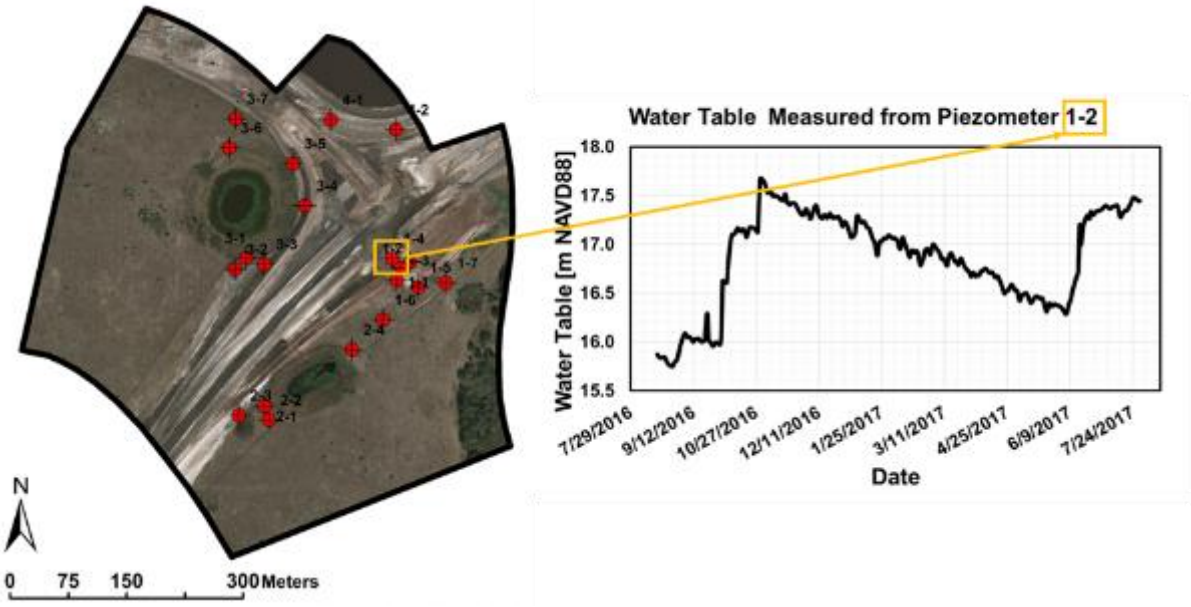

Figure 4-10. Locations of the installed piezometers and the seasonal variation of water level measured from Piezometer 1-2

Table 4-2. Annual-averaged water table elevation measured from 20 piezometers

Piezometer Name	Water Table [m NAVD88]
1-1	15.65
1-2	16.86
1-3	15.5
1-4	17.99
1-5	19.43
1-6	18.81
1-7	16.8
2-1	17.95
2-2	18.71
2-3	18.94
2-4	15.38
3-1	18.48
3-2	18.03
3-3	13.27
3-4	17.5
3-5	17.51
3-6	15.78
3-7	19.67
4-1	17.86
4-2	17.27

After the calibration process, the simulated water levels and the observed water levels matched satisfactorily. The R2 was 0.45 as shown in Figure 4-11, indicating a reasonable match between simulated water levels from the calibrated groundwater model and the observed water levels from the field-measured hydrologic data from the *in situ* piezometers. The adjusted hydraulic conductivities (K) of each layer are shown in Figures 4-12a, 12b, 12c, 12d, 12e, 12f, 12g, and 12h, and the spatial variation of the calibrated water table elevation is shown in Figure 4-13.

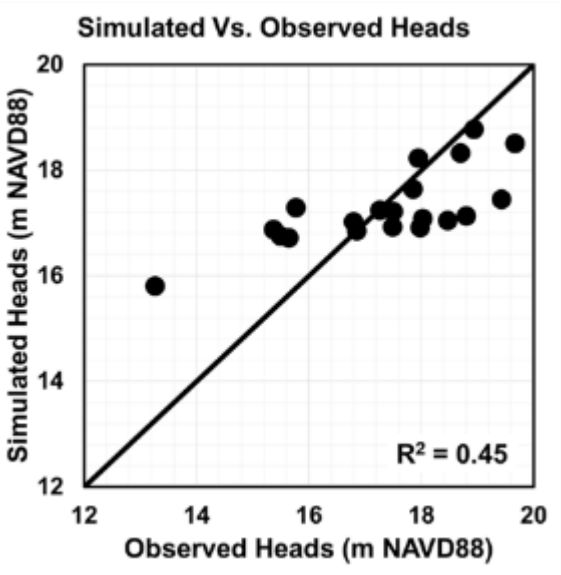

Figure 4-11. Relationship between simulated heads and the observed heads

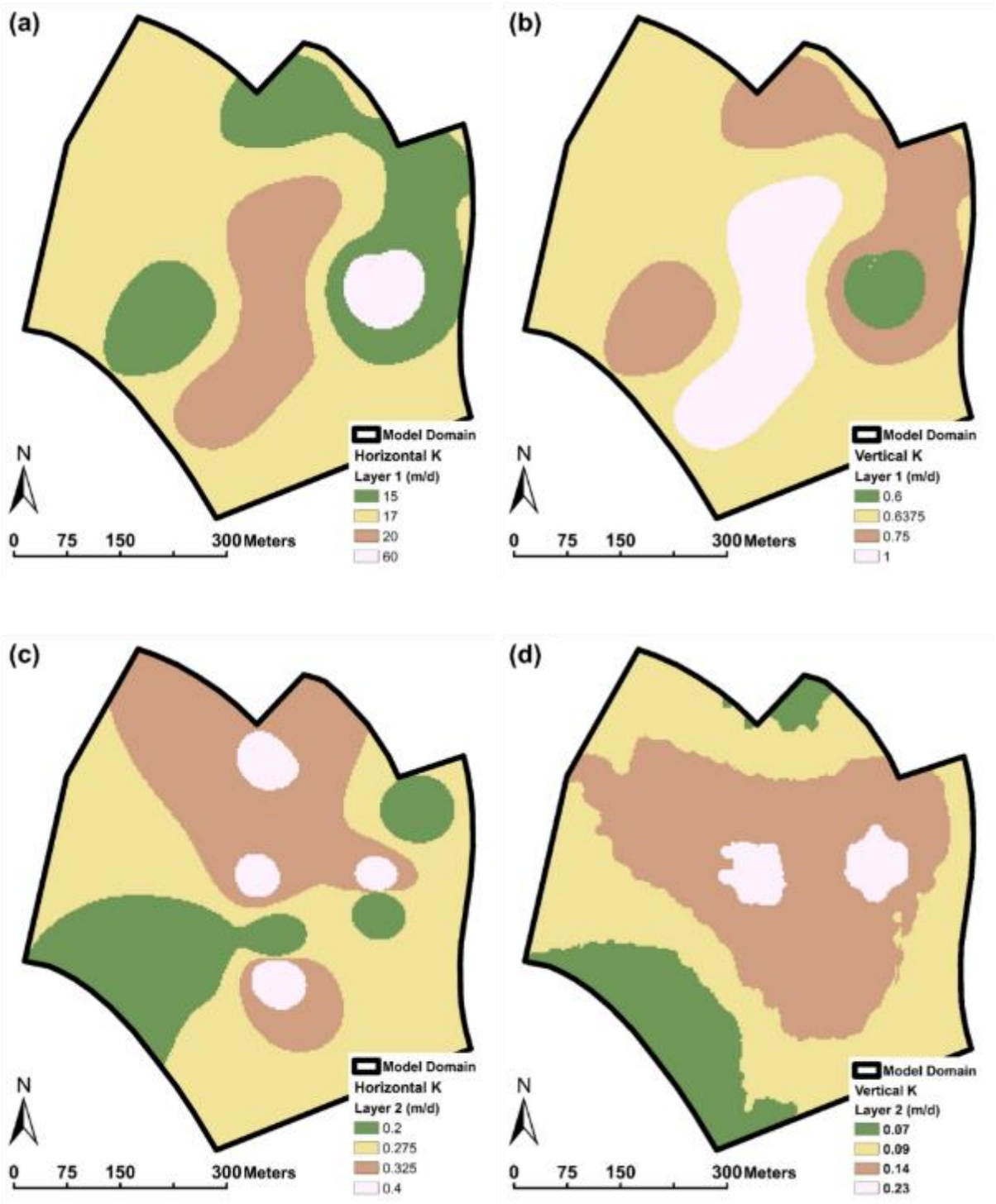

Figure 4-12. Calibrated hydraulic conductivity, (a) Layer 1, K_h, (b) Layer 1, K_v, (c) Layer 2, K_h, (d) Layer 2, K_v, (e) Layer 3, K_h, (f) Layer 3, K_v, (g) Layer 4, K_h,, and (h) Layer 4, K_v

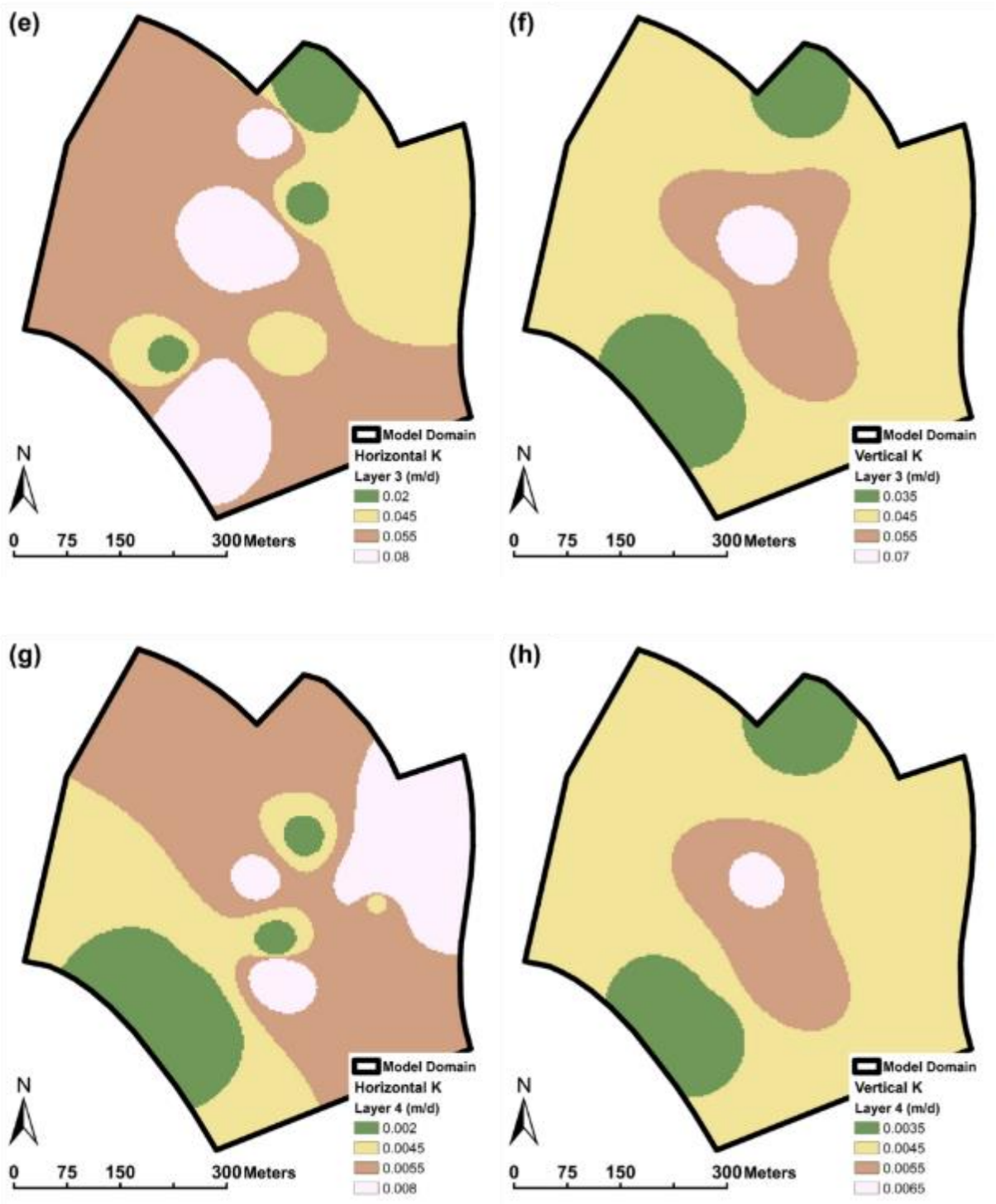

Figure 4-12. Calibrated hydraulic conductivity, (a) Layer 1, K_h, (b) Layer 1, K_v, (c) Layer 2, K_h, (d) Layer 2, K_v, (e) Layer 3, K_h, (f) Layer 3, K_v, (g) Layer 4, K_h,, and (h) Layer 4, K_v

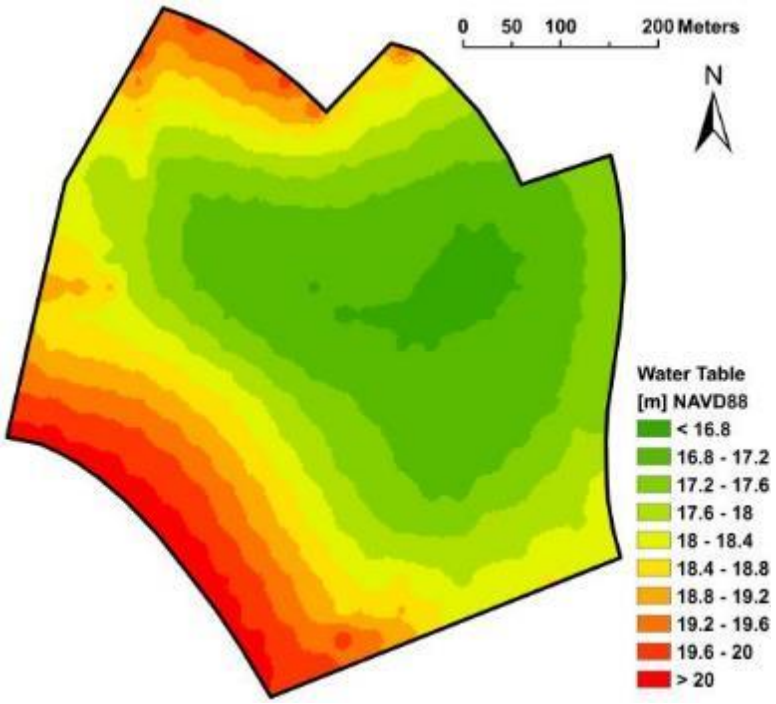

Figure 4-13. Calibrated water table elevation for Site 1

4.3. Numerical Modeling of the Newberry Detention Pond Site

4.3.1. Model Development

The same model development procedure used for the Wekiva Parkway site (Site 1) was used for the Newberry Detention Pond site (Site 2). The regional-scale model including the surficial aquifer, the upper confining unit and the Floridan aquifer was first developed to simulate the spatial variation of water levels in the surficial sand layer and the confined limestone layer. The output of the regional-scale model (especially the simulated water levels of each layer) provided the input data for developing the high-resolution local-scale model. The local-scale high-resolution model was then calibrated with the measured piezometers data in the field.

4.3.2. Regional-Scale Model

Model Domain

The study area was near the intersection of W. Newberry Road (SR-26) and SW. 242nd Street at Newberry, Florida, as shown in Figure 4-14. However, the boundaries of the regional-scale model domain marked by a black solid-line curve in Figure 4-14 (located in central Florida near the city of Newberry, including the detention pond located at the center) was extended off-site in order to: (1) minimize the boundary effect, (2) reduce simulation error caused by local scale groundwater flow simulation, (3) include more field-measured geologic, geophysical data, and (4) include more hydrologic and hydrogeologic data. The boundaries of the model domain were characterized by

the hydrologic boundaries normal to the flow direction or parallel to the flow direction depending on flow rate. The hydrologic boundaries were obtained from simulated water levels from the north-central Florida Groundwater Flow model – a developed and calibrated groundwater flow model from St. Johns River Water Management District utilized to simulate groundwater flow in the north-central Florida area. The boundary of the model domain is characterized by the hydrologic boundaries either normal to the flow direction or parallel to the flow direction depending on the flowrate.

Discretization

For the regional-scale model, the model domain was horizontally discretized into 320 rows and 252 columns with a uniform grid spacing of 30 m by 30 m. The model domain was vertically divided into two layers based on the hydro-stratigraphy of Site 2 (due to the shallow bedrock depth). Layer 1 represents the surficial layer primarily composed of fine to medium sand, and Layer 2 represents the limestone layer. The top elevation of each layer is shown in Figures 4-15 and 4-16. The top elevation of Layer 1 representing the land surface elevation was obtained from USGS National Elevation Dataset which provides basic bare earth elevation information for earth science studies and mapping applications in the United States. The top elevations of Layers 2 were obtained from the maps showing the locations and elevations of various hydro-stratigraphic units within the study area (Williams & Kunainsky, 2016).

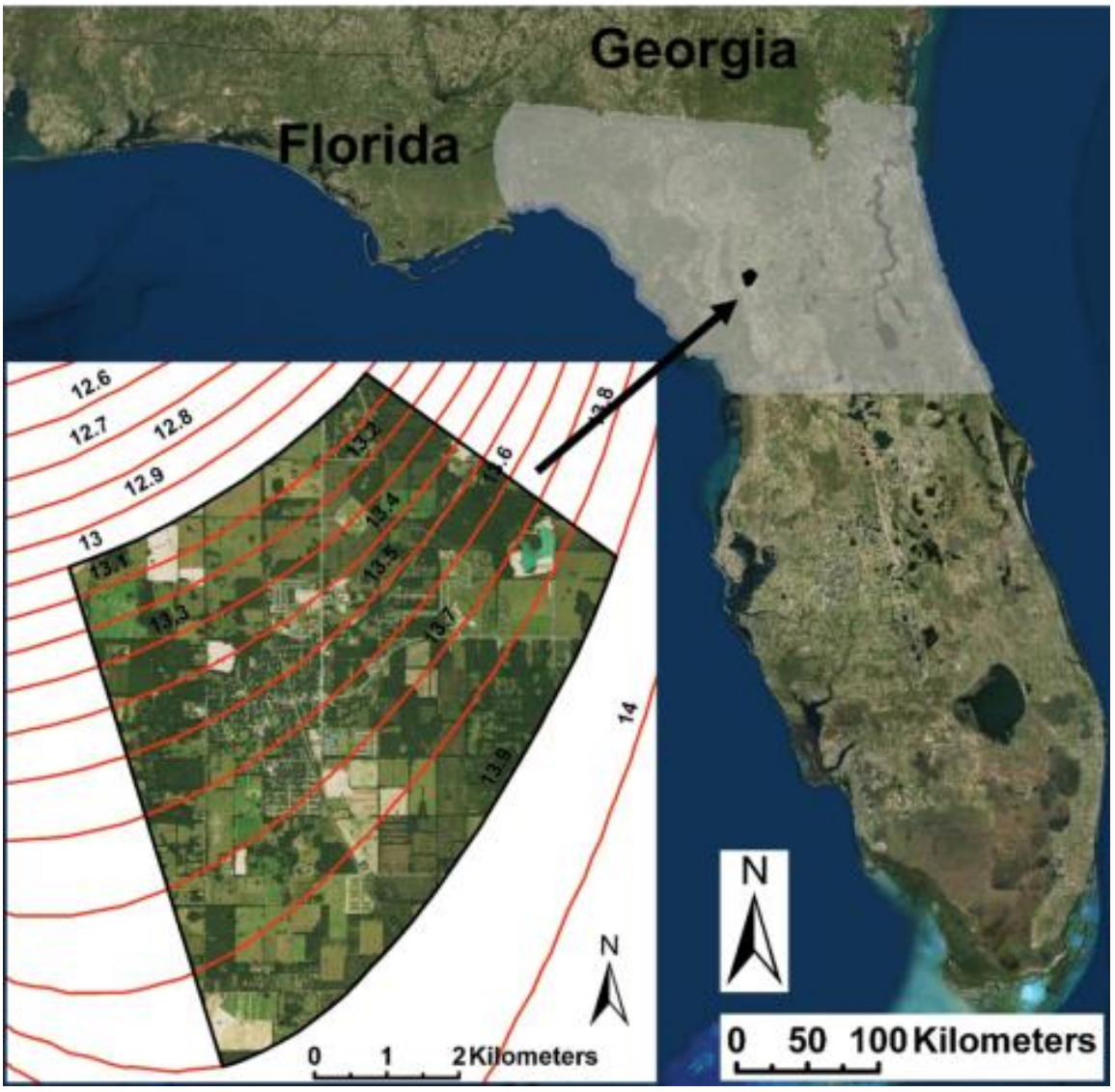

Figure 4-14. Model domain for Site 2

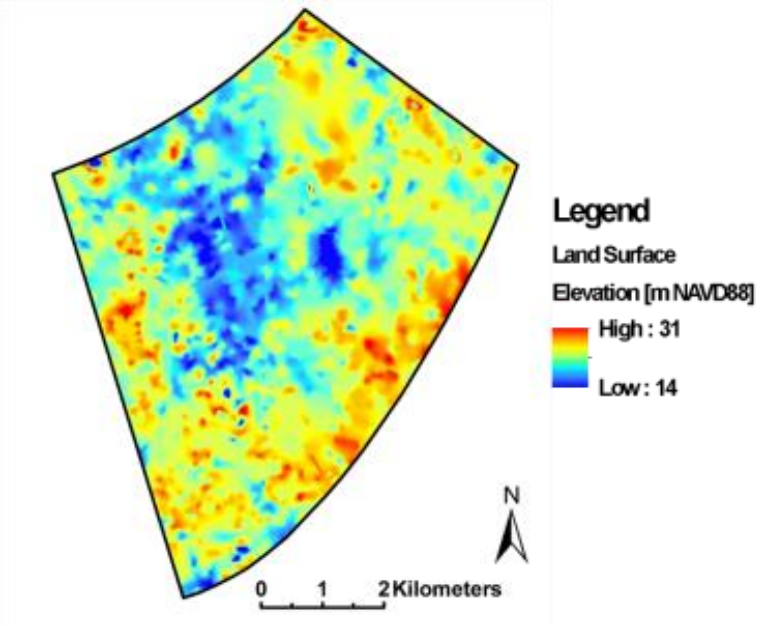

Figure 4-15. Land surface elevation map for Site 2

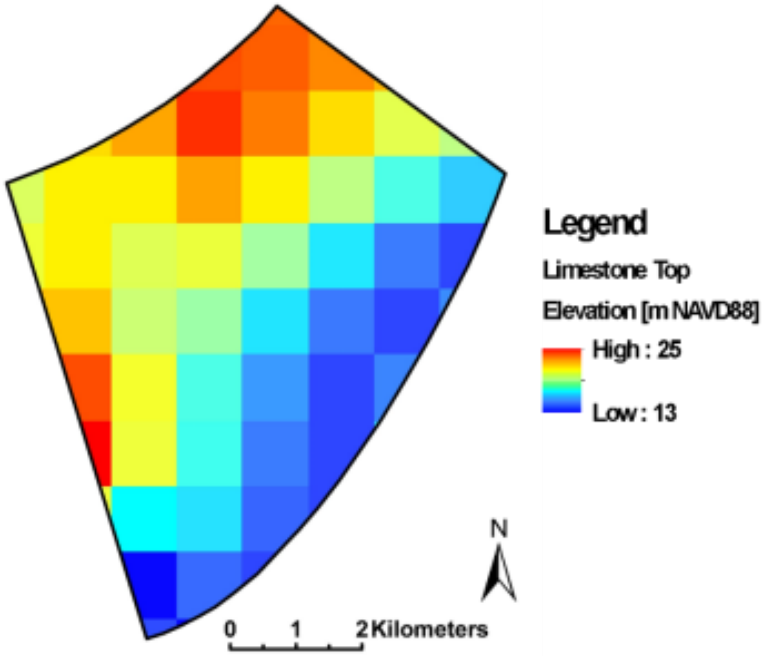

Figure 4-16. Top of limestone elevation map for Site 2

Parameters

Because of the limitations of available field-measured data, estimation of relevant hydrogeologic parameters based on field measured data were not conducted. Instead, the calibrated hydrogeologic parameters from the developed and calibrated north-central Florida Groundwater Flow model (Motz et al. 1995) shown in Table 4-3 was utilized. For Layer 1, the horizontal and vertical hydraulic conductivities were 10 and 1 m/d, respectively, and the porosity was 0.4. For Layer 2, the horizontal and vertical hydraulic conductivity were 400 and 40 m/d, respectively, and the porosity was 0.4.

Table 4-3. Hydrogeologic parameters for Site 2

Layer	Parameter	Value
1	Horizontal Hydraulic Conductivity	10 [m/d]
	Anisotropy	0.1
	Porosity	0.4
2	Horizontal Hydraulic Conductivity	400 [m/d]
	Anisotropy	0.1
	Porosity	0.4

Boundary Conditions

For Layers 1 and 2, no-flow boundary and general-head boundary were used to represent the hydrologic boundaries. The no-flow boundary was assigned to the inactive areas that were located outside the model domain since the groundwater flows in the inactive areas were not simulated. The general-head boundary was assigned to the model boundary where a groundwater exchange between the inside and outside of the model domain occurred. The reference water levels and values of conductance were obtained from the developed and calibrated north-central Florida Groundwater Flow model. Recharge boundary and evapotranspiration boundary were used to represent the exchange between surface water and groundwater on top of Layer 1. The no-flow and general head boundaries used for Layers 1 and 2 are shown in Figure 4-17. For Layer 1, the recharge boundary and evapotranspiration boundary was used to represent groundwater and surface water exchange, dependent on land use and land cover (Figure 4-18). In order to set up the values for the recharge boundary, the infiltration rate was calculated from the daily recorded measured rainfall from rain gauge SR46A operated by St. Johns River Water Management District. In order to set up the values for the evapotranspiration boundary, the potential evapotranspiration was obtained from USGS Florida Evapotranspiration Network data collection sites, and the extinction depth was determined from the updated land use and land cover map from St. Johns River Water Management District. The recharge and evapotranspiration boundaries assigned to Layer 1 are shown in Figures 4-19 and 4-20, respectively.

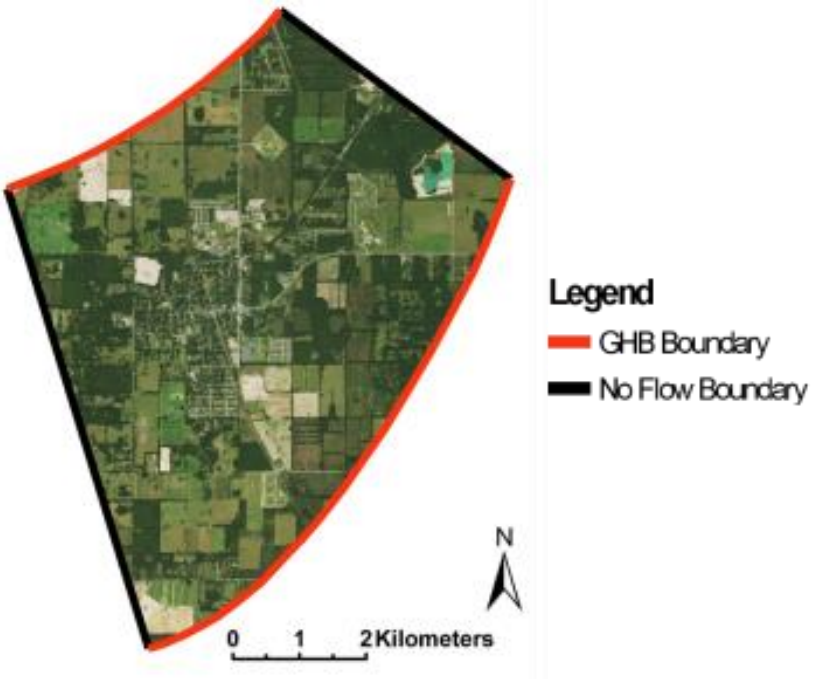

Figure 4-17. No-flow and general-head-boundary for Site 2

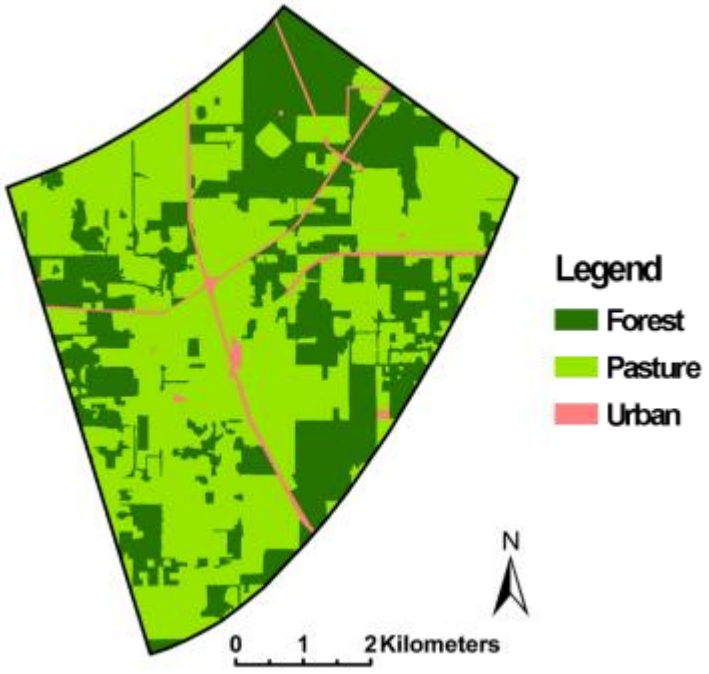

Figure 4-18. Land use and land cover map for Site 2

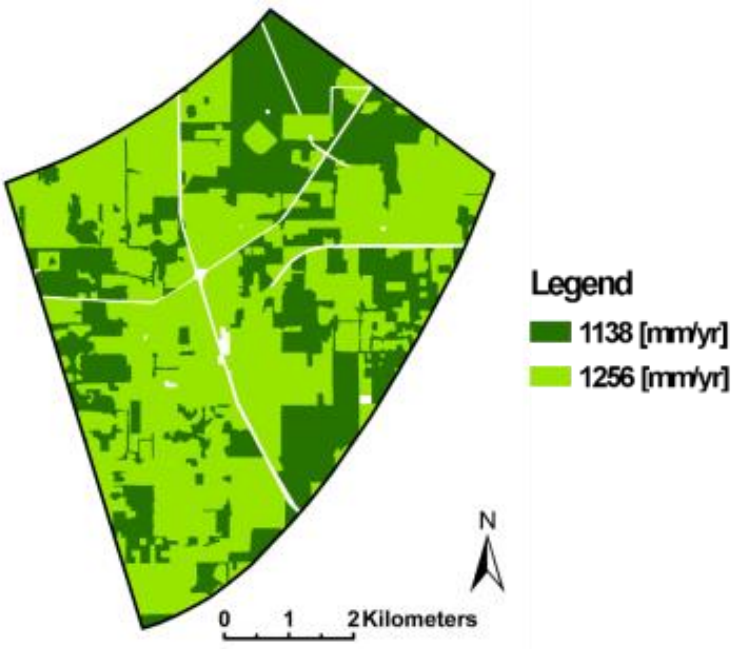

Figure 4-19. Recharge boundary map for Site 2

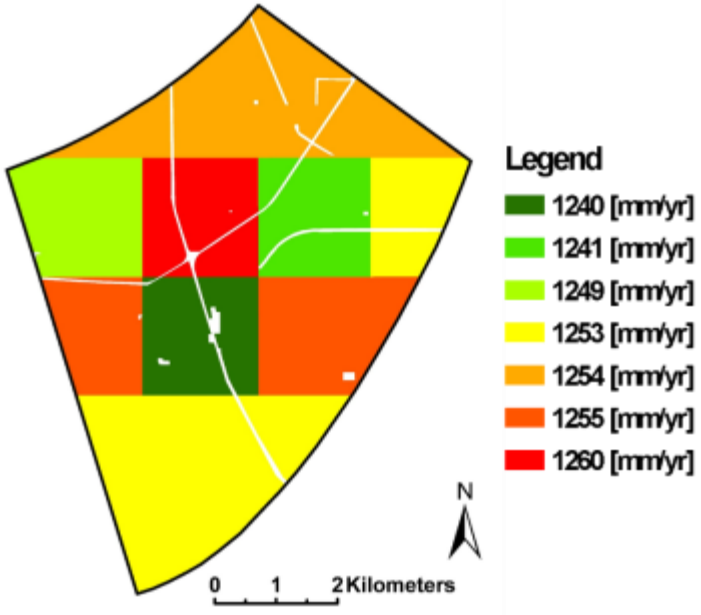

Figure 4-20. Evapotranspiration boundary map for Site 2

Initial Conditions

The initial conditions of water levels of each layer were obtained from the output of the developed and calibrated north-central Florida Groundwater Flow model.

Simulation Results

The simulated water level of Layer 1, which represented the water table elevation, is shown in Figure 4-21. The simulated water level of Layer 2, which represented the potentiometric level elevation, is shown in Figure 4-22. Based on the simulation results, contours of water level were generated. Based on the generated contours, the general groundwater flow pattern can be observed from southwest to northeast. Based on the generated contours, the boundary of the local-scale high-resolution model can be generated. The model domain of the local-scale high-resolution model is shown in Figure 4-23. The objective of developing the regional-scale model was to understand the general pattern of groundwater flow in the study area and its vicinity to identify and delineate the model domain of the local-scale high-resolution model. The regional-scale groundwater model acts as a 'pre-run' model, and the output of the regional-scale groundwater model provides the input data for developing the local-scale high-resolution model. The local-scale high-resolution model is calibrated by the water levels measured with the piezometers, and the output of the calibrated local-scale high-resolution model is used for further analysis on the development of high-resolution recharge map, regression model for estimating recharge rate, and diagram showing the risk level of potential sinkholes for each recharge level.

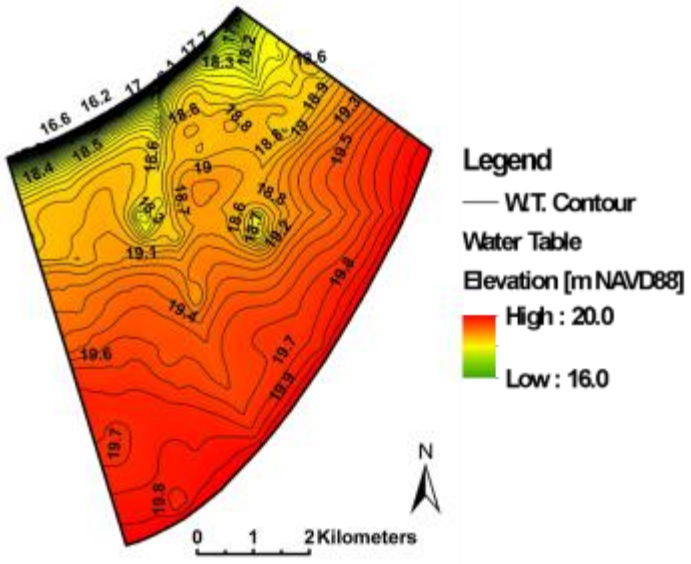

Figure 4-21. Groundwater level in the soil layer for Site 2

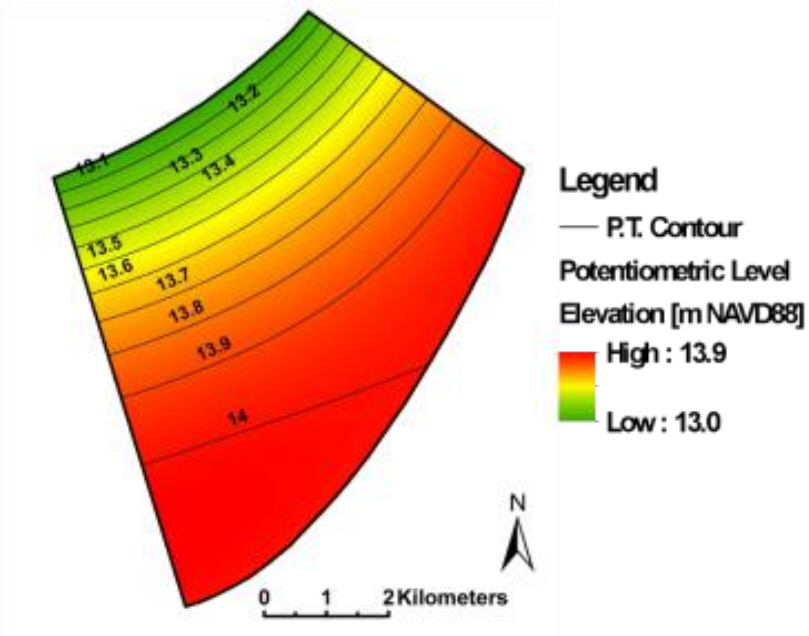

Figure 4-22. Groundwater level in the limestone layer for Site 2

4.3.3. Local-Scale Model

Model Domain

The study area was the Detention Pond Site (FDOT drain basin) located at the center of the regional-scale MODFLOW model domain as shown in Figure 4-23. The boundary of the model domain was marked in black, as shown in Figure 4-23. The boundary of the model domain was characterized by the hydrologic boundaries either normal to the flow direction or parallel to the flow direction as indicated by the simulated water level from the above-mentioned regional-scale model. The criterion for defining the boundary of the local-scale high-resolution model was identical as the criterion for defining the boundary of the regional-scale model described earlier.

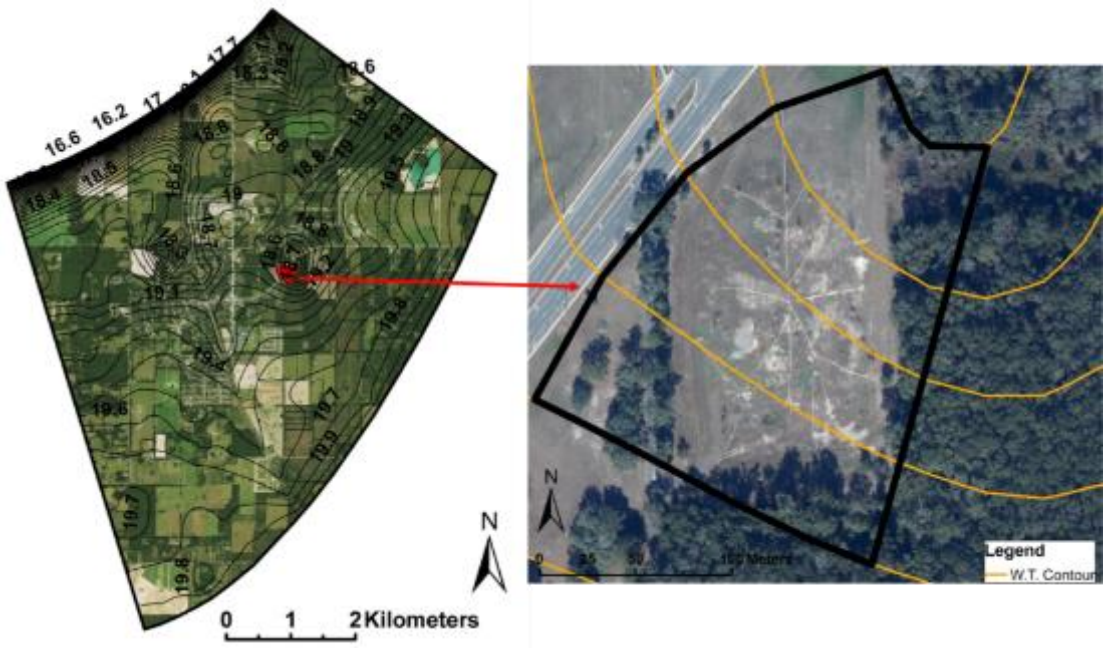

Figure 4-23. Location of the model domain in the regional model (Site 2)

Discretization

Horizontally, the model domain was discretized into 86 rows and 78 columns with a uniform grid spacing of 3 m by 3 m; vertically, the model domain was divided into three layers. This was different from the discretization criterion of the regional-scale model with a uniform grid spacing of 30 m horizontally and 2 layers vertically. For the local-scale high-resolution model, the model domain was discretized into 3 layers based on the soil properties collected from the SPT borings. Based on soil classifications identified by SPT boring logs, Layer 1 represented the mixed sand/clay layer, and Layer 2 represented the top layer of weathered limestone, and Layer 3 represented the weathered limestone. The locations of the SPT boring logs are shown in Figure 4-24. The soil stratigraphy output from one of the SPT boring logs (SPT Boring Log A-120) is also shown in Figure 4-24. It can be observed that the overburden soil above the limestone layer was a mixture of sandy clay and sand. Layer 1 was a mixture of sandy clay and sand. Layer 2 was the top layer of weathered limestone with an average RQD of 65%. Layer 3 was weathered limestone with an average RQD of 95%. The spatial discretization of the model domain is shown in Figure 4-25.

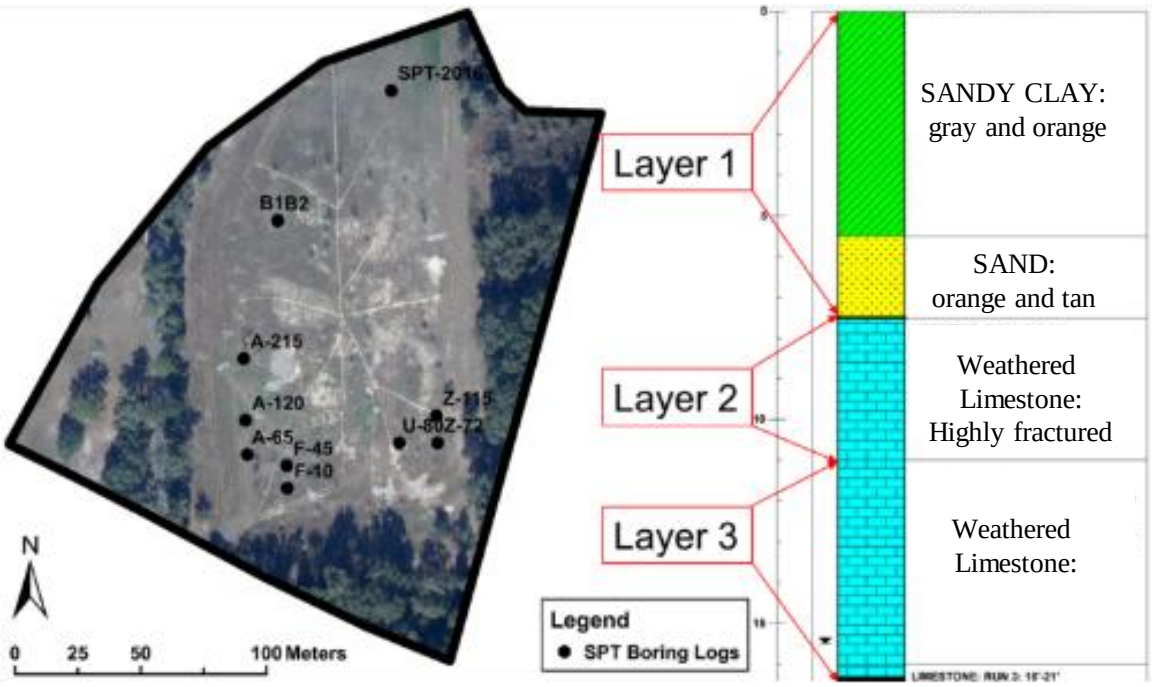

Figure 4-24. Location of the performed SPTs at Site 2

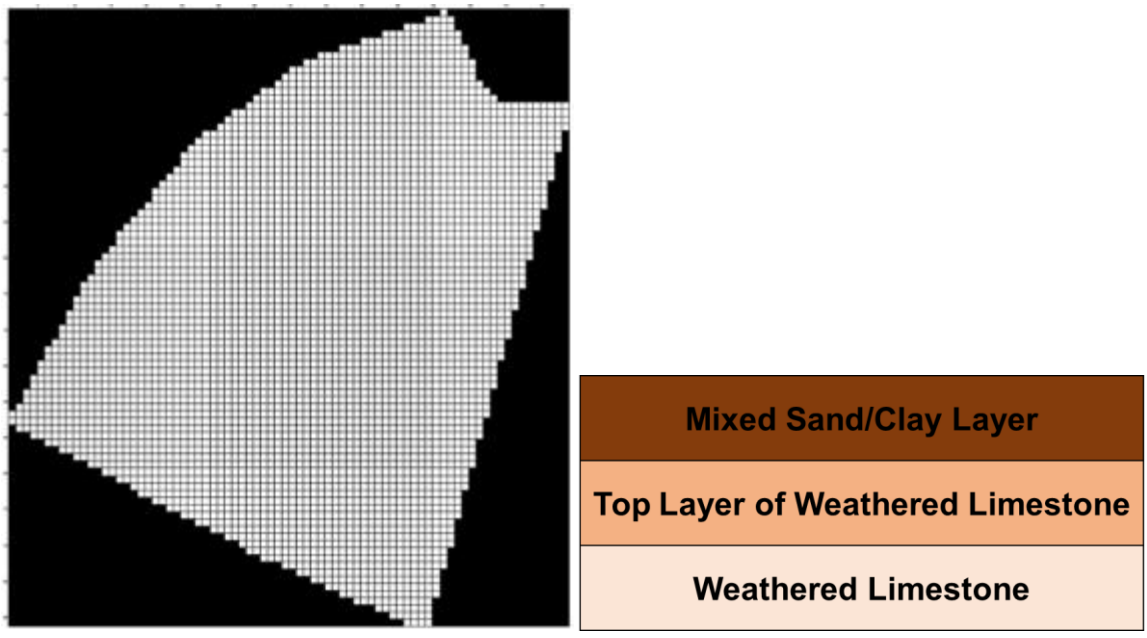

Figure 4-25. Spatial discretization of model domain (left) and vertical discretization layers (right)

Parameters

The local-scale model was discretized into three layers. Layers 1 represents the overburden surficial soil, Layer 2 represents the top layer of weathered limestone, and Layer 3 represents the weathered limestone. The spatial variation of hydraulic conductivity of each layer was different because the hydrogeologic characteristics were different in each layer, and the hydrogeologic characteristics were spatially varied. In the regional-scale model developed previously, the spatial variation of hydraulic conductivity was not considered due to lack of *in situ* field measured soil data. However, in the local-scale groundwater model, the spatial variation of hydraulic conductivity was taken into consideration since the SPTs can provide soil and rock properties to some extent. The data from the 10 SPTs enabled estimating the spatial variation of hydraulic conductivity in high-resolution. The criterion of determining the spatial variation of hydraulic conductivity is presented below.

In total, there were 10 SPT boring performed within the model domain of the local-scale groundwater model. Take the boring log named 'A-120' for example (Figure 4-24). From Figure 4-24, it was concluded there are two layers above the limestone layer, including sandy clay and sand. Each type of soil has its own characteristics. For sand, the typical range of hydraulic conductivity varies from 0.02 – 20 m/d (Domenico & Schwartz 1990). Thus, the hydraulic conductivity value selected to represent sand was chosen as 10 m/d (the average value of 0.02 m/d and 20 m/d). For sandy clay, the typical range of hydraulic conductivity varies from 0.001 – 0.01 m/d (Domenico & Schwartz 1990). Thus, the hydraulic conductivity value selected to represent sandy clay was chosen as 0.005 m/d (the average value of 0.001 m/d and 0.01 m/d). Layer 1 is a mixture of sandy clay and sand, and the effective hydraulic conductivity of this mixed soil is calculated. For limestone, the typical range of hydraulic conductivity varies from 0.1 – 2000 m/d (Domenico & Schwartz 1990). The hydraulic conductivity of limestone is highly dependent on the RQD (Qureshi et al. 2014). Based on the RQD and the empirical equation, the hydraulic conductivity values selected to represent Layers 2 and 3 were 0.1 to 5.1 m/d, respectively.

Note that there are 10 SPT boring logs capable of identifying soil classifications. The soil characteristics collected from the other 9 SPT boring logs were analyzed in the same manner and the hydraulic conductivity values were obtained in the same way. Once the hydraulic conductivity values at the 10 SPT boring logs sites were obtained, a kriging interpolation method was applied to generate the spatial variation of hydraulic conductivity for model input. The spatial variation of hydraulic conductivity in Layers 1, 2, and 3 were imported into the high-resolution model. It should be noted that these values were estimated values in that the exact values of hydraulic conductivity are still unknown. They were initial values and later adjusted in the calibration procedure.

Boundary Conditions

The no-flow boundary, general-head boundary, recharge boundary, and evapotranspiration boundary were used to generate the high-resolution local-scale model.

For Layer 1, no-flow boundary and general-head boundary were used to represent the hydrologic boundaries that have zero flux exchange and non-zero flux exchange. The no-flow boundary was assigned to Layer 1 for the following conditions: (1) the inactive areas that are outside the study area and groundwater flows in those areas are not simulated and (2) the lateral boundary that the groundwater flow direction is parallel to it. The general-head boundary was assigned to the model boundary where a groundwater exchange between the inside and outside of the model domain occurred. The reference water levels and conductance values were obtained from the output of the regional-scale groundwater model. Recharge boundary and evapotranspiration boundary were used to represent the exchange between surface water and groundwater on top of Layer 1. The no-flow and general-head boundary assigned to Layer 1 is shown in Figure 4-26. Vertically, the recharge boundary and evapotranspiration boundary were applied to the top of Layer 1, and the boundary values were calculated from the output of the regional-scale model. The recharge boundary was dependent on land use and land cover, and is shown in Figure 4-27. The evapotranspiration boundary is shown in Figure 4-28, and the extinction depth set to the evapotranspiration boundary is shown in Figure 4-29. A constant head boundary was assigned to the entire area of Layer 2 because the potentiometric level in Layer 2 was constant throughout the model domain.

Figure 4-26. Flow boundaries applied to Layer 1

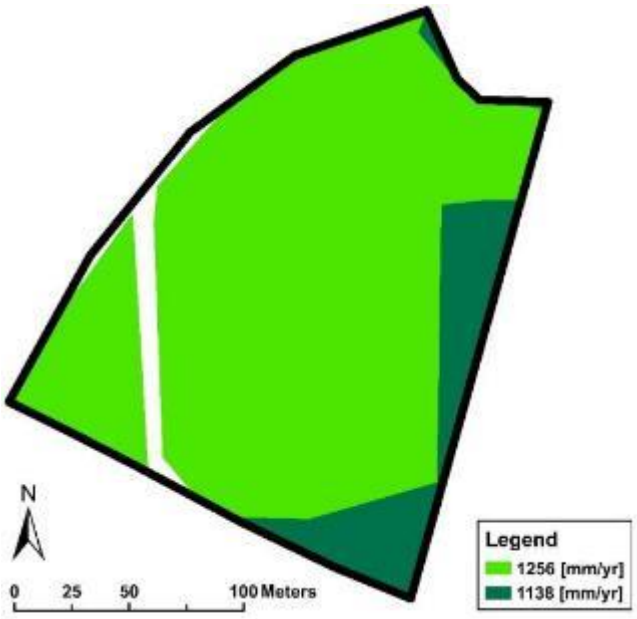

Figure 4-27. Recharge boundary applied to Layer 1

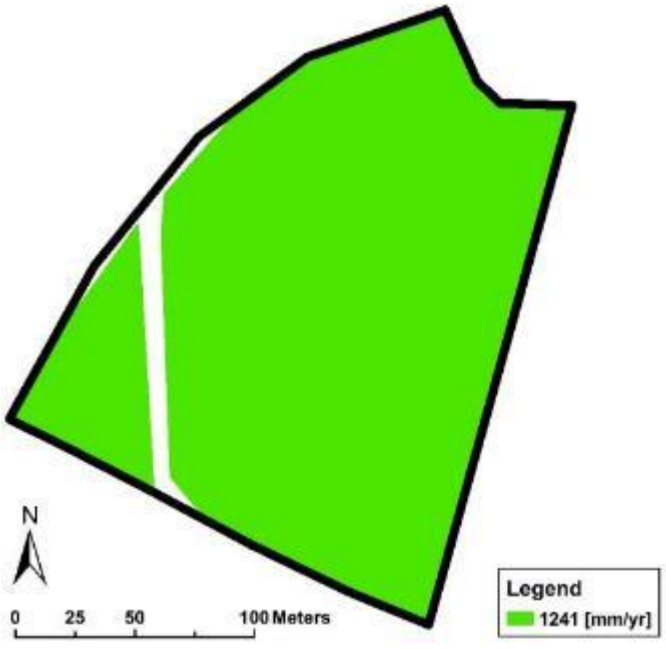

Figure 4-28. Evapotranspiration boundary applied to Layer 1

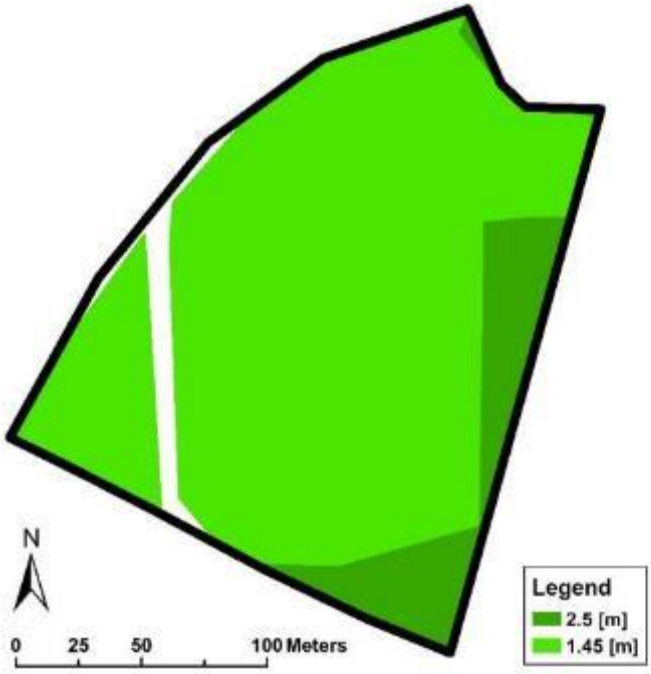

Figure 4-29. Extinction depth applied to Layer 1

Initial Conditions

The initial conditions refer to the initial water table elevation and potentiometric elevation before simulation. The initial water table elevation and potentiometric elevation were obtained from the output of the regional-scale model described previously.

4.3.4. Calibration

The water table elevation simulated by the local-scale model was then calibrated against the observed water table elevation measured by the *in situ* piezometers. The model calibration was achieved through a trial-and-error method by modifying the values of hydraulic conductivity of each layer until the simulated water levels match the observed water levels to a satisfactory degree. However, the values of hydraulic conductivity of Layers 1, 2, and 3 were adjusted within a reasonable range (not allowed to exceed the maximum typical value while not allowed to be lower than the minimum typical value).

In total, there were 20 piezometers installed to measure water table elevations from December 21, 2016 to December 15, 2017, as shown in Figure 4-30. The water table elevation varies seasonally dependent on the seasonal rainfall. The annual-averaged water table elevation measured from the 20 piezometers are tabulated in Table 4-4. The simulated water level from Layer 1 was used for calibration, since it represents the simulated site water table.

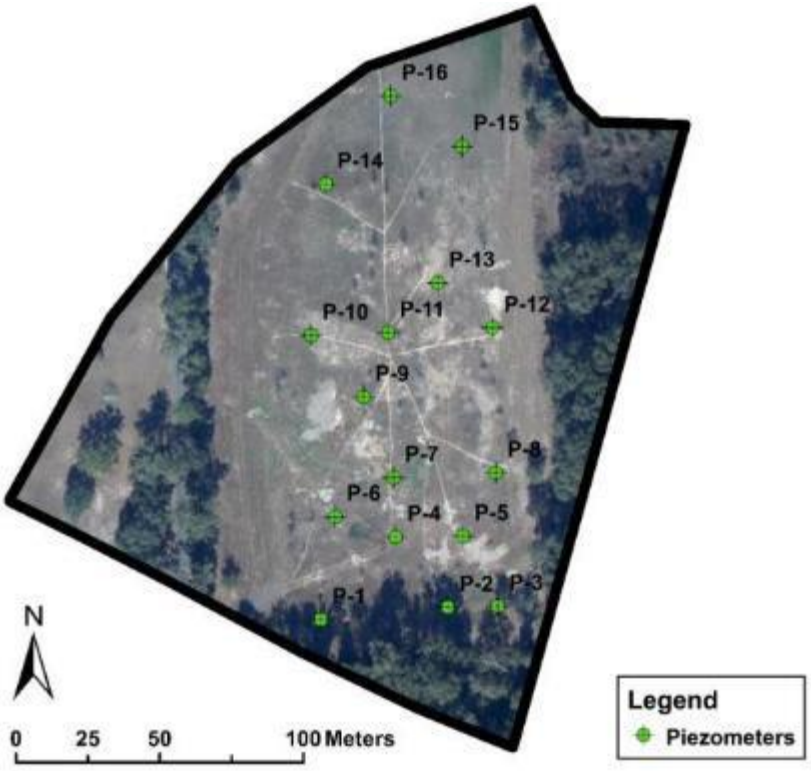

Figure 4-30. Locations of the installed piezometers at Site 2

Table 4-4. Annual-averaged water table elevation measured from 16 Piezometers

Piezometer Name	Water Table [m NAVD88]
P-1	16.16
P-2	15.32
P-3	15.61
P-4	15.27
P-5	14.42
P-6	15.8
P-7	15.31
P-8	13.91
P-9	15.44
P-10	14.38
P-11	14.43
P-12	13.65
P-13	14
P-14	14.07
P-15	12.23
P-16	13.8

After the calibration, the simulated water levels and the observed water levels matched satisfactorily. The R2 was 0.66 as shown in Figure 4-31, indicating a good agreement between simulated water levels from the calibrated groundwater model and the observed water levels from the field-measured hydrologic data from the *in situ* piezometers. The adjusted hydraulic conductivities of each layer are shown in Figure 4-32a, 32b, 32c, and 32d, and the spatial variation of the calibrated water table elevation is presented in Figure 4-33. Recall, isotropic conditions were assumed for Layer 2 and Layer 3.

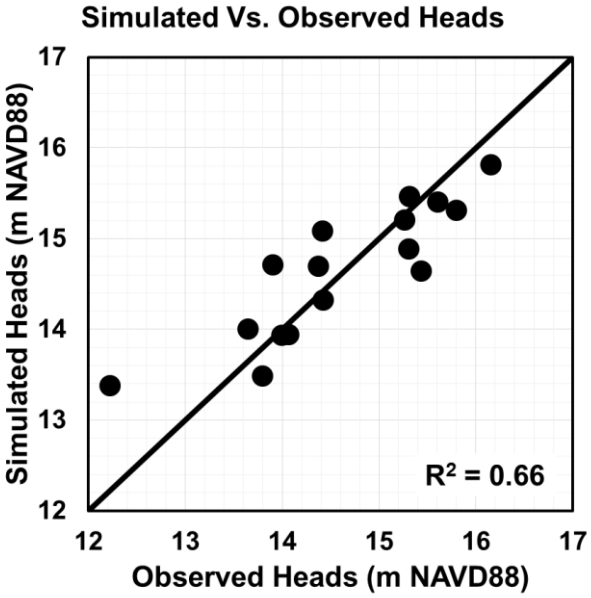

Figure 4-31. Relationship between the simulated heads and the observed heads at Site 2

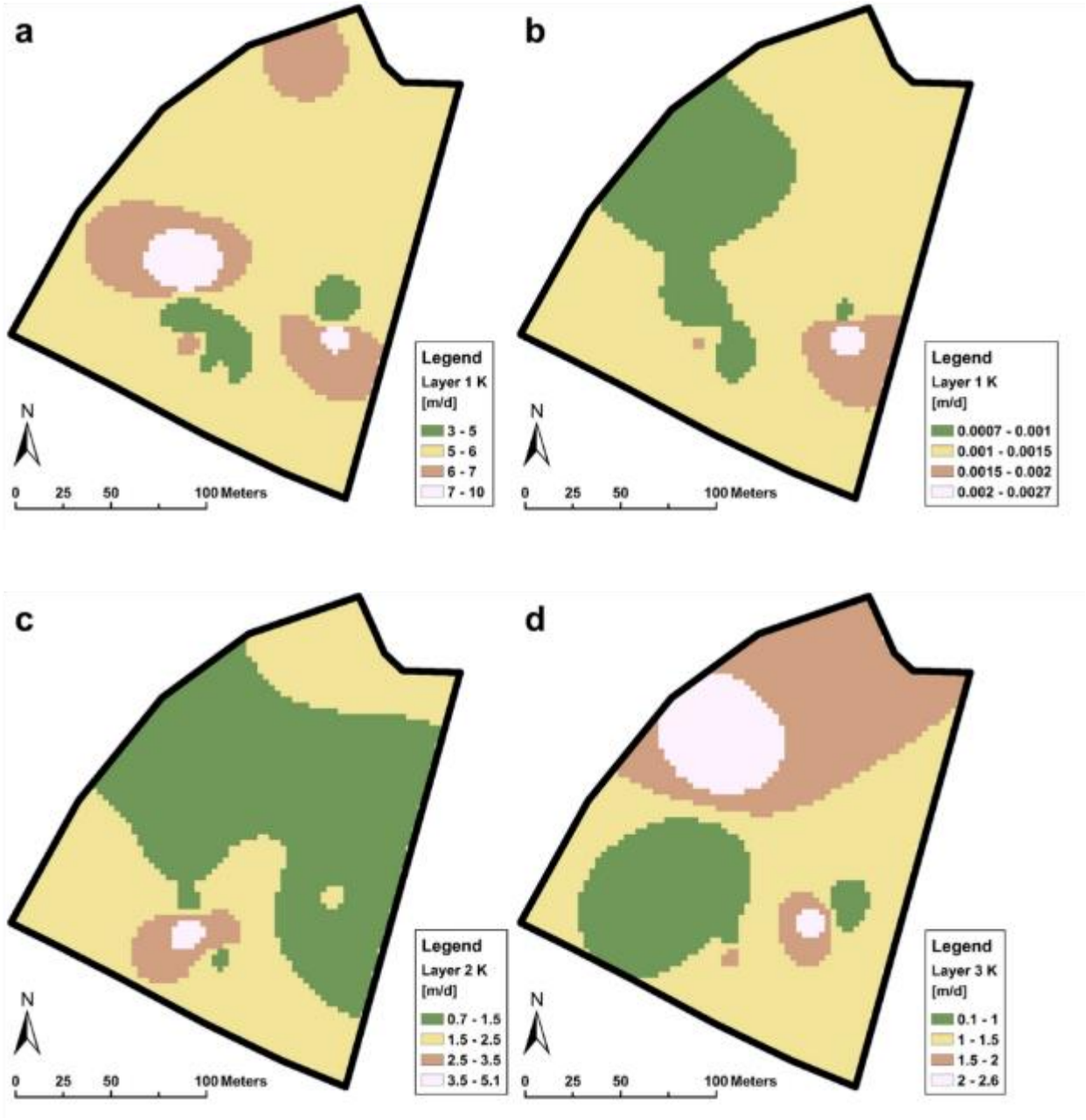

Figure 4-32. Calibrated hydraulic conductivities for Layer 1 (a) K_h and (b) K_v, Layer 2 (c), and Layer 3 (d)

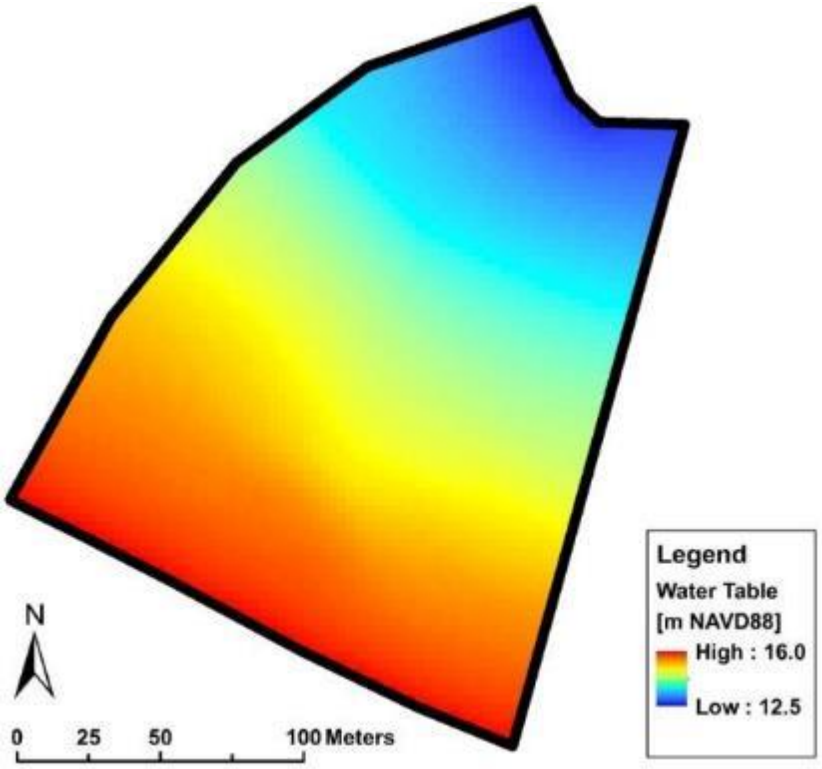

Figure 4-33. Calibrated water table elevation map for Site 2

4.4. High-Resolution Recharge Maps

The high-resolution recharge map for the Wekiva Parkway site was generated based on the output of the local-scale model as shown in Figure 4-34. The recharge rate is the downward seepage rate of groundwater from the surficial layer (Layer 1) to the limestone layer (Layer 5). Positive values of recharge rate indicate downward seepage and negative values indicate upward seepage.

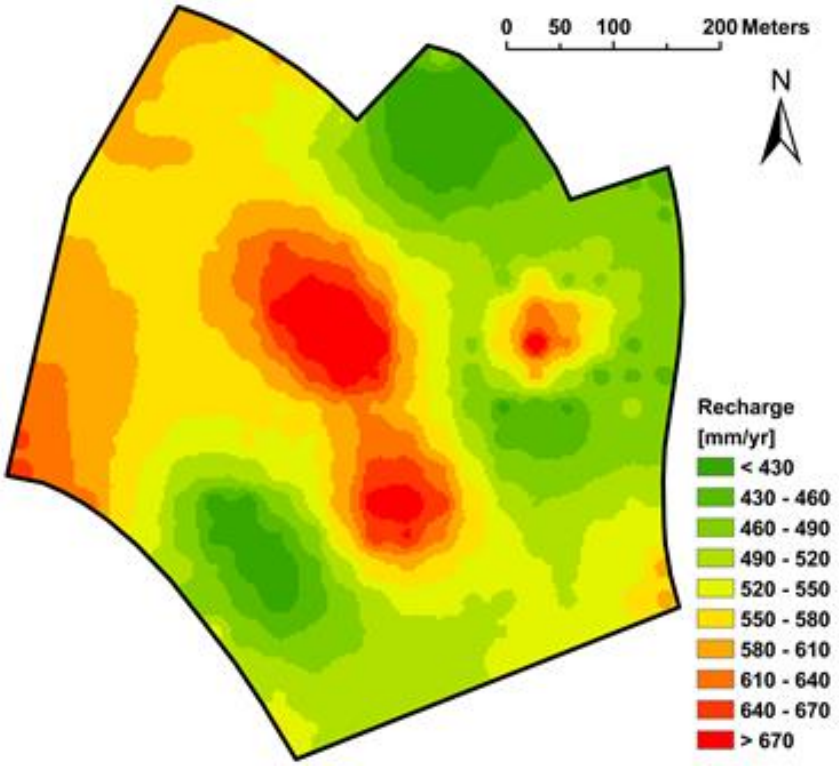

Figure 4-34. High-resolution recharge map for Site 1

The high-resolution recharge map for the Newberry Detention Pond site was generated based on the output of the local-scale model as shown in Figure 4-35. The recharge rate is the downward seepage rate of groundwater from the surficial layer (Layer 1) to the limestone layer (Layer 3). Positive values of recharge rate indicate downward seepage and negative values indicate upward seepage. The unit of recharge rate for both figures is millimeter per year and the higher rates of recharge are represented by the warmer (red) colors. As shown, the maximum recharge rate is higher at Site 2 which should be expected since the site is an excavated detention pond, thus removal of natural overburden soils has created a less-impeded path for groundwater to flow into the limestone layer.

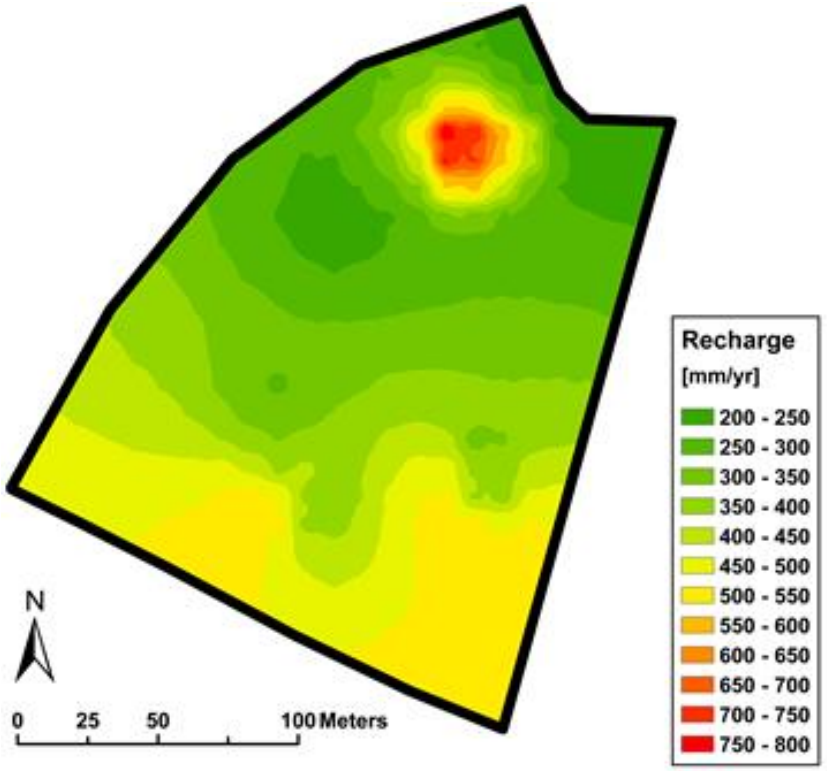

Figure 4-35. High-resolution recharge map for Site 2

4.5. Risk Level of Sinkhole Activity

For both sites at the Wekiva Parkway Bridge at Mt. Plymouth, Florida (Site 1) and the detention pond at Newberry, Florida (Site 2), the risk level of sinkhole occurrence is estimated based on the simulated recharge rate. Wilson and Beck (1992) pointed out that sinkhole occurrence frequency is highly related to groundwater recharge. Xiao et al. (2016) also showed a strong correlation between sinkhole spatial density and the spatial variation of recharge rate and found that sinkhole occurrence frequency increases linearly with increasing recharge rate. Therefore, a sinkhole risk map was constructed based on the computed groundwater recharge.

Three steps were employed to construct the recharge-based sinkhole risk map. In the first step, the criteria of sinkhole risk categories were established with the correlation between sinkhole occurrence and recharge for a larger scale area, which is east-central Florida. Figure 4-36 shows the reported sinkholes projected on the recharge map developed by the St. Johns River Water Management District (SJRWMD). Also, shown in Figure 4-37, SJRWMD defines four recharge categories which include: (i) Class 1: < 0 mm/yr, (ii) Class 2: between 2 and 127 mm/yr, (iii) Class 3: between 127 and 254 mm/yr, and (iv) Class 4: > 254 mm/hr. Sinkhole density (defined as the number of sinkhole per 100 km^2) was computed for each class and the result show a strong correlation. Thus, Classes 1 through 4 correspond to the sinkhole risk levels of Discharge, Low, Medium, and High, respectively.

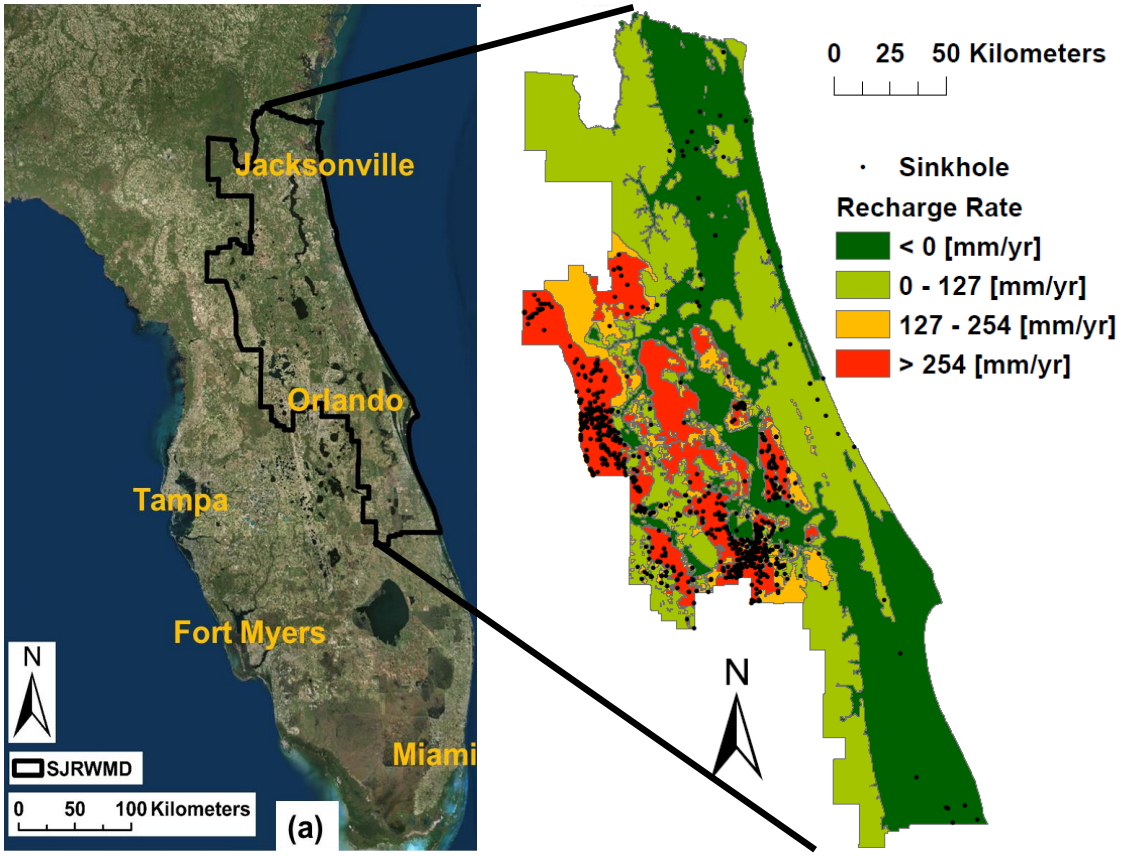

Figure 4-36. Development of sinkhole risk category criteria: reported sinkholes projected onto the recharge map (by SJRWMD)

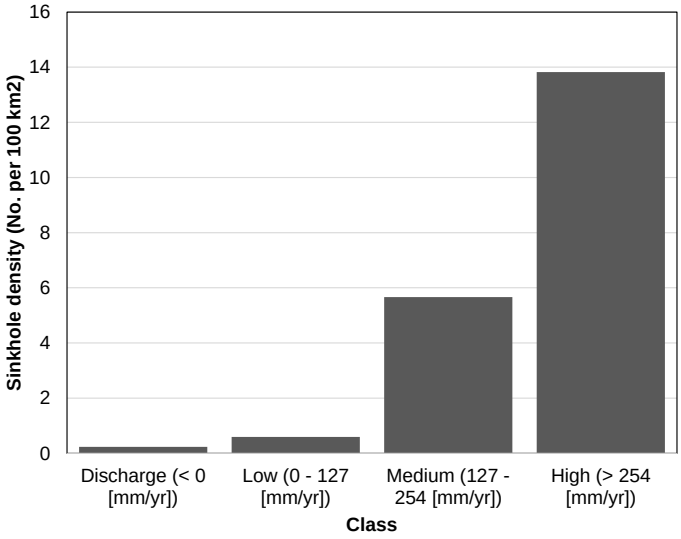

Figure 4-37. Sinkhole spatial density vs. four sinkhole risk categories

In the second step, the sinkhole risk categories are applied to the high-resolution recharge maps constructed by MODFLOW modeling. Figures 4-38a and 38b shows the recharge-based sinkhole risk maps of the Wekiva Parkway site (see Figure 4-35) and the detention pond at Newberry (see Figure 4-36), respectively. It could be observed from Figure 4-38b that: (1) the areas marked in red color have a High risk of sinkhole occurrence, (2) the areas marked in dark yellow color have a Medium risk of sinkhole occurrence, (3) the areas marked in light and dark green color have a Low risk of sinkhole occurrence. It can also be observed that the whole area of Site 1 has a high-risk level of sinkhole occurrence, and the majority area of Site 2 has a high-risk level of sinkhole occurrence.

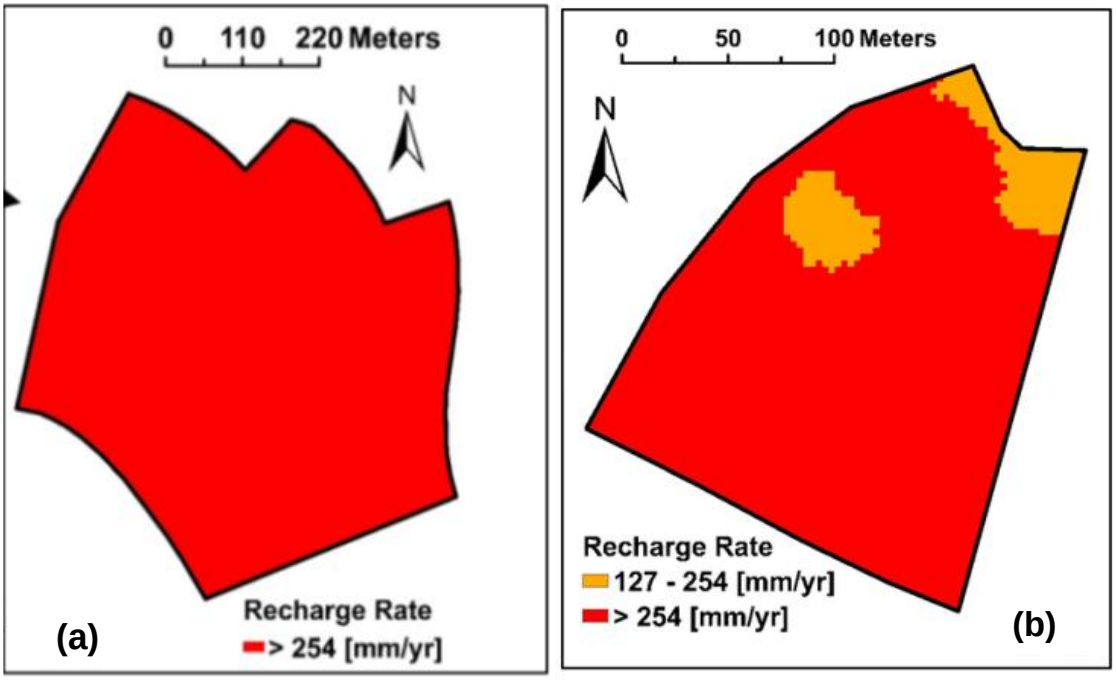

Figure 4-38. Groundwater recharge criteria for (a) Site 1 and (2) Site 2

In the third step, sub-classification can be applied to the risk map to further delineate the relative level of sinkhole risk. For example, the whole area of Wekiva Parkway (Site 1) is High risk, showing only red on the map as seen in Figure 4-38a. The relatively lower and higher risk levels at Sites 1 and 2 are further classified into five categories, including Category I, Category II, Category III, Category IV, and Category V, based on the variation of recharge rate. The corresponding ranges of recharge rate for each category is summarized in Table 4-5. After applying these five risk categories criteria, the revised sinkhole risk maps for Sites 1 and 2 are presented in Figures 4-39a and 4-39b, respectively.

Table 4-5. Sub-classes of relative sinkhole risk level associated with recharge rate

Sub-risk category	Recharge rate (mm/yr)
Category I	< 400
Category II	400 – 500
Category III	500 – 600
Category IV	600 – 700
Category V	> 700

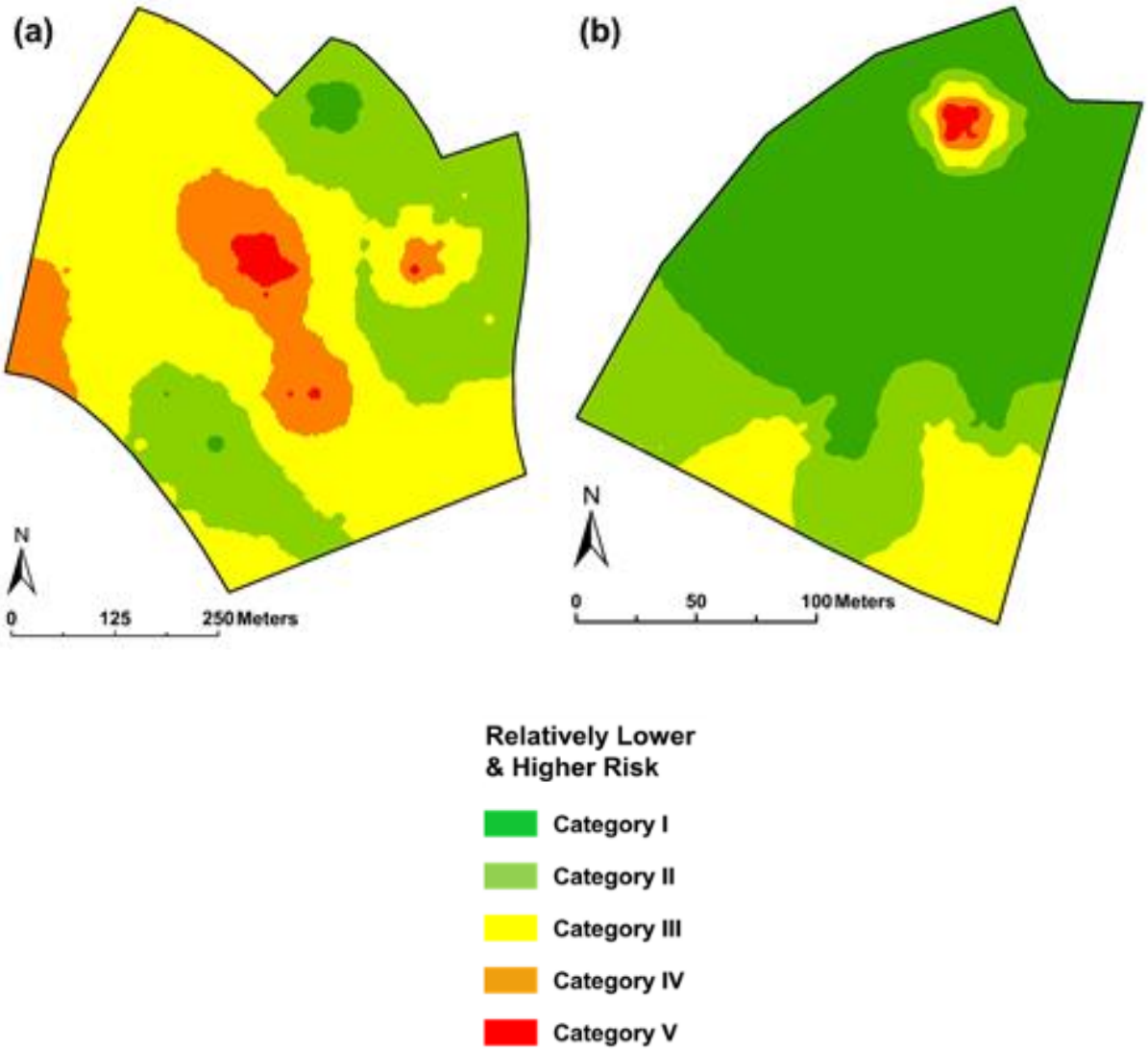

Figure 4-39. Derived relative risk level map of sinkhole occurrence for each study site

4.6. Regression Model for Estimating Recharge Rate

Due to limitations of available field-measured data, as well as the time required to develop and calibrate a groundwater model, it is not always efficient to use a groundwater model to simulate the recharge rate. In short, it is necessary to develop a method to estimate recharge rate instead of using a groundwater model. Thus, a regression analysis was conducted to explore the relationship between recharge rate and its key controlling factors based on the recharge rate simulated by the local-scale model. The objective of developing this regression model is to simplify the procedures for estimating recharge rate.

From Darcy's Law, the key controlling factors of the recharge rate include vertical hydraulic conductivity, water level of the surficial sand layer, water level of the limestone layer, and thickness of the confining layer. These controlling factors should be taken into consideration for the regression analysis. The mathematical expression to estimate recharge rate based on Darcy's Law is shown in the equation below.

$$Re = K_z \times \frac{H_S - H_L}{L} \qquad \text{.....Eq. 4.1}$$

Where, Re = Recharge rate (m/d)
K_Z = Vertical hydraulic conductivity (m/d)
H_S = Water level of the surficial sand layer (m)
H_L = Water level of the limestone layer (m)
L = Thickness of the confining layer (m)

Recharge rate is directly proportional to the water level difference between the surficial sand layer and the limestone layer. Therefore, recharge rate increases if the water level difference increases and decreases if the water level difference decreases. In general, water level difference is affected by rainfall and evapotranspiration. Since recharge rate is influenced by rainfall, evapotranspiration, vertical hydraulic conductivity, and thickness of confining layer, all of these controlling factors were included in the regression analysis. The mathematical expression of the regression analysis is shown in the next equation.

$$Re = a \times (K_z \times \frac{P - ET}{L}) + b \qquad \text{.....Eq. 4.2}$$

Where, P = Mean daily rainfall (m)
ET = Mean daily evapotranspiration (m)
a, b = Regression coefficients

Mean daily rainfall was calculated from the measured rainfall data recorded by rain gauge SR46A operated by St. Johns River Water Management District. Mean daily evapotranspiration was calculated from the potential evapotranspiration data collected by Florida Evapotranspiration Network data collection sites. Effective vertical hydraulic conductivity was computed from the

calibrated vertical hydraulic conductivity and thickness of confining layer. Thickness of confining layer was the difference between the top elevation of the confining unit and the top elevation of the limestone layer. Recharge rate was obtained from the developed and calibrated local-scale model. Through data fitting as shown in Figure 4-40, the regression coefficients *a* and *b* were equal to 448.17 and 377.77, respectively. The mathematical expression of the regression model is also shown in Figure 40. The R^2 is 0.40, indicating a reasonable fit of the developed regression model to the data. The developed simple regression model and the derived expression could be applied to other similar sites to estimate recharge rate as well as determine the risk level of sinkhole occurrence without the necessity to develop and calibrate a groundwater model.

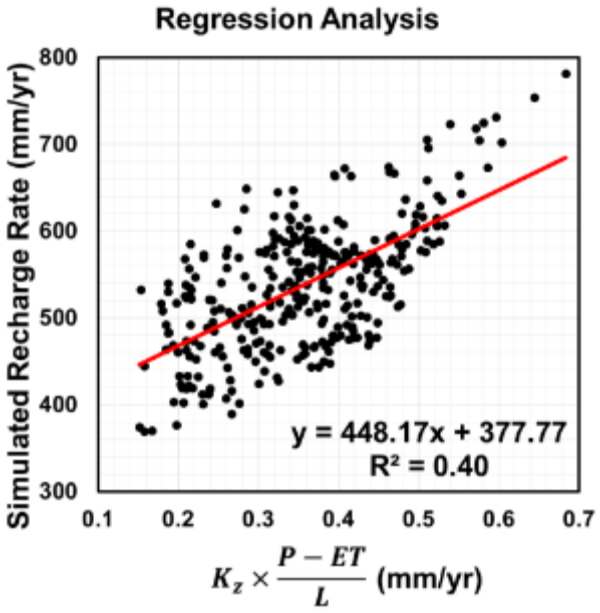

Figure 4-40. Regression analysis for estimating recharge rate

4.7. Summary

The model development and calibration was conducted through Groundwater Vistas, which is a software package for 3D groundwater flow and contaminant transport modeling using MODFLOW. The recharge rate was computed by Darcy's law input into MODFLOW. Recharge to the Floridan aquifer occurs in areas where the elevation of the water table of the surficial aquifer is higher than the elevation of the Floridan aquifer potentiometric surface. Although this difference in head is apparent in the majority of the central and north peninsula of Florida, the recharge rate is also dependent on the encountered soil layers and the regional groundwater flow conditions. Therefore, a methodology was developed to model and estimate the recharge rates into the Floridan aquifer at higher resolutions. The higher resolution can then provide a better assessment tool to identify potential problematic areas regarding sinkhole formation. Recommendations on piezometer spacing, required for calibration of the model parameters, as well as further implementation, is discussed in Chapter 7.

5. SINKHOLE ASSESSMENT USING CPT

5.1. Introduction

Sinkholes have been forming naturally in Florida for thousands of years. Much of Central Florida's circular ponds and lakes are attributed to karst geology and some type of sinkhole subsidence activity over time. Methods of detecting sinkhole anomalies tend to fall within the Geotechnical engineer's scope of work. Subsurface exploration tests such as Standard Penetration Test (SPT) and Cone Penetrometer Test (CPT) are commonly used by geotechnical engineers to determine soil engineering parameters at required depths depending on the type of structure being designed. In central Florida-- where the depth to encountered limestone can vary greatly-- it is common for subsurface exploration tests to be performed completely through the overburden (or soil overlaying the bedrock) and terminate when the bedrock is encountered. This is beneficial for sinkhole detection since natural sinkholes in Florida originate at the bedrock-soil interface and propagate towards the surface over time (Gray 1994; Rupert et al. 2004; Sinclair 1986). The internal erosion and migration of the overburden soil into the cracks and cavities of the limestone bedrock creates a zone of loose, or disturbed, soil usually found above the weathered limestone interface.

5.2. Internal Soil Raveling and Detection

The primary driving mechanism for this internal soil erosion in central Florida soils is *vertical* groundwater seepage. The Floridan aquifer system (FAS) is a deep semi-confined aquifer which underlays most the state. Separating the FAS and the surficial groundwater table aquifer is a group of generally impermeable silty and clayey soil known as the Hawthorn Group. In certain areas in central Florida, the Hawthorn Group can vary greatly in thickness and permeability and can even be non-existent from the soil strata (Figure 5-1). In these areas, vertical flow of groundwater between the surficial and Floridan aquifers is less impeded and the recharge rate (infiltration of water into the Floridan aquifer) is high. As shown in the highlighted red section in Figure 5-1, these areas coincide with the central Florida region. When cavities in the limestone bedrock are abundant, the vertical flow of groundwater between aquifers can cause soil migration and further erosion of the cavities. The soil migration and erosion of overburden, overtime, expands further into the overburden strata. This process is known as soil raveling, and is the main mechanism of natural sinkhole formation in central Florida.

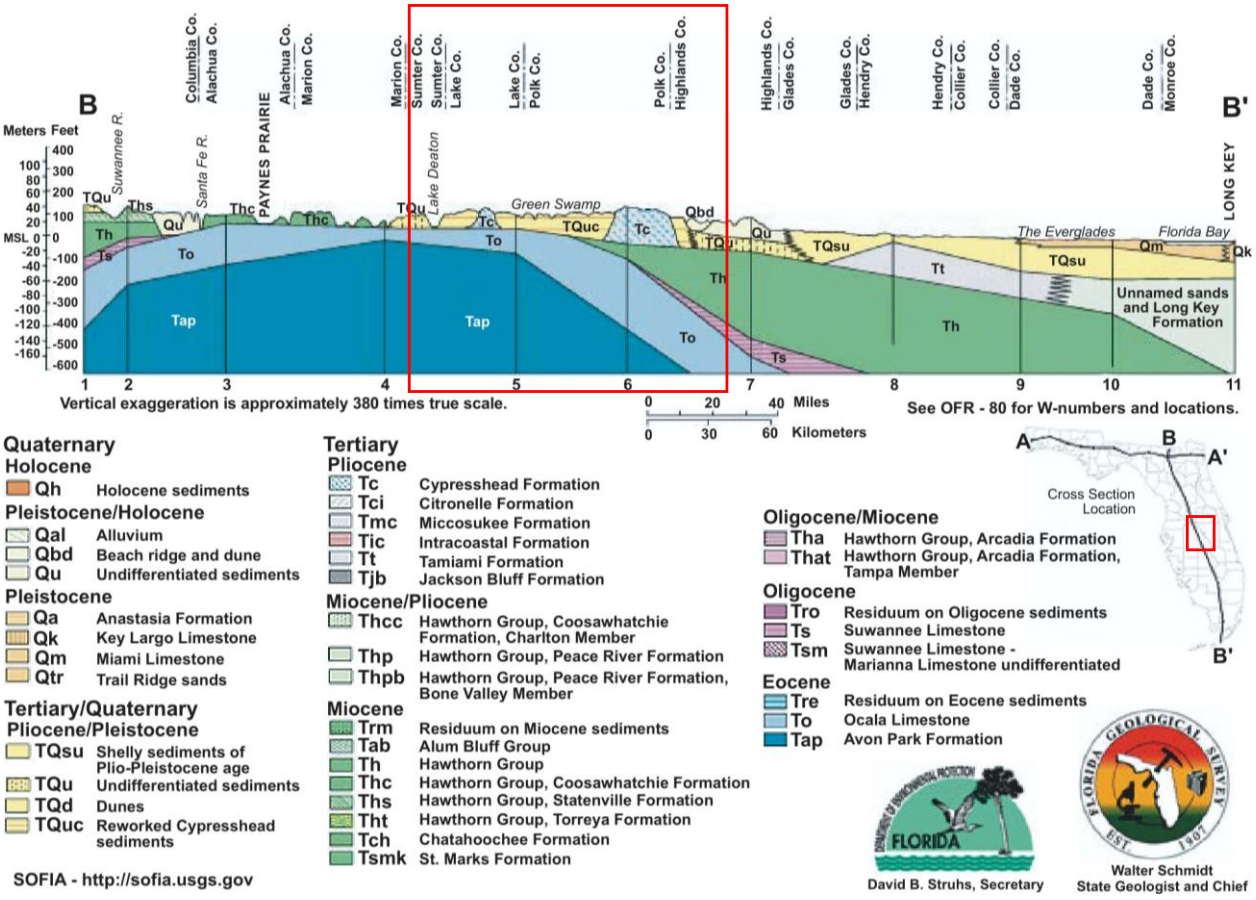

Figure 5-1. Geologic cross-section of Florida Peninsula -- North to South
(Source: (Florida Geological Survey, 2001))

Identifying any possible soil raveling is the primary method of detecting a forming sinkhole before any evidence may be present on the ground surface. The sinkhole raveling process, SPT detection, and formation due to the process of soil raveling is presented in Figure 5-2. Here we see the soluble bedrock overlain by a relatively thinner confining unit and then medium dense to dense clayey and silty sands above that. The breach in the confining unit (Hawthorn Group soils) acts almost like a funnel which magnifies the seepage forces in that area, thus causing the concentrated internal erosion. The medium dense sands and clayey sands commonly found in central Florida can withstand slight arching stresses, transmitting overburden weight around the softening soil, enabling a void to form. It is important to note that the raveling erosion does not necessarily always form a complete void or subterranean cavern. Rather, the soil in that specific area becomes extremely loose and its unit weight drastically decreases. This is evident in multiple CPTs and SPTs performed in sinkhole-active sites such that the split-spoon-sampler is still retrieving soil samples at the depths where the soil resistance is drastically and abnormally low. The internal soil erosion is also prevalent in the physical modeling of sinkhole formation performed in the laboratory (Perez et al., 2017).

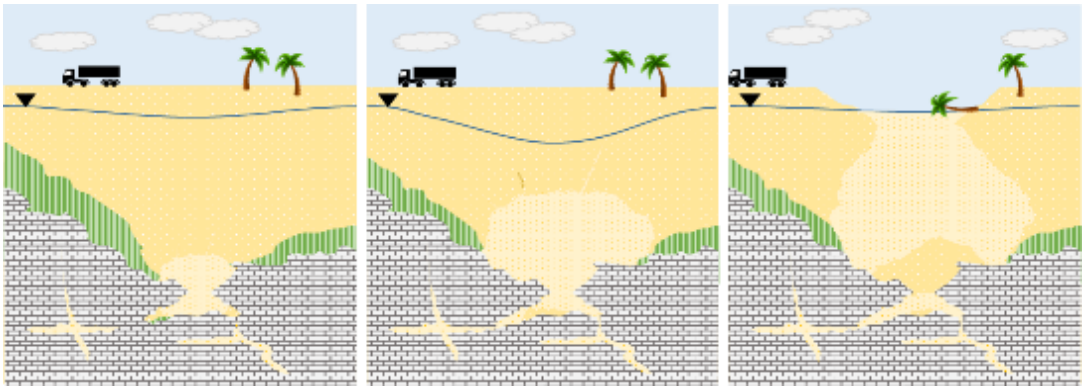

(a) Cover collapse sinkhole progression

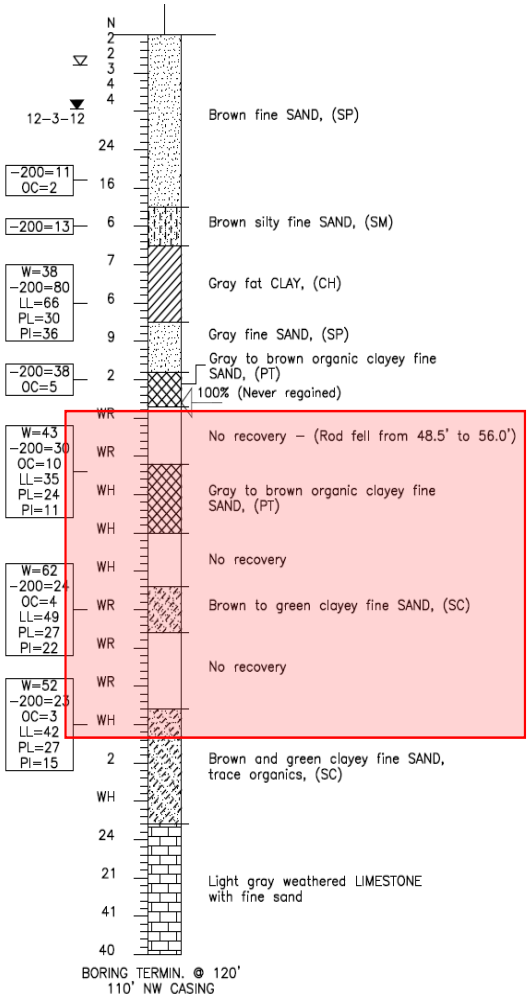

(b) Typical SPT boring log suggesting raveled soil encountered

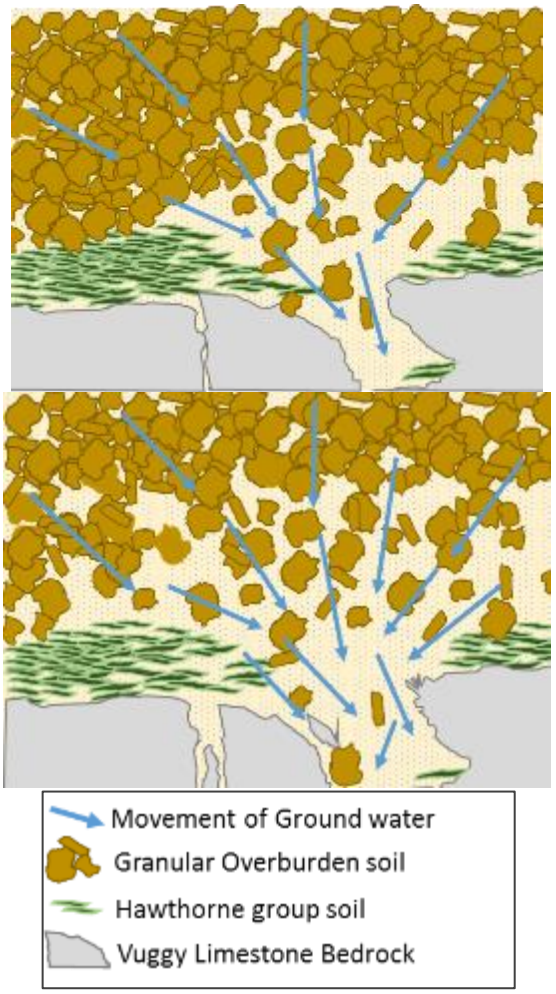

(c) Raveling mechanism over time

Figure 5-2. Soil raveling process

5.3. Development of CPT-Based Raveling Chart

The assessment techniques presented in this chapter focus primarily on implementing the Cone Penetration Test (CPT) results. Much like the Standard Penetration Test, CPT is a common subsurface exploration tool, used in the initial site investigation. However, instead of the blow count (N) obtained by the SPT, CPTs record penetration resistance in the form of tip resistance (q_c) and sleeve friction (f_s) by pushing a probe hydraulically at a constant rate (~2 cm/s). This method is much more accurate at locating discrete horizons or discrepancies in the soil strata since the soil resistance measurements are recorded at a higher frequency than those of the SPT. Cone Penetration Tests are also much more sensitive to fine grained material which typically produce lower resistance values. Although one can argue CPTs provide greater accuracy and consistency when measuring the soil resistance, the inability to obtain soil samples for lab testing or visual classification is a major limitation of CPT, especially when using a single test to estimate site stratigraphy or geohazard potential. Therefore, "ground-truthing" is a common technique used when implementing CPTs for subsurface investigation. By conducting a CPT next to a conventional boring with samples (such as SPT), the CPT soil strength measurements (q_c and f_s) can be validated with actual soil type and index properties to provide a more accurate stratigraphy estimation. This technique is especially important when characterizing soils at a site with known karst geology. Once ground-truthing has been performed, CPTs can be performed throughout the site at a much quicker rate than that of SPTs, allowing for an efficient subsurface exploration and characterization of sinkhole risk (Rogers, 2006).

The primary objective of this task is to use CPTs as an effective test method to evaluate sinkhole potential. The end goal is to develop a processing method geotechnical engineers can use when analyzing CPTs performed in central Florida which suggest a potential sinkhole anomaly. The popular CPT soil behavior type programs, which correlate CPT measurements to soil classifications, are believed to not best represent soil in central Florida's karst landscapes, especially when raveling may be present. For example, a soil stratum which possesses very low penetration resistance may be falsely represented as sensitive fine grained, organic material, or a fat clay if classified using the latest Soil Behavior Type (SBT) estimations used on many of the commercial CPT processing software (Robertson P. K., 2016). To better understand and identify trends in CPTs measurements relating to sinkhole raveling and formation, subsurface data was collected from multiple known sinkhole-active sites in central Florida within the same geotechnical and hydrogeological conditions.

5.3.1. Data Collection and Preparation

A historical CPT database from central Florida's active sinkhole project sites was provided by FDOT District 5 and SMO engineers. The database consisted of subsurface data for 12 sinkholes occurring in or near central Florida's highways within the last 15 years. Also used in this study was an extensive amount of subsurface exploration test for the Wekiva Parkway project, showing large volumes of low-resistance soil anomalies; suggesting the possibility of a sinkhole formation. An empirically developed CPT resistance criterion was developed from the provided case histories that can be used to indicate probable sinkhole conditions during the initial site investigation.

It is important to note that geology in central Florida, although relatively similar in age and lithology, varies greatly over even a couple miles. For convenience, USGS and FGS have characterized Florida into different geologic categories and present the information on color-coded maps, called “geologic maps”. These categories are created by grouping soils together based on their bedrock age, residual soil formation, depth to bedrock, majority soil types, and permeability. Therefore, when comparing residual soil condition data between different project sites, analysis only was performed between the sites within the similar geologic formation category near the land surface. Out of the 12 total sinkhole occurrence sites provided by FDOT with CPT data, three were located within the same geological formation as the Wekiva Parkway project. Figure 5-3 presents a map of central Florida with the three sinkhole sites, the Wekiva Parkway site, and the similar residual soil geologic formation – the Cypresshead Formation.

The Cypresshead Formation (represented by Tc) is composed primarily of siliciclastics and occurs only in the Florida peninsula and eastern parts of Georgia. This formation originates from the upper Pliocene epoch (~5.3 to 2.5 million years before present) and consists of reddish brown, unconsolidated to poorly consolidated, fine to very course, clean to clayey sands (Florida Geological Survey, 2001).The Cypresshead Formation is also considered to be very permeable and its sands form part of the surficial aquifer system. In central Florida, the Cypresshead Formation is underlain by the Hawthorn Groups (Th) and Ocala Limestone Formation (To), as shown in Figure 5-1.

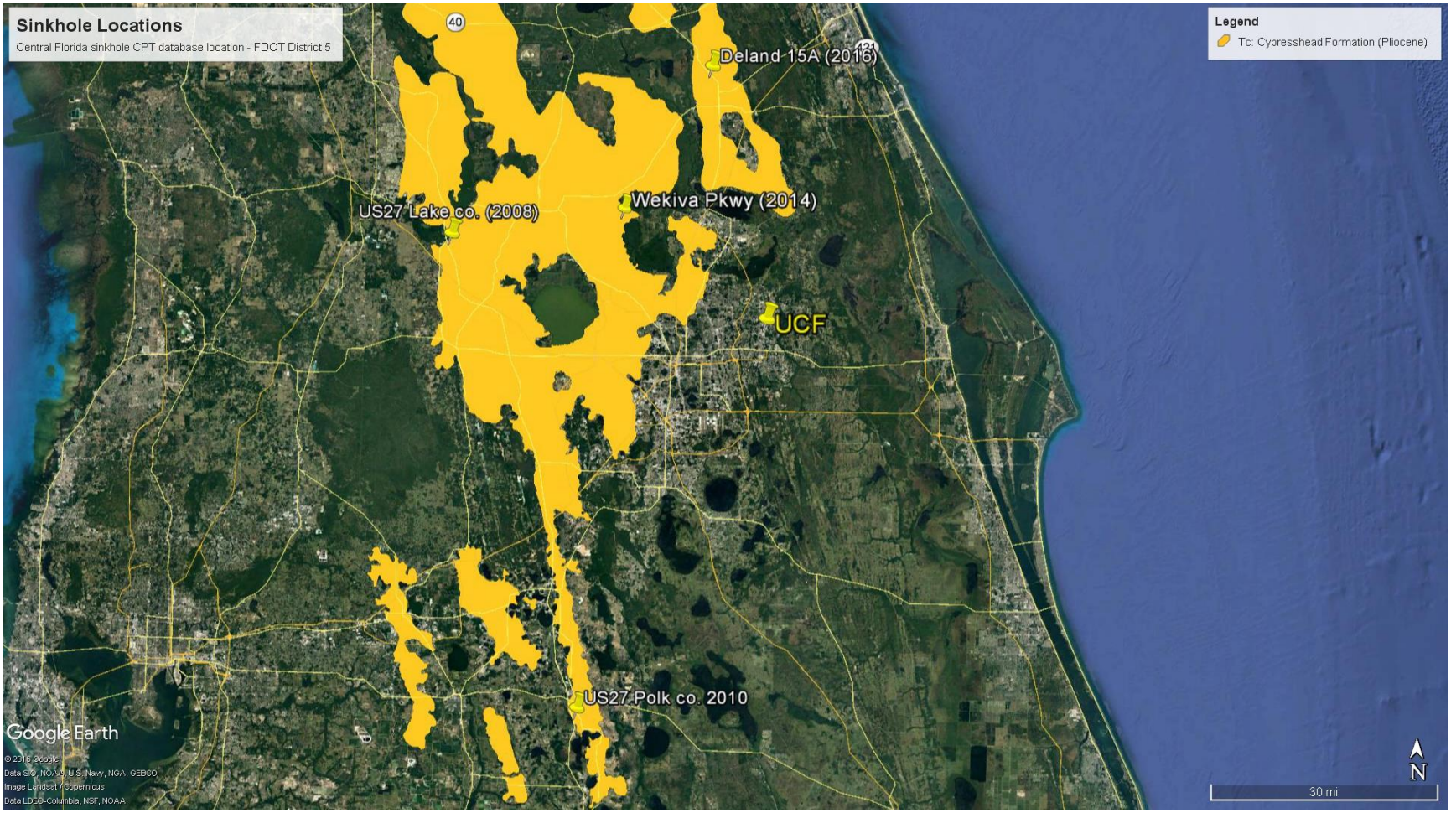

Figure 5-3. Location of sinkhole sites within the Cypresshead geological formation

5.3.2. Data Processing

Although data was obtained in similar geological conditions, the suspected raveling zones are located at varying depths above the limestone. Therefore, to correct for overburden stresses, a normalization procedure was performed on all CPTs analyzed. The normalization equations used in this study follow the procedure outlined in Robertson and Wride (1998); as follows:

$$Normalized\ Cone\ Resistance: \quad Q_{tn} = \left(\frac{q_c - \sigma_{vo}}{P_a}\right)\left(\frac{P_a}{\sigma'_{vo}}\right)^n \qquad \text{.....Eq. 5.1}$$

$$Normalized\ Friction\ Ratio: \quad F_R = \frac{f_s}{q_c - \sigma_{vo}} * 100\% \qquad \text{.....Eq. 5.2}$$

Where q_c is the measured cone tip resistance, f_s is the measured sleeve friction resistance, P_a is the atmospheric pressure in the same units as q_c, and σ_{vo} and σ'_{vo} are the total and effective overburden stresses, respectively. The *n* value is the stress exponent and varies from 0.5 in sands to 1.0 in clays (Olsen & Malone, 1988). The objective of this process was strictly for comparison purposes; therefore, an assumed value of n was 0.65 for all of the CPT results since the encountered soil at the four projects sites consisted primarily of fine sands and silty fine sands. An original assumption of γ_{sat} = 110 lb/ft^3 for the entire soil column was made, and a sensitivity analysis showed the ranges of expected unit weight soils at each site would produce negligible differences in Q_{tn} and R_f in the suspected raveled zones. It should also be noted that the measured sleeve friction value (f_s) was not normalized or corrected for overburden stresses. Normalization of f_s is a highly-debated topic and is not well established in the current literature. Groundwater depth information is also needed prior to applying the normalization equations to determine the effective stress, σ'_{vo}. Most groundwater information for each CPT was obtained from nearby SPT boring logs; which provided an encountered depth to water table. If no nearby SPT was present, an assumed depth to water table was set as 10 feet; which was consistent with the average encountered water table for most analyzed central Florida sites in this study. This normalization procedure is also commonly integrated in commercial CPT processing software.

The CPT is an ideal test for sinkhole detection because of its ability to detect the slightest strength change in the soil strata (collecting data every 2 cm of penetration). Consequently, this results in approximately 140 data groups (f_s and q_c) for every ten feet of penetration. For the derivation of the raveling criteria and raveling identification chart, 125 individual CPTs were analyzed, ranging in depth from 50 to 120 feet. Therefore, a filtering guideline was established and applied to each CPT dataset in efforts to identify any trends which specifically relate to raveled soils. The following filtering procedure was performed based on the CPT resistance data. Figure 5-4 shows an example of the filtering process performed on a CPT along with the corresponding SPT corrected blow count (N_{60}) values performed within the proximity to the CPT. The remaining CPT

data post-filtering is then considered to be eroded, raveled data, exhibiting abnormal resistance characteristics from its original deposition.

1. CPTs performed within the proximity to SPT borings suggesting raveling conditions (e.g., significant WH/WR conditions, no recovery, or loss of drilling circulation in soil above the limestone interface), an expected depth-of-raveling was established and only data within that window was kept. For most CPTs, this window was around the 50 to 100 feet depth-mark, although there were some outlier CPTs with much shallower or deeper raveling zones. A strong correlation was observed between abnormally low q_c values in the CPT profiles and WH/WR (weight-of-hammer or weight-of-rod) conditions in the SPTs performed nearby.

   For CPTs performed without any nearby SPT borings available for validation, the raveled soil zone was assumed to be the abnormally low q_c values directly above the refusal layer. The only project sites analyzed which did not have validation SPT borings were those which had a sinkhole collapse occur. Therefore, the assumption that the encountered loose soils were indicative of sinkhole activity was validated by the nearby collapsed sinkhole.

2. Once the raveled soil depths were determined, further filtering was performed to account for the heterogeneity of the soil. The goal of this filtering process was to identify the data in which only raveled soils were encountered. Even in the raveled soil zones, the penetrating cone can push into interbedded layers of harder material such as limestone lenses or phosphates. Since the penetrating cone records data ever 2 cm, even the slightest inconsistency in material density will be revealed in the q_c and f_s profiles. This is more common in central Florida since the raveling of soil originates within the Hawthorn Group. This geological formation consists of silty or clayey sand interbedded with abundant phosphate particles; which can range from a couple millimeters to a couple inches in diameter. Any penetration through an intact phosphate particle can create a "spike" in the CPT q_c profile within the raveled zone, which may give a false indication of the thickness of denser materials. Therefore, to account for this uncertainty, any abnormal "spikes" in q_c measured within the raveled zone were filtered out. Similarly, if thicker lenses of denser materials are encountered, then these data points are also excluded since it is theorized that the raveling phenomenon may travel upwards laterally in some other areas once water flow and piping occurs within the sandy overburden soils (Gray, 1994). The respective sleeve friction and friction ratios were also filtered at the specific depths corresponding to the spikes of q_c.

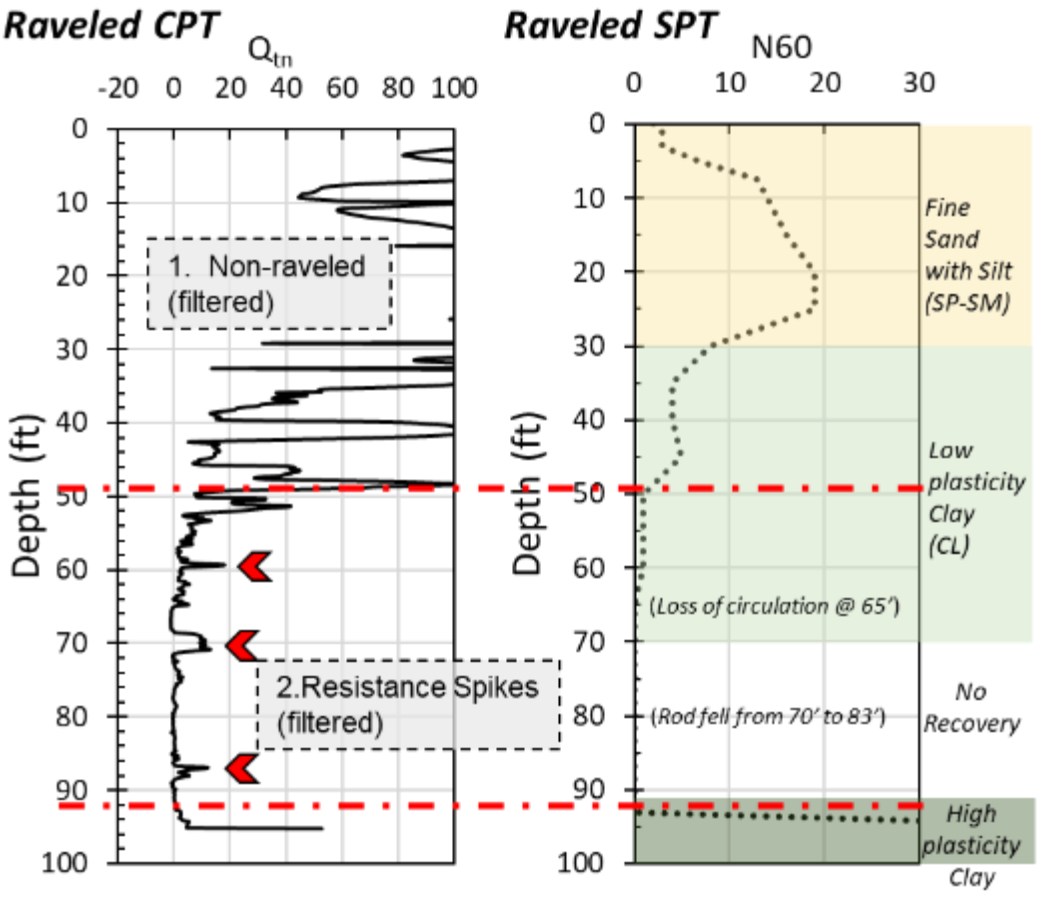

Figure 5-4. Example of filtering steps used for a CPT Q_{tn} profile

5.3.3. Resulting CPT Database

The filtering procedure performed on the CPT data greatly decreased the amount of unwanted data in the raveling analysis. Figure 5-5 shows the resulting data histograms before and after filtering. The effect of normalizing the tip resistance is also apparent when comparing part (a) and part (b) in Figure 5-5. Within the raveled zones, there is a much higher frequency of low Q_{tn} values than in the measured tip resistance values (q_c) of the entire sounding. Both histograms show the CPT results within the raveled zones at these sinkhole sites follow what appears to be a log-normal distribution. After filtering of non-raveled soils and of any encountered "spikes" in the raveled zone, the typical range of q_c and Q_{tn} values were within the range of 2 – 32 tsf (192 – 3064 kPa) and 0 – 26, respectively. This finding suggests that raveled soils may produce tip resistances (q_c) larger than 10 tsf, which is the current recommendation for detecting raveled material in central Florida, as suggested by Gray (1994). Likewise, the range of encountered sleeve friction (f_s) values within the raveled zone of soils was -0.5 – 1.0 tsf (-48 – 96 kPa); which has yet to be established for central Florida soils by other investigators. Viewing the histograms of CPT data can be of assistance to more precisely identify the raveled soils at known active sinkhole sites.

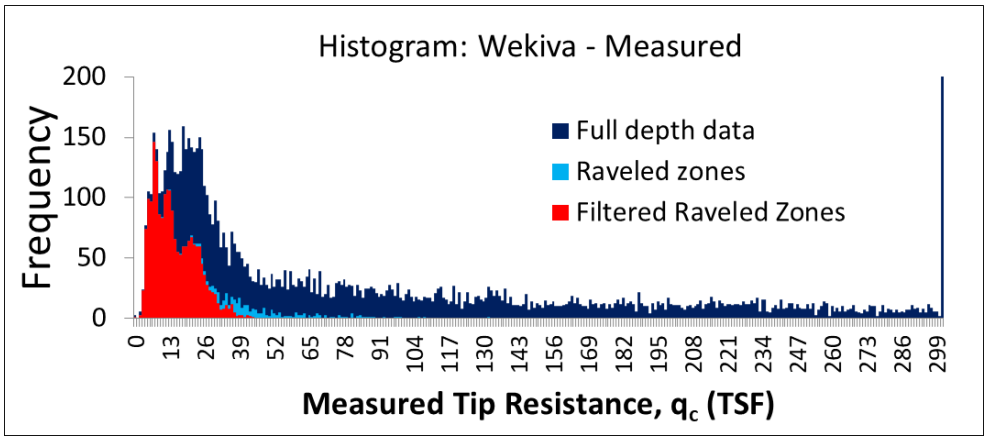

(a) Histograms of CPT measured tip resistance (q_c) data after filtering

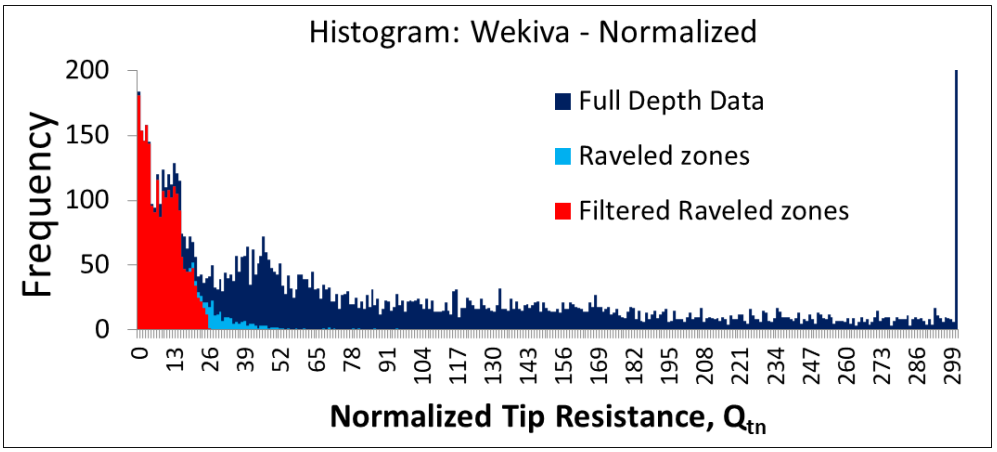

(b) Histograms of CPT normalized tip resistance (Q_{tn}) data after filtering

Figure 5-5. Effects of normalization and filtering of the CPT data from the Wekiva Parkway

The same data presented in Figure 5-5 can also be shown on a scatter plot to view the relationship between Q_{tn}, f_s, and F_R. As shown in Figure 5-6, the CPT values encountered at the Wekiva Parkway site seem to visually fit within the same ranges of data from the CPT values obtained from the collapsed sinkhole repair sites. CPT datasets from the known raveled soils (sinkhole collapsed sites) and suspected sinkhole raveling site (Wekiva) are plotted in Figure 5-6. A strong correlation is shown between the two datasets, suggesting that the suspected raveled soils encountered at the Wekiva site may be indicative of an early stage of sinkhole formation.

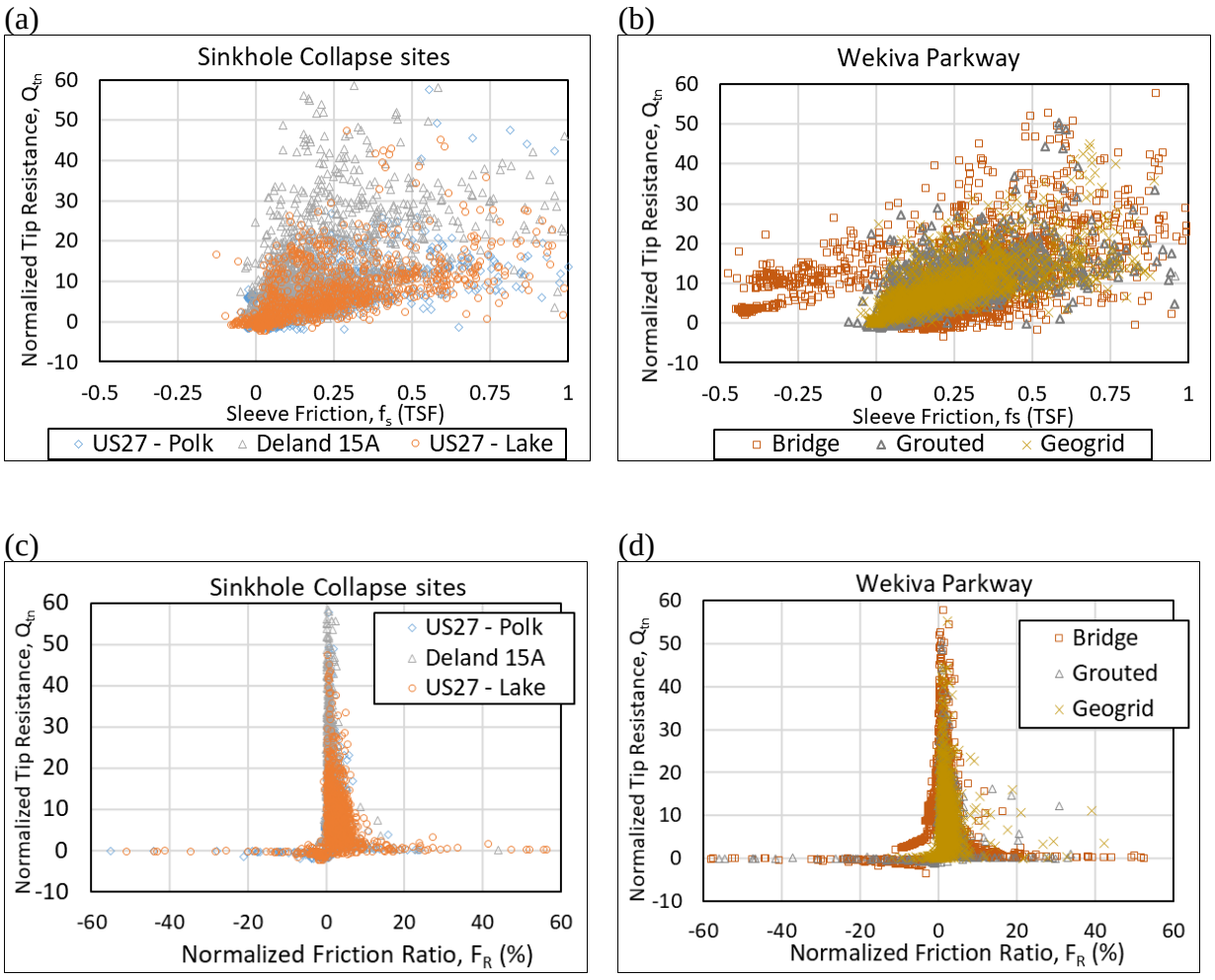

Figure 5-6. Effects of normalization and filtering of CPT data at Wekiva Parkway

Normalizing the friction ratio for soils with very low tip resistance became problematic due to the resulting large number of outliers. This result is shown in Figure 5-6 (c and d) by the large scatter of F_R values as Q_{tn} approaches zero. The normalization equation used for friction ratio has the measured tip resistance (q_c) in the denominator. Therefore, when q_c decreases, the resulting F_R value will increase, especially when q_c is less than one. These outliers within the F_R data are not considered for the SBT correlations and CPT data normalization. Therefore, the charts developed in this study to identify raveled soils exclude F_R values and are only developed using Q_{tn} and f_s data.

The similarity of CPT data between the known raveled soils at the sinkhole-active sites and the suspected raveling zones at the Wekiva Parkway project allowed the data to be combined into one "raveled data-set". Out of the 125 total CPTs included in this study, 107 showed signs of raveling soils which suggest sinkhole activity is being encountered. The remaining 18 CPTs that were

performed (all at the Wekiva Parkway site) did not encounter any loose soil anomalies. These CPTs reveal profiles consistent with competent stratigraphy with no anomalous raveling zones; therefore, at depths where the raveling would start, the "safe" CPTs reveal a refusal layer or a layer with higher q_c values to resist the raveling. The normalized tip resistance and sleeve friction data from the 18 "safe" CPTs were plotted with the respective data from the filtered "raveled" CPTs from both Wekiva and sinkhole-active sites. No filtering was performed on the "safe" CPTs since there was no defined raveling zone within these profiles.

A clear distinction between the two data groups is apparent in both the normalized tip resistance (Q_{tn}) and the sleeve friction (f_s) values. The normalized tip resistance data was plotted in log scale since most of the data was within the range of 1 to 5. As shown in Figure 5-7, there is a significant amount of overlapping scatter between the two groups for f_s in the approximate range of 0–0.5 tsf (0–48 kPa) and Q_{tn} in the approximate range of 5–12. These ranges are believed to be data collected in the partially disturbed Hawthorn Group of soils, which were verified by SPTs and CPTs performed at the sinkhole collapse sites. It is common to find a transitional zone of partially raveled material with decreasing q_c values tapering into the more apparent raveled zone. This zone is believed to be the initiation of internal erosion and is held intact by residual cohesive forces for the short-term. Physical sinkhole modeling performed in the lab has shown similar results when re-creating a cover-collapse sinkhole (Perez et al., 2017). The next step of the analysis was to develop a statistical method to derive the threshold values separating the two bi-variable datasets.

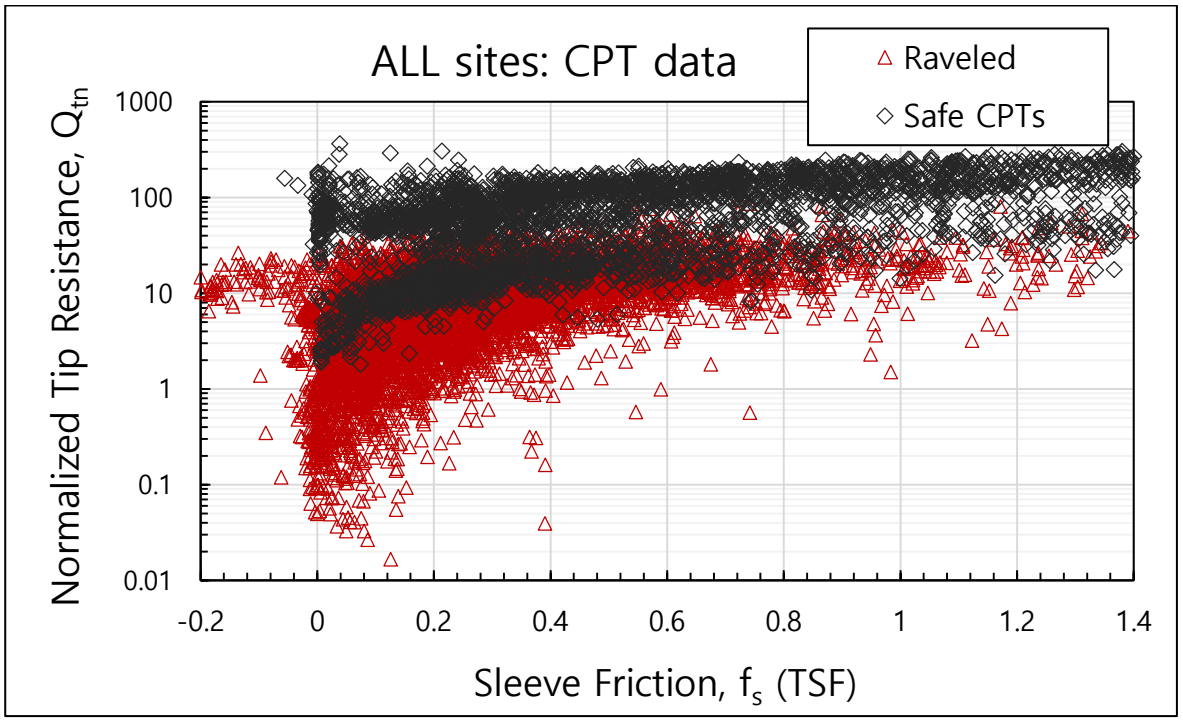

Figure 5-7. CPT data scatter from ALL sites containing both raveled and "safe" tests, (Q_{tn} vs. f_s)

5.3.4. Statistical Derivation

Raveled Data

The combined CPT-raveled dataset consisted of a total of 7,334 data points (i.e., Q_{tn}, f_s). As shown on the previous scatter plots, there is an apparent band of the raveled data. Based strictly on visual observation, the majority of the data seems to fall within the values of 0–26 for Q_{tn}, and 0–1.4 tsf (0–134 kPa) for sleeve resistance. However, the relationship between minimum Q_{tn} and maximum f_s is not as easy to define. As shown in Figure 5-7, the CPT-raveled data loses its density as f_s increases. Therefore, to properly define this boundary of data containment, a moving histogram analysis was conducted for f_s in terms of its Q_{tn} bin ranges. The values of Q_{tn} were ranked in numerically increasing order and separated into 19 bins of equal sample size. Since there is a total 7,334 data points, each bin consisted of 386 data points (i.e., 7,334/19 = 386). The corresponding mean, quartiles, and inter-quartile ranges were then calculated for the f_s data in each respective Q_{tn}-bin. Figure 5-8 shows the results of this statistical analysis. The "+1.5*IQR" data points were calculated by determining the interquartile range (IQR) for the sleeve resistance values in each Q_{tn} bin. By multiplying the IQR by 1.5 and adding it to the third quartile value, a data point representing the upper "whisker" for that specific bin data was obtained. The upper whisker data point represents the value of f_s which is greater than approximately 98% of the remaining f_s in that bin (assuming each isolated bin consists of a normally distributed dataset). Therefore, this value can be used as a conservative maximum and that any f_s encountered less than this value, for a specific range of Q_{tn}, was representative of raveled soils. When this analysis is performed for each Q_{tn}-bin, a clear trend was observed in the resulting means and upper interquartile range whiskers (1.5*IQR). Using a power-law regression for the upper whiskers in f_s data, an upper envelope of f_s and lower envelope of Q_{tn} within the CPT-raveled dataset can be obtained.

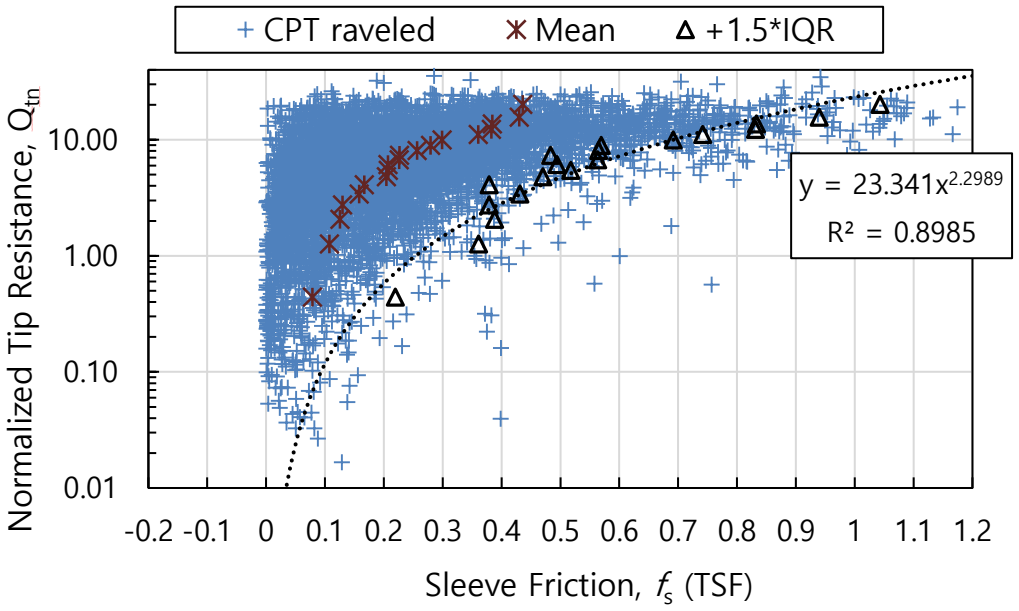

Figure 5-8. CPT-raveled data scatter with upper bound f_s quartile threshold line

Non-Raveled

A similar data analysis was performed for the CPT database of non-raveled material (obtained from the Wekiva Parkway site). However, no filtering was performed on this dataset since there was no clear trend in the Q_{tn} data profiles suggesting raveling. Therefore, the resulting data ranges were much larger, as expected, than the raveling dataset. The final non-raveled data group consisted of a total of 4,244 data points. Therefore, to be consistent with the raveling analysis, a total of 12 Q_{tn} bins were used to assess the f_s histogram plots (resulting in 362 data points in each bin). Figure 5-9 presents the results of the same mean and upper "whisker" calculations for the CPT-non-raveled dataset. However, there is a clear discrepancy in the data's mean values of f_s as the Q_{tn} bins increase. This clear jump in the results of the upper and lower ranges of Q_{tn} (shown boxed in Figure 5-9) suggest that the CPT-non-raveled dataset can be separated into two separate datasets. Recall that this CPT-non-raveled dataset did not have any filtering procedure applied to it. Even though the CPT profiles of Q_{tn} did not suggest raveling was encountered, smaller zones of loose material (low Q_{tn}) were still present in many of the tests. These smaller zones of loose soils may still indicate soil internal erosion, but on a less severe scale as the ones in the raveled dataset. Therefore, this "transition" of raveled-to-non-raveled soil data is significance and will be incorporated into the soil-raveling chart. Since the verified raveled soil range of Q_{tn} appeared to have a maximum value of 26, the transitional range of raveled soil conservatively includes values of Q_{tn} up to 50. The upper f_s envelope within this Q_{tn} range was also calculated using the same technique as the raveled dataset. However, the upper envelope regression of f_s in this specific range follows more of a linear trend than an exponential.

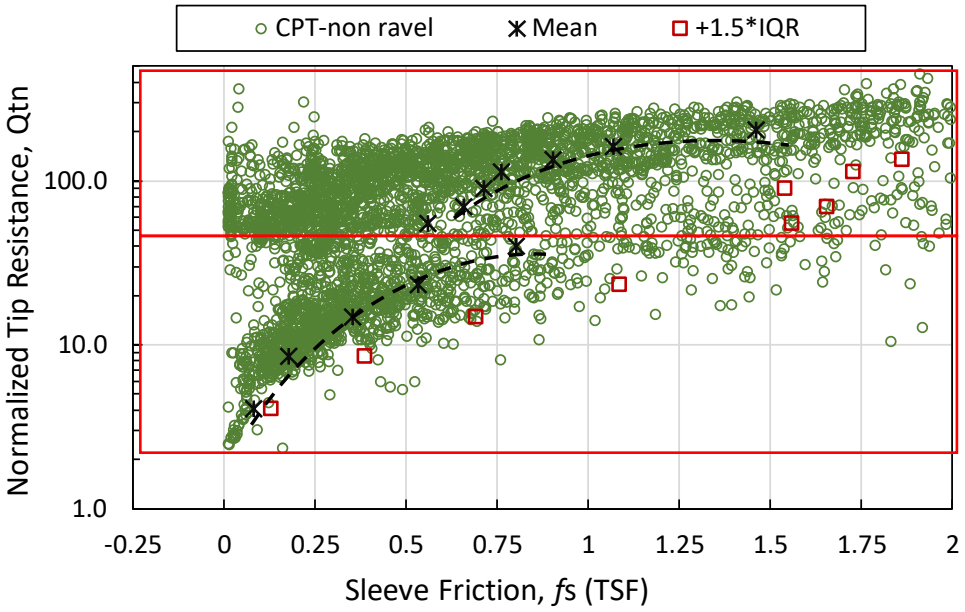

Figure 5-9. CPT-non-raveled data scatter with two distinct upper-bound mean envelopes

5.3.5. CPT-Based Raveling Chart

The comparison of raveled and non-raveled CPT datasets, presented in the previous sections, were used to develop a CPT-based raveled chart for central Florida sites within the Cypresshead Formation of residual soils. This chart, presented in Figure 5-10, was developed as a tool to identify potential raveled soils from Q_{tn} and f_s values obtained from CPTs. Practitioners can quickly plot the CPT parameters on this chart to estimate the likelihood of sinkhole-forming raveled soils. The five categories which make up the chart represent the most likely degree of raveling encountered within the soil. The boundary lines were created using the statistical analysis detailed in the previous sections, and equations for these threshold limits are shown in Table 5-1. During site investigation, if a considerable amount of CPT data falls within the "Raveled Soil" category, then the data coincides with CPT resistance parameters measured from sites which have experienced internal erosion and needed immediate remediation. The Raveled Soil* category was included as a provisional or transitional stage. If data from a CPT falls within this zone, but not within the "Raveled Soil" category, then these soils are likely undisturbed or at least have not experienced a great amount of raveling but are sensitive to raveling. When plotting the resistance values with depth information (shown in Figure 5-11), engineers can easily determine the "critical" depths at which the soils are showing resistance values indicative of internal erosion. The categories labeled "Out of Range" indicate that conclusive results could not be drawn due to the lack of data within those ranges. However, due to the few isolated occurrences of $f_s < 0$, any data falling in this zone will represent very loose and sensitive soils that could indicate raveling, but further investigation should be performed to verify this conclusion.

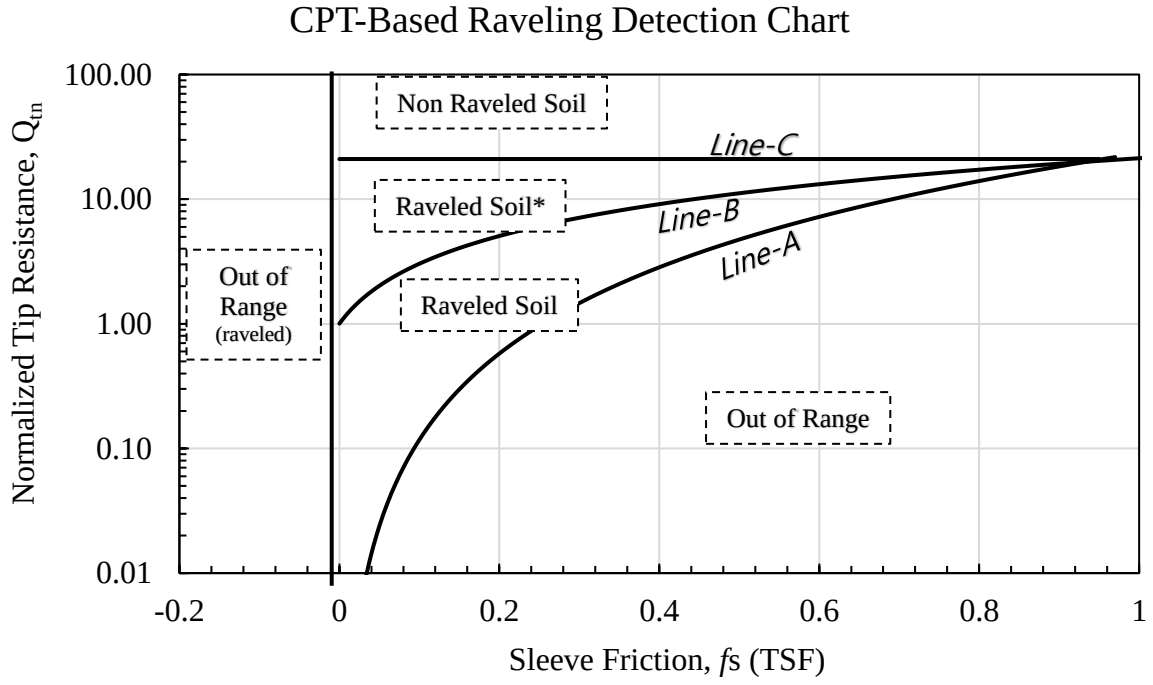

Figure 5-10. Proposed Florida raveling soils detection chart using CPT data, (Q_{tn} vs. f_s)

Table 5-1. Threshold line Equations for CPT raveling detection chart (f_s in TSF)

Line	Threshold function
A	$Q_{tn} = 23.34 * (f_s)^{2.2989}$
B	$Q_{tn} = 25.00 * f_s + 0.984$
C	$Q_{tn} = 26$

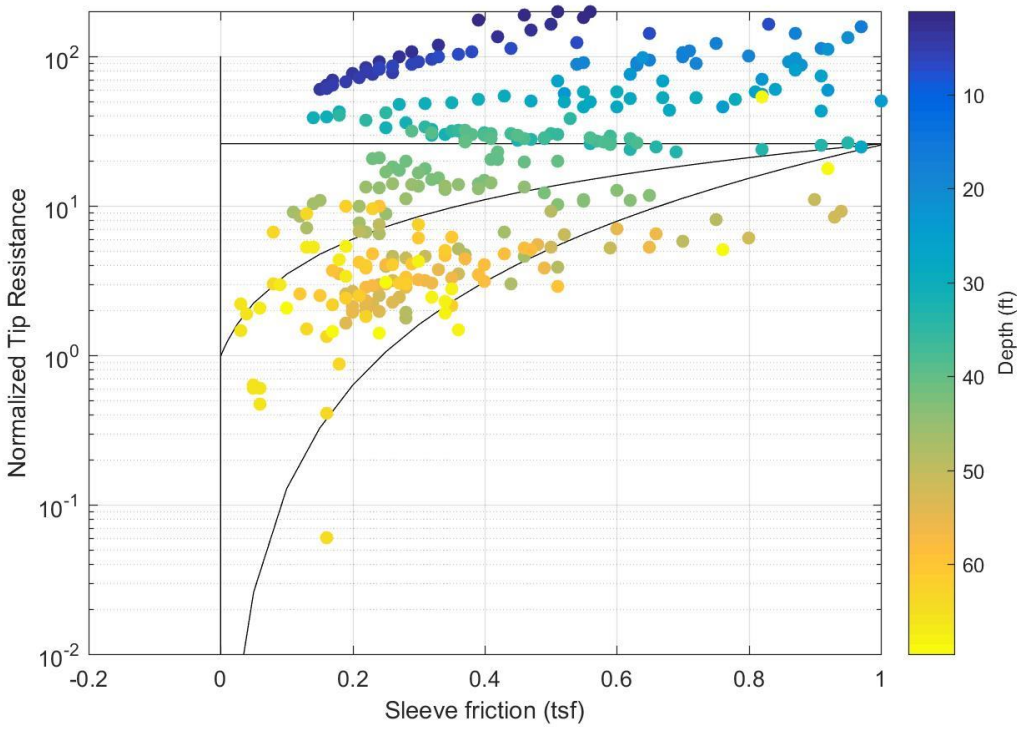

Figure 5-11. Example of applying proposed raveling chart to identify depths of internal erosion

(*Figure continued next page*)

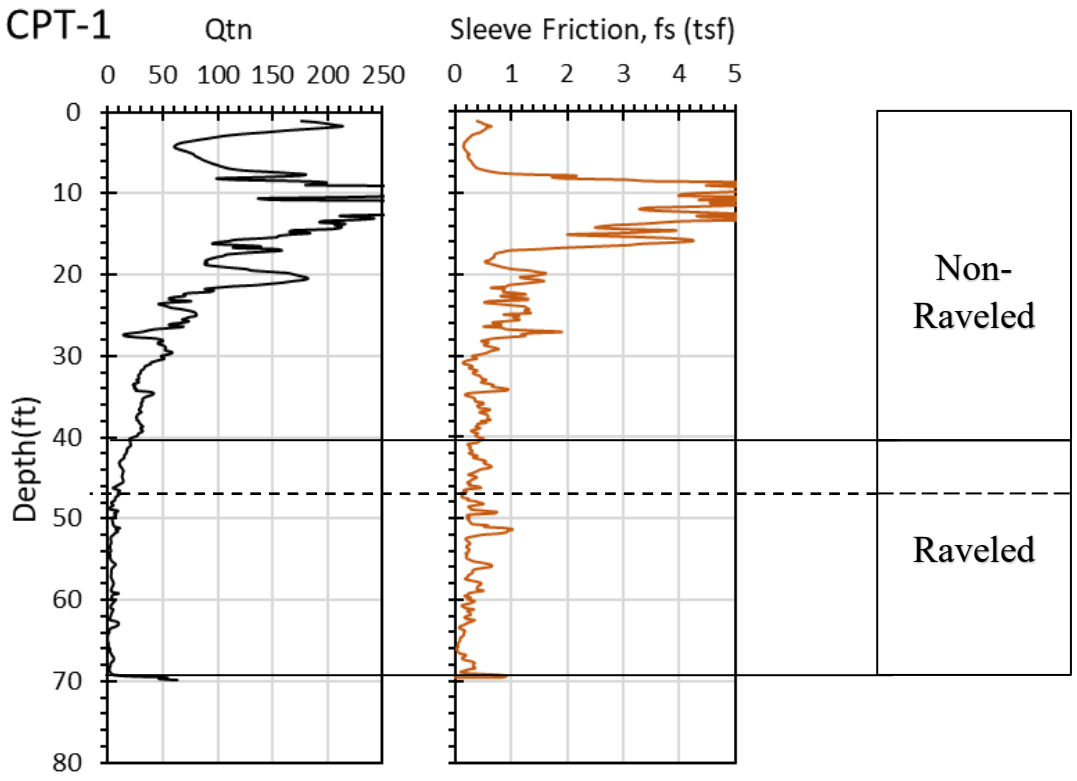

Figure 5-11. Example of applying proposed raveling chart to identify depths of internal erosion

5.4. Indices of Sinkhole Vulnerability Evaluation

The proposed chart and updated criteria presented in the previous section provides a tool when detecting loose soil anomalies which are indicative of sinkhole formation, or raveled soils. However, this procedure lacks a quantitative measure in which comparison between project sites can occur, aiding in site sinkhole assessment. Therefore, an analysis of the current and proposed index systems for characterizing sinkhole risk in central Florida was performed and discussed in the following sections. The proposed updated raveling index ratio incorporates averaged values of tip resistance within the raveled and the overburden soils, adding a strength characteristic input to the current raveling index. The updated raveling index is coined the Sinkhole Resistance Ratio (SRR), such that the larger the result, the higher the estimated resistance to sinkhole formation at the sounding location. The resulting indices allow geotechnical engineers to compare a group of nearby CPTs and map (or contour) the results to pinpoint the areal expanse of a forming sinkhole.

5.4.1. Raveling Index (RI)

The Raveling Index (RI), suggested by Foshee and Bixler (1994), can be a useful tool to quickly evaluate the sinkhole risk by using a CPT or SPT. The index is defined as the thickness of the raveled soil layers divided by the depth to the top of the raveled zone. This ratio gives a relative indication of the degree of erosion which has occurred in the overburden sandy soils. The raveling

index equation and example calculation can be seen in Figure 5-12. Although useful, this index has two major limitations presented below:

- *No consideration of q_c spikes:* Since the Raveling Index is a simple ratio of estimated layer thicknesses, there is no consideration for the actual average value of q_c within the raveled zones or the overburden layers. As shown earlier, raveled soil layers may still produce isolated "spikes" in the q_c profile as the cone encounters phosphate particles or pockets of denser material. Although these spikes may not increase the total strength of that particularly raveled zone greatly, the data can mask the progression and severity of the raveling phenomena.
- *Not sensitive to the depth of encountered raveling:* The raveling index provides a value to identify the % of overburden that has been raveled. Therefore, it is possible to get a value for RI for a variety of different encountered soil raveling thicknesses which may result in various sizes of sinkholes. For example, an encountered 2-foot-thick raveled zone with 10 feet of competent, overburden soils will produce a RI value of 0.2. The resulting sinkhole in this case, if collapse occurs, may only be a few feet in diameter. If another site has an encountered raveling zone of 10 feet thick with 50 feet of overburden soil, the resulting RI value will also be 0.2, but the resulting sinkhole will most likely be of greater size.

With these limitations in mind, a new sinkhole risk-related index was developed to be used in conjunction with CPTs performed in central Florida.

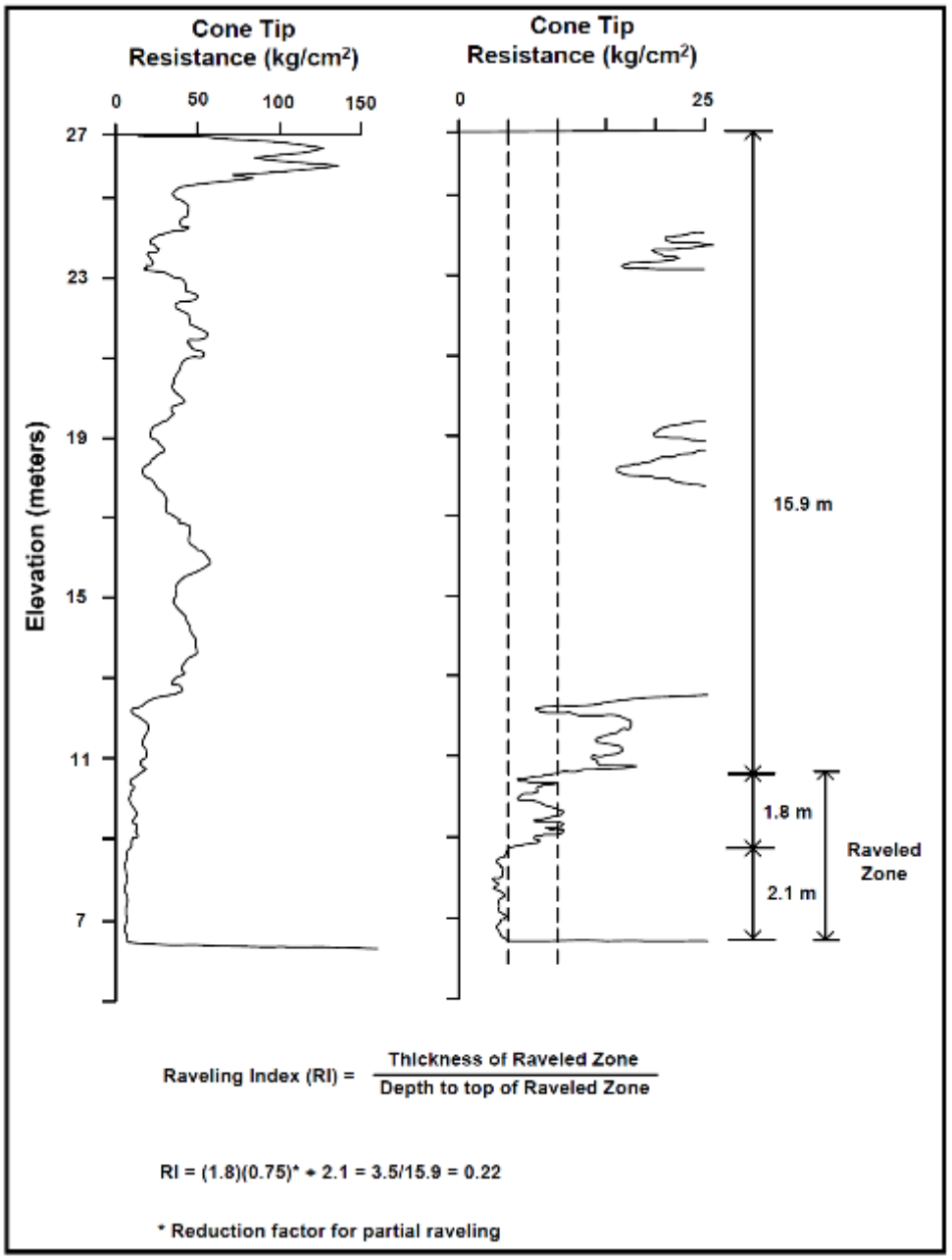

Figure 5-12. Example of calculation of RI from CPT (from Gray 1994)

5.4.2. Sinkhole Resistance Ratio (SRR)

A proposed update to the raveling index was developed in the form of a resistance ratio. Preliminarily coined by the authors as the Sinkhole Resistance Ratio (SRR), shown in the following equation; the larger the SRR, the less likely there is of sinkhole formation in that testing location. The lower the SRR, the greater the risk there is of sinkhole occurrence within the encountered stratigraphy of that CPT sounding.

Sinkhole Resistance Ratio (SRR):

$$SRR = \left(\frac{t_{over}}{t_{ravel}}\right) * \left(\frac{q_{over} + q_{ravel}}{100\sigma'_v}\right) \quad \text{.....Eq. 5.3}$$

Where, q_{over} = Average measured cone resistance in overburden, competent soils (tsf)
q_{ravel} = Average measured cone resistance in raveled zone (tsf)
t_{over} = Depth to encountered raveled zone (i.e., thickness of overburden soil) (ft)
t_{ravel} = Thickness of raveled zone (ft)
σ'_v = Effective vertical stress created from overburden soils (tsf)

The depths where raveling is occurring is determined via the methods shown in the previous section (e.g., Figure 5-11). However, to account for any uncertainty in determining the exact depth to the top of the raveling zone (i.e., the transition or partially raveled soils) and to account for any inconsistency in the raveled soil strength, the average values of q_t for overburden and raveled soils were used in this analysis. The normalized tip resistance values were only used to determine the depths of encountered raveled soils. For the SRR equation, the averaged tip resistance values should be either the raw measured (q_c) or the tip resistance values corrected for pore-water pressure (q_t), if applicable.

The stability analysis of subterranean voids using finite element modeling (discussed in Chapter 6) suggests that an increase in both the overburden soil and the raveled soil strength, will decrease the likelihood of collapse. Therefore, both factors are included in the numerator of the SRR equation. Likewise, the larger the competent overburden soil thickness, the greater the possibility of arching to support the loose soils underneath, thus delaying the possibility of collapse. Adversely, the larger the encountered raveled thickness, the greater the risk of collapse; therefore, this term is in the denominator. The vertical effective stress calculated at the top of the raveled zone is meant to normalize the ratio with depth. The values of stress in tons-per-square-foot is generally a fraction of the numerical values of tip resistance; therefore, this parameter has little influence on the SRR and is primarily used as a normalization factor. However, not only is it necessary to create a dimensionless SRR result, but the deeper the raveling void is encountered, the greater the calculated σ'_{vo}, thus decreasing the value of SRR. Deeper voids have a greater potential of forming larger diameter sinkholes at the ground surface, as proven by the FEM and in many case histories of sinkhole occurrences. Figure 5-13 presents an example calculation from a CPT performed at the US-27 Polk County sinkhole. It is important to note that the overburden *in situ* stress (σ'_v) was determined using a correlation between CPT and soil unit weight (Roberston & Cabal, 2010). Whether using a correlation, additional geotechnical testing, or simply using engineering judgement, the approximated unit weight of soil was shown to not have a large influence on the SRR value. This was shown through a sensitivity analysis of the SRR with respect to the estimated soil overburden soil unit weight.

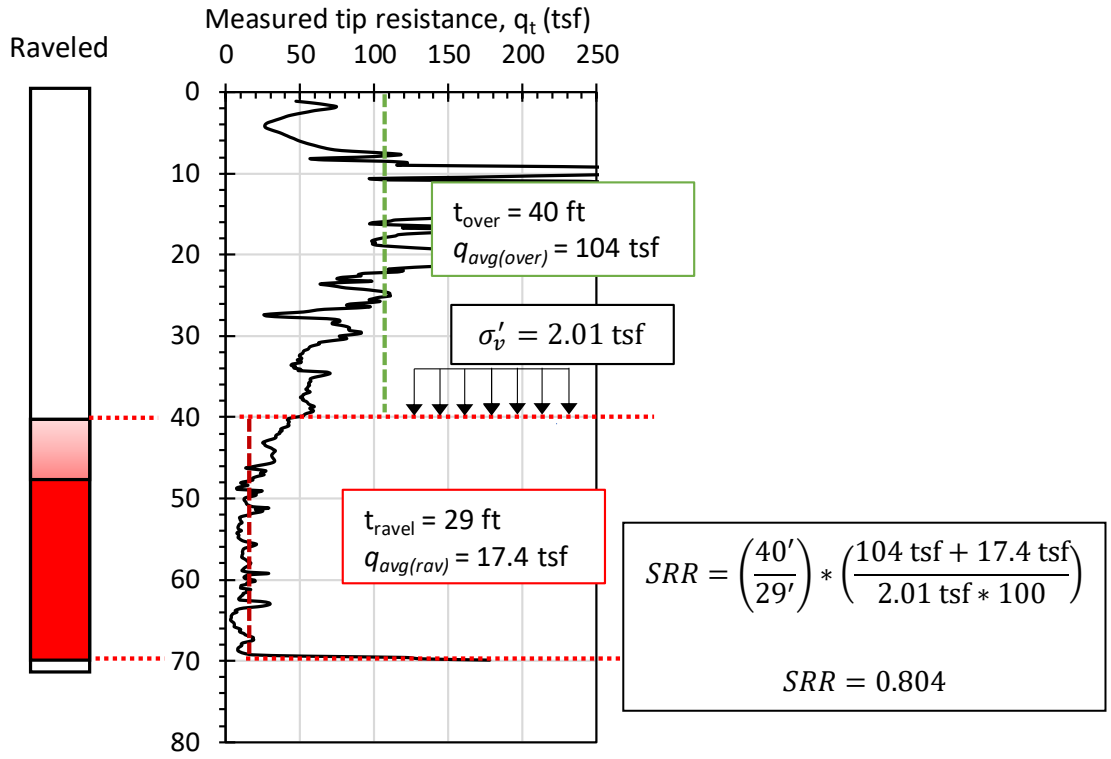

Figure 5-13. Example calculation of SRR from CPT

5.4.3. Index Comparison

Initial comparison between the two indices suggest that the SRR is a better representation of premature sinkhole formation than the Raveling Index. Table 5-2 shows the calculated RI and SRR values for a group of CPTs performed at the Wekiva Parkway. The color gradient shows the most severe indices in warm colors, while the less severe values are in greener shades. There are multiple instances where the RI produces similar values, but the SRR values differ greatly (as shown in the blue boxed areas). This is because the RI only accounts for the thickness of the strata, while the SRR input includes the measured tip resistance averages. The two indices were calculated and compared for all CPTs at both the Wekiva Parkway project and the sinkhole collapse study sites. When comparing the results, it is apparent that the sinkhole collapse sites' indices are more severe than those calculated from the Wekiva CPT raveled and "safe" data. This is expected since, despite the evidence of raveled soils, no collapse or subsidence was recorded at the Wekiva Parkway site.

Table 5-2. Comparison of RI and SRR values from CPTs performed at Wekiva Parkway site

Zone 3 - Bridge Area	*Thickness (ft)*		*Measured q_c (TSF) average*		σ_v' *(TSF)*	RI [4]	SRR [5]
CPT	*Overburden*	*Raveled*	*Overburden*	*Raveled*			
CPT-51a	55.94	51.67	99.35	13.60	1.86	0.92	0.66
FDOT-8	68.41	54.46	134.51	25.84	2.14	0.80	0.94
CPT-23	67.42	46.26	129.55	14.13	2.17	0.69	0.96
CPT-55	72.83	40.69	121.94	9.60	2.41	0.56	0.98
CPT 1-1	44.78	21.82	133.22	21.22	1.37	0.49	2.31
CPT 1-2	51.67	21.66	82.42	19.79	1.73	0.42	1.41
CPT-62	37.73	14.93	128.55	16.62	1.40	0.40	2.62
CPT 1-4	43.14	16.74	165.77	26.43	1.34	0.39	3.70
CPT 1-6	43.80	15.26	86.73	13.72	1.36	0.35	2.12
CPT-24	42.32	13.95	112.70	18.80	1.34	0.33	2.98
CPT-53	48.72	14.60	95.80	8.01	1.65	0.30	2.11
CPT 1-3	54.30	16.24	115.59	33.92	1.74	0.30	2.87
CPT 1-7	35.76	9.68	119.11	17.17	1.42	0.27	3.55
CPT-58	37.57	9.35	112.64	17.72	1.33	0.25	3.95
CPT-54	39.21	9.51	122.96	21.39	1.43	0.24	4.15
CPT-61	42.65	10.01	104.91	10.93	1.48	0.23	3.32
CPT-52	58.23	12.31	104.48	14.68	1.95	0.21	2.88
CPT-18	50.52	9.68	80.84	24.81	1.69	0.19	3.26
CPT-56	65.94	12.14	129.68	25.32	2.23	0.18	3.78
CPT-22	52.49	7.71	88.80	27.30	1.70	0.15	4.64
CPT-60	51.02	7.21	115.04	17.54	1.73	0.14	5.42
CPT-57	42.32	4.76	123.07	13.62	1.49	0.11	8.13
CPT-59	58.23	6.40	100.86	22.35	1.94	0.11	5.77

Figure 5-14 shows the comparison between Ravel Index (a) and SRR (b) calculated from the CPTs used in this study. The CPTs were grouped into three categories depending on the level of raveling detected and why the CPT was performed. The three categories are: *NONE* (no severe raveling detected), *YES* (severe raveling was detected but the site had no sign of collapse or subsidence), and *COLLAPSE* (CPTs performed around the perimeter or within the backfill of a collapsed sinkhole). As shown in this figure, there appears to be a better separation of data between the three categories for the calculated SRR values compared to the RI results. The distribution of SRR values imply that it is a more accurate means to assess CPT results for future investigations. Although, it was created from a dataset within a similar geological condition (Cypresshead Formation in central Florida), and comparing additional CPTs within other geological conditions are warranted. Since the SRR is preliminary, further analysis should be performed to validate its comparable accuracy.

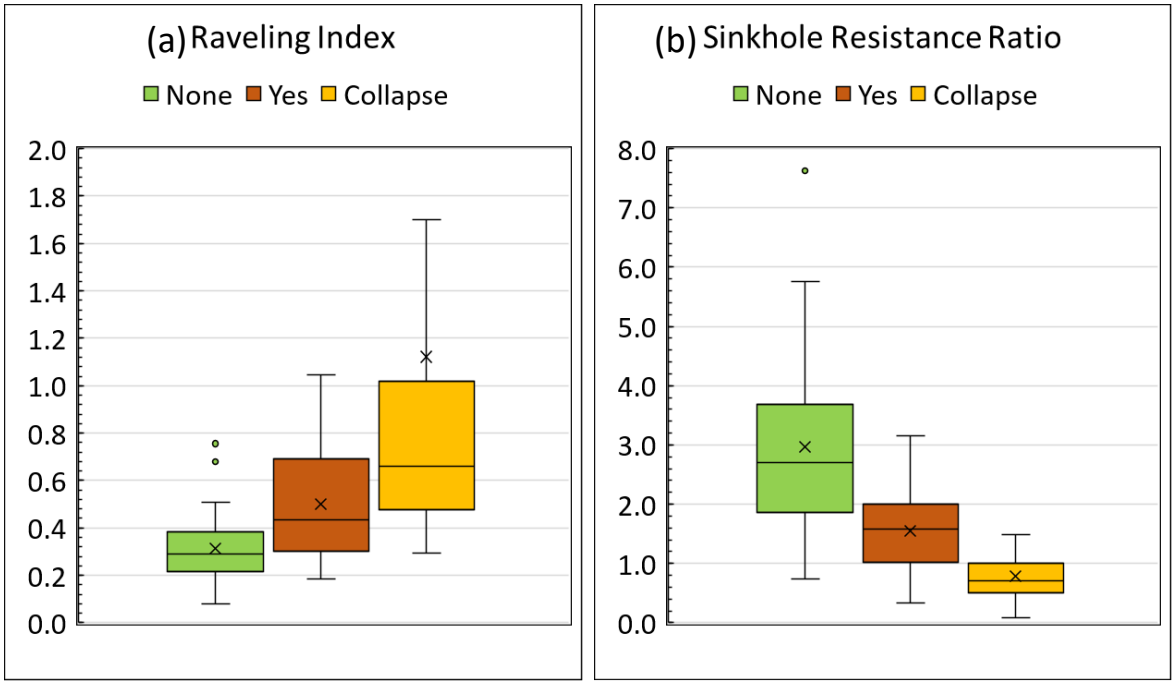

Figure 5-14. Box and whisker representation and comparison of proposed SRR values with the Raveling Index

5.5. Summary

This chapter presents several analysis tools to detect and assess the vulnerability of internal erosion during a site investigation using the Cone Penetration Test. CPTs are ideal for detection of geohazards since they are easily repeatable and provide a high-resolution profile of soil resistance. Although CPTs are unable to penetrate very stiff soils or rock, it has been proven that subterranean sinkhole formations are found above the limestone interface and generally consist of extremely loose soils. The result of this study was the CPT-based raveling chart, developed to identify and characterize soil zones which show high probability of having experienced internal erosion. Once these soil zones are detected, further assessment can be performed by calculating the respective Sinkhole Resistance Ratio for each CPT. This value can be used as a comparative tool for multiple CPT soundings to better understand the areal extent of karst formation. Further analysis and updating should be performed once more data from sinkhole-active sites has been collected. However, these initial tools have shown a strong correlation between the CPT data collected from sinkhole sites in central and north Florida.

6. SINKHOLE STABILITY ANALYSIS AND MODELING

6.1. Introduction

In this chapter, the development, methodology, and procedures of how to investigate the mechanical behavior of sinkholes, using numerical modeling and analysis, are discussed. Particularly, the study focused on the sinkhole stability (i.e., stability chart) for practical use by engineers. Two sites were selected for the stability analysis, including the Wekiva Parkway site and US-441 which is a post Hurricane Irma sinkhole site. Testing data from the sites were used to estimate the soil profile and parameter input values. A numerical model of the site was developed using the finite element software, PLAXIS 2D. Subsurface soil raveling conditions was simplified by a circular cavity in the model, which is common practice for sinkhole numerical modeling. A hardening soil model was used for the overburden soil layers to predict the deformations above the cavity. Constitutive soil parameters were determined by using published correlations in technical literature and the site-specific subsurface investigation data. The stresses and deformations around subsurface cavities were assessed. Additionally, site-specific stability charts were developed in terms of factor of safety and maximum surface deformation. The use of these charts requires the knowledge of various subsurface conditions such as cavity depth, cavity size, soil strength, and the overburden stresses. These parameters can be determined by site investigation techniques, and once obtained, the stability condition can be assessed using the site-specific charts.

6.2. Numerical Analysis

6.2.1. Plastic Analysis

Plastic analysis, which considers the nonlinear and plastic behaviors of soils, is used to perform an elastic-plastic deformation analysis. The calculation is carried out according to the small deformation theory. The stiffness matrix for the calculation is based on the original undeformed geometry. Using this calculation allows a fully drained analysis that can evaluate long-term deformations.

6.2.2. Safety Analysis

The safety calculation is used to compute the global safety factor of the numerical model, which is also known as the Strength Reduction Factor (SRF). The strength parameters of the model are reduced by a specific value of SRF, such that:

$$\tau = \frac{c' + \sigma' tan\varphi}{SRF} \qquad \text{.....Eq. 6.1}$$

The SRF value is successively increased until the analysis results do not converge (i.e., model collapses). This method is widely used in soil and rock engineering (Griffiths & Lane, 1999), and it was previously used to define the sinkhole stability number by Drumm and Yang (2005).

6.3. Constitutive Soil Model

Two soil constitutive models were used for this study - Mohr-Coulomb (MC) and Hardening Soil Model (HSM). The HSM model was selected because it is better suited to detect the nonlinear and plastic behaviors of soils.

The Hardening Soil Model (HSM) was employed over the Mohr-Coulomb (MC) model to better estimate ground deformations. The stiffness in the HSM is stress dependent and stress-path dependent which provides a more accurate stiffness definition than the MC model. In contrast to an elastic perfectly-plastic model, the yield surface of a hardening plasticity model is not fixed in the principal stress space, but it can expand due to plastic straining. The HSM comprises two main types of hardening: shear hardening and compression hardening. Shear hardening is used to model irreversible strains due to primary deviatoric loading. Compression hardening is used to model irreversible plastic strains due to primary compression in oedometer (1D constrained) loading and isotropic loading.

6.3.1. Hardening Soil model

The Hardening Soil Model (HSM) was initially introduced in the PLAXIS 2D software, in the framework of the theory of plasticity, as an extension of the Mohr–Coulomb Model (Nordal, 1999). An additional cap was implemented to the HSM to take the pre-consolidation pressure into account. The total strains are calculated using a stress-dependent stiffness, which varies between both loading and unloading/reloading conditions. Isotropic hardening is assumed to be dependent on the plastic shear and volumetric strains. The frictional hardening follows a non-associated flow rule; whereas the cap hardening adopts an associated flow rule. Schanz et al. (1999) and Brinkgreve (2002) explained the formulation and verification of the Hardening Soil Model. Surarak et al. tabulated the input parameters of the HSM as presented in Table 6-1.

The stress–strain relationship in this model can be well approximated by a hyperbola (Kondner and Zelasko, 1963) as depicted in Figure 6-1. The yield curves from standard triaxial tests can be defined by:

$$\varepsilon = \frac{q_a}{2E_{50}} \frac{(\sigma_1-\sigma_3)}{q_a-(\sigma_1-\sigma_3)} \quad \text{for } (\sigma_1 - \sigma_3) < q_f \qquad \text{.....Eq. 6.2}$$

where q_f is the ultimate deviator stress, derived from Mohr-Coulomb failure criterion involving the strength parameters c' and φ', and defined by:

$$q_f = \frac{6\sin\varphi_p}{3-\sin\varphi_p}\left(p + c * \cot\left(\varphi_p\right)\right) \qquad \text{.....Eq. 6.3}$$

and the quantity q_a is the asymptotic value of the shear strength and defined as:

$$q_a = \frac{q_f}{R_f} \qquad \text{.....Eq. 6.4}$$

where R_f is the failure ratio. If R_f = 1.0 (i.e., $q_f = q_a$), then the failure criterion is satisfied and perfectly plastic yielding occurs.

Table 6-1. Parameters of Hardening Soil Model

Parameter	Description	Parameter Evaluation
φ’	Internal friction angle	Slope of failure line from MC failure criterion
c’	Cohesion	y-intercept of failure line from MC failure criterion
R_f	Failure ratio	$\frac{\sigma_1-\sigma_3}{(\sigma_1-\sigma_3)_{ult}}$
ψ	Dilatancy angle	Function of εa and εv
E_{50}^{ref}	Reference secant stiffness from drained triaxial test	y-intercept in log (σ3/pref) – log(E50) space
E_{oed}^{ref}	Reference tangent stiffness from oedometer primary loading	y-intercept in log (σ1/pref) – log(Eoed) space
E_{ur}^{ref}	Reference unloading/reloading stiffness	y-intercept in log (σ3/pref) – log(Eur) space
m	Exponential power	Slope of trendline in log (σ3/pref) – log(E50) space
ν_{ur}	Unloading/reloading Poisson’s ratio	0.2 (default setting)
K_0^{NC}	Coefficient of earth pressure at rest (NC state)	1-sinφ (default setting)

As shown in Figure 6-1, the stress–strain behavior for primary loading is highly non-linear. The parameter E_{50} is a confining stress dependent stiffness modulus for primary loading, and is calculated as:

$$E_{50} = E_{50}^{ref}\left(\frac{c'\cos\varphi' - \sigma'_3\sin\varphi'}{c'\cos\varphi' + p^{ref}\sin\varphi'}\right)^m \qquad \text{……Eq. 6.5}$$

where E_{50}^{ref} is a reference stiffness modulus corresponding to the reference stress p_{ref}.

In PLAXIS 2D, a default setting of p_{ref} = 100 kPa is used. The actual stiffness depends on the minor effective principal stress, σ_3, which is the effective confining pressure in a triaxial test. Note that in PLAXIS 2D, σ_3 is negative in compression. The amount of stress dependency is given by the power “m”. To simulate a logarithmic stress dependency, as observed for soft clay, m should be taken as 1. (Soos, 2001) reported a range of m values from 0.5 to 1 in different soil types with the values of 0.9 to 1 for clays.

The stress dependent stiffness modulus for unloading and reloading stress paths is expressed by:

$$E_{ur} = E_{ur}^{ref}\left(\frac{c'\cos\varphi' - \sigma'_3\sin\varphi'}{c'\cos\varphi' + p^{ref}\sin\varphi'}\right)^m \qquad \text{……Eq. 6.6}$$

where E_{ur}^{ref} is a reference stiffness modulus for unloading and reloading that corresponds to the reference stress p_{ref} (p_{ref} = 100 kPa). PLAXIS 2D assumes E_{ur}^{ref} is equal to $3E_{50}^{ref}$.

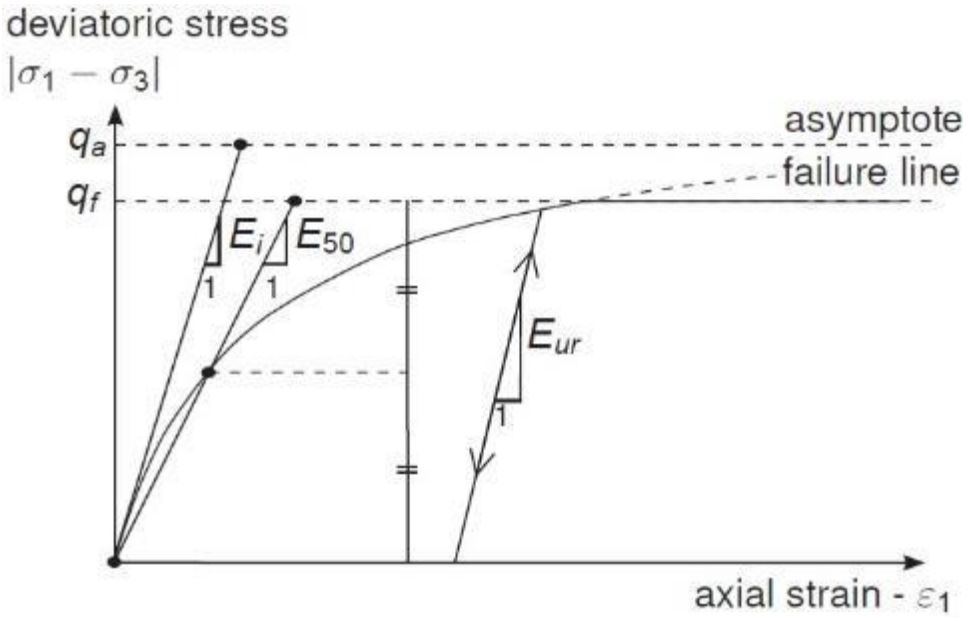

Figure 6-1. Hyperbolic stress-strain relationship in primary loading for a standard drained triaxial test from Schanz et. al (1999)

The HSM is defined by shear hardening yield surfaces and cap yield surfaces as illustrated in Figure 6-2. The surfaces in this figure were plotted for the no-cohesion condition (c' = 0). The reference oedometer modulus (E_{oed}^{50}) controls the magnitude of the volumetric cap strain (ε_v^{pc}). Similar to E_{50} and E_{ur}, this modulus follows the stress dependency law, and is given by:

$$E_{oed} = E_{oed}^{ref}\left(\frac{c'\cos\varphi' - \sigma'_3\sin\varphi'}{c'\cos\varphi' + p^{ref}\sin\varphi'}\right)^m \quad \text{.....Eq. 6.7}$$

The shear hardening yield function (f_s) in the HSM is:

$$f_s = \bar{f} - \gamma^p \quad \text{.....Eq. 6.8}$$

$$\bar{f} = \frac{q_a}{E_{50}}\left\{\frac{(\sigma'_1 - \sigma'_3)}{q_a - (\sigma'_1 - \sigma'_3)}\right\} - \frac{2(\sigma'_1 - \sigma'_3)}{E_{ur}} \quad \text{.....Eq. 6.9}$$

$$\gamma^p \approx \varepsilon_1^p - \varepsilon_2^p - \varepsilon_3^p = 2\varepsilon_1^p - \varepsilon_v^p \approx 2\varepsilon_1^p \quad \text{.....Eq. 6.10}$$

where $\varepsilon_1^p, \varepsilon_2^p$, and ε_3^p are the plastic strains in the principal directions, and ε_v^p is the plastic volumetric strain.

The cap yield surfaces are dependent on the plastic volumetric strain measured in the isotropic compression condition, and defined as:

$$f^c = \frac{\tilde{q}^2}{\alpha^2} + p^2 - p_p^2 \quad \text{.....Eq. 6.11}$$

$$p = \frac{-(\sigma'_1 + \sigma'_2 + \sigma'_3)}{3} \quad \text{.....Eq. 6.12}$$

$$\tilde{q}^2 = \sigma'_1 + (\delta - 1)\sigma'_2 - \sigma'_3 \quad \text{.....Eq. 6.13}$$

$$\delta = \frac{(3 + sin\varphi')}{(3 - sin\varphi')} \quad \text{.....Eq. 6.14}$$

where α is an auxiliary model parameter related to K_0^{NC} and $\tilde{q}$ is the special stress measure for deviatoric stress.

The hardening law, which relates the pre-consolidation pressure (p_p) to the volumetric cap strain (ε_v^{pc}), is defined as:

$$\varepsilon_v^{pc} = \frac{\beta}{1 - m}\left(\frac{p_p}{p^{ref}}\right)^{1-m} \quad \text{.....Eq. 6.15}$$

The cap parameters α and β are not adopted by PLAXIS 2D as input parameters. However, they can be calculated as

$$\alpha = K_0^{NC} \quad \text{.....Eq. 6.16}$$

$$\beta = E_{oed}^{ref} \quad \text{.....Eq. 6.17}$$

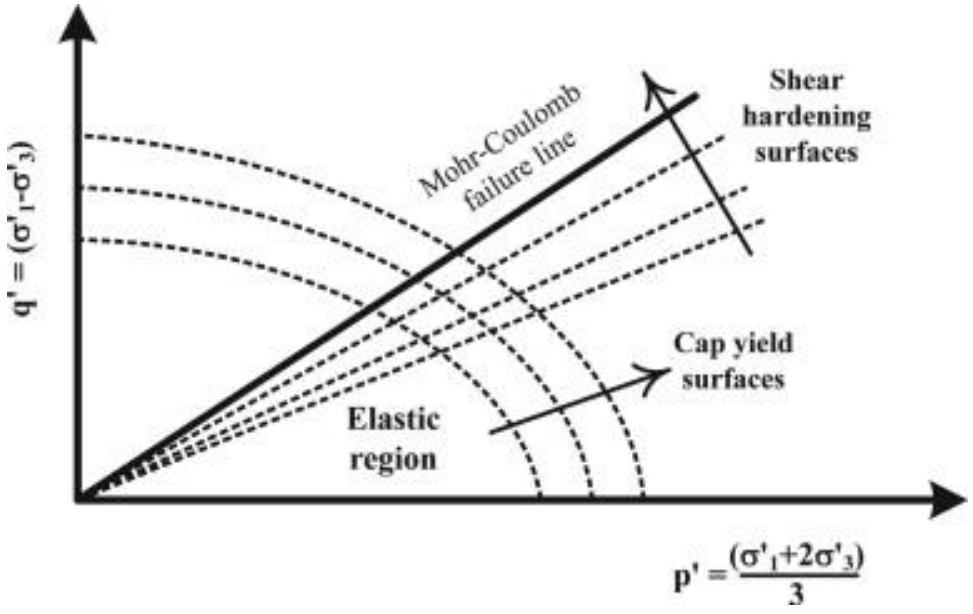

Figure 6-2. Shear hardening and cap yield surfaces in the HSM from Schanz et al. (1999)

6.4. Site Characterization and Input Parameters

6.4.1. Site Investigation Data

Wekiva Parkway – Lake County

Site investigation data, from the geotechnical reports of the Wekiva Parkway project, were used to determine the soil stratigraphy and properties at this site. Figure 6-3 shows a layout of the site testing program for the SR-46 connector bridge over Wekiva Parkway (SR-429). SPT boring: PSI-18 and CPT sounding: CPT-52, both located at the bridge approach (ST 41+50), were used to identify a representative soil profile and the soil parameter values using published correlations. Figures 6-4 and 6-5 depict the SPT boring (PSI-18) and the CPT sounding (CPT-52) (Wekiva Parkway), respectively. It can be observed from the boring log in Figure 6-4 that the ground surface and the groundwater table are at elevations +84 and +69 feet NGVD, respectively. The boring indicated very loose sands (SP) in the upper 15 feet followed by 24 feet of loose silty sands (SM). Alternating layers of highly plastic clay (CH) and low plasticity clay (CL) were encountered from depths of 39 to 49 feet followed by 10 feet of dense sands with silt. Below, the boring indicated the presence of raveled soils including mixed clays and sands. All the previous soil layers were underlain by weathered limestone at an elevation of -10 feet NGVD (i.e., 94 feet depth). Figure 6-5 depicts the values of tip resistance (q_c), sleeve friction (f_s) and friction ratio (R_f) versus depth from the CPT sounding. The sounding terminated at approximately 99 feet, which indicated the presence of the bedrock layer. The soil profile was estimated from the CPT data using Robertson's chart for soil classification (Robertson P. , 1990). The estimated profile shows alternating layers of sand with silt and silty sands for the top 30 feet followed by approximately 14 feet of clay. Below, a 14-feet silty sand layer followed by clay where the sounding showed very low resistance and friction values indicating the presence of raveled soils until its terminating depth.

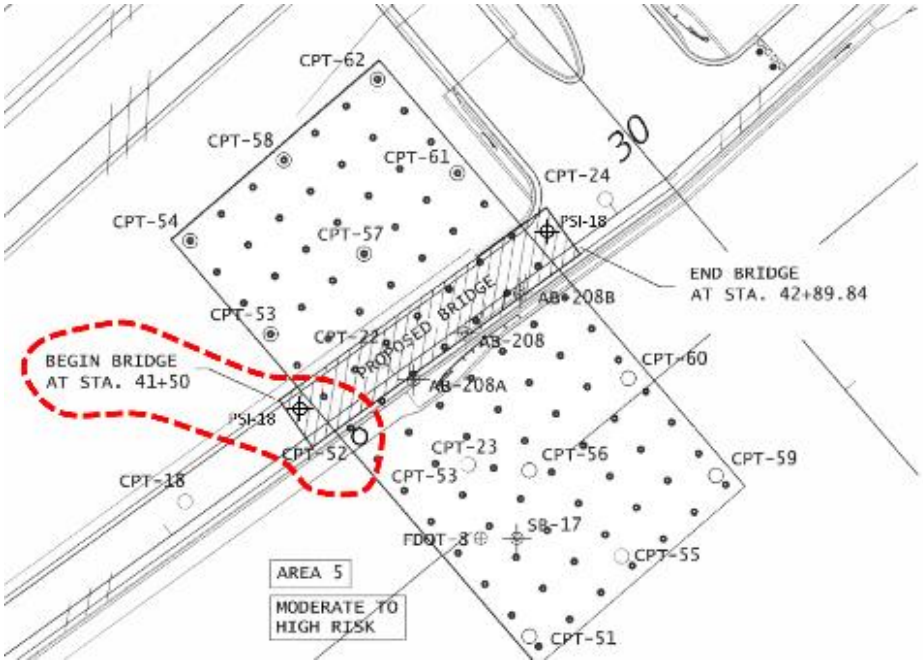

Figure 6-3. Site layout of SR-46 connector bridge over SR-429

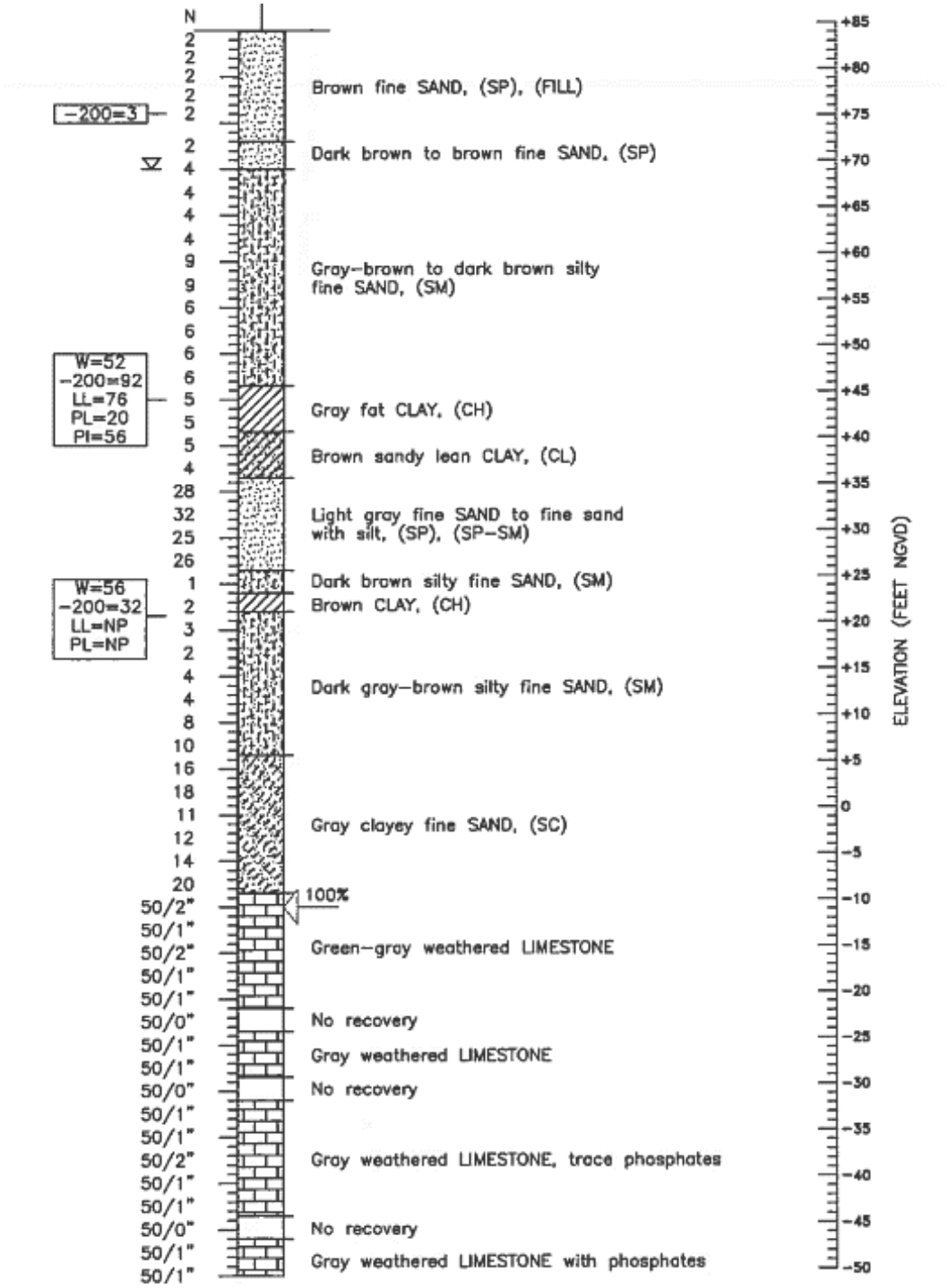

Figure 6-4. SPT log at Station 41+50 on SR-429, Wekiva Parkway (Professional Services Industries Inc., 2014)

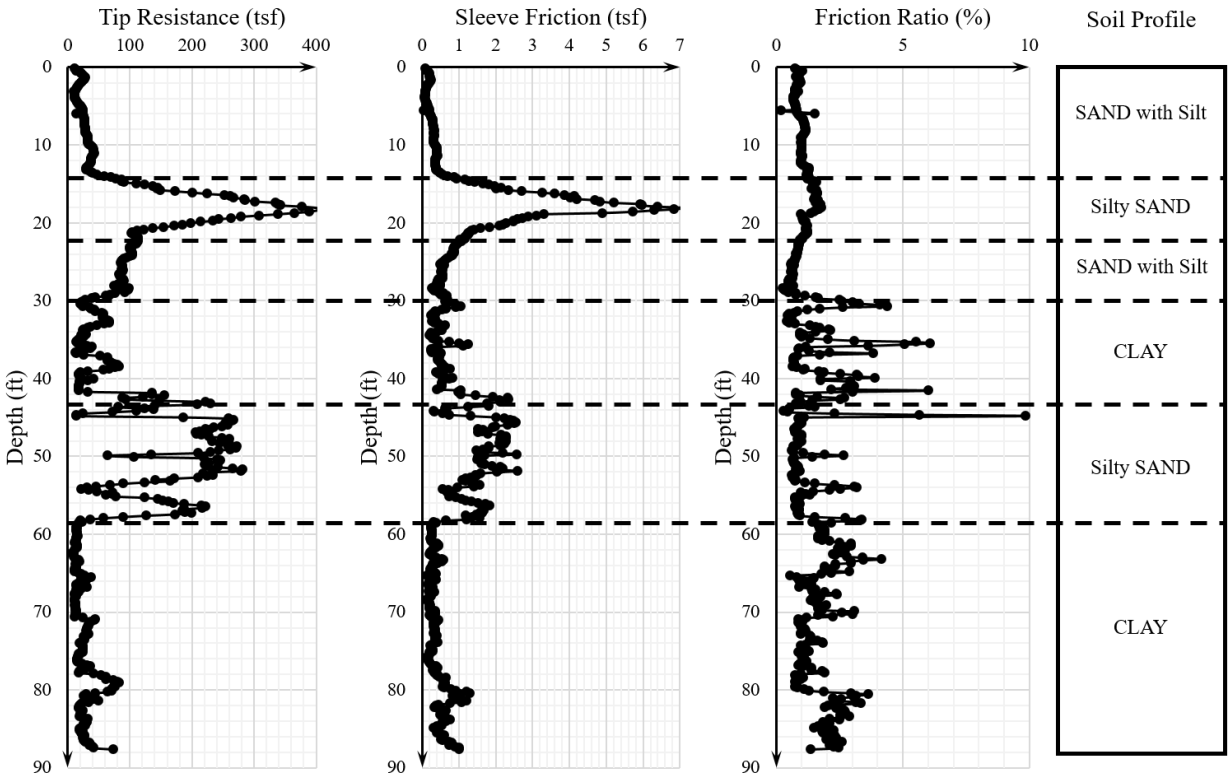

Figure 6-5. CPT resistance profiles at STA 41+50 on SR-429

Route US-441 – Marion County

Similarly, site investigation data from US-441 were used to determine the representative soil profile of this sinkhole site. Figure 6-6 shows the layout of the sinkhole location and the Cone Penetrations Tests performed in its vicinity. The reported sinkhole was 15 feet in diameter and 10 feet in depth. Eleven CPT soundings were performed around the sinkhole. CPT-7, CPT-3, CPT-9, and CPT-12 showed severe raveling conditions. The worst raveling was encountered in CPT-7. On the other hand, CPT-1 and CPT-6 showed non-raveled soil behavior. CPT-1 was then used to determine a soil profile of the site assuming that it represents the initial soil conditions before raveling took place. Tip resistance, sleeve friction and friction ratio versus depth from CPT-1 are presented in Figure 6-7. Using Robertson's soil classification chart, the CPT data showed a soil profile comprised of 7 feet of silty sands followed by 18 feet of very stiff to hard clays. The sounding terminated at a depth of 25 feet which was assumed to be the weathered limestone interface.

Figure 6-6. CPTs and sinkhole location at US-441 in Marion County (Terracon , 2017)

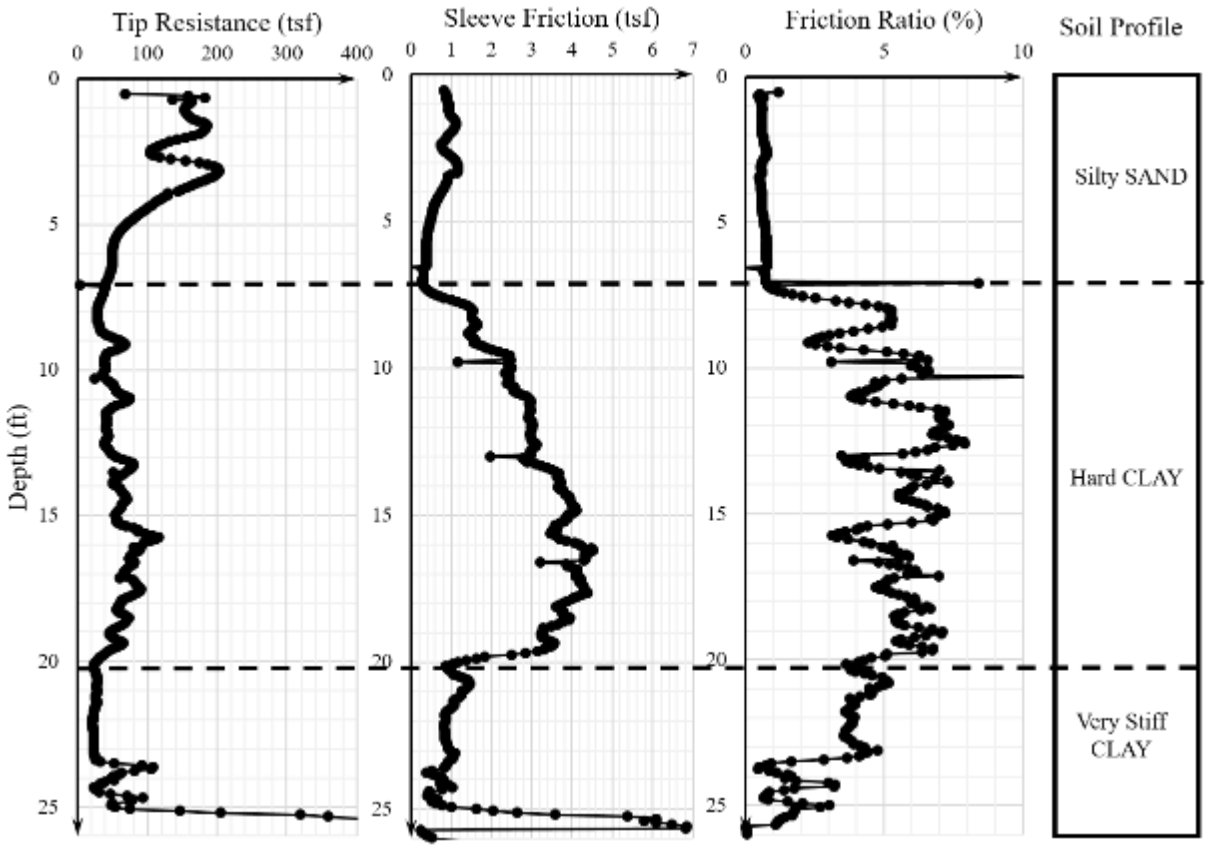

Figure 6-7. CPT-1 sounding from US-441 sinkhole site

6.4.2. Correlations between Input Parameters and CPT Data

The CPT data was used to calculate the parameter input values for the numerical model. Published correlations were used to calculate strength and stiffness values from the tip resistance values versus depth. The correlations used for this analysis are tabulated in Table 6-2. Three friction angle values for each sand layer were obtained using correlations by Robertson and Campanella (1983), Meyerhof (1974), and (Mayne, 2007). For clay layers, the undrained shear strength was determined using Kulhawy and Mayne's (1990) correlation with an N_k value of 15 which is recommended for electric cone penetrometer results. Using Bowles' (1998) correlation, the stiffness of each layer was calculated using constant "α" values: 1.5 (for silty sands), 2.0 (for medium dense to dense sands), and 6.0 (for clays).

Table 6-2. CPT correlations

Parameter	*Correlation*	*Reference*
Friction Angle	$\varphi = \tan^{-1}(0.1+0.38\log(q_c/\sigma'_v)$ σ'_v : Effective Vertical Stress	Robertson and Campanella, 1983
	$\varphi = 29^\circ + (q_c)^{0.5}$	Meyerhof, 1974
	$\varphi = 17.6 + 11*\log(q_c)$	Mayne, 2007
Undrained Shear Strength	$S_u = (q_c - \sigma_{v0})/N_k$ σ_{v0} : Total Vertical Stress N_k : Constant	Kulhawy and Mayne, 1990
Stiffness (Secant Modulus)	$E_s = \alpha*q_c$ α : Constant (Soil Type)	Bowles, 1988

Wekiva Parkway

Figure 6-8 shows the parameter values versus depth for the Wekiva Parkway site. The friction angle values of the top sand layer ranged between 30˚ – 40˚, and the stiffness values were around 40–80 tsf (4–8 MPa). The second silty sand layer had friction angle values between 30˚ – 50˚; whereas the stiffness values ranged from 200–600 tsf (20–60 MPa). The friction angle of the third layer (sand with silt) was between 32˚ – 42˚, and the stiffness was nearly 200 tsf (20 MPa). The undrained shear strength of the clay layer (fourth layer) ranged from 1–5 tsf, and the stiffness was between 100–500 tsf (10–50 MPa). The fifth layer (silty sand) had friction angles between 36˚ – 46˚, and stiffness between 200–800 tsf (20–80 MPa). For the sixth layer (clay), the undrained shear strength ranged from 0.8–2 tsf (80–200 kPa) and the stiffness was roughly 60 tsf (6 MPa). It is worth noting that the groundwater level at the location of CPT-1 was recorded at a depth of 26 feet (7.9 meters).

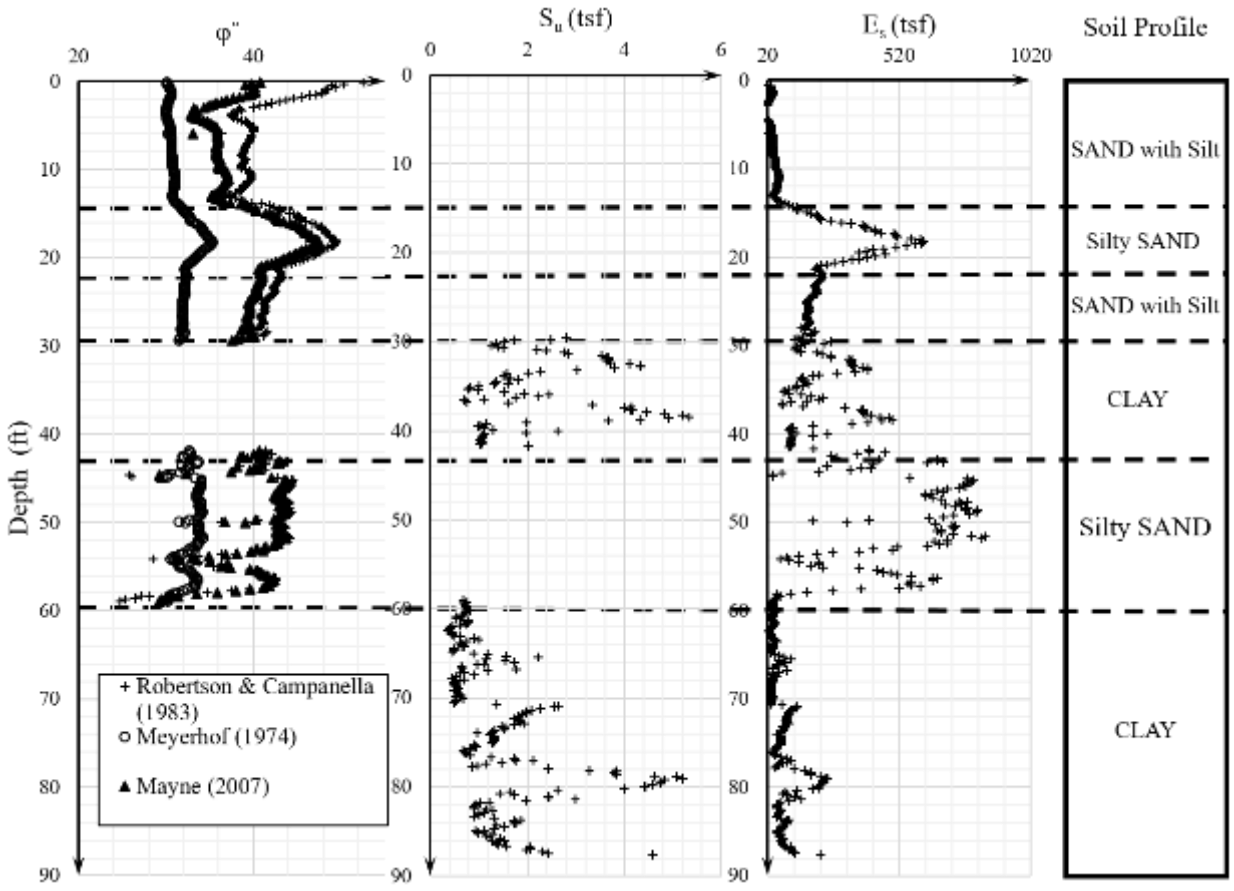

Figure 6-8. Strength and stiffness parameters values vs. depth (Wekiva Parkway)

Route US-441

Figure 6-9 shows the parameter values versus depth for the US-441 site. The friction angle of the silty sand layer ranged between 34˚ – 48˚. Whereas, the undrained shear strength values of the underlying clays were nearly 2–5 tsf (200–500 kPa) for the hard clay and the very stiff clay layers. The silty sand layer showed an average stiffness value of 240 tsf (24 MPa). While the stiffness values of the clay layers were approximately 400 tsf (40 MPa) for the hard clay and nearly 180 tsf (18 MPa) for the very stiff clay.

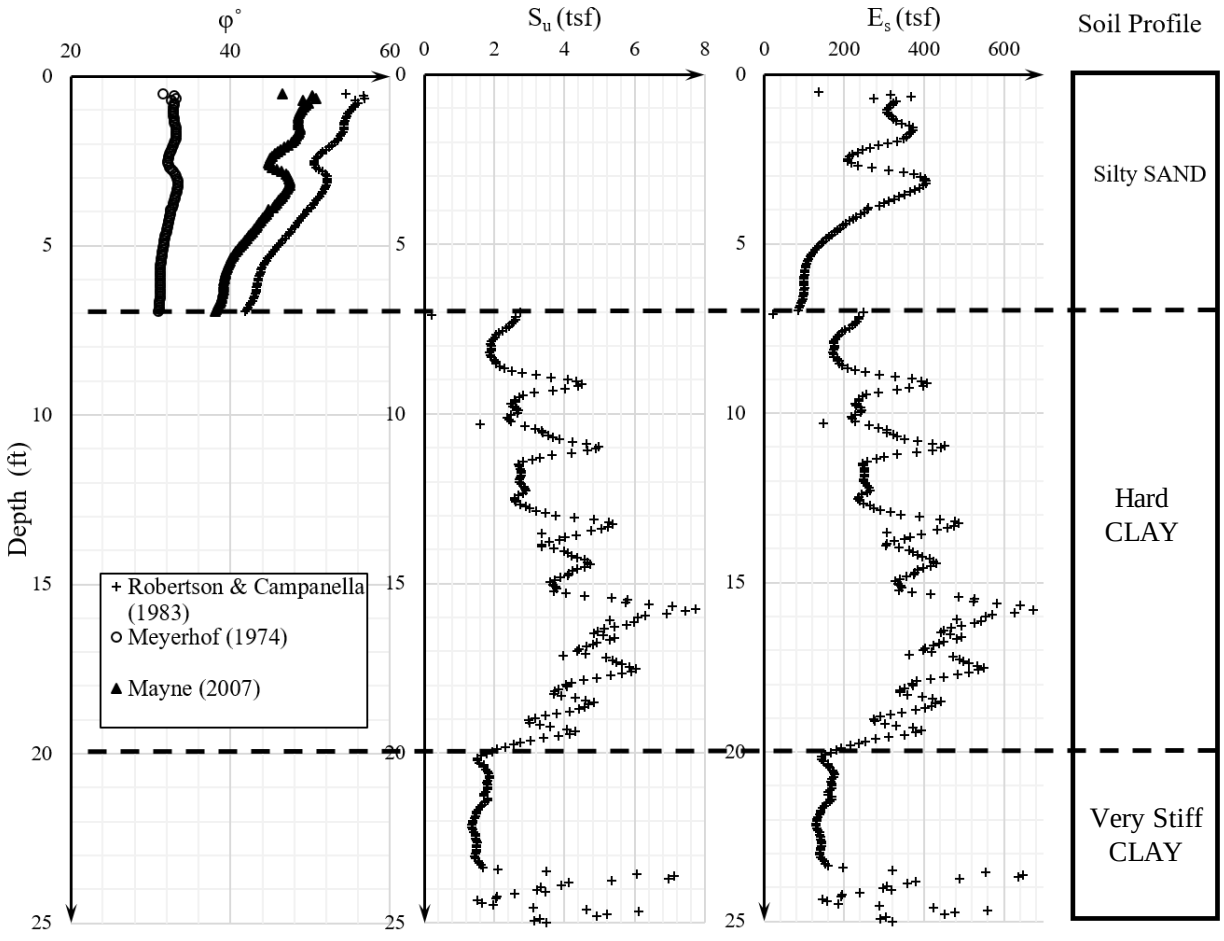

Figure 6-9. Strength and stiffness parameter values vs. depth (US-441)

6.4.3. Soil Profile and Geotechnical Parameters

The soil classifications from the SPT and CPT along with the calculated parameter values were used to identify the soil layer profile of the Wekiva Parkway study area (see Figure 6-10). Also, the strength and stiffness parameter values per layer are summarized in Table 6-3. The estimated soil profile and parameter values of the sinkhole site at US-441 are presented in Figure 6-11 and Table 6-4.

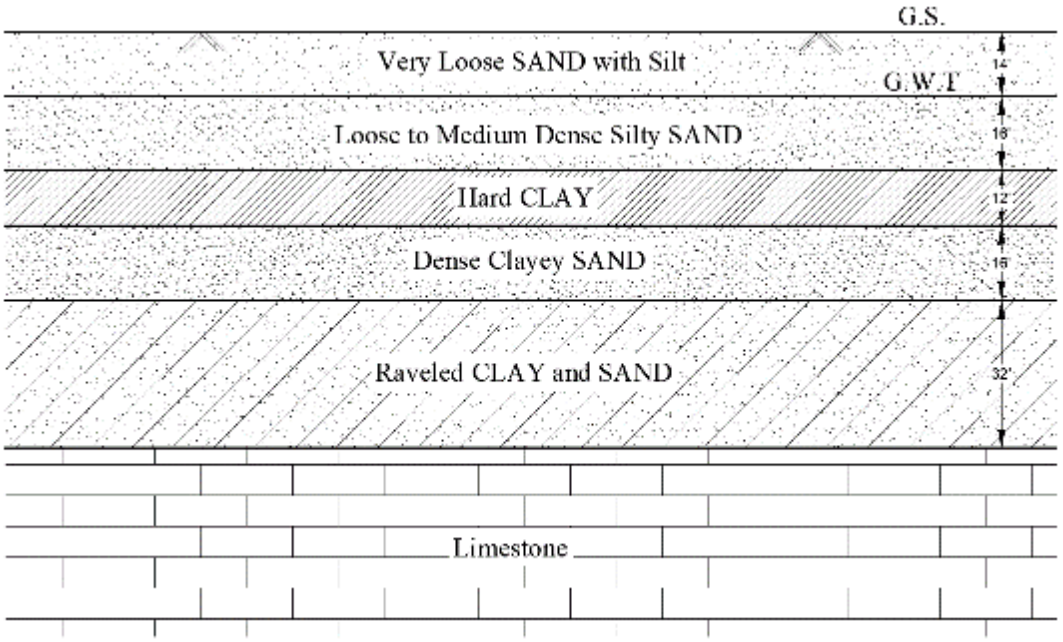

Figure 6-10. Geotechnical section of bridge area at Wekiva Parkway

Table 6-3. Parameter values of soil layers (Wekiva Parkway)

Layer No.	1	2	3	4	5	6
Depth	0 – 14 ft	14 – 20 ft	20 – 30 ft	30 – 42 ft	42 – 58 ft	58 – 90 ft
Classification	Very Loose SAND with Silt	Medium Dense Silty SAND	Loose Sand with Silt	Hard CLAY	Dense Clayey SAND	Raveled Clays and Sands
S_u	-	-	-	3 tsf	-	2 tsf
Φ’	32˚	36˚	34˚	-	38˚	-
E_s	60 tsf	400 tsf	200 tsf	300 tsf	600 tsf	100 tsf

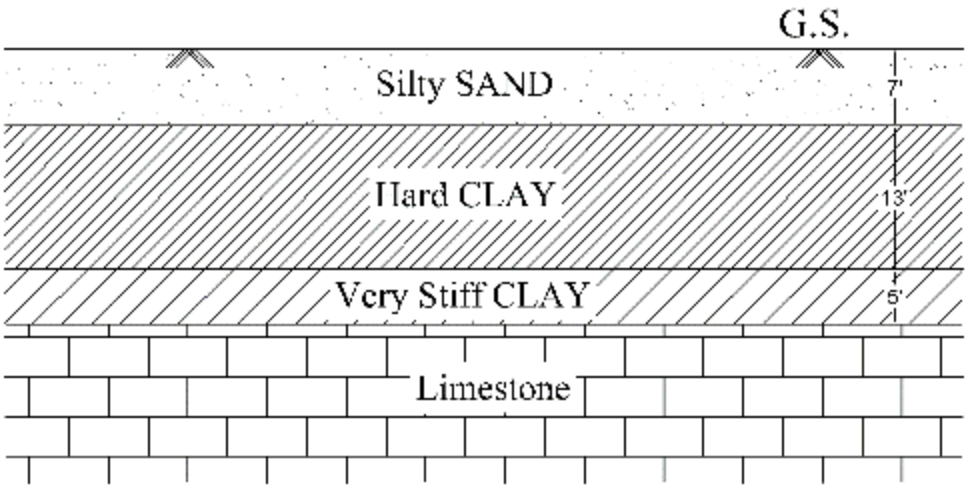

Figure 6-11. Geotechnical section of sinkhole area at US-441

Table 6-4. Parameter values of soil layers (US-411)

Layer No.	1	2	3
Depth	0 – 7 ft	7 – 20 ft	20 – 25 ft
Classification	Silty SAND	Hard CLAY	Very Stiff CLAY
S_u	-	5 tsf	2 tsf
Φ’	36˚	-	-
E_s	240 tsf	400 tsf	180 tsf

6.5. Finite Element (FE) Modeling

6.5.1. Cavity Modeling

Field test results from sinkhole susceptible areas in central Florida often show a zone of raveled soil overlying the limestone bedrock. Figure 6-12 presents the results of SPT and CPT from a sinkhole-susceptible site. The SPT boring log shows a reduction in the blow count with depth starting at a depth of nearly 20 feet. “Weight of Hammer (WH)” and “Weight of Rod (WR)” observations were recorded between depths 45 feet and 94 feet, which indicate very loose (raveled) soils. In addition, the data shows that the rod fell and no soil samples were recovered at depths from 70 feet to 83 feet. Likewise, an inverted strength profile can be noticed from the CPT sounding, where the tip resistance and the sleeve friction values decrease versus depth for soils deeper than 20 feet.

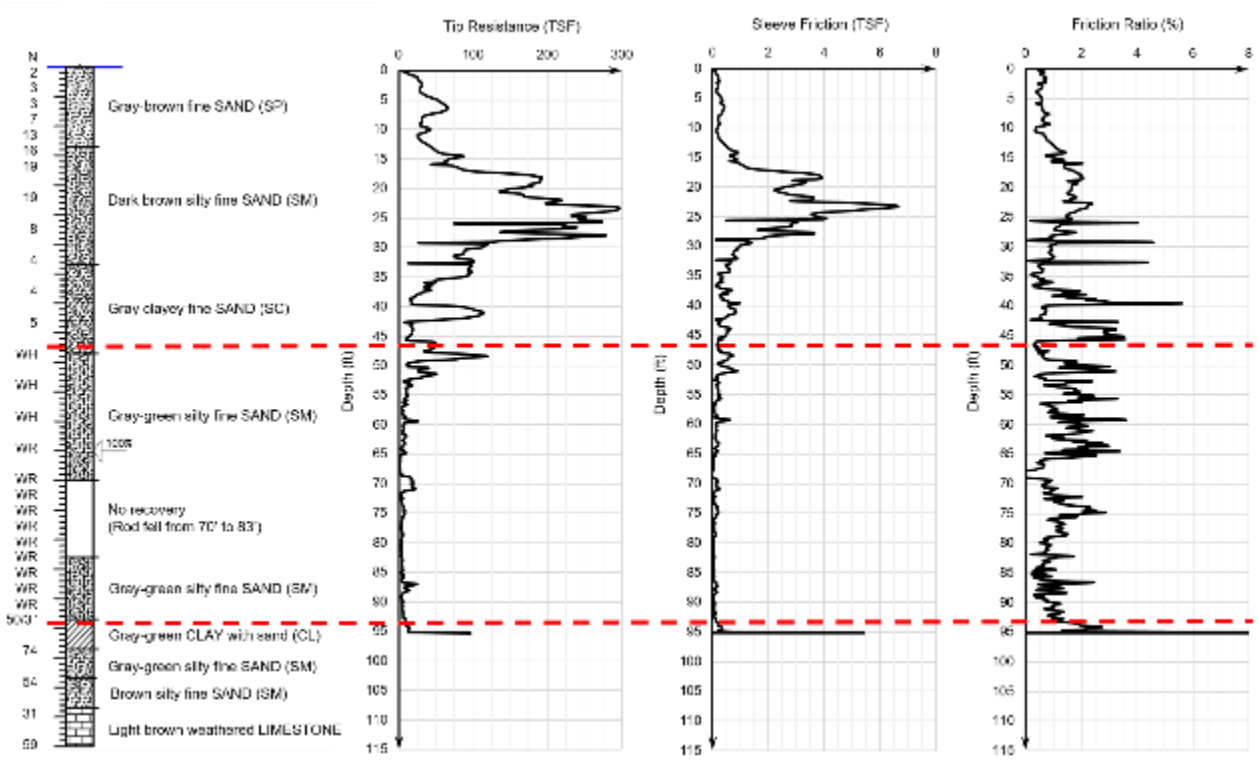

Figure 6-12. Sample SPT and CPT resistance curves/values from a sinkhole investigation site

In this study, an underground cavity at a sinkhole-active area is numerically modeled as a circular void for simplification, which is common practice for numerical modeling of a sinkhole (Drumm & Yang, 2005). Figure 6-13 presents a schematic diagram of a typical CPT sounding in the vicinity of a reported sinkhole and the corresponding model proposed for numerical modeling. The figure shows an overburden soil layer of thickness "H" overlying the bedrock, and a circular cavity of diameter "D" lying at depth "h" from the ground surface. The soil stratigraphy in the central Florida area spatialy varies in properties and depths but commonly consists of a shallow silty sand layer, underlain by a thick mostly overconsolidated clay layer of Hawthorn Group, which overlies the bedrock (limestone). For this analysis, the site conditions were determined from the site investigation reports including CPT soundings and/or SPT borings. Soundings/Borings that showed the most competent soil condition at each site were used to estimate the soil profiles at initial conditions supposedly before soil raveling occurred. Published correlations were used to calculate the input parameter values for modeling purposes. A plane strain condition was used in PLAXIS 2D. A hardening soil small-strain model was used to simulate the soil layers overlying the cavity, where most of the deformations were expected to occur. The underlying bedrock was model by Mohr-Coulomb parameters. For each model in this study, a plastic analysis was performed to determine the magnitude of deformations considering the serviceability limit state (SLS), where excessive deformations correspond to cover-subsidence sinkholes. In addition, a safety analysis was performed to calculate the factor of safety of each model based on the ultimate limit state (ULS), where failure without initial surface settlement corresponds to a cover-collapse sinkhole.

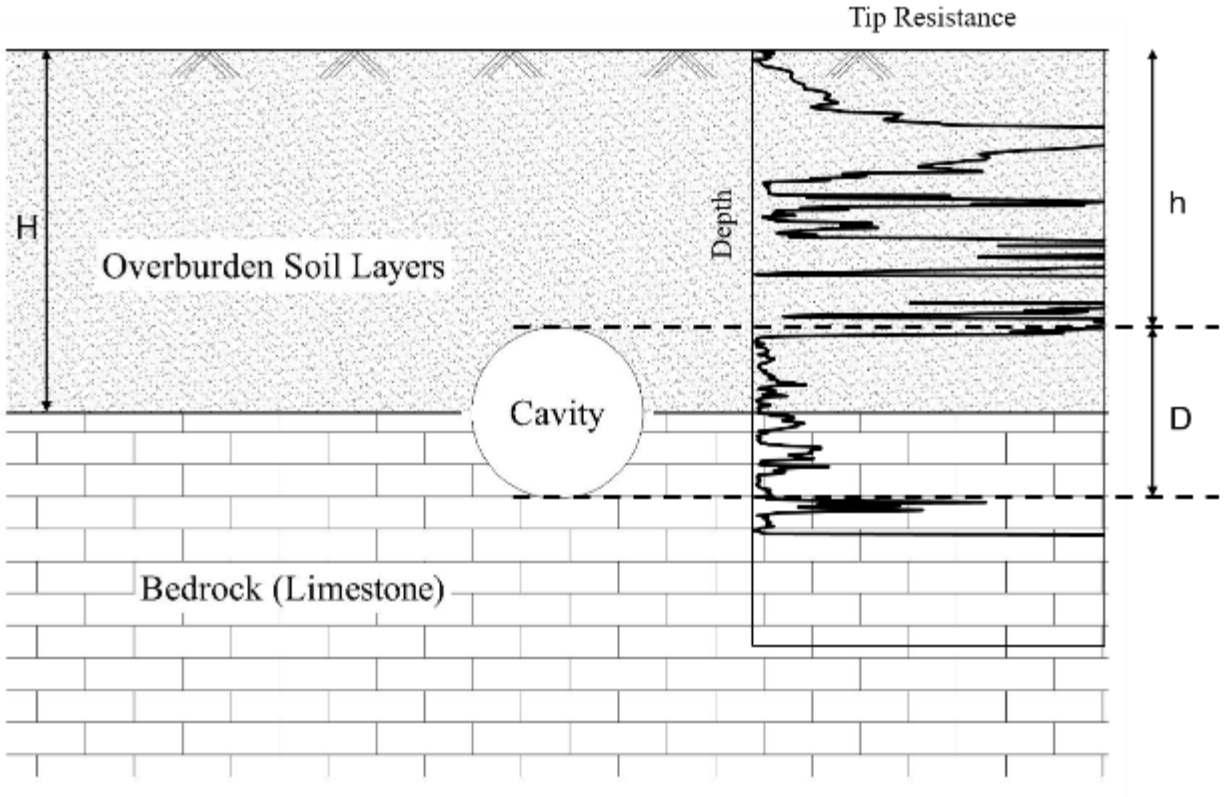

Figure 6-13. Schematic diagram of the model based on CPT data

6.5.2. Finite Element (FE) Model

Figures 6-14 and 6-15 show the finite element meshes simulated in PLAXIS 2D for the Wekiva Parkway and US-441 sites, respectively. In Figure 6-14, the numerical model dimensions were 147.6 ft x 196.8 ft (45 m x 60 m), and plane strain conditions were assumed. The model adopted the soil profile shown in Figure 6-10. Total thickness of soil layers overlying the bedrock was 78.7 ft (24 m). The overburden soil layers from top to bottom were 13.1 ft (4 m) of loose sand with silt, underlain by 16.4 ft (5 m) of medium dense silty sand, followed by 13.1 ft (4 m) of hard clay, then 16.4 ft (5 m) of clayey sand, and below 32.8 ft (10 m) of mixed clays and sands. The water table was defined as 6.5 ft (2 m) below the ground surface, and hydrostatic pressure conditions were applied. The numerical analysis was performed using the Hardening Soil Model (HSM) for all the overburden soil layer; whereas the bedrock was modeled using the Mohr-Coulomb failure criterion. The constitutive soil parameters of each layer are summarized in Table 6-5, which used the strength and stiffness values presented in Table 6-3. Similarly, the US-441 site was modeled as presented in Figure 6-15, and the constitutive parameters are tabulated in Table 6-6. Two meters of medium dense silty sands were followed by 13.1 ft (4 m) of a hard clay layer, and then 6.5 ft (2 m) of very stiff clays. All these layers were underlain by the bedrock (limestone).

The horizontal and vertical deformations were constrained at the bottom and side boundaries.

Initial stresses were generated in a first calculation step assuming non-raveled soil conditions (no subterranean cavities). A cavity was then created by deactivating a circular cluster of diameter "D" in a second calculation step. The center of this cavity lied at the soil-rock contact surface. The cavity varied in diameter (size) in different analyses to estimate the stability at different raveling conditions. The second calculation step adopted the plasticity theory to investigate mechanical behavior of soils around underground cavities with respect to stresses, strains, and deformations. In addition, a safety analysis was carried out for the model using the shear strength reduction technique. This analysis evaluated the factor of safety against sinkhole failure for a specific cavity size and soil conditions. It was also used to depict the estimated failure surface. It is worth noting that a more refined finite-element mesh was used around the cavity and in the overlying soil clusters where the failure surface ultimately occurred.

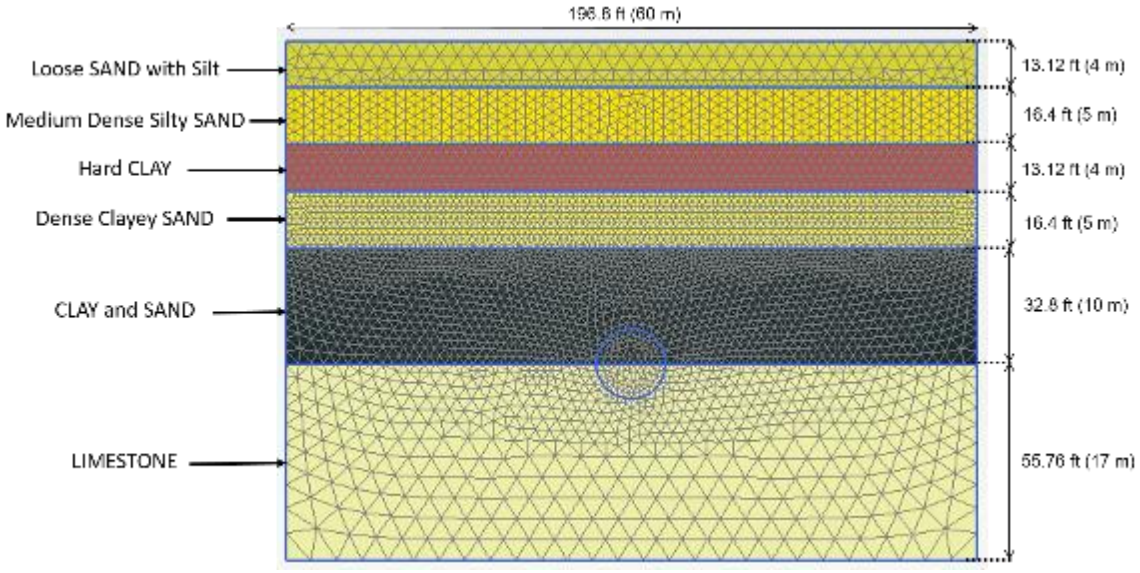

Figure 6-14. Numerical model of Wekiva Parkway site in PLAXIS 2D

Table 6-5. Constitutive parameter values of the numerical model (Wekiva Parkway)

Parameter / Layer	c' (tsf)	φ' (˚)	E_s (tsf)	E_{oed} (tsf)	E_{ur} (tsf)	R_f	ν_{ur}	m	γ_{total} (lb/ft^3)
Loose SAND with Silt	0.05	32	60	60	180	0.9	0.2	0.5	102
Medium Dense Silty SAND	0.1	35	$3x10^2$	$3x10^2$	$9x10^2$	0.9	0.2	0.5	108
Hard CLAY	0.7	32	$3x10^2$	$3x10^2$	$9x10^2$	0.9	0.2	1	121
Dense Clayey SAND	0.2	38	$6x10^2$	$6x10^2$	$18x10^2$	0.9	0.2	0.5	115
CLAY and SAND	0.4	30	$2x10^2$	$2x10^2$	$6x10^2$	0.9	0.2	0.7	108
LIMESTONE	5	45	$2x10^8$	(Mohr-Coulomb model was used)					159

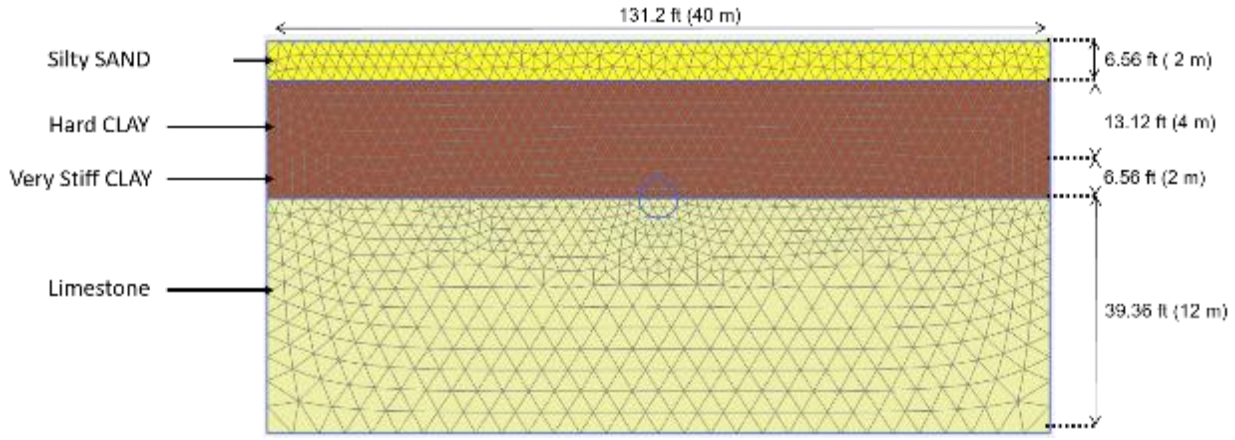

Figure 6-15. Numerical model of the Route US-441 site in PLAXIS 2D

Table 6-6. Constitutive parameter values of the numerical model (US-441)

Parameter / Layer	c' (tsf)	φ' (˚)	E_s (tsf)	E_{oed} (tsf)	E_{ur} (tsf)	R_f	ν_{ur}	m	γ_{total} (lb/ft^3)
Medium Dense Silty SAND	0.05	36	$2.4x10^2$	$2.4x10^2$	$7.2x10^2$	0.9	0.2	0.5	108
Hard CLAY	0.8	32	$4x10^2$	$4x10^2$	$12x10^2$	0.9	0.2	1.0	121
Very Stiff CLAY	0.6	32	$1.8x10^2$	$1.8x10^2$	$5.4x10^2$	0.9	0.2	1.0	115
LIMESTONE	5	45	$2x10^8$	(Mohr-Coulomb model was used)					159

6.6. Analysis and Results

6.6.1. Stress Analysis

Wekiva Parkway

Results of the FEM simulation are presented in Figures 6-16 through 6-19 by the plastic analysis in PLAXIS 2D. Figure 6-16 shows the distribution of effective vertical stress which significantly affects the state of shear stress in the model. A reduction of effective vertical stress occurred at the top of the cavity, compensated by a stress concentration at its sides. This can be interpreted as a result of the arching effect leading to an increase of stresses at the sides of the cavity compensating for the stress reduction occurring above it. This also led to an increase of the shear stresses at the corners of the cavity as depicted in Figure 6-17. The figure shows the relative shear stress τ_{rel} contours where τ_{rel} is the ratio of the maximum shear stress τ_{max} to the mobilized shear strength τ_{mob} at any point in the model. Yielding (τ_{rel} = 1.0) was observed at the corners of the cavity.

Relatively high relative shear stresses were noticed in the silty sand layers. Whereas, the lowest τ_{rel} values were in the hard clay layers due to its high strength and stiffness properties. The principal stress tensors, depicted in Figure 6-18, shows the magnitude and the direction of principal stresses in the model. The lowest stress magnitudes were observed above the cavity; whereas, the highest stress magnitudes were at its sides. In addition, a rotation of stress direction around the cavity and a concentration of the tensors at its side were observed.

The curved deformation contours shown in Figure 6-19 provide the amount of vertical displacement and the influence area around the cavity. The highest deformation values were observed along the centerline of the cavity. The deformation decreased as the distance from the centerline increased in a pattern that reflected the shape of the failure surface. Additionally, Figure 6-20 shows the deformation contour in cases of model failure by applying the shear strength reduction method (safety calculation). Significant high deformations were recorded in meters as illustrated in the figure. This contour provides an indication of the failure surface (cover-collapse sinkhole) due to a cavity in these soil conditions.

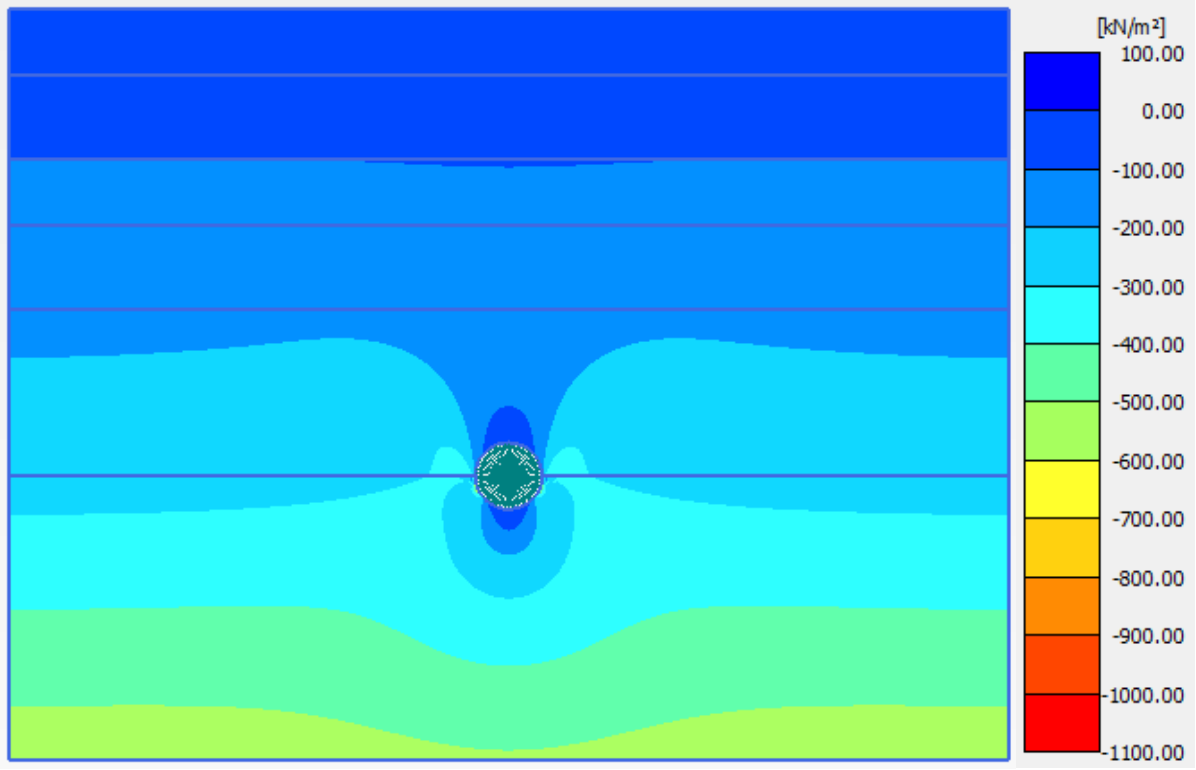

Figure 6-16. Effective vertical stress contour – Wekiva (1 kN/m^2 = 0.01 tsf)

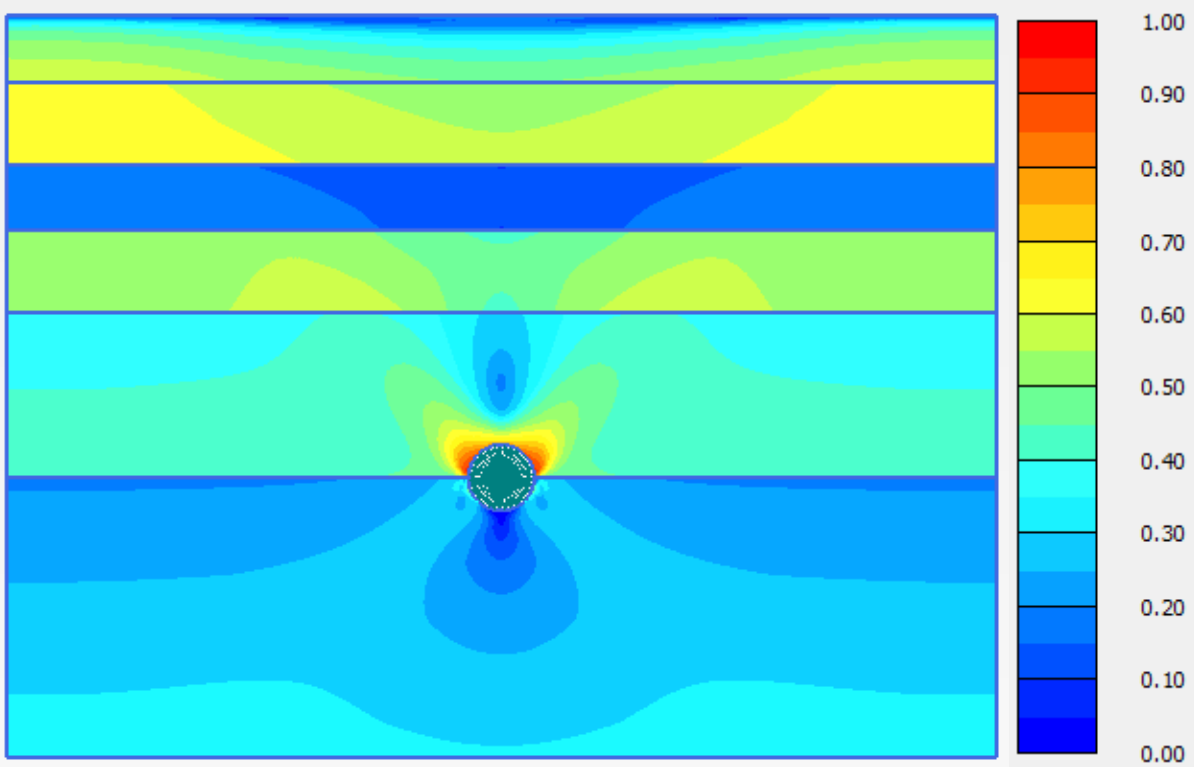

Figure 6-17. Relative shear stress contour – Wekiva

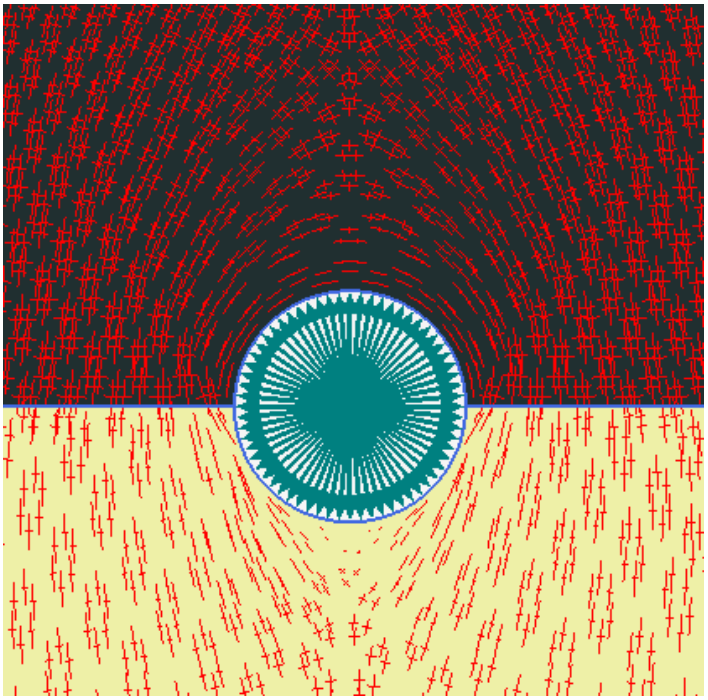

Figure 6-18. Tensor display of principal stress directions around the cavity – Wekiva

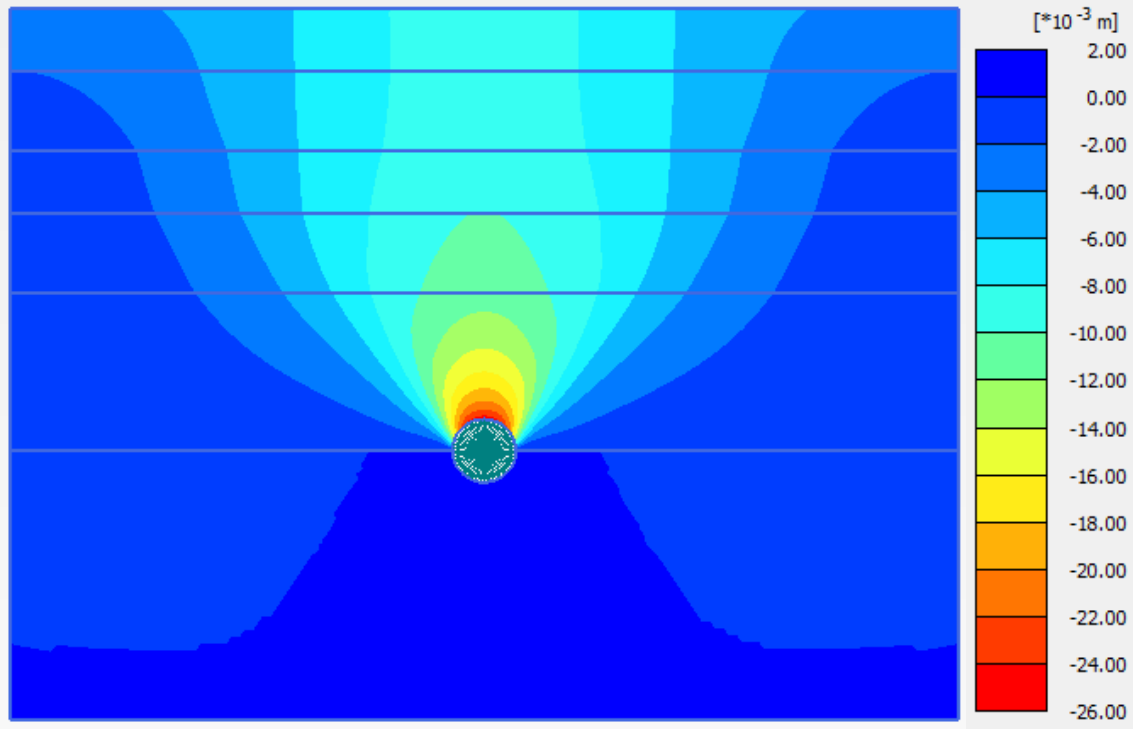

Figure 6-19. Vertical displacement (plastic calculation in PLAXIS 2D) -Wekiva (1 m = 3.28 ft)

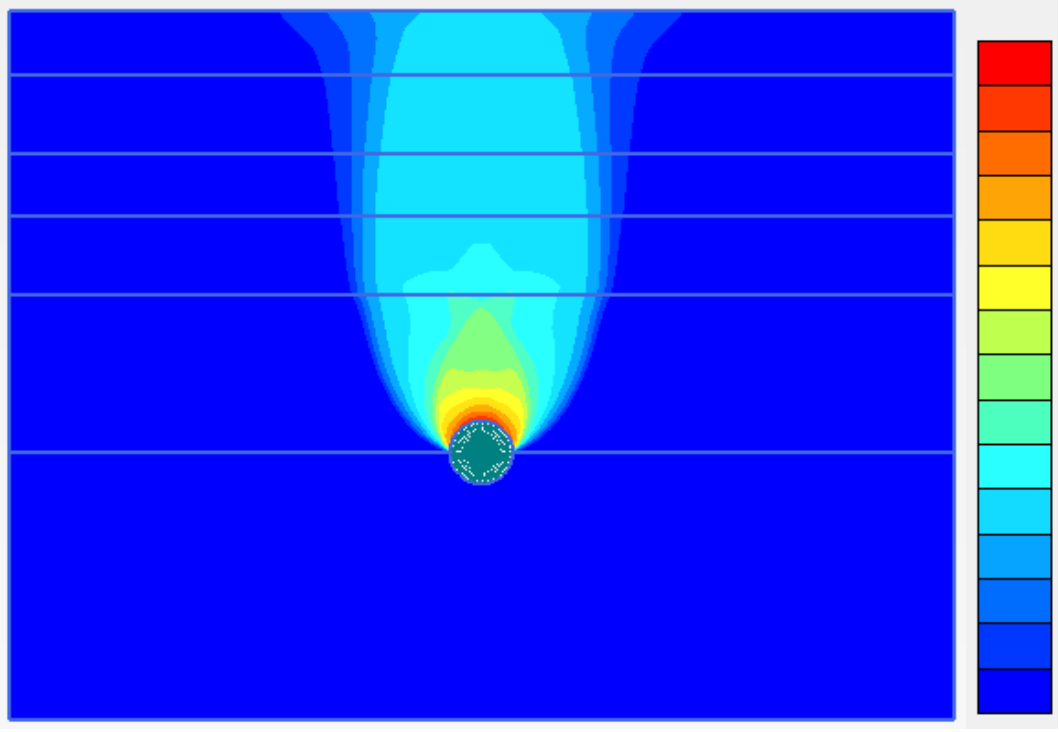

(Note: The contour shows relative displacements and failure planes but not actual displacement values)

Figure 6-20. Vertical displacement (safety calculation in PLAXIS 2D) – Wekiva

Route US-441

The analysis results from the US-441 site, assuming a subsurface cavity size of 2 m, are presented in Figures 6-21 through 6-24. A stress reduction at the top of the cavity was observed in the effective vertical stress contour (see Figure 6-21). High relative shear stresses are noticed around the perimeter of the cavity and at the top of the silty sand layer (see Figure 6-22). However, the relative shear stresses are nearly zero along the top half of the thick hard clay layer due its relatively high strength. This consequently caused sufficient stability of the model against collapse. The tensor display of the principal stresses, as seen in Figure 6-23, clearly depicts the arching effect taking place around the cavity. Deformation contours (see Figure 6-24) show very low vertical displacements at the ground surface with a maximum surface settlement of around 1 mm. However, relatively high subsurface deformations can be observed around the cavity, which are nearly 3 cm at its top. This indicates that the conditions at this site could represent a cover-collapse sinkhole mechanism with no significant deformations before a sudden collapse. Additionally, Figure 6-25 shows the deformation contours resulting from a safety analysis which provide an indication of the shape of the failure surface in case of a collapse.

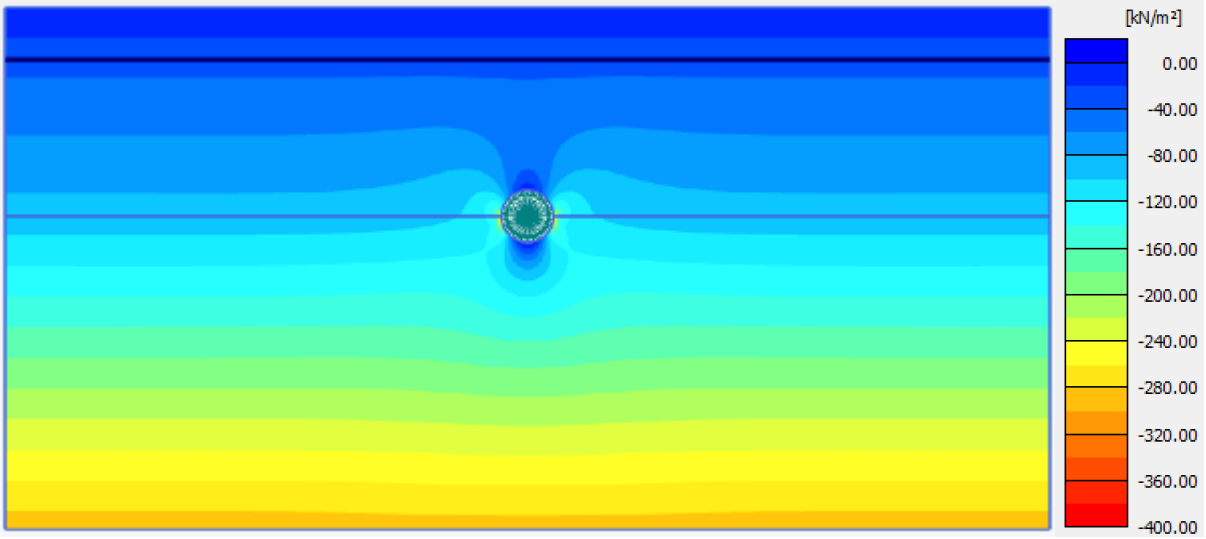

Figure 6-21. Effective vertical stress contour – US-441

(1 kN/m^2 = 0.01 tsf)

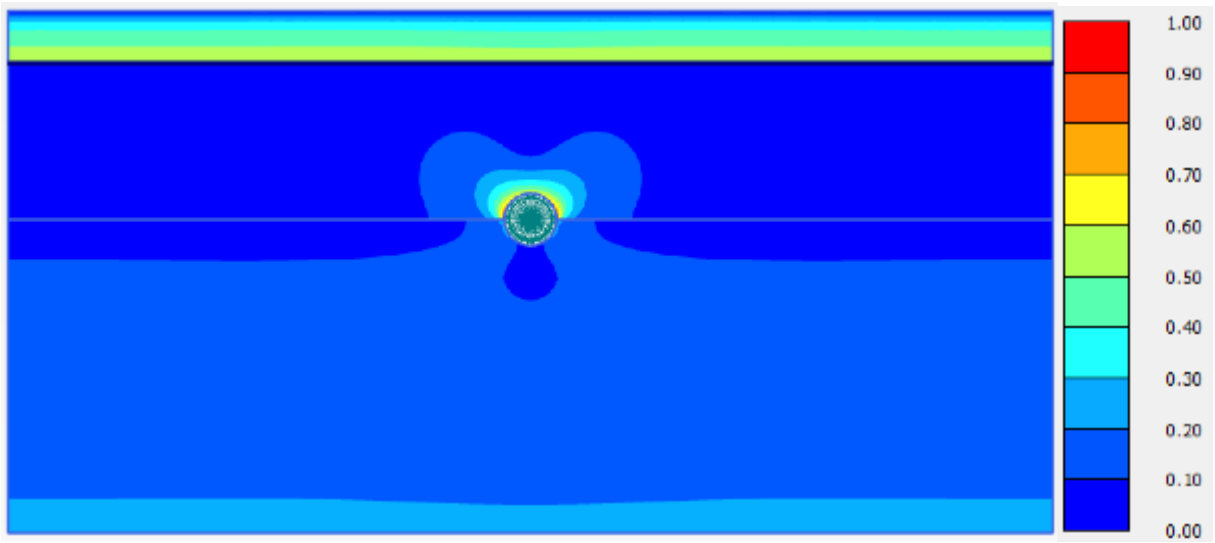

Figure 6-22. Relative shear stress contour - US-441

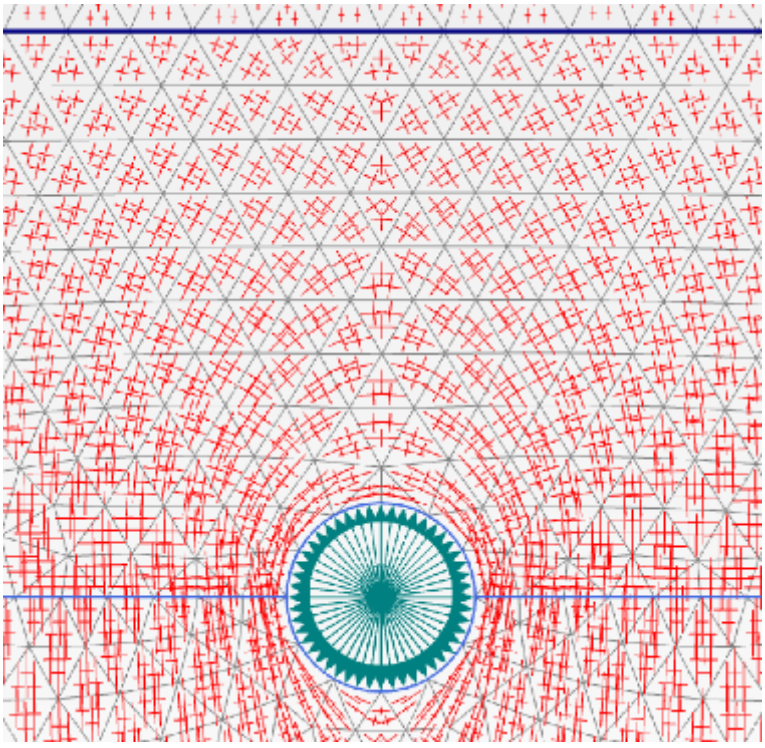

Figure 6-23. Tensor display of principal stress directions around the cavity - US-441

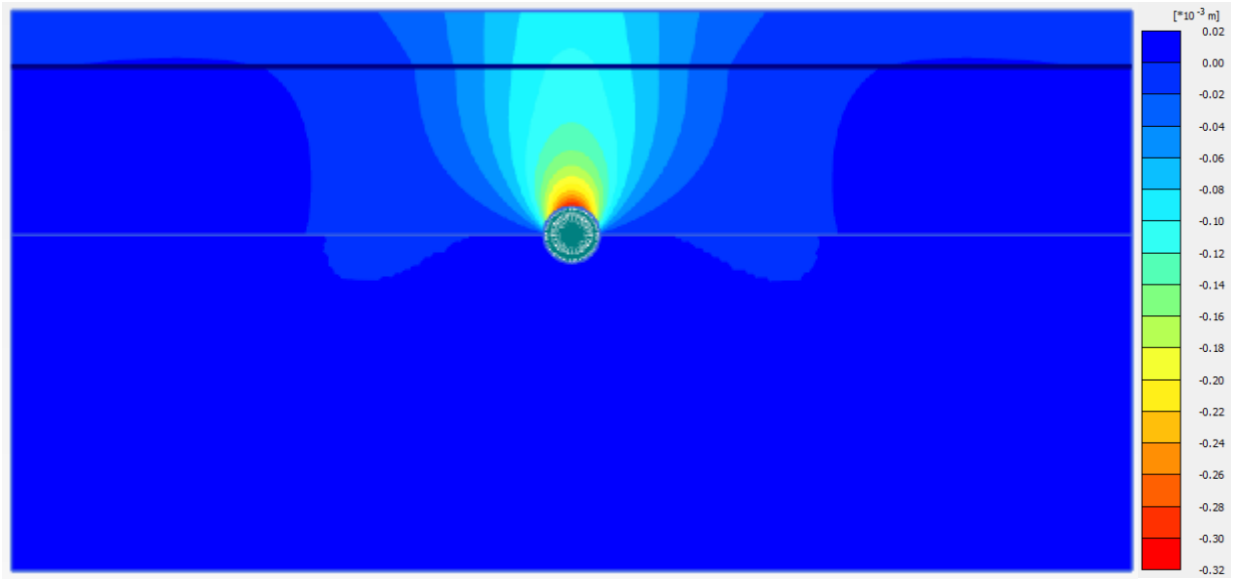

Figure 6-24. Vertical displacement (plastic calculation in PLAXIS 2D) – US-441

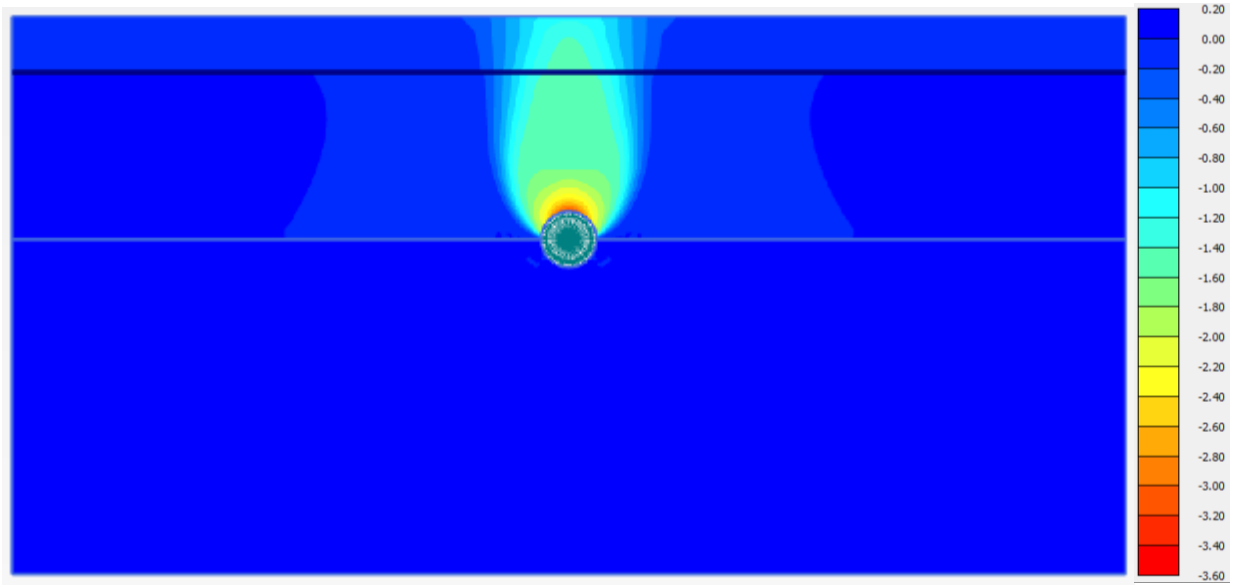

Figure 6-25. Vertical displacement (safety calculation in PLAXIS 2D) – US-441

(1 m = 3.28 ft)

6.6.2. Sinkhole Stability Charts

Based on field testing data it was observed that most of the raveled soils are encountered closer to the top of limestone bedrock. It has been reported that the cohesion value is a predominant factor on the deformations and the stress distributions around subsurface cavities (Soliman et al. (2018)). Therefore, the sinkhole formation is triggered by reducing the cohesion (i.e., strength) of the deep overburden soils surrounding the underground cavities. Plastic and safety analyses were performed in PLAXIS 2D using plasticity theory and shear strength reduction (SSR) method, respectively. In each analysis, the strength values of the deep soil layers overlying the bedrock were varied, and simultaneously different cavity sizes were modeled. Each scenario represents one combination of specific soil strength and cavity size. Each stability condition is reported as a factor of safety from the safety analysis.

Stability charts were then constructed as shown in Figures 6-26 and 6-27 for the Wekiva Parkway and US-441 sites. The charts represent two main parameters governing the stability of the sinkhole: geometric conditions and stress state. The geometric conditions are defined by the ratio of soil cover above the cavity (h) to the size of the cavity (D) as depicted in Figure 6-13. On the other hand, the stress state is expressed by the ratio of the average soil cohesion above the cavity (i.e., soil strength) to the effective vertical stress at the cavity top (γ'h). In the stability charts, the vertical and horizontal axes represent the geometry conditions (h/D) and the stress state, respectively. The factors of safety for each scenario are plotted as individual points on the chart.

Safety contour lines were obtained by interpolation and plotted on each chart. As h/D increases (thicker overburden thickness or smaller cavity size), the factor of safety increases. In addition, as the cohesion increases, the factor of safety increases. It is noticed from the charts that the ranges of safety factors at the US-441 site are higher than those at the Wekiva Parkway site. This may be due to the presence of the thick clay layer with relatively high cohesion values at US-441.

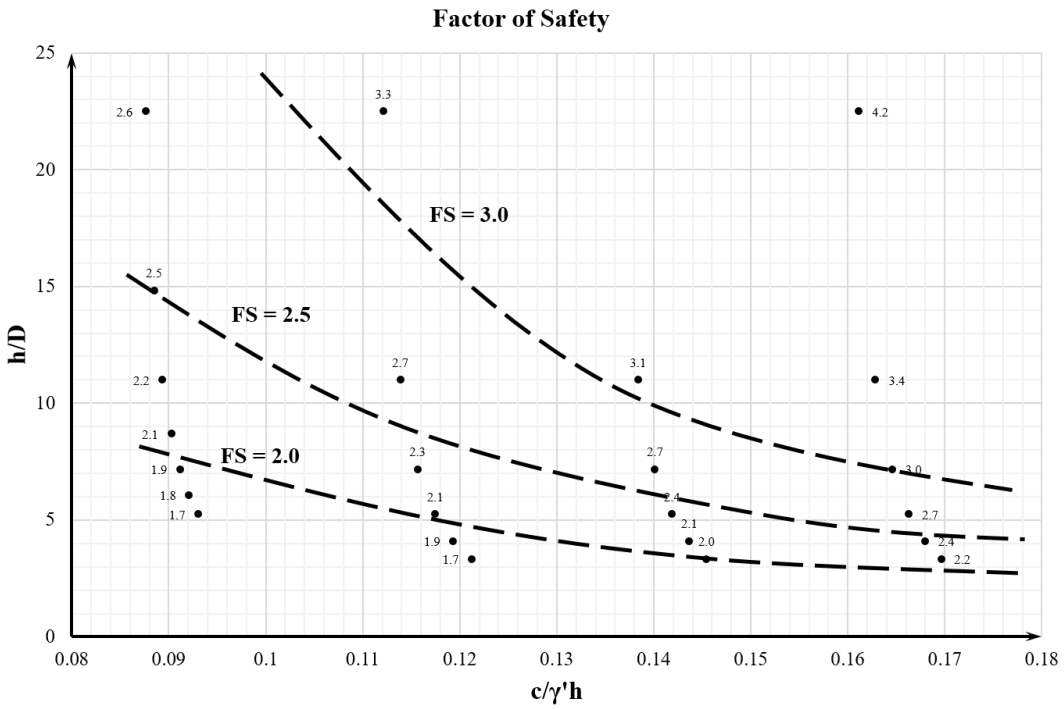

Figure 6-26. Safety Chart developed for the Wekiva Parkway site

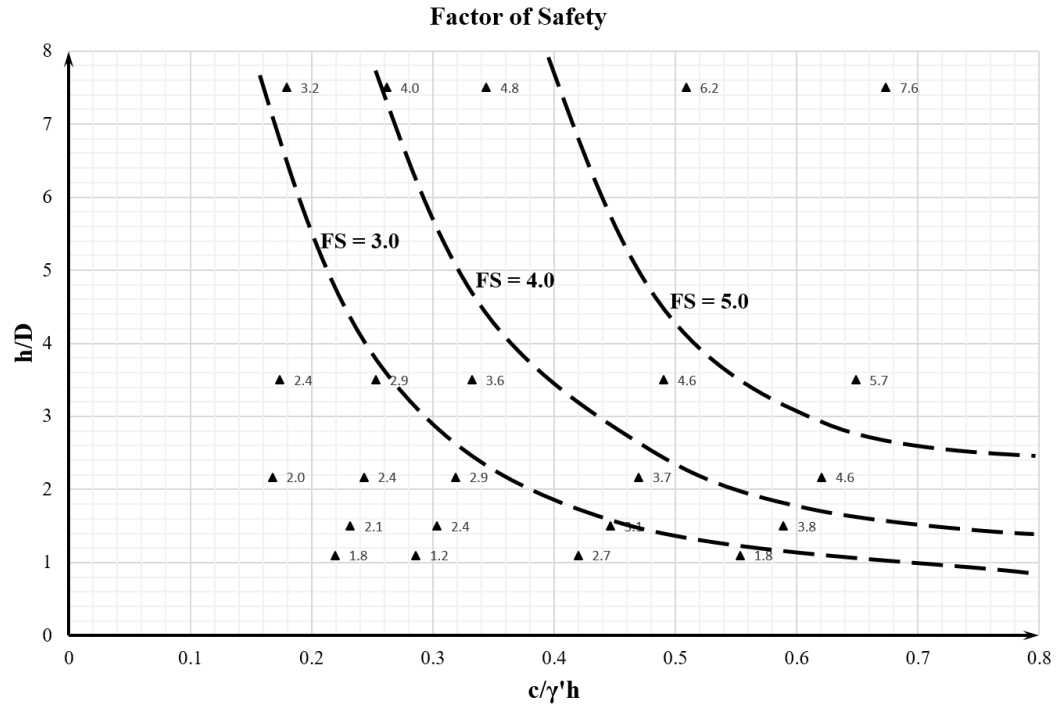

Figure 6-27. Safety Chart developed for the US-441 site

The stability charts of Wekiva Parkway and US-441, which represent somewhat different geotechnical site conditions, were combined to develop a general Sinkhole Stability Chart for use at other sites. The combined stability chart is presented in Figure 6-28. The performance of the combined chart was evaluated by simulating two severely raveled cases, which were CPT-7 and CPT-9 from US-441 (see Figure 6-6). All CPT profiles were visually checked, and these two CPT soundings were selected as representing the worst raveled conditions to validate the stability chart. The calculated FSs for these two CPT soundings are presented in Figure 6-28. Each CPT was analyzed using the same numerical modeling procedure by the strength reduction techniques described above. A cavity diameter of 5 m was used in each model corresponding to severely raveled soil zones shown in Figure 6-29. The data for CPT-7 and CPT-9 provided FS of 1.1 and 1.2, respectively, which would be considered "failure" conditions. It is important to note that the stability chart provides a good indicator of the stability for specific conditions of cavity geometry and soil property (e.g., cohesion); however, the FS values (FS≤1) might not necessarily predict a "failure" condition. Based on the author's experiences throughout the project, it is recommended that FS=2.0 be a threshold value for a "high sinkhole susceptibility" versus a "low sinkhole susceptibility".

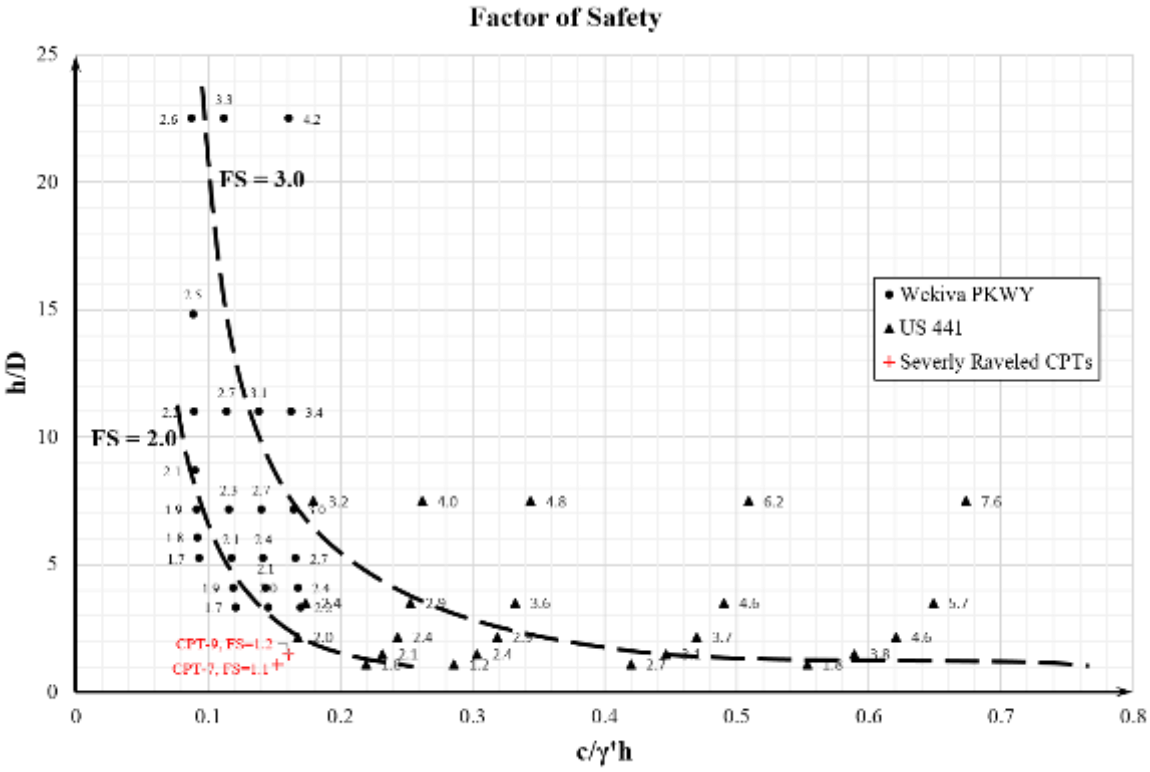

Figure 6-28. Combined Sinkhole Stability Chart

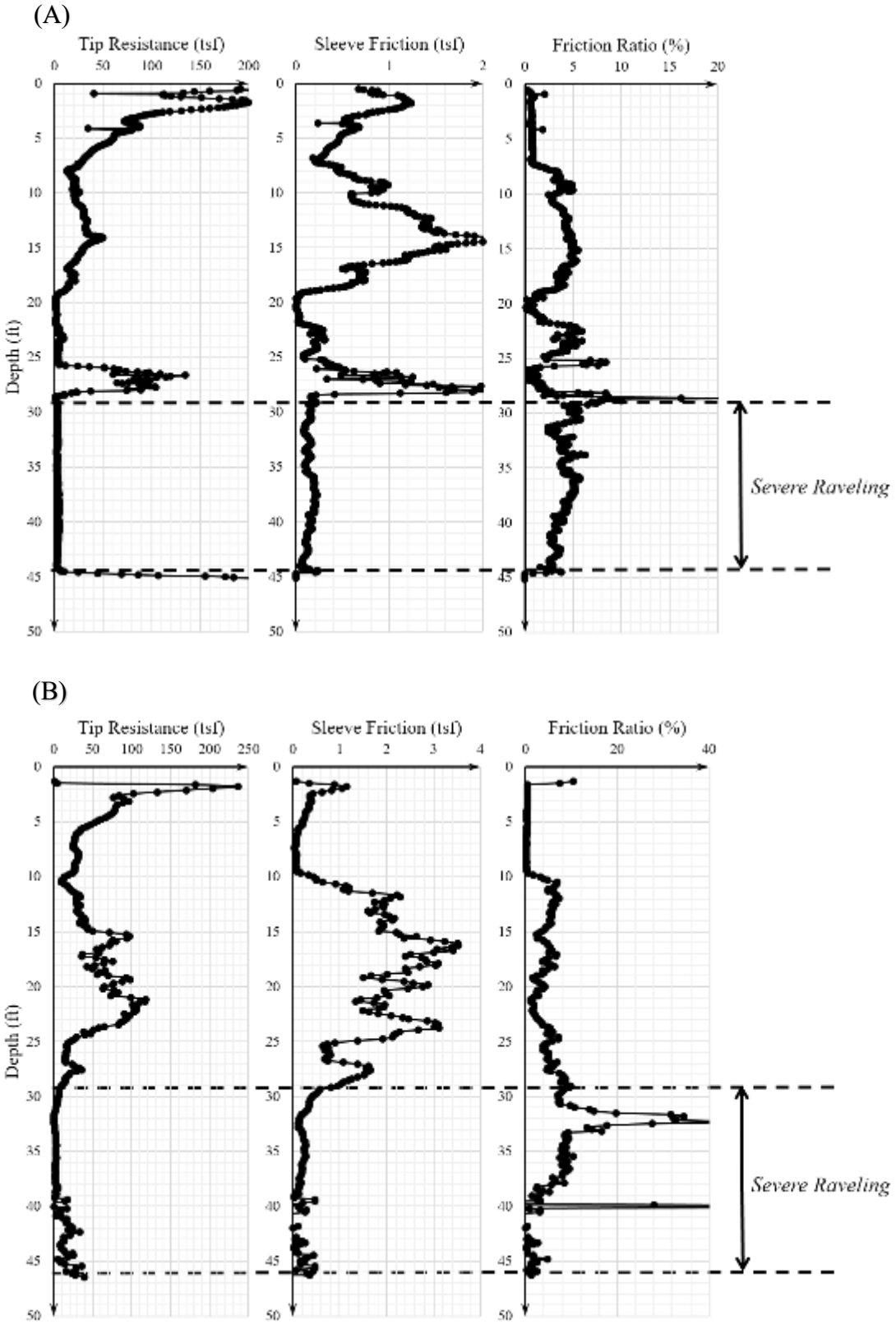

Figure 6-29. CPT resistance profiles at US-441 for (a) CPT-7 and (b) CPT-9 (in Figure 6-9)

7. FLORIDA SINKHOLE RISK EVALUATION GUIDELINE

7.1. Sinkhole Assessment Overview

A complete evaluation and assessment of sinkhole risk for a project site is in no-way a simple task. Due to the multidisciplinary nature of sinkhole formation, collapse, and infrastructural repercussions, it is difficult to derive a comprehensive assessment guideline which can simply be "copied-and-pasted" to each project with suspected soil raveling and sinkhole activity. However, based on the findings presented in this research project, the authors have developed several characterization tools which can be implemented for sinkhole vulnerability assessment of a project from a geotechnical and hydrogeological perspective. These tools may either be implemented separately, or together, to better understand the vulnerability of sinkhole formation. The assessment techniques presented in Chapters 3, 4, 5, and 6 can be organized into three distinct categories, as shown in Figure 7-1. Each category consists of a specific assessment tool which can be used independently, or together, to better assess the severity of sinkhole formation and subsequent vulnerability of collapse.

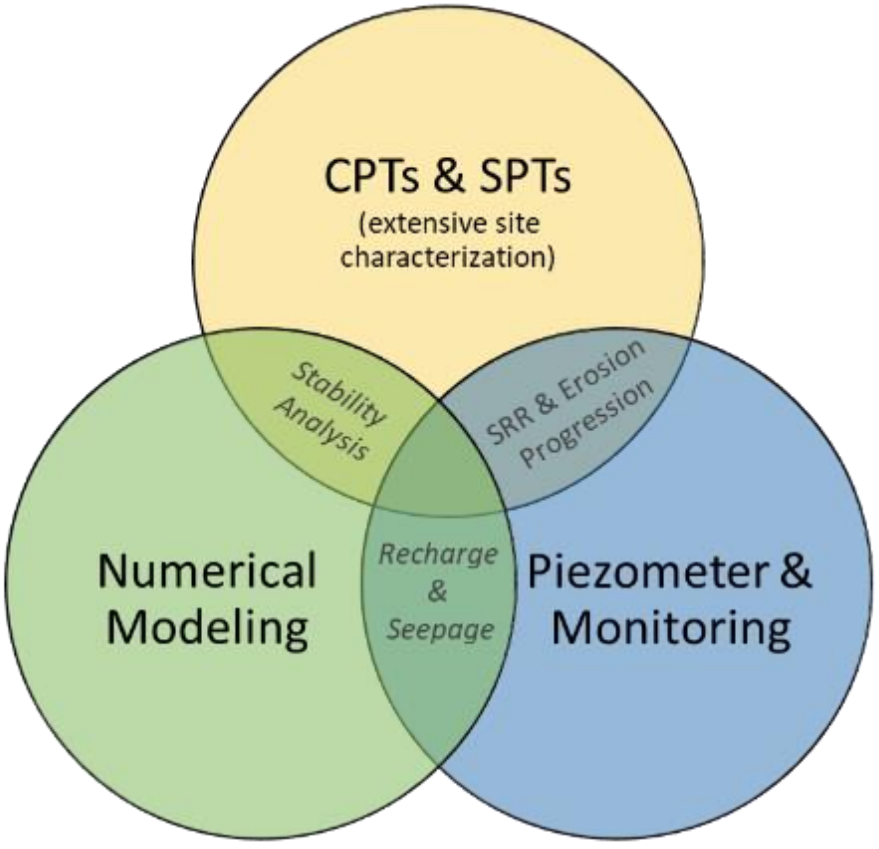

Figure 7-1. Sinkhole assessment tool and their relationships to each-other

The assessment tools presented in the previous chapters are as follows: multiple CPTs with SPTs, installation and monitoring of subsurface piezometers, and numerical modeling platforms such as MODFLOW or PLAXIS 2D. Together, these tools can be used to assess the encountered sinkhole formation for severity and potential collapse from geotechnical (i.e., detection and stability) and hydrogeological (i.e., internal erosion and formation) perspectives.

7.1.1. Site-Characterization-Based Assessment Guidelines

Proper site characterization at a known karst terrane is critical to ensure a safe design and longevity of the site's intended use. Karst geohazards can vary in size and severity and can often be missed in the standard geotechnical subsurface investigation. To aid in the detection of these karst anomalies early in the investigation, the CPT-based raveling chart (see Chapter 5.3) was developed. This chart is meant to be implemented for Cone Penetrometer Test (SPT) results used in conjunction with the Standard Penetration Test (SPT). The following subsurface exploration testing procedure, shown in Figure 7-2, is suggested to maximize the chance of detecting problematic premature sinkhole formations in known karst terranes.

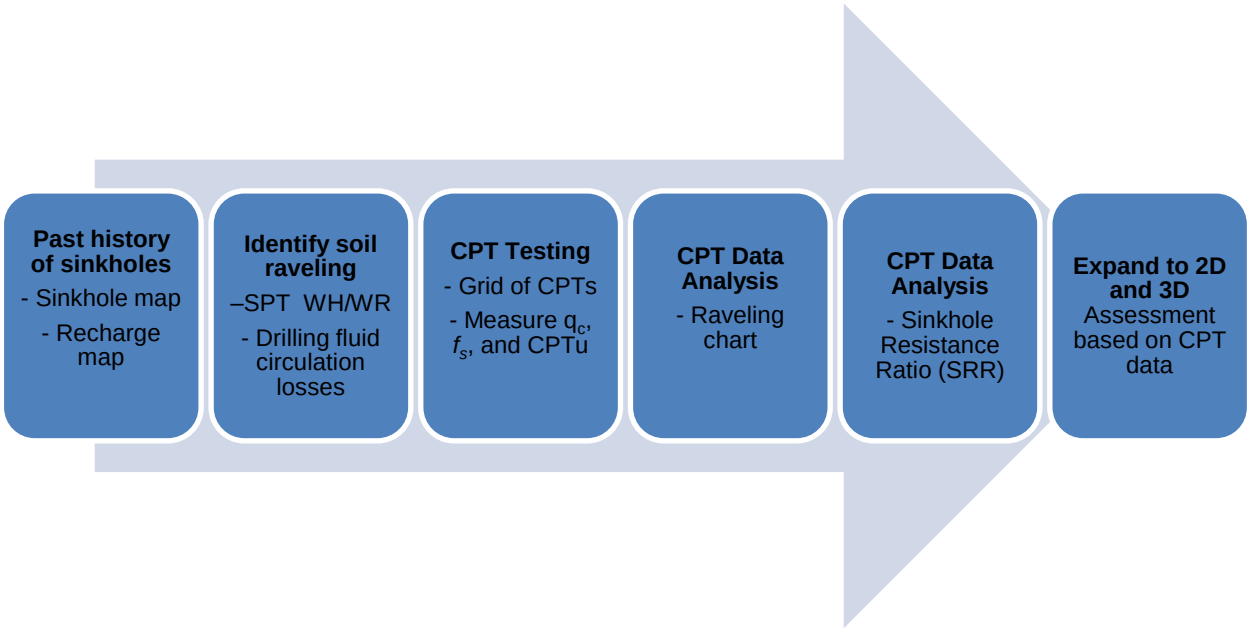

Figure 7-2. Procedure of site characterization based on sinkhole vulnerability evaluation

The key considerations and detailed descriptions from each step shown in Figure 7-2 are summarized as below:

1. Review past history of sinkholes (e.g., sinkhole maps) and groundwater recharge maps to have a sense of the frequency potential of sinkhole occurrence in the area of study. This first check is based on a regional scale not a site-specific scale.

2. Find evidence of sinkhole raveling in the study area. Identify borings with very low SPT N-values and extensive zones where the it was indicated that the drill rods "fall by weight of rod (WR) and hammer (WH)". Note borings logs where it was observed that there were drilling fluid circulation losses due to the existing underground voids and/or channels.

3. If initial exploratory borings or Standard Penetration Testing encounters a significant layer of low resistance material, especially soft sandy clay or loose clayey sand, then CPTs should be performed within the proximity of the anomalous soils. Obtain profiles (with depth) of tip resistance (q_c), sleeve friction (fs), and excess pore water pressures (if piezocones are performed). An initial grid of CPTs should be performed around the problematic SPT at a given distance depending on the depth to top of weathered bedrock, or the thickness of encountered loose soils. Engineering judgement should be practiced when determining the testing layout.

4. For each of the CPTs performed around the problematic SPT, normalized the tip resistance (Q_{tn}) and plot it, along with its corresponding sleeve friction (f_s) value, on the proposed raveling chart (shown in Chapter 5.3). The depth range of encountered raveled soils can be determined using this chart. It is suggested to include any data falling within the "partially raveled" ranges on the chart with the complete depth range of raveled soils, especially if those depths lie directly above the depths where data is categorized as "severely raveled."

5. Once the depth range of raveled material is determined for each CPT, calculate the Sinkhole Raveling Resistance (SRR) ratio for each sounding (following the procedure presented in Chapter 5.4.2). The SRR can be used to quantify the sounding location in terms of progression of soil raveling. The lower the SRR value, the more severely raveled the soil at that specific sounding location. It is important to note that the SRR is a 1D (point-based) assessment of the CPT sounding profile.

6. Extend the SRR to the full area of the sinkhole investigation. When SRR values are calculated for a grid of CPTs close to each other, the resulting mapping/contouring of the values can be used to estimate the "throat" of a sinkhole (represented by the CPT soundings with the lowest SRR values). Mitigation techniques can then be focused within that vicinity to inhibit future internal soil erosion.

7.1.2. Stability Analysis Guidelines

The procedure and methodology to develop the stability charts using numerical modeling and subsurface exploration data was presented in Chapter 6. The general procedure is summarized in the five steps below:

1) **Site Investigation**: Site investigation data from geotechnical reports can be used to determine the soil stratigraphy and properties at the location to be modeled. From SPT borings and CPT profiles, identify the general geotechnical profile and conditions of the site. Underground voids or raveled zones of soils can be investigated. Use soil classifications from SPTs and soil behavior correlations from CPTs, along with the correlated parameters, to identify the soil layer profile.

2) **Input Parameters:** The CPT data are used to determine the parameter values for numerical modeling (finite element model). Published correlations can be used to calculate strength and stiffness values from the tip resistance values versus depth.

3) **Finite Element (FE) Modeling:** Based on the soil profile and input parameters estimated from field tests, develop a finite element (FE) model in PLAXIS 2D. A raveled zone identified by the CPT profile can be modeled as a circular cavity. The FE modeling employs a Hardening Soil Model (HSM) for all the overburden soil layers and a Mohr-Coulomb failure criterion for the bedrock.

4) **Stress Analysis:** Different stresses and strains can be visually evaluated, but the relative shear stress contour and the vertical displacement are the most important variables in the analysis.

5) **Stability Chart:** A safety analyses can be performed with the PLAXIS 2D shear strength reduction (SSR) technique. Each stability condition is evaluated by the factor of safety from the safety calculation, and the stability chart is constructed (see Figure 6-28). For the stability chart, the geometry condition (h/D) is plotted on the vertical axis versus the stress state on the horizontal axis, with a series of curves for varying factors of safety.

The stability charts developed in Chapter 6 are suggested as a tool to understand the relative risk of sinkhole formation in terms of the Mohr-Coulomb's soil failure criteria (i.e., shear failure). Although the sinkhole collapse progression has been shown to develop in stages (Perez A. L., 2017), the proposed stability charts were developed assuming any factor of safety less than 1.0 may result in a potential of sinkhole collapse at the ground surface. Therefore, these charts should not used to estimate the overall diameter of the resulting sinkhole; but rather, to estimate how close the encountered soil conditions are to an overall failure (sinkhole collapse).

It is also important to note that the developed stability charts are site specific, thus FS values vary depending on site conditions. In addition, the FS values might not necessarily predict a collapse condition at the surface. Based on the author's experiences throughout the project, it is recommended that FS=2.0 be used as a threshold value for a "high sinkhole susceptibility" versus a "low sinkhole susceptibility".

7.1.3. Groundwater-Based Assessment Guidelines

Implementing and calibrating numerical modeling techniques, such as MODFLOW, can help better identify potential areas within a project that may be of a high vulnerability (or risk) of sinkhole formation. However, this tool requires model calibration through input of piezometric data within the project site. When piezometric data is not available within the project boundary, installation of piezometers can be performed as presented in Chapter 3. To maximize the effectiveness of the piezometer data for the development and calibration of the groundwater recharge model, the following guidelines are recommended:

Recommendations for Piezometer Spacing

1. Collect any available data from the site, including geological maps, sinkhole maps, subsurface tests (e.g., CPT, SPT, GPR, etc.), soil profile and properties, etc. Available geological maps and reported sinkhole maps provide general information on a large scale. On the other hand, site visits and subsurface test data can provide site specific information associated with hydrogeological and geotechnical conditions.

2. Existing subsurface tests (e.g., CPT, SPT, water table observations, etc.) can provide a snapshot of the water table at a given point at the site. Water table contours can be generated based on the existing subsurface information. Figure 7-3 shows an example of a water table contour based on existing GWT data.

3. These generated water table contours provide a general flow pattern at the site of interest. Direction of groundwater flow can also be estimated by drawing lines perpendicular to the groundwater contours. Potential points of recharge can be identified from the generated flow lines, where two or more flow lines from opposite directions appear to converge at a point.

4. For a large area, zoning for the sensor installation will be necessary. Based on existing subsurface information, key features (e.g., relic sinkholes and topographical pinnacles) can be considered as candidate sites for sensor installation and monitoring due to the groundwater flow. Figure 7-4 shows an example of how zoning was used for this project. A total of four zones were selected to understand and measure regional and localized groundwater flow (or points of recharge).

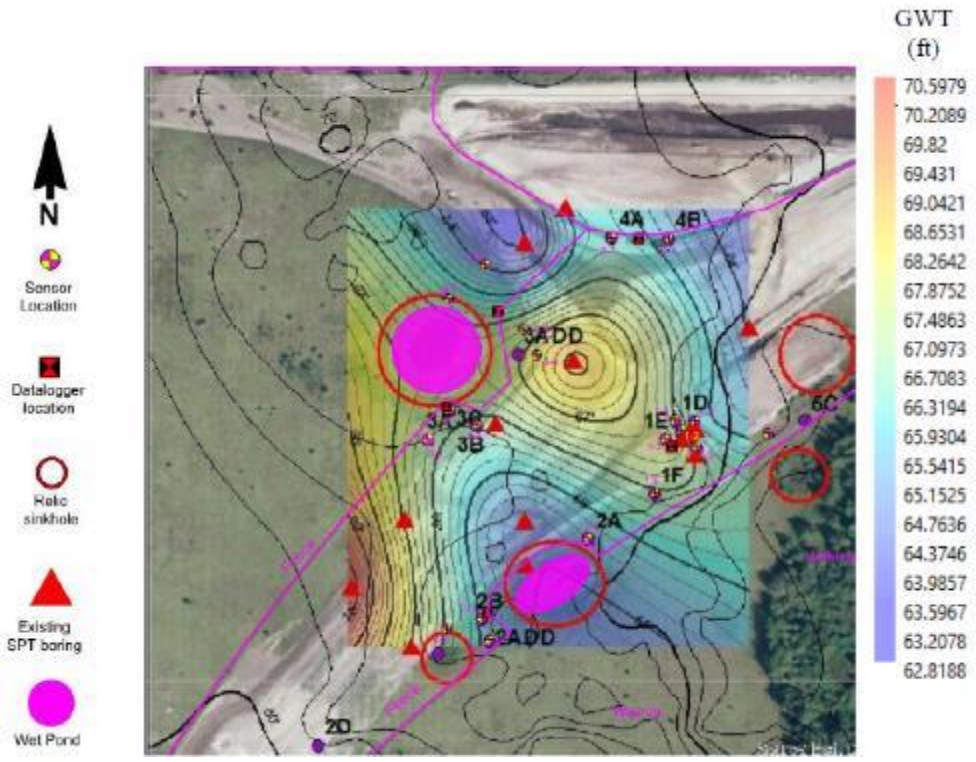

Figure 7-3. Initial investigation of surface groundwater table based on existing data

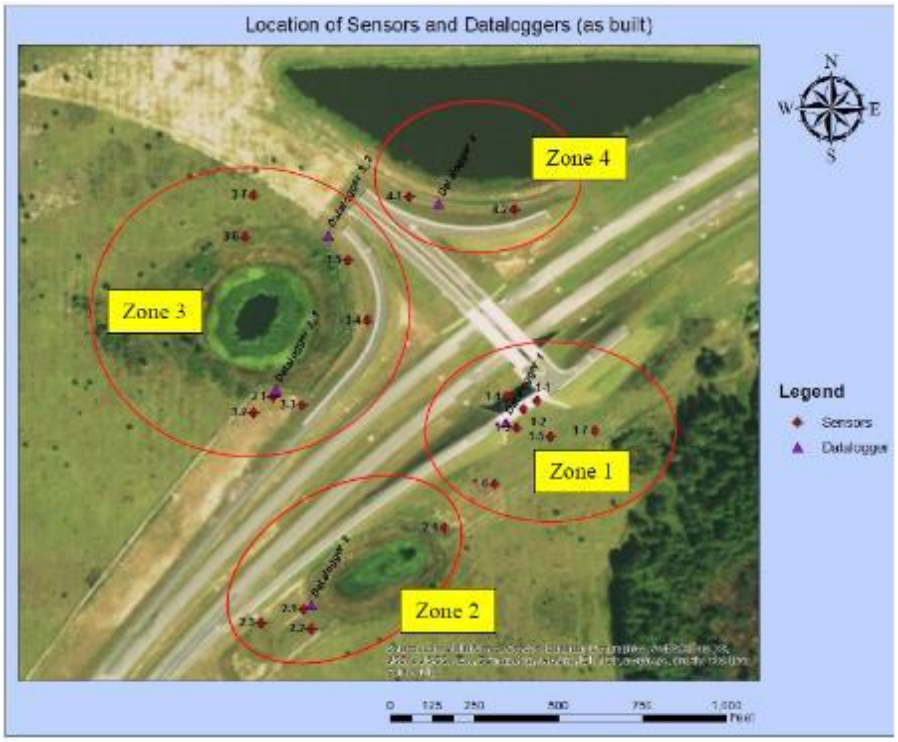

Figure 7-4. Zoning based on localized stratigraphic and topographic features

5. For each point of recharge (i.e., zone) identified, installation of at least five piezometers is recommended. As shown in Figure 7-5, one piezometer should be installed in the center of the suspected point of recharge. Two piezometers should be installed along the flow lines to the point of recharge, radially at 90 degrees away from each other. This layout of piezometers should form concentric circles about the piezometer installed at the suspected recharge point. Each pair of piezometers along the same flow line can be used to estimate the hydraulic gradient, thus estimating the soil seepage rate to the point of recharge. For this installation procedure, the greater number of piezometers installed along a flow line will result in higher resolution of groundwater behavior at that specific point.

6. The spacing of piezometers can be determined based on the estimated local hydraulic gradient. It is recommended that each pair of piezometers along a flow line should be expected to measure a water table difference (Δh) of one to two feet. Therefore, the maximum distance between two same-flow-line piezometers can be estimated using the following translation of the hydraulic gradient formula.

$$dl \leq C/i \qquad \text{.....Eq. 7.1}$$

Where, C = 1 to 2 (ft)
i = hydraulic gradient observed from GWT contouring (unitless)
dl = distance between piezometer sensors along same flow line (ft)

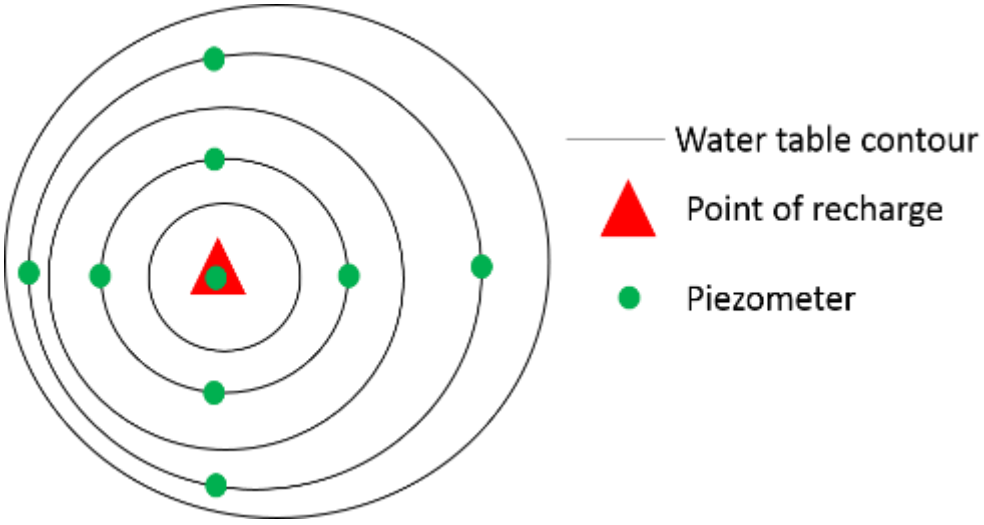

Figure 7-5. Recommended number of piezometer sensors to efficiently capture the groundwater flow

Piezometer Spacing - Example

Taking the Wekiva site as an example, the piezometer spacing is determined using the following steps:

a) Water table contours are generated from existing data (e.g., SPT, boring, etc.) as shown in Figure 7-7.

b) The potential points of recharge are identified from the contours (i.e., local minimum water levels). A piezometer is placed at the center of each of these potential recharge points. For example, point SB-26 is a potential point of recharge.

c) Compute the hydraulic gradient along the flow lines. The hydraulic gradient is computed as the head difference between two points along a flow line divided by the distance between the two points. For example, the hydraulic gradient between SB-16 to SB-26 is 0.007 and the hydraulic gradient between DB-2 to SB-11 is 0.009.

d) If $\Delta h = 1$ ft is used (recommended), the piezometer spacing along the flow line from SB-26 to west can be determined by: $\frac{\Delta h}{g} = \frac{1\,ft}{0.007}$ =143 ft (44 m). In other words, the sensor spacing from SB-26 to west (toward SB-16) is about 143 ft. Similarly, the estimated sensor spacing between DB-2 and SB-11 it would be: $\frac{\Delta h}{g} = \frac{1\,ft}{0.009} = 111$ ft (34 m), which is a denser piezometer spacing due to a higher hydraulic gradient. If the project budget is limited, a head difference (Δh) of 2 ft can be used to increase the sensor spacing (reducing the number of sensor installations), but will result in a lower spatial resolution.

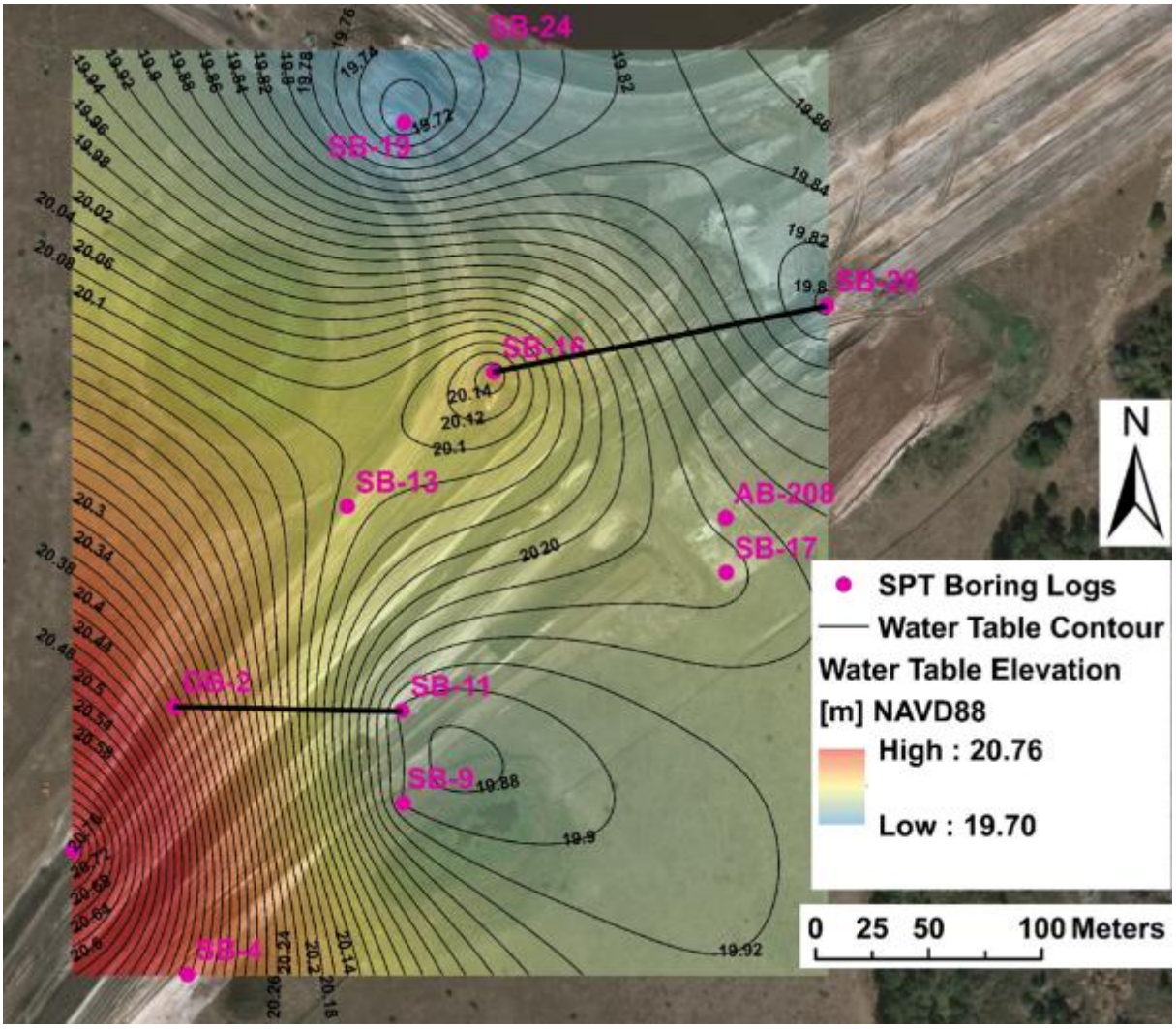

Figure 7-6. Demonstration of determining the distance of piezometers within the Wekiva site

7.2. Implementation Recommendations

Recommendation for CPT-Based Vulnerability Assessment Implementation

As shown in Figure 5-7, the SRR values (following the procedure outlined in Chapter 5) for each CPT performed within a project can be mapped with either point-color categories or SRR range contouring. This allows for easy site comparison and identification of potential areas of interest which may require further investigation or mitigation against sinkhole collapse (such as redesign or injection grouting to fill/strengthen the raveled soils). From Figure 7-7 and Figure 7-8, we can clearly see a grouping of severely low SRR values (corresponding to a high degree of raveling) at the locations where CPTs were performed in a grid pattern. Also apparent are several locations where higher SRR values can be found in close proximity to much lower values. This phenomenon highlights how variable the soil conditions can be, spatially, within a karst terrain.

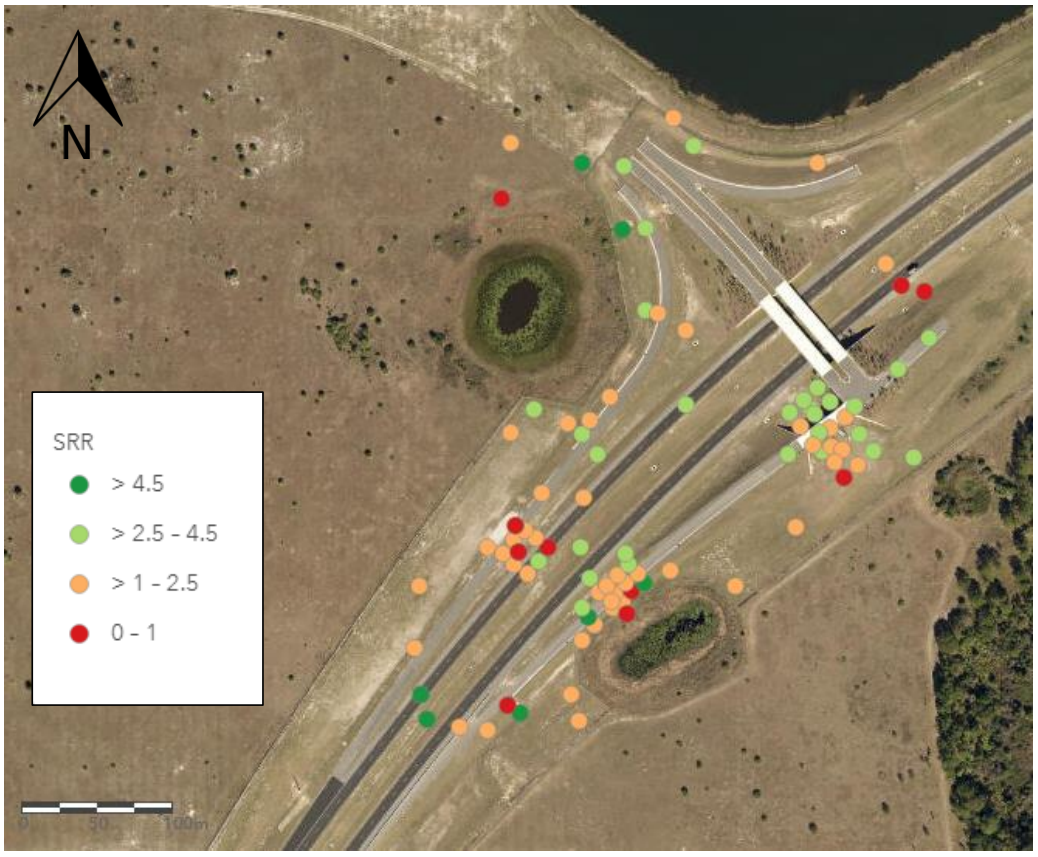

Figure 7-7. SRR values plotted on map of Wekiva Parkway site

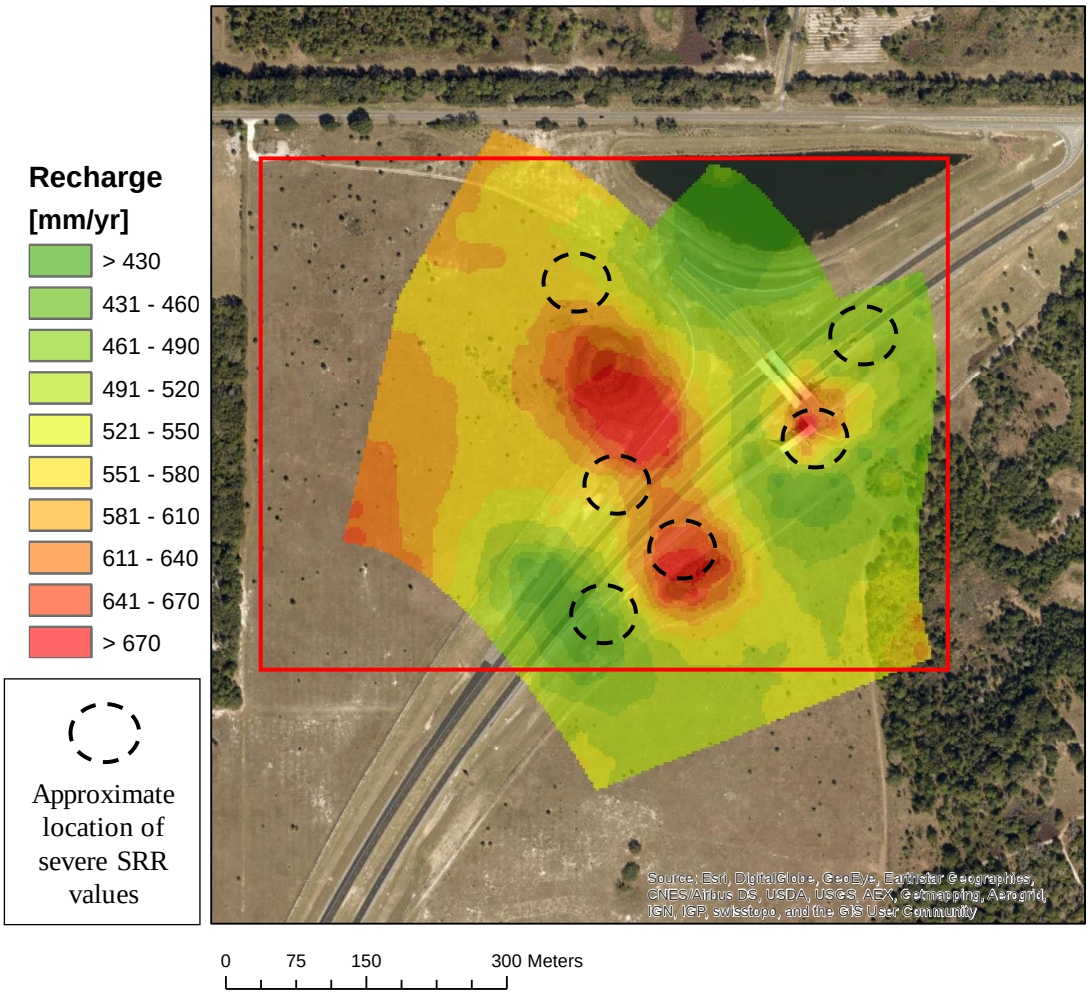

Figure 7-8. High-resolution recharge map with highlighted areas of severe SRR values.

Recommendation for Recharge Modeling-Based Implementation

Regional-scale groundwater modeling has been conducted for agricultural and water management purposes. Even though groundwater recharge (i.e., seepage downward) has been considered as a major cause of soil internal erosion, the use of a regional-scale recharge mapping has not been a standard tool for geotechnical engineering projects due to its large scale and low resolution. This project developed guidelines to use MODFLOW-based groundwater modeling to provide high-resolution groundwater recharge maps that can identify points of recharge (considered as source of sinkholes) and to quantify the risk of sinkhole occurrence at a project site. The information can be implemented in the design stage of the transportation infrastructure (e.g., roadway, bridge, culvert, etc.) to assess the site conditions and determine if remediation is needed. In addition, the developed MODFLOW model can be utilized to simulate a variety of scenarios such as seasonal change in groundwater flow regime, rainfall events (e.g., hurricane, tropical storm), and so on. Two implementation plans are recommended for practical use:

1. ***Develop monthly (or seasonal) recharge-based sinkhole risk charts:*** By using the recommended MODFLOW model, the engineer can construct both a seasonal/monthly recharge map and sinkhole risk map. The water levels of surficial and confined acquirers vary by season due to the cycle of wet and dry seasons; thus, the seasonal impact may be significant. From this, the engineer can assess the range of sinkhole risk throughout a year so that the roadway and/or bridge can be properly designed, including any recommended remediation procedures.

2. ***Develop rainfall event scenario-cased sinkhole risk charts:*** Extreme rainfall events (e.g., hurricane, tropical storm) can create new sinkholes throughout the state of Florida. For example, Hurricane Irma has caused numerous sinkholes in central Florida within a week after the hurricane. Extreme rainfall events after a long period of drought can cause significantly large head differences between surficial and confined aquifers due to the surficial aquifer being recharged much faster than the confined aquifer. The MODFLOW-based recharge model can simulate the effect of rainfall events as well as seasonal changes in groundwater flow.

The benefit of numerical modeling is that future predictions and scenario-based simulations can be performed. The developed MODFLOW model is also able to provide high-resolution groundwater table elevations at the project sites, which is important information to geotechnical and roadway engineers. Results of the MODFLOW numerical modeling can be used as inputs for seepage and stormwater management analyses.

8. SUMMARY AND CONCLUSIONS

8.1. Summary

Comprehensive sinkhole risk and vulnerability assessment on a regional, or site-specific scale, is a multidisciplinary task. Not only are there geotechnical and hydrogeological considerations to where and when a sinkhole may form, but complete risk assessment involves land developers, urban planning, and many more disciplines which fall out of the conventional geoscience practices. However, risk in terms of vulnerability of collapse, from a geotechnical and hydrogeological standpoint, is still an important aspect of a site's sinkhole evaluation.

The three analysis categories discussed in this report include: *in situ* groundwater monitoring (piezometers), subsurface exploration tests (focused on CPTs), and numerical modeling (MODFLOW and PLAXIS 2D). Each category was implemented to form specific analysis tools to aid in sinkhole vulnerability assessment. The specific tools developed include: long-term critical hydraulic gradient identification, predictive groundwater recharge model, sinkhole resistance ratio site mapping from CPTs, and numerical stability modeling of detected raveled cavity.

The first technique, discussed in Chapter 3, is the installation and monitoring of piezometers at a project site to detect irregular groundwater elevations. Through strategic spacing of piezometers, long-term monitoring, and spatial interpolation/contouring of results; it is possible to identify zones experiencing large hydraulic gradients. Since it is established that soil raveling primarily initiates from groundwater recharge through breaches in the confining layer over the weathered limestone (bedrock), detection of a groundwater cone of depression, or extreme closed piezometric contour, is believed to be an indication of a possible sinkhole "throat" or piping phenomenon. The piezometric elevations at a site, obtained from the piezometers, is also required for calibration of the groundwater recharge predictive model (discussed below).

The next technique (discussed in Chapter 4) is the development of a high-resolution groundwater recharge map, using MODFLOW. This tool was developed based on the same principle that sinkhole formation is directly proportional to the rate groundwater is recharging the Floridan aquifer system. The areas where there is a higher recharge rate allow for higher seepage rates that expedite sinkhole formation. This has been shown to be directly correlated to sinkhole occurrence in various studies performed in central Florida (Gray, 1994; Xiao et al., 2016). This study expands upon this principle and furthers the study by developing a high-resolution numerical model to estimate the groundwater recharge rate within a project area, and directly correlate this value to the risk of sinkhole occurrence. Using the numerical model program, MODFLOW, along with piezometric and hydrogeological input parameters, a map of recharge rates was developed for two sites with a grid resolution of 9.8 x 9.8 ft (or 3 x 3m). The resulting maps were used to predict the amount of groundwater recharge at various locations within a project and to identify locations which may be the most vulnerable to sinkhole formation, especially when used in conjunction with the CPT analysis tools presented in Chapters 5 and 6 (discussed below).

Another technique developed was a CPT-based raveling identification chart and the Sinkhole Resistance Ratio indexing procedure. CPT resistance values within verified raveled soils (indicative of sinkhole formation) were statistically grouped to create a simple identification chart to be used for the analysis of CPT data in conjunction with sinkhole investigations. The normalized tip resistance (Q_{tn}) and sleeve friction (f_s) values obtained during a CPT can be plotted on the chart, and any significant raveled soils will fall within the designated areas on the chart. The exact depths at which raveled soils were encountered can then be determined from the chart. An update to the CPT comparison index was formulated, with the addition of resistance and estimated *in situ* stress parameters. The proposed Sinkhole Resistance Ratio (SRR) can be calculated for each CPT sounding and be used to identify the areal expanse and severity of the site's current condition to soil raveling (and the potential for sinkhole formation).

The final analysis technique developed is the creation of stability charts using FEM through PLAXIS 2D (discussed in Chapter 6). These stability charts allow for quick estimation of the safety against stability collapse. When a high density of subsurface testing information is available (as suggested by the authors for known karst environments), a numerical model of the estimated soil strength and raveled soil zone can be developed using PLAXIS 2D. A Mohr-Coulomb failure criteria analysis with a shear strength reduction of the overburden soils was performed to create the these stability charts. These charts were used to estimate the *Factor of Safety* against shear failure of the current soil raveling condition encountered. Any soil conditions yielding a FS close to, or less than 1.0, is believed to be an extremely unstable condition and highly susceptible to sinkhole formation and surface collapse. These charts can also be helpful when estimating how an additional surface loading may affect the stability of the current karst soil conditions.

8.2. Conclusions

Based on the results of this study, the following conclusions and recommendations are made and summarized below:

- Groundwater flow is one of the most important factors to trigger sinkhole collapse (due to soil internal erosion and/or piping); thus, points of groundwater recharge are hypothesized as potential sinkhole sources. Piezometer sensors should be installed at multiple locations (about 20 sensors in this study) and groundwater heads monitored over time. Creating contours of the groundwater table identifies these points of recharge and changes in groundwater flow regime, which can be used as indicators of sinkhole formation. In addition, this groundwater data is needed as a critical input to calibrate the high-resolution recharge model (discussed below).

- The spatial resolution of a groundwater recharge model needs to be enhanced up to 30 m by 30 m to be adequate for geotechnical engineering purposes. This high-resolution recharge model needs to be calibrated with *in situ* piezometer data. The calibrated model can then be used to create a recharge map with the spatial resolution of 30 m by 30 m, providing a tool to assess a site's sinkhole vulnerability. Another use of this groundwater model can be to simulate any scenarios in which hydrogeological conditions change over

time due to extreme rainfall events.

- The sinkhole raveling chart was shown to be a powerful tool to identify whether soils are raveled or not and how severely raveled the soils are at the locations where CPT soundings were performed. In addition, the raveling chart can be used as a criterion to divide the raveled and non-raveled layers for the CPT sounding's profile so that the sinkhole resistance ratio (SRR) can be determined (discussed below).

- The SRR is an index to quantify the severity of sinkhole raveling and can be practically used by geotechnical engineers. The SRR accounts for both CPT tip resistance (q_c) and the geometry of raveled soils, which was shown to be an improvement to the existing Raveling Index (RI). The SRR is a point-based index; however, it can be expanded to two and three dimensions (referred to as line and area scanning) depending on the number of CPT tests and coverage.

- Finite element (FE) analysis can be used to further investigate sinkhole sites including areas of interest with respect to stress/strain and factors of safety in greater detail. A series of FE simulations with different scenarios (e.g., cavity size, overburden soil thickness, strength parameter, etc.) can be constructed to develop a sinkhole stability chart. This stability chart is site specific and provides factors of safety to estimate how susceptible the current site conditions may be to sinkhole formation.

8.3. Recommendations for Future Studies

The authors believe each analysis technique presented can be implemented to effectively detect and evaluate the current vulnerability of sinkhole collapse at a project site. However, like any study, there is always room for improvement. The following items are limitations of the current study, and subsequent suggestions for future endeavors would greatly benefit engineers in their practice of detection and risk management of premature sinkhole formations:

- The techniques presented, with the exception to the long-term groundwater monitoring, either detects or assess the current sinkhole formation at a project site. Sinkholes have been forming and collapsing in Florida over a very long period of time and paleo-sinks (or ancient/relic sinkholes) are abundant throughout the peninsular. Over geologic time, some of these ancient sinkholes may have either been naturally filled or filled through means of early anthropogenic terraforming. Therefore, when present-day subsurface explorations detect vast zones of loose (apparent) raveled material in karst areas, it is not always clear whether this is a result of ancient activity or if the raveling process is still occurring today. Therefore, the time aspect must be integrated into the detection processes to fully quantify the *risk* of sinkhole formation from a geotechnical or hydrological perspective. The authors suggest either CPT or SPT testing over time (e.g., twice a year) in suspected raveling areas to better understand the rate (if any) that the soil structure is being degraded. Laboratory testing can be performed to model this raveling to estimate erosion rates of soils under

varying hydraulic gradient conditions.

- Although the authors believe the CPT-raveling chart is a valuable means of identifying raveled soil zones in central Florida, further testing and data collection can help verify its thresholds for other geological conditions. The CPT-raveling chart was developed using sinkhole sites located within a certain geological stratum (i.e., Cypresshead Formation). Although preliminary comparison with other geological formations show promise, there is an insufficient amount of data from sinkhole collapses in these areas to effectively draw any statistical conclusions. Further CPTs in karst terrains, with both active and ancient sinkholes, will help refine the detection criteria to be used in the implementation of the CPT-raveling chart. Finite element modeling, and testing in controlled soil groups in both the field and laboratory setting, of the CPT resistance measurements can help refine the sensitivity for CPTs to detect soils with little-to-no-stiffness.

- Stability charts developed in this study are site specific and the computed factor of safety may vary from site to site; thus, they may not represent general criteria of sinkhole stability. Therefore, multiples sites where geotechnical and hydrogeological conditions are similar can be analyzed, and all computed charts can be combined to construct a general-purpose stability chart. A reasonable number of sites, along with careful site selection, will be necessary to establish the factor of safety threshold values.

- Mean groundwater data was used to calibrate the high-resolution groundwater model. However, long-term groundwater monitoring will be necessary to better understand how groundwater and soil behave while raveling is occurring. When a breach occurs in the confining layer, groundwater flow regime would be significantly affected, influencing the sinkhole stability. In addition, a change of groundwater contour over time needs to be investigated so that seasonal impacts (e.g., precipitation) on groundwater flow regime can be better understood and how groundwater behaves as the raveling is progressing. An example of groundwater contour monitoring is presented in the Appendix.

REFERENCES

Anderson, M. P., & Woessner, W. W. (2001). *Applied Groundwater Modeling: Simulation of Flow and Advective Transport.* London: Academic Press.

Beck, B. F., & Sinclair, W. C. (1986). *Sinkholes in Florida.* Orlando, Florida: U.S. Geological Survey.

Bowles, J. (1988). *Foundation Analysis and Design, 4th Edition.* New York: McGraw Hill.

Brinkgreve, R. (2002). PLAXIS Finite Element Code for Soil and Rock Analysis-version 8 . Balkema, Rotterdam, Netherlands.

Bullock, P. J., & Dillman, A. (2003, Dec. 8-12). "Sinkhole Detection in Florida Using GPR and CPT". *Presented at the 3rd International Conference on Applied Geophysics, Hotel Royal Plaza.* Orlando, Dec. 8-12.

Domenico, P. A., & Schwartz, F. W. (1990). *Physical and Chemical Hydrogeology.* New York: John Wiley & Sons.

Drumm, E. C., & Yang, M. Z. (2005). "Preliminary screening of residual soil stability in karst terrain". *Environmental & Engineering Geoscience*, 11(1): 29-42.

Environmental Systems Research Institute (ESRI). (2016). *How inverse distance weighted interpolation works*. Retrieved from http://pro.arcgis.com: http://pro.arcgis.com/en/pro-app/help/analysis/geostatistical-analyst/how-inverse-distance-weighted-interpolation-works.htm

Florida Geological Survey. (2001). *Text to Accompany the Geologic Map of Florida.* Tallahassee, Florida: Florida Geological Survey.

Florida Office of Insurance Regulation. (2010). *Report on Review of the 2010 Sinkhole Data Call.* Tallahassee, Florida: Florida Office of Insurance Regulation.

Foshee, J., & Bixler, B. (1994). "Cover-Subsidence Sinkhole Evaluation of State Road 434, Longwood, Florida". *Journal of Geotechnical Engineering*, 120(11): 2026-2040.

Geokon. (2016, September 23). Instruction Manual: Model 4500 Series Vibrating Wire Piezometers. Lebanon, New Hampshire, United States of America.

Gray, K. M. (1994). *Central Florida Sinkhole Evaluation.* Deland, FL: Florida Department of Transportation.

Griffiths, D. V., & Lane, P. A. (1999). "Slope Stability Analysis by Finite Elements". *Geotechniques* , 49(3): 387-403.

Harbaugh, A. W. (2005). *MODELFOW - 2005, the U.S. Geological Survey modular groundwater model - the groundwater flor process.* U.s. Geological Survey Techniques and Methods 6-A16.

Kondner, R. L. (1963). "Hyperbolic stress-strain response cohesive soils". *Journal of Soil Mechanics and Foundations, ASCE 89*, 115-143.

Kulhawy, F. H., & Mayne, P. W. (1990). *Manual on estimating soil properties for foundation design (No. EPRI-EL-6800).* Ithaca, NY (USA): Cornell University.

Mayne, P. W. (2007). *Cone Penetration Testing, National Cooperative Highway Research Program.* Transportation Research Board.

Meyerhof, G. (1974). "Ultimate Bearing Capacity of Footings on Sand Layer Overlying Clay". *Canadian Geotechnical Journal*, 11(2): 223-229, https://doi.org/10.1139/t74-018.

Motz , L. H., Beddow , W. D., Caprara, M. R., Gay, J. D., & Sheaffer, S. M. (1995). *North-Central Florida regional groundwater investigation and flow model (Final Report).* St. Johns River water Management District special publication SJ95-SP7.

Nordal, S. (1999). "Present of Plaxis" . *International symposium, Beyond 2000 in computational geotechnics;* (pp. 45-54). Rotterdam: Balkema.

Olsen, R. S., & Malone, P. G. (1988). "Soil classification and site characterization using the cone penetrometer test". *Penetration Testing*, 887-893.

Perez, A. L. (2017). *Physical Hydrogeological Modeling of Florida's Sinkhole Hazard.* Retrieved from Elctronic Theses and Dissertations: http://stars.library.ucf.edu/etd/5363

Perez, A., Nam, B., Chopra, M., & Sallam, A. (2017). "Understanding of Florida's sinkhole hazard: A hydrogeological laboratory study". *ASCE Geofrontier.* Orlando.

Professional Services Industries, Inc. . (2014). *Sinkhole and Engineering Evaluations Wekiva Parkway and State road 46.* Orlando.

Qureshi, M. U., Khan, K. M., Bessaih, N., & Sadrani, K. A. (2014). "An emprical relationship between insitu permeability and RQD of discontinous sedimentary rocks". *Electronic Journal of Geotechnical Engineering*, 4781-4790.

Reddi, L. N., & Bonala, M. V. (1997). "Critical shear stress and its relationship with cohesion for sand-kaolinite mixtures". *Canadian Geotechnical Journal*, 34(1): 26-33, https://doi.org/10.1139/t96-086.

Rizzo, R., & Dettman, M. (2017). "Sinkhole Early Detection System". *Geofrontiers.* Orlando: ASCE.

Roberston , P., & Cabal, K. (2010). "Estimating soil unit weight from CPT". *2nd International Symposium on Cone Penetration Testing.* Huntington Beach, CA: CPT'10 Organizing Committee.

Robertson, P. (1990). "Soil Classification using the Cone Penetrometer test". *Canadian Geotechnical Journal*, 27(1): 151-158, https://doi.org/10.1139/t90-014.

Robertson, P. K. (2016). "Cone Penetration test (CPT)-based soil behavior type (SBT) classification system - an update". *Canadian Geotechnical Journal*, 53(12): 1910-1927, https://doi.org/10.1139/cgj-2016-0044.

Robertson, P. K., & Campanella, R. G. (1983). "Interpretation of Cone Penetration Tests. Part 1: Sand.". *Canadian Geotechnical Journal, 20(4)*, 20(4): 718-733, https://doi.org/10.1139/t83-078.

Robertson, P. K., & Wride, C. E. (1998). "Evaluating cyclic liquefaction potential using the cone penetration test". *Canadian Geotechnical Journal*, 35(3): 442-459, https://doi.org/10.1139/t98-017.

Rogers, D. J. (2006). "Subsurface Exploration Using the Standard Penetration Test and the Cone Penetration Test". *Environmental & Engineering Geoscience*, 12(2): 161-179. doi: https://doi.org/10.2113/12.2.161.

Rupert, F., & Spencer, S. (2004). Florida's Sinkholes. *Poster 11*. Tallahassee, Florida: Florida Geological Survey, Department of Environmental Protection.

Schanz, T., Vermeer, P. A., & Bonnier , P. (1999). "The hardening soil model: formulation and verification". *Beyond 2000 in Computational Geotechnics.* Rotterdam: Balkema.

Sheets, R. A. (2002). *Use of Electrical Resistivity to Detect Underground Mine Voids in Ohio.* USGS Numered Series.

Sinclair, B. F. (1986). *Sinkholes in Florida.* Orlando: The Florida Sinkhole Research Institute.

Soliman, M. H., Nam, B. H., Youn, H., & Cho, S. (2018, January). "Numerical Analysis on the Mechanical Behavior of Sinkholes". *Transportation Research Board*. Washington D.C., USA: Poster.

Soos. (2001). Properties of Soil and Rock (in German), Grundbautaschenbuch, Vol. 1, 6th Ed. Berlin: Ernst and Son.

Terracon . (2017). *Geotechnical evaluation report US 441 sinkhole at NW 148th street.* Florida Department of Transportation.

Tihansky, A. B. (1999). *Sinkholes, west-central Florida.* United States: U.S. Geological Survey Circular 1182, p. 121-140.

Tu, T. (2016). *Sinkhole Monitoring Using Groundwater Table Data.* Retrieved from Electronic Thesis and Dissertations: http://stars.library.ucf.edu/etd/5236

U.S. Geological Survey. (2009). *http://nationalmap.gov/elevation.html.* Retrieved from National elevation dataset.

Williams, L. J., & Kunainsky, E. L. (2016, March). *Revises hydrogeologic framework of the Floridan aquifer system in Florida and parts of Georgia, Alabama, and South Carolina .* (ver. 1.1., March 2016): U.S. Geological Survey Professional Paper 1807, 140p., 23 pls., http://dx.doi.org/10.3133/pp1807.

Wilson, L. W., & Beck, F. B. (1992). "Hydrogeologic Factor Affecting New sinkhole Development in the Orlando Area, Florida". *National Ground Water Association* (pp. 918-930). Blackwell Publishing Ltd.

Xiao, H., Kim, Y. J., Nam, B. H., & Wang, D. (2016). "Investigation of the impactos of local scale hydrogeologic conditions on sinkhole occureence in East-Central Florida, USA.". *Environmental Earth*, 75:1274.

Zisman, E. D., & Clarey, D. J. (2013). "If It's Weight of Hammer Conditions, It Must Be A Sinkhole?". *13th Sinkhole Conference* (pp. 45-52). Carlsbad, New Mexico: NCKRI Symposium 2.

APPENDIX

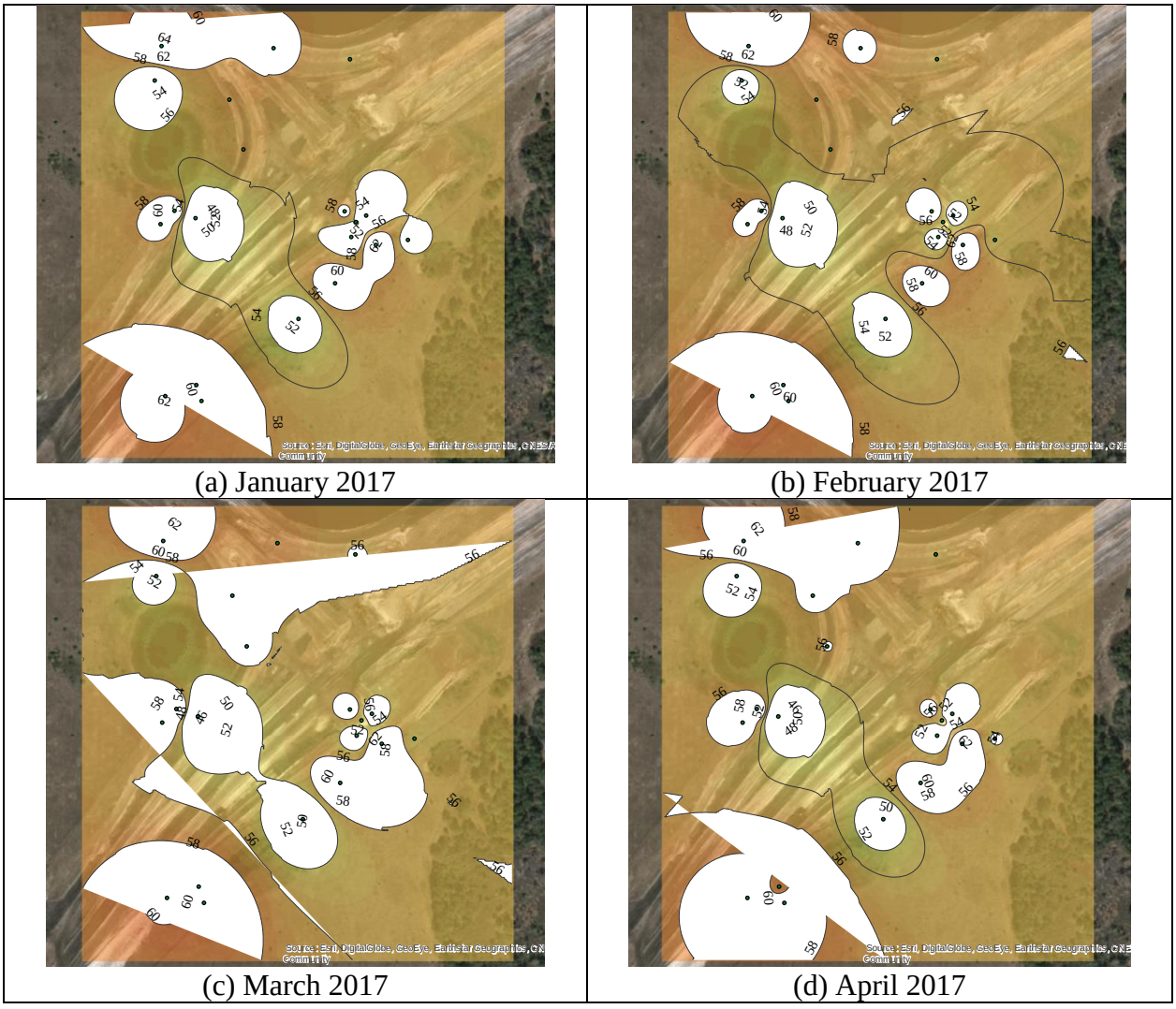

(a) January 2017

(b) February 2017

(c) March 2017

(d) April 2017

Figure A-1: Groundwater table contour of Wekiva Parkway site (January through April)

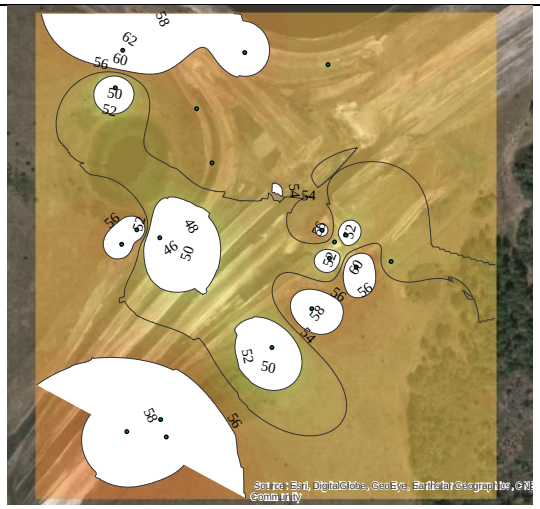

(e) May 2017

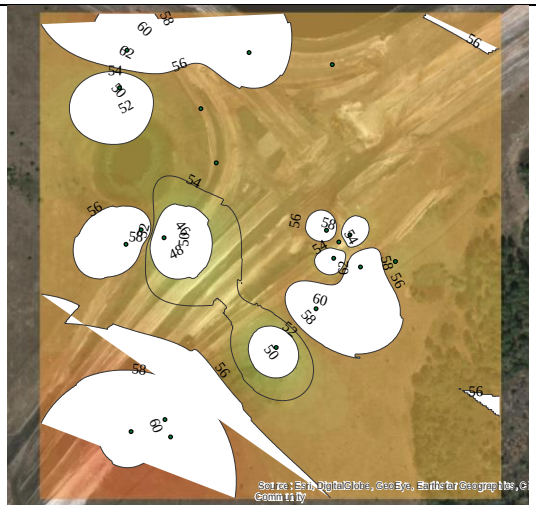

(f) June 2017

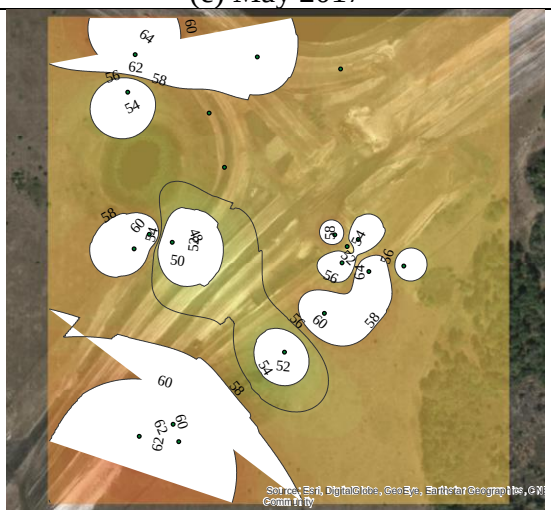

(g) July 2017

(h) August 2017

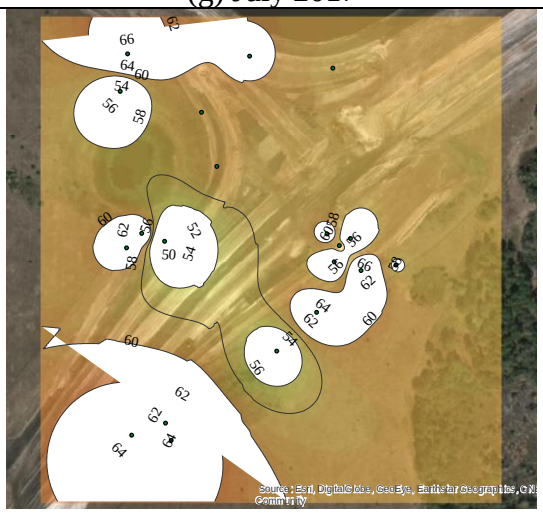

September 2017

Figure A-1: Groundwater table contour of Wekiva Parkway site (May through September)